Inaugural dissertation

for

obtaining the doctoral degree

of the

Combined Faculty of Mathematics, Engineering and Natural Sciences

of the

Ruprecht - Karls - University

Heidelberg

Presented by

M. Sc. Bahar Aksan

born in: Stuttgart, Germany

Oral examination: 28th May 2024

Molecular mechanisms of neuronal structural maintenance and plasticity

Referees: Prof. Dr. Hilmar Bading

Prof. Dr. Daniela Mauceri

Summary

Dendrites receive and process synaptic inputs and thereby coordinate the connections and wiring between neurons which is essential for appropriate brain function. Dendritic structural plasticity is essential throughout development, however in adulthood, dendrites are stabilized and maintained to survive for years, if not throughout a neuron's lifetime, to preserve optimal brain circuitry and cognitive function. Nevertheless, a degree of structural plasticity remains within mature neurons, allowing adaptation to diverse stimuli and experiences. Imbalances in the equilibrium between structural plasticity and stability, such as atrophy or maladaptive plasticity, have been implicated in various neurological disorders. Despite the significance of this delicate balance, the understanding of molecular and cellular mechanisms governing it remains limited. Vascular Endothelial Growth Factor D (VEGFD) is a crucial factor in preserving dendrite morphology of mature neurons. However, its participation in the context of structural plasticity remains uninvestigated. Moreover, its downstream signaling pathways and how they affect the neuronal cytoskeleton to preserve dendrites is unknown.

This thesis shows that VEGFD expression is low in developing or adult neurons during activity-induced structural plasticity to allow morphological changes of dendrites. Employing time-lapse imaging coupled with machine-learning tracking of dendrites, I demonstrated that VEGFD achieves this by maintaining the existing morphological state of neurons, through limiting dendrite elongation and destabilizing newly formed dendrites. Furthermore, I characterized the functions of ezrin and c-Raf in dendrite morphology, two cytoskeleton-related proteins identified as potential downstream targets of VEGFD signaling through phospho-proteomic screening. Using both pharmacological and genetic tools, I demonstrated that VEGFD causes the dephosphorylation of ezrin at tyrosine 478 via activation of the striatal-enriched protein tyrosine phosphatase (STEP). Further, I showed through overexpression of a phospho-mutant ezrin that ezrin is a mediator of the VEGFD-induced preservation of dendrite structure during structural plasticity. Additionally, immunoprecipitation of VEGFD's receptor followed by mass spectrometry revealed the splicing regulator neuro-oncological ventral antigen 2 (nova2) as a potential candidate protein in VEGFD signaling, offering a new path for future research.

Overall, this work identified the downstream molecular and cellular processes of VEGFD signaling in plasticity and proposes that VEGFD regulates the balance between neuronal structural maintenance and plasticity by suppressing morphological alterations in dendrites.

Zusammenfassung

Dendriten empfangen und verarbeiten synaptische Inputs und koordinieren so die Verbindungen und Vernetzungen zwischen Neuronen, die für eine angemessene Gehirnfunktion unerlässlich sind. Strukturelle Plastizität von Dendriten ist während der gesamten Entwicklung von wesentlicher Bedeutung. Im Erwachsenenalter werden die Dendriten jedoch stabilisiert und bleiben jahrelang, wenn nicht sogar ein ganzes Neuronenleben lang erhalten, um eine optimale Verschaltung des Gehirns und kognitive Funktionen zu gewährleisten. Dennoch bleibt in reifen Neuronen ein gewisses Maß an struktureller Plastizität erhalten, das die Anpassung an verschiedene Reize und Erfahrungen ermöglicht. Ein Ungleichgewicht zwischen struktureller Plastizität und Stabilität, wie Atrophie oder maladaptive Plastizität, wurde bei verschiedenen neurologischen Erkrankungen festgestellt. Trotz der Bedeutung dieses empfindlichen Gleichgewichts ist das Verständnis der molekularen und zellulären Mechanismen, die es steuern, nach wie vor begrenzt. Der Vascular Endothelial Growth Factor D (VEGFD) ist ein entscheidender Faktor für die Erhaltung der Dendritenmorphologie reifer Neuronen. Seine Beteiligung an der strukturellen Plastizität ist jedoch noch nicht erforscht. Darüber hinaus sind seine nachgeschalteten Signalwege und wie diese das neuronale Zytoskelett zur Erhaltung der Dendriten beeinflussen, unbekannt.

Diese Dissertation zeigt, dass Expression von VEGFD in sich entwickelnden oder, im Rahmen aktivitätsinduzierter struktureller Plastizität, in erwachsenen Neuronen gering ist, um morphologische Veränderungen von Dendriten zu ermöglichen. Mit Hilfe von Zeitraffer-Aufnahmen in Verbindung mit maschinellem Lernen zum Tracken von Dendriten habe ich gezeigt, dass VEGFD dies durch die Aufrechterhaltung des bestehenden morphologischen Zustands von Neuronen erreicht, indem es die Dendritenverlängerung begrenzt und neu gebildete Dendriten destabilisiert. Darüber hinaus habe ich die Funktionen von ezrin und c-Raf in der Dendritenmorphologie charakterisiert, zwei Proteine, die mit dem Zytoskelett in Verbindung stehen und durch phospho-proteomisches Screening als potenzielle nachgeschaltete Ziele des VEGFD Signals identifiziert wurden. Mit Hilfe pharmakologischer und genetischer Methoden konnte ich zeigen, dass VEGFD die Dephosphorylierung von ezrin an Tyrosin 478 durch Aktivierung der striatal-enriched protein tyrosine phosphatase (STEP) bewirkt. Außerdem konnte ich durch Überexpression einer Phospho-Mutante von ezrin zeigen, dass ezrin ein Vermittler der VEGFD-induzierten Erhaltung der Dendritenstruktur bei struktureller Plastizität ist. Darüber hinaus wurde durch Immunpräzipitation des VEGFD-Rezeptors und anschließende Massenspektrometrie der Spleißregulator neuro-oncological ventral antigen 2 (nova2) als potenzielles Kandidatenprotein für die VEGFD-Signalübertragung identifiziert, was einen neuen Weg für zukünftige Forschungen eröffnet.

Insgesamt wurden in dieser Arbeit die nachgelagerten molekularen und zellulären Prozesse des VEGFD Signalweges bei Plastizität identifiziert und es wird vorgeschlagen, dass VEGFD das Gleichgewicht zwischen neuronaler Strukturerhaltung und Plastizität reguliert, indem es morphologische Veränderungen in Dendriten unterdrückt.

Acknowledgements

I would like to thank everyone who supported and helped me complete my doctoral thesis.

First and foremost, I would like to express my gratitude to Prof. Dr. Daniela Mauceri for her invaluable guidance and support throughout my PhD studies. I feel incredibly fortunate to have had the opportunity to do my PhD under your exceptional supervision and I am truly grateful for your support throughout my time here. You have done so much for me that I appreciate. For example, you made it possible for me to visit Milano as a scientist, and you always encouraged and assisted me to apply for grants and to present at conferences. Moreover, you created a warm and welcoming atmosphere in the lab by organizing events like lab outings and Christmas market visits. I am extremely grateful for all that you have done.

I would like to extend my appreciation to my thesis advisory and examination committee members: Prof. Dr. Hilmar Bading, Prof. Dr. Gudrun Rappold, Dr. Ana Oliveira, and Prof. Dr. Christoph Schuster for their invaluable input, expertise, and guidance.

I want to thank my current and former colleagues, especially Adriana Schneider, Ann-Kristin Kenkel, Dr. Christian Litke, Dr. Janina Kupke, Javier Sánchez Romero, Dr. Katja Baur, Dr. Ricardo Da Cruz Vieira, Stefanos Loizou, and Dr. Stephanie Zeuch. Going through the PhD journey was both rewarding and challenging, but your support and friendship made the lab a great place to work every day.

I would also like to appreciate the experimental contributions of Ann-Kristin Kenkel, Javier Sánchez Romero and Dr. Jing Yan to this project. I would like to thank Dr. Gillian Queisser and Madison Shoraka for their efforts in constructing a mathematical model. I am also incredibly grateful for the technical support provided by my students and HiWis, including Carmen Leibold, Florian Schreiner, Laura Pieper, Lisa Evangelista, and Paula Zimmer.

I want to thank the Department of Neurobiology for all their assistance and support during my work. I especially want to thank Dr. Anna Hertle for taking the time to teach me calcium imaging.

Next, I want to thank Iris Bünzli-Ehret for consistently providing primary neurons over the years, and Monika Schwab, Oliver Teubner, Dr. Otto Bräunling, Dr. Anna Hertle, Antje König, and Irmela Meng for their invaluable technical and administrative support.

I also want to extend my thanks to Dr. Elena Marcello, Dr. Silvia Pelucchi, and Prof. Dr. Monica DiLuca for their ongoing collaboration and for giving me the opportunity to work and learn new techniques in their lab as a visiting scientist.

I am also thankful to the Joachim Herz Stiftung for welcoming me into their network, their inspiring meetings, and their financial support of my experiments.

Ein besonderer Dank geht an meine Familie, die mich bedingungslos unterstützt hat. Vor allem möchte ich meinem Vater danken, der mein Interesse an der Wissenschaft geweckt hat und meiner Mutter für ihre liebevolle Unterstützung. Ohne euren Rückhalt wäre all das nicht möglich gewesen, und dafür bin ich euch zutiefst dankbar.

Abschließend möchte ich Max von ganzem Herzen danken. Deine emotionale Stütze, Geduld und Liebe haben mir in den herausfordernden Zeiten Halt gegeben. Ich bin unendlich dankbar, dich an meiner Seite zu haben.

Table of Contents

List of publications

The thesis encompasses a submitted publication:

Aksan B, Kenkel AK, Yan J, Sánchez Romero J, Missirlis D, Mauceri D. VEGFD signaling balances stability and activity-dependent structural plasticity of dendrites.
In revision at Cellular and Molecular Life Sciences (11.03.2024)

In the course of this thesis, I additionally contributed to the following publications:

Stringhi R, Targa L, D'Andrea L, **Aksan B**, Mauceri D, Pelucchi S, Marcello E. CAP2 as a novel regulator of mitochondria function in neurons.
Manuscript in preparation; Submission planned for first half of 2024.

Padovani A, Pilotto A, Pelucchi S, D'Andrea L, Stringhi R, **Aksan B**, Caratozzolo S, Benussi A, Mauceri D, Canale A, Archetti S, Borroni B, di Luca M, Marcello E. The synaptic marker Cyclase-associated protein 2 is increased in Alzheimer's disease and correlates with Tau pathology.
Manuscript in preparation; Submission planned for first half of 2024.

Pelucchi S, Vandermeulen L, Pizzamiglio L, **Aksan B**, Yan J, Konietzny A, Bonomi E, Borroni B, Padovani A, Rust MB, Di Marino D, Mikhaylova M, Mauceri D, Antonucci F, Edefonti V, Gardoni F, Di Luca M, Marcello E (2020). Cyclase-associated protein 2 dimerization regulates cofilin in synaptic plasticity and Alzheimer's disease. Brain Commun 2:fcaa086. https://doi.org/10.1093/braincomms/fcaa086

Schlüter A, **Aksan B**, Diem R, Fairless R, Mauceri D (2020). VEGFD Protects Retinal Ganglion Cells and, consequently, Capillaries against Excitotoxic Injury. Mol Ther Methods Clin Dev 17:281-299. https://doi.org/10.1016/j.omtm.2019.12.009

Schlüter A, **Aksan B**, Fioravanti R, Valente S, Mai A, Mauceri D (2019). Histone Deacetylases Contribute to Excitotoxicity-Triggered Degeneration of Retinal Ganglion Cells In Vivo. Mol Neurobiol 56:8018-8034. https://doi.org/10.1007/s12035-019-01658-x

Abbreviations

4AP	4-aminopyridine
AD	Alzheimer's Disease
ADP/ATP	adenosine di-/triphosphate
AFM	atomic force microscopy
AMPAR	α-amino-3-hydroxy-5-methyl-4-isoxazolepropionic acid receptor
AP1	activator protein 1
AP2	adaptor protein complex 2
ap2m1	adaptor related protein complex 2 subunit mu 1
Ara-C	arabinofuranoside
Arp2/3	actin-related protein 2/3
ATF	activating transcription factor
bdnf	brain-derived neurotrophic factor
Bic	bicuculline
CamK	calcium-calmodulin-dependent protein kinase
CAP2	cyclase-associated protein 2
CB7	chicken beta actin (CB7)
CBP	CREB binding protein
CFC	cued fear conditioning
CMV	cytomegalovirus
CR	conserved region
c-Raf	rapidly accelerated fibrosarcoma
CREB	cAMP response element binding protein
CRK I/II	C10 regulator of kinase
CsA	cyclosporin A
CTD	C-terminal domain
DAG	diacylglycerol
DARPP-32	dopamine/adenosine-3',5'-monophosphate-regulated phosphoprotein 32
DIV	days in vitro
DM	dissociation medium
DMEM	Dulbecco’s modified eagle medium
EB3	microtubule plus-end-binding protein 3
ECM	extracellular matrix
EGR	early growth response protein
ERAD	endoplasmic reticulum-associated degradation
ERK	extracellular signal-regulated kinase
ERM	ezrin radixin moesin
ERMAD	ERM-association domain
ESARE	enhanced synaptic activity-regulated element
FAK	focal adhesion kinase
FERM	four point one ERM
FIGF	c-fos-induced growth factor
flk1	foetal liver kinase 1
flt4	fms-like tyrosine kinase 4
FosB	FBJ murine osteosarcoma viral oncogene homolog B
FRAP	fluorescence recovery after photobleaching

fyttd1	forty-two-three domain-containing protein 1
G/F-actin	globular/filamentous actin
GDP/GTP	guanosin di-/triphosphase
GM	growth medium
GRB2	growth-factor-receptor-bound protein
GSKα/β	glycogen synthase kinase 3
HBS	HEPES-buffered saline solution
HDAC	histone deacetylase
HEK	human Embryonic Kidney
HiNF	histone nuclear factor
HNF4	hepatocyte nuclear factor 4α
homo	homogenate
hrGFP	humanized *Renilla reniformis* green fluorescent protein
hsc70	heat shock cognate protein 70
hsp70	heat shock protein 70
hspa8	heat shock protein family A member 8
HSPG	heparan sulphate proteoglycans
hsyn	human synapsin
IF	intermediate filament
Ig	immunoglobulin
IMDM	Iscove's modified Dulbecco's medium
IP	immunoprecipitation/immunoprecipitate
IP3	inositol 1, 4, 5-trisphosphate
ITR	inverted terminal repeat
IQGAP1	IQ-motif-containing GTPase-activating protein 1
JMD	juxtamembrane domain
JNK	c-Jun N-terminal kinase
kdr	kinase insert domain-containing receptor
LTR	long terminal repeat.
MAFB	v-maf musculoaponeurotic fibrosarcoma oncogene homolog B
MAP2	microtubule Associated Protein 2
MAP3K	mitogen-activated protein kinase kinase kinase
MAPK	mitogen-activated protein kinase
MEF2	myocyte enhancer factor 2
MEK	MAPK kinase
mEPSCs	miniature excitatory postsynaptic currents
MKK4	mitogen-activated protein kinase kinase 4
MPS	membrane-Associated Periodic Skeleton
MSK1	mitogen stress-activated kinase 1
MT	microtubule
mTOR	mammalian target of rapamycin
N	number
NCK	non-catalytic region of tyrosine kinase
NFAT	nuclear factor of activated T cell
NF-L, -M, -H	light, medium, heavy neurofilament
NF-κB	nuclear factor κ-light-chain-enhancer of activated B cells
NGF	nerve growth factor

NMDA/NMDAR	N-methyl-D-aspartate/N-methyl-D-aspartate receptor
nova2	neuro-oncological ventral antigen 2
NRP	neuropilin
PBS	phosphate buffered saline
PDGF	platelet-derived growth factor
PI3K	phosphatidylinositol-3-kinase
PIP2	phosphatidylinositol 4,5-bisphosphate
PIP3	phosphatidylinositol-3,4,5-trisphosphate
PKA	cyclic AMP (cAMP)-dependent protein kinase
PKC	Ca^{2+}-dependent protein kinase C
PLA	proximity ligation assay
PLC-γ	phospholipase-C-γ
PlGF	placenta growth factor
POU2-Oct	POU2-domain-octamer transcription factor
PP1	protein phosphatase 1
Prox1	prospero-related homeobox 1
PSD	postsynaptic density
PTP	phosphotyrosine phosphatase
qRT-PCR	quantitative real-time polymerase chain reaction
rAAV	recombinant adeno-associated virus
ras	rat sarcoma virus
ROCK	rho-associated protein kinase
rplp2	large ribosomal subunit protein P2
RT	room temperature
RTK	receptor tyrosine kinase
rVEGFC/D	recombinant VEGFC/D
SCR	scrambled
SDS-PAGE	sodium dodecyl sulfate polyacrylamide gel electrophoresis
SGG	salt-glucose-glycine
SH2	src homology 2
SHC	src homology and collagen homology related adaptor protein)
shRNA	small hairpin RNA
snrpd3	small nuclear ribonucleoprotein Sm D3
SNT	simple neurite tracer
STEP	striatal-enriched protein tyrosine phosphatase
t	time
TIF	triton insoluble fraction
TKD	tyrosine kinase domain
TM	transfection medium
TSAd	T-cell specific adaptor
TSF	triton soluble fraction
u2af1	U2 small nuclear RNA auxiliary factor 1
vdac3	voltage-dependent anion-selective channel protein 3
VEGF	vascular endothelial growth factor
VEGFR	vascular endothelial growth factor receptor
VHD	VEGF homology domain
WT	wildtype

List of Figures

List of Tables

Chapter 1. Introduction

1.1 Neuronal architecture

Every brain function is a result of complex neuronal networks. Neurons communicate within the network by transmitting electrochemical signals to other neurons via their tree-like protrusions. A neuron must form the right branches and synapses to properly connect with the right neurons to meet the network requirements (Häusser et al., 2000; Segev et al., 2000). Thus, adaptations of the neuronal circuit and, consequently, the behavioral outcome are established by the highly specialized morphology of single neurons (Cline et al., 2008; Jan et al., 2003; London et al., 2005; Spruston, 2008).

To both transmit and receive signals, neurons have developed a polarized morphology. A neuron generally extends a very long branch, known as the axon, to transmit impulses to other neurons while numerous shorter highly branched structures, called dendrites, receive and process incoming signals (López-Muñoz et al., 2006). Signals are passed from axons to dendrites through synapses that are, in the case of excitatory synapses, often located on small bulbous structures on dendrites, called dendritic spines (Bourne et al., 2008).

The cytoskeleton, consisting of microtubules (MT), actin, and neurofilaments (NF), is the underlying architecture that provides and maintains neuronal morphology (Gentile et al., 2022; Jan et al., 2003; Kapitein et al., 2015). To accommodate the requirements of the functionally and morphologically distinct compartments of neurons, each element of the cytoskeleton is strategically localized and assumes distinct conformations within specific regions (Gentile et al., 2022; Jan et al., 2003; Kapitein et al., 2015) (Figure 1).

1.1.1 Intermediate filaments

NFs are class IV intermediate filaments (IF), with the other classes being class I (acidic keratins), class II (basic keratins), class III (vimentin, desmin, peripherin, and glial fibrillary acidic protein, class V (nuclear lamins), and class VI (nestin) (Yuan et al., 2017). In developing neurons, the class III IF vimentin and the class VI IF nestin are present but are successively replaced by NFs throughout neuronal maturation (Yuan et al., 2017). NFs are 10 nm heteropolymers made up from a combination of five subunits: light (NF-L), medium (NF-M), and heavy (NF-H) molecular mass neurofilament protein, α-internexin, and peripherin. Two subunits form together polarized dimers which arrange to antiparallel tetramers without polarity. Eight of such tetramers anneal laterally to

build a cylindrical so-called unit-length filament. NFs are elongated by the longitudinal end-joining of these unit-length filaments (Yuan et al., 2017). Unlike MTs or actin, neurofilaments are not polarized nor require nucleotide-binding for polymerization (Yuan et al., 2017). NFs are most abundant in myelinated axons where they mechanically support axon shape and diameter and thereby control conduction velocity (Yuan et al., 2017). NFs are also found in dendrites and even spines and are suggested to play a role in synaptic function (Gürth et al., 2023; Yuan et al., 2017). Therefore, NFs received increasing attention in the last years, however knowledge on the involvement of NFs in synaptic function is still limited (Gürth et al., 2023; Yuan et al., 2017). Nevertheless, NFs are considered as rather stationary structures with slow turnover rates in the range of months (Yuan et al., 2012), whereas dynamic morphological changes in neurons are thought to be established by MTs and actin (Coles et al., 2015).

1.1.2 Microtubules

MTs are composed of α-tubulin and β-tubulin heterodimers that attach head-to-tail to form a protofilament in an alternating pattern, leading to a polarization of the MT with α-tubulin on one end, referred to as the minus end and β-tubulin on the other, called plus end. 13 protofilaments with the same polarity assemble parallel to each other to form the final microtubule of 25 nm diameter (Desai et al., 1997). Assembly and disassembly of tubulin dimers occur primarily at the more dynamic plus end, while the minus end is less dynamic. MTs are elongated by the addition GTP-bound tubulin heterodimers (Desai et al., 1997; Walker et al., 1988). Shortly after incorporation into the filament, GTP bound to β-tubulin hydrolyses to guanosin diphosphase (GDP). Due to the time interval between polymerization and GTP hydrolysis, there remains a region of GTP-tubulin, called GTP cap, at the plus end which enables further assembly of tubulin (Mitchison et al., 1984). Loss of the GTP cap, due to hydrolysis or dissociation, induces a rapid disassembly of the MT, called catastrophe (transition from polymerization to depolymerization), until the MT returns to normal growth, called rescue (transition from depolymerization to polymerization). This behavior of sudden switch between growth and shrinkage phases is termed dynamic instability and is a hallmark of MT dynamics (Mitchison et al., 1984).

MTs are found as overlapping bundles that are regularly spaced in dense arrays along the whole length of axons and dendrites (Baas et al., 2016). Single MTs within the array are highly diverse regarding their size, number, dynamics and polarity (Baas et al., 2016). New MTs are nucleated de novo via γ-Tubulin complexes at MT organizing centers at the centrosomes of young neurons that start to differentiate axons and dendrites but switch early on in their development to decentralized MT nucleation and anchoring, such as at the Golgi apparatus, on existing MTs or by severing existing

MTs (Delandre et al., 2016; Kapitein et al., 2015). This gives rise to different orientations of plus- and minus-ends of MTs in neurons. In axons, MTs primarily grow away from the soma toward the periphery, while MTs in dendrites are found with mixed polarity allowing retrograde communication and feedback between synapses and the soma (Baas et al., 2011; Kapitein et al., 2011a) (Figure 1).
MTs provide structural support to axons and dendrites but also generate force via polymerization or sliding through the motor proteins dynein and kinesin to drive axon or dendrite formation and elongation (Kapitein et al., 2015; Poulain et al., 2010; Roossien et al., 2014). Apart from structural functions, MTs also serve as highways for transport of proteins and organelles using the motor forces of kinesin and dynein and as hubs for signaling (Kapitein et al., 2011a; Kapitein et al., 2015).

1.1.3 Actin

Actin is made up of 43 kDa monomeric globular actin (G-actin) molecules that assemble to right-handed double-helical filamentous polymers (F-actin) of a diameter of 7 nm (Amann et al., 2000), which can also organize to higher order structures, such as parallel bundles, branched networks, or rings to give rise to more complex shapes (Blanchoin et al., 2014). F-actin has polarized ends, called barbed or pointed end, respectively. Polymerization occurs with the addition of adenosine triphosphate (ATP)-bound G-actin molecules primarily to the barbed end. Within the filament, ATP is hydrolyzed to adenosine diphosphate (ADP) which reduces G-actin binding affinity. ADP-bound G-actin is largely found at the pointed end from where it dissociates (Amann et al., 2000). F-actin is in a constant state of treadmilling, where polymerization on one side and depolymerization on the other occur simultaneously. When both are at an equilibrium, there is no net change in filament length. This equilibrium can quickly be disrupted by shifting the equilibrium towards more polymerization or depolymerization to remodel filament length (Amann et al., 2000). However, even if F-actin is mostly polymerizing at the tip of a neurite, it drifts backwards due to the physical restriction by the plasma membrane at the neurite tip and due to proximal myosin II-induced contractile forces that pull F-actin backwards (Mallavarapu et al., 1999; Nichol et al., 2016). Tethering of actin to the extracellular substrate via ‘clutch’ molecules, such as cell adhesion molecules, transmits the force of retrograde flow to the substrate, thereby creating a traction force that enables F-actin to push the membrane forward and initiate neurite formation and extension, as well as spine expansion (Mallavarapu et al., 1999; Minegishi et al., 2023; Mitchison et al., 1988; Nichol et al., 2016; Svitkina, 2018). On the other side, reducing linkage to the substrate and increasing pulling forces contribute to neurite retraction (Mallavarapu et al., 1999; Mitchison et al., 1988; Nichol et al., 2016). MTs then invade and structurally support the newly established branch (Georges et al., 2008; Sainath et al., 2015).

In developing neurons or during regenerative growth, actin serves as the major structural component in the guidance of growth cones located on the tips of undifferentiated neuronal processes, called neurites (Gomez et al., 2014; Omotade et al., 2017). In the peripheral regions of growth cones, flat or long thin actin-rich protrusions, called lamellipodia or filopodia, respectively, scan the environment for guidance cues by constant extension and retraction (Lowery et al., 2009; Omotade et al., 2017). Lamellipodia are made up of a dense branched actin network, whereas filopodia contain long unbranched parallel actin bundles (Lowery et al., 2009; Omotade et al., 2017). The central region of growth cones is low of actin and harbors primarily MTs that invade growth cones from the neurite shaft and contribute to axon elongation (Lowery et al., 2009; Sánchez-Huertas et al., 2021). Short F-actin branches are organized as an arc around the central zone in perpendicular orientation to the F-actin bundles of the periphery to control and guide microtubule expansion into the periphery during neurite elongation (Burnette et al., 2008; Medeiros et al., 2006).

In the differentiated axonal compartments, actin plays a crucial role in the organization and transport of proteins at the axon initial segment - a region of 20–60 μm at the beginning of the axon where action potentials are generated, and which demarcates the border between somatodendritic and axonal compartments (Leterrier, 2018) – and the transport and docking of synaptic vesicles at the presynaptic boutons (Doussau et al., 2000).

At the postsynaptic site, actin is 18x more enriched in dendritic spines than in the dendritic shaft (Honkura et al., 2008). Actin is crucial for spine morphogenesis and spine shape. Linear and branched actin networks fill the entire spine from the spine neck to the bulbous head defining whether a spine is a thin filopodium with barely a spine head, short and stubby or mushroom-shaped (Gentile et al., 2022) (Figure 1). The spine actin cytoskeleton is critical for synaptic activity, as spine morphology is tightly linked to synaptic strength (Cingolani et al., 2008; Yuste et al., 2001), but also due to its contribution to the organization of the postsynaptic signaling machinery (Koleske, 2013).

Besides actin, dynamic MTs transiently invade spines, a process that is regulated by synaptic activity and possibly involved in the transport of postsynaptic proteins to spines and transient changes of spine shape (Jaworski et al., 2009; Kapitein et al., 2015).

Despite being mostly enriched in spines, actin is involved in the control of the entire neuronal shape in the form of a network that lies as a thin layer directly underneath the plasma membrane (Gentile et al., 2022; Mikhaylova et al., 2020). This structure, also called cell cortex, is interconnected by non-muscle myosin II motor proteins (Mikhaylova et al., 2020; Salbreux et al., 2012). Myosin moves along F-actin under ATP hydrolysis causing the actin filaments at both ends of the myosin bundle to come closer together (Mikhaylova et al., 2020; Salbreux et al., 2012). As a result, the actomyosin structure

contracts. This mechanism generates membrane tension and controls cell shape and elasticity (Mikhaylova et al., 2020; Salbreux et al., 2012). In the somas of neurons, the cell cortex is found as a lattice that is interconnected by α- and β-spectrin heterotetramers (D'Este et al., 2015; Han et al., 2017). However, in tubular structures of neurons, such as axons, dendrites, and spine necks, the cell cortex is organized as periodical rings made from two braided actin filaments that are stabilized by the actin-capping protein adducin and separated every 180-190 nm by spectrins (Bär et al., 2016; D'Este et al., 2015; Mikhaylova et al., 2020; Xu et al., 2013) (Figure 1). This structure is also referred to as the Membrane-Associated Periodic Skeleton (MPS). Apart from providing structural support (Gentile et al., 2022), the MPS is also involved in the organization of membrane proteins and acts as a signaling platform (Zhou et al., 2022; Zhou et al., 2019). In axons, myosin-induced contractility of actin ring size controls the axon diameter and thereby might control its electrophysiological properties and play a role in the passage of large axonal cargoes (Costa et al., 2021). The MPS might also play a role in MT guidance and stabilization and might serve as a track for motor proteins (Costa et al., 2021; Qu et al., 2017). In dendritic spines, MPS contractility is needed to shorten spine necks and thereby plays an important role in spine maturation (Mikhaylova et al., 2020). In dendrites, but not in axons, Lavoie-Cardinal et al. (2020) reported that actin ring structures may transform into longitudinal actin fibers upon synaptic activity and calcium signaling (Figure 1). These longitudinal fibers do not only run in parallel but can even criss-cross the dendrite (Xu et al., 2013). Their function is still unclear, but they might play a role in the transportation of plasticity-relevant proteins (Lavoie-Cardinal et al., 2020).

Formation of filopodia, precursors of axons, dendrites, and spines (Heiman et al., 2010; Leondaritis et al., 2015; Scott et al., 2001), is thought to be mediated by patches of concentrated branched F-actin at the dendritic plasma membrane (Konietzny et al., 2017; Korobova et al., 2010; Sainath et al., 2015) (Figure 1). Neurite formation is initiated by polymerization of F-actin which generates a force to push the membrane forward (Kessels et al., 2011; Svitkina, 2018). Similar to the formation of cellular protrusions, filopodia formation may also require local detachment of the cortical actin cytoskeleton from the plasma membrane (Bisaria et al., 2020; Welf et al., 2020). Actin patches, with the help of myosin motors, also trap proteins and organelles and are thus involved in their anchoring and organization (Venkatesh et al., 2020).

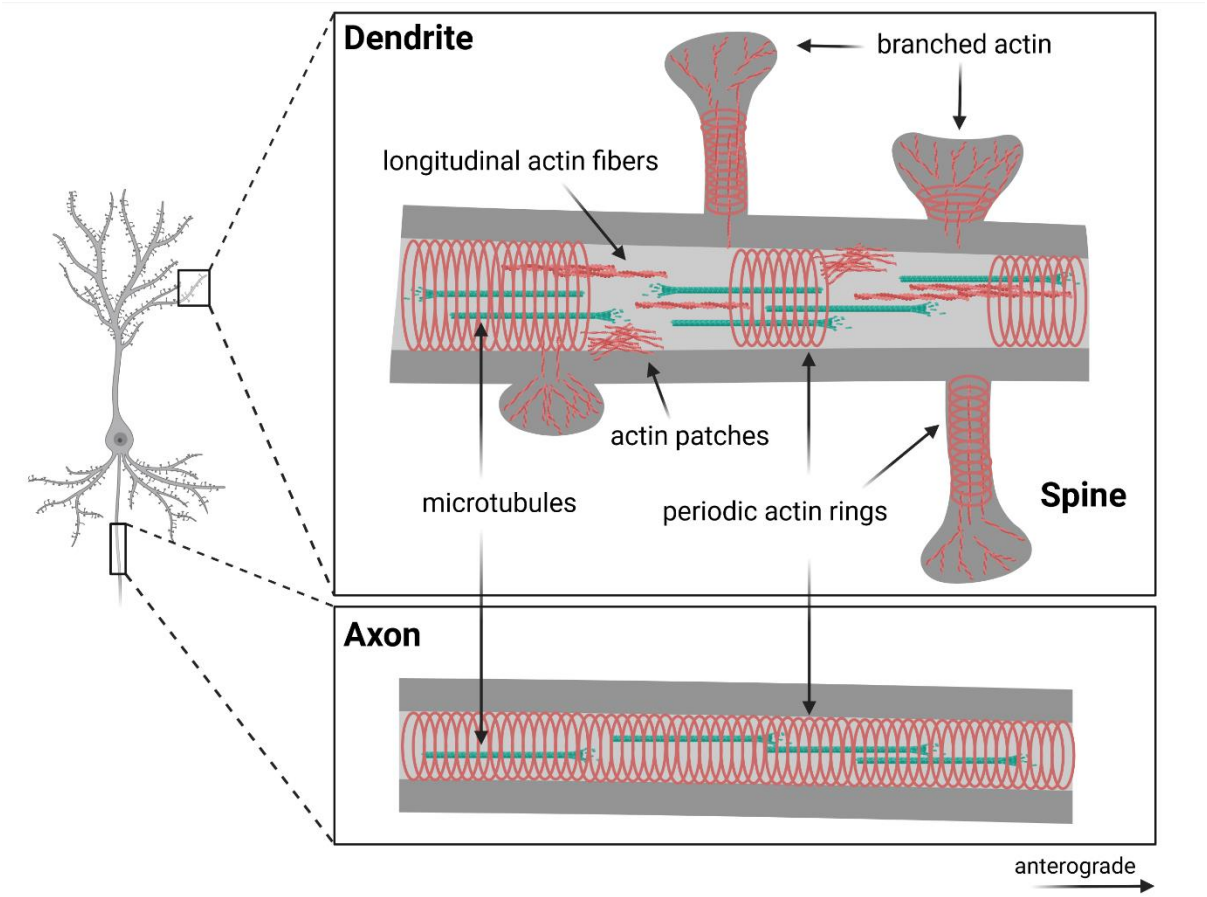

Figure 1. Structure and subcellular distribution of cytoskeletal elements in neurons. *Actin forms periodic rings that line the inner walls of both dendrites and axons. However, in dendrites, actin is observed as longitudinal actin fibers or patches of F-actin, rather than consistently present rings. Microtubules densely array along the entire length of both axons and dendrites. In contrast to axons, dendritic microtubules exhibit bidirectional growth, occurring both anterograde and retrograde. Actin is enriched in dendritic spines, where periodic actin rings line the spine neck, and linear and branched actin networks span the entire structure from the neck to the bulbous head.*

1.1.4 Regulation of neuronal morphology

The cytoskeleton undergoes constant dynamical remodeling, with a turnover of a few seconds to minutes allowing quick rearrangements of the cytoskeleton to guide the growth of neurites during development or to remodel dendrites and synapses during structural plasticity (Koleske, 2013). However, the overall neuronal morphology in mature neurons remains relatively stable for months or years (Koleske, 2013). This seeming discrepancy is possible due to a tight spatial and temporal control of cytoskeletal dynamics that ensures that only a part of the cytoskeleton is remodeled while the other part preserves the overall structure (Koleske, 2013).

MTs are regulated by a plethora of microtubule-associated proteins (MAPs) that control MT dynamics (plus- or minus-end binding proteins), cross-link MTs to bundles (e.g. MAP2 or Tau) or control MT nucleation or severing, and by motor proteins (e.g. dynein or kinesin) that generate

forces or transport proteins along MTs (Kapitein et al., 2015). Furthermore, MTs can be composed from seven α- and eight β-tubulin isoforms in mice or eight α- and nine β-tubulin isoforms in human as well as be posttranslationally modified by the addition of tyrosine, acetyl, glycine or glutamate to create a tubulin code that affects MT intrinsic properties and recruitment of MAPs and motor proteins (Park et al., 2018).

Actin is regulated by different actin-binding proteins that modulate its polymerization or depolymerization by either capping (e.g. profilin) or severing F-actin (e.g. cofilin) or by regulating the availability of G-actin for incorporation into F-actin (Konietzny et al., 2017). A prominent example for the latter is the cyclase associated protein (CAP) which dissociates ADP-actin from F-actin but also exchanges ADP to ATP on G-actin, thereby increasing the pool of G-actin for polymerization (Rust et al., 2020).

Actin nucleators initiate the de novo formation of F-actin and thereby regulate its number and branching. Best studied actin nucleators are formins and the actin-related protein 2/3 (Arp2/3) complex (Konietzny et al., 2017). Actin nucleation by formins results in straight unbranched F-actin that can form bundles, which is typically found in filopodia (Hotulainen 2009), whereas Arp2/3-induces nucleation from existing F-actin to generate branched networks which plays a role in spine head enlargement (Spence et al., 2016).

MTs and actin often cooperate to maintain or induce morphological changes and therefore must be spatially and temporally coordinated with each other. This is achieved by an intricate crosstalk between MAPs and ABPs and was shown to play a crucial role for proper dendrite morphology (Coles et al., 2015; Georges et al., 2008).

The expression and regulation of cytoskeletal regulatory proteins vary in different morphological compartments and throughout different stages of neuronal morphogenesis, accounting for the distinct structures observed (Gentile et al., 2022; Jan et al., 2003; Kapitein et al., 2015). This is controlled by various signaling pathways that are induced by intrinsic cues, such as genetic programs, or extracellular cues (Dong et al., 2015; Jan et al., 2010). Genetic programs provide the construction plan for the overall shape, but it is mainly the extracellular signals that tailor a neuron's shape to its environment (Tavosanis, 2012).

Neurons receive extracellular cues from neighboring cells or the extracellular matrix which are sensed and translated to the cytoskeleton by cell surface receptors such as plexin, ephrin receptors, cadherins, immunoglobulin superfamily receptors and integrins (Dong et al., 2015; Jan et al., 2010). These cues regulate dendritic pattern to ensure optimal wiring by avoiding excessive overlap of dendrites from the same neuron, or of neighboring neurons and by promoting synaptotrophic growth (Wit et al., 2023).

Synaptic activity plays a major role throughout the whole life cycle of a neuron in synaptotrophic growth, structural plasticity, as well as structural maintenance as it indicates the necessity of synaptic connections within the neural circuitry (Lin et al., 2010; Redmond et al., 2005; Tavosanis, 2012). Calcium is a key factor in translating synaptic activity to morphological changes. Upon activity, intracellular calcium levels at the postsynaptic compartment are elevated by the influx of calcium via N-methyl-d-aspartate receptors (NMDAR) or voltage sensitive calcium channels or via the release of calcium from internal storages (Hagenston et al., 2011). This activates the calmodulin-dependent protein kinase I and II (CaMK) and mitogen-activated protein kinase (MAPK)/ extracellular signal-regulated kinase (ERK) signaling pathways that directly act on the local cytoskeleton to mediate filopodia formation and dendrite growth (Hagenston et al., 2011; Redmond et al., 2005). Entrance of calcium into the nucleus, CaMKIV activation and MAPK/ERK signaling additionally activate transcription factors in the nucleus, such as the cAMP response element binding protein (CREB), and induce a delayed but longer lasting and global effect on morphology at the transcriptional level (Hagenston et al., 2011; Redmond et al., 2005). One of the results of synaptic activity-induced transcription is the production and secretion of neurotrophins, such as the brain-derived neurotrophic factor (BDNF), nerve growth factor (NGF) and neurotrophins 3 and 4 which regulate dendrite and axonal growth by acting on the cytoskeleton via multiple signaling pathways, including MAPK, phosphatidylinositol-3-kinase (PI3K)-Akt-mTOR (mammalian target of rapamycin), phospholipase-C-γ-Ca^{2+} (PLCγ-Ca^{2+}) and Rho GTPases (Gonzalez et al., 2016). On the other side, lack of synaptic input or excitotoxicity due to the activation of extrasynaptic NMDARs leads to the inactivation of MAPK/ERK signaling and CREB and Ca^{2+} dysregulation which results in dendrite destabilization and atrophy (Bading, 2017; Cline et al., 2008; Koleske, 2013; Schonfeld-Dado et al., 2009; Vaughn et al., 1988; Verma et al., 2022).

1.1.5 Morphology in development and adulthood

The formation of the intricate, tree-like structure of neurons is a complex and lengthy process. Neuronal stem cells give rise to neuronal progenitors, which then undergo proliferation, differentiation, and long-distance migration (Paridaen et al., 2014). After reaching their designated location within the brain, neurons start with the extension of lamellipodia from their cell bodies. Then, undifferentiated neurites that are guided by growth cones protrude from the lamellipodia. One of them undergoes rapid cytoskeletal reorganization making it grow faster than the others and become an axon. The other neurites develop a few days later into dendrites leading to the distinctive neuron-specific polarization into somato-dendritic and axonal compartments. As neurons mature, dendrites undergo growth and branching, forming secondary and tertiary branches and

thereby give rise to an intricate architecture known as the dendritic tree. Eventually, filopodia appear on the dendritic shaft and develop into spines to form synaptic connections leading eventually to the formation of a network (Craig et al., 1994; Ziv et al., 1996).

The dendritic arbor does not simply develop by growing and addition of dendrites but is in fact under constant remodeling: branches are stochastically overproduced to allow exploration of the surrounding for presynaptic partners. However, only a few find a presynaptic target leading to their activity-dependent stabilization while the other branches are eliminated (Cline et al., 2008; Jan et al., 2003; Vaughn et al., 1988). This mechanism allows morphological adaptation to available synaptic partners by favoring synaptotrophic growth and persists at a slower rate until adulthood, suggesting similar dynamics between developmental and adult plasticity (Cline, 2001; Wong et al., 2002). However, in mature neurons, growth and retraction are more balanced resulting in little net growth of the dendritic arbor (Cline, 2001; Wong et al., 2002). In fact, once the overall dendrite morphology is established at the onset of adolescence, dendrites are increasingly stabilized (Koleske 2013). At this stage up to early adulthood, neurons enter a phase of spine pruning, where certain spines are eliminated while others are retained and mature (Sakai, 2020; Trachtenberg et al., 2002). While up to this point, developmental dendritic growth and stabilization depended on synaptic input, the dendritic arbor is maintained during spine pruning. This allows refinement and elimination of unnecessary synaptic connections and circuits without affecting the overall dendritic arbor (Koleske, 2013). Then, with the beginning of adulthood, spines also become mostly stabilized. The stabilization of dendrites and spines during adulthood is a long-lasting process that can persist for months, years, or even decades (Koleske, 2013; Trachtenberg et al., 2002). It plays a vital role in preserving the structural integrity and functional connectivity of the nervous system. Nevertheless, after completion of neuronal development, a certain degree of structural plasticity, on the level of spines but also dendrites, remains essential in adulthood for normal brain function such as learning and memory and adaptations to a changing environment (Simonetti et al., 2021; Tavosanis, 2012; Trabalza et al., 2012).

Structural plasticity and structural maintenance in adulthood are in a balance to enable the brain to preserve important neural circuits while still possessing the capacity to adapt to the environment (Koleske, 2013; Tavosanis, 2012). As the organism ages, the capacity for structural changes and the preservation of neuronal connections decreases leading to synapse loss and dendritic simplification. As a result, cognitive functions decline with age (Dickstein et al., 2007; Pannese, 2011).

1.1.6 Neuronal morphology during pathological conditions

Development, plasticity, and maintenance of neuronal morphology is a dynamic process involving intricate regulation at various levels. Deregulation at any stage of a neuron's lifetime can lead to malfunction of the circuitry and is a hallmark of many neurological disorders (Kulkarni et al., 2012; Tavosanis, 2012).

Deregulated or impaired structural plasticity and failure to refine synaptic connections during development frequently result in reduced dendrite complexity and spine number, which are commonly observed in developmental disorders. For instance, in Rett syndrome and schizophrenia, there is a reduction in dendrite complexity and spine density across different brain regions (Armstrong et al., 1995; Armstrong et al., 1998; Broadbelt et al., 2002; Glantz et al., 2000; Kolomeets et al., 2007). This reduction is attributed to delayed dendrite and spine maturation in Rett syndrome (Fukuda et al., 2005) and aberrant spine pruning in schizophrenia (Howes et al., 2023). Similarly, autism spectrum disorder is associated with reduced dendrite branching in the hippocampus, accompanied by increased spine density (Hutsler et al., 2010; Raymond et al., 1995).

In adulthood, as neurons enter a stabilization phase to maintain their overall morphology (Koleske, 2013), deficits in maintenance processes can lead to dendrite shortening or spine loss in neurodegenerative disorders such as Alzheimer's disease (AD) (Anderton et al., 1998; El Hachimi et al., 1990; Terry et al., 1991), Parkinson's disease (Stephens et al., 2005; Villalba et al., 2018), Amyotrophic Lateral Sclerosis (Gulino, 2023; Takeda et al., 2014) and Huntington's disease (Ferrante et al., 1991; Guidetti et al., 2001). These maintenance deficits are suggested to manifest as initial symptoms preceding neuronal loss (Bloss et al., 2011). The mechanisms underlying neurodegenerative morphological atrophy differ from those observed during normal aging, where only slight neuronal death occurs (Dickstein et al., 2007; Pannese, 2011). Furthermore, stress, depression and injuries, such as stroke or traumatic brain injury, are pathological conditions characterized by dendritic atrophy and spine loss (Bianchi et al., 2005; Gao et al., 2011; Mauceri et al., 2020; Radley et al., 2004; Soetanto et al., 2010; Sousa et al., 2000; Warner-Schmidt et al., 2006).

On the other hand, increased dendrite branching, spine density, or aberrant spine morphology can also lead to maladaptive plasticity and be detrimental for brain function. In various developmental disorders, mental retardation often exhibits spine dysgenesis. Fragile X syndrome, for example, is characterized by an increased density of immature filopodia-like spines (Rudelli et al., 1985), whereas Down syndrome shows decreased dendrite length and spine density, with unusually long spines coexisting with normally shaped spines (Becker et al., 1986; Marin-Padilla, 1972). De-regulated bursts of neuronal activity in epilepsy can result in maladaptive dendritic sprouting (Ribak et al., 2002). Additionally, neuropathic or chronic inflammatory pain and drug exposure have been

shown to induce dendrite remodeling and aberrant spine formation, potentially contributing to the development of chronic pain and addiction, respectively (Ehlinger et al., 2012; Lu et al., 2012; Metz et al., 2009; Simonetti et al., 2013). Numerous molecules involved in regulating cytoskeletal dynamics have been found to be deregulated in these disorders. For instance, in Rett syndrome and depression, the trophic factor bdnf is implicated (Larimore et al., 2009; Smith et al., 1995; Zhou et al., 2006), while Rho GTPases and cell adhesion molecules are associated with Schizophrenia, AD and Fragile X syndrome (Bongmba et al., 2011; Dahlhaus et al., 2010; Hill et al., 2006; Südhof, 2008; Youn et al., 2007). Scaffolding proteins like shank3 are implicated in autism spectrum disorder and schizophrenia (Durand et al., 2007), and actin-related proteins such as CAP2 and cofilin in AD (Pelucchi et al., 2020). However, the precise mechanisms underlying the dysregulation of these molecules are not fully understood. Excitotoxicity is considered one of the mechanisms that induces morphological atrophy and cell death in many neurodegenerative diseases (Bading, 2017; Verma et al., 2022).

1.2 VEGFD

This thesis investigates the role of Vascular Endothelial Growth Factor D (VEGFD) in neuronal morphology. The following chapter provides an overview of VEGFD and the VEGF family.

1.2.1 The VEGF family

VEGFD was identified for the first time by Orlandini et al. (1996b) as a c-fos-induced growth factor (FIGF) that drives morphological changes in fibroblasts. Later, it was discovered that VEGFD is a secreted protein that is widely expressed in various tissues such as the heart, lung, liver, skeletal muscle, colon, small intestine, and skin throughout development and adulthood (Achen et al., 1998a; Avantaggiato et al., 1998; Lohela et al., 2009; Stacker et al., 1999b). More recent research, however, has revealed expression of VEGFD in neurons, specifically in the hippocampus and cortex, with in some cases higher expression than in endothelial cells (Lein et al., 2007; Mauceri et al., 2011; Saunders et al., 2018; Uhlén et al., 2015; Zeisel et al., 2018).

VEGFD is a member of the VEGF family that plays a crucial role in endothelial cell proliferation, migration, and survival to coordinate the formation and continuous upkeep of the cardiovascular and lymphatic systems (Lohela et al., 2009). VEGFs are however, also involved in neuronal functions, which will be covered in section 1.2.8.

In mammals, the VEGF family comprises the following members: VEGFA (also called just VEGF in older literature), placenta growth factor (PlGF), VEGFB, VEGFC and VEGFD (Lohela et al., 2009).

Structurally related VEGF-like proteins were also recently discovered in some viruses (VEGFE) and snake venom (VEGFF) (Lohela et al., 2009; Yamazaki et al., 2006). VEGFC is structurally the closest homologue to VEGFD, and both are classified as a subfamily within the VEGF family (Achen et al., 1998a; Joukov et al., 1997).

All VEGF family members share a common VEGF homology domain (VHD) (Olsson et al., 2006). The VHD harbors the receptor binding site and a cystine knot motif of eight or nine, in the case of VEGFD and VEGFC, regularly spaces cysteine residues, which is characteristic for the platelet-derived growth factor (PDGF)/VEGF superfamily that the VEGF family is part of (Achen et al., 1998a; McDonald et al., 1993; Olsson et al., 2006). The cystine knot motif allows the stabilization of VEGF dimers via cysteine-disulfide bridges (Olsson et al., 2006). VEGFs exist either as monomers or form homodimers. VEGFA can also form heterodimers with PlGF (Persico et al., 1999) or VEGFB (Olofsson et al., 1999). Monomers arrange in an anti-parallel manner to form covalent dimers (Muller et al., 1997; Stacker et al., 1999b). Homodimers of mature VEGFD and VEGFC, however, are predominantly non-covalently bound (Joukov et al., 1997; Stacker et al., 1999b).

1.2.2 Processing of VEGFs

In addition to the different subtypes within the VEGF family, alternative splicing, protein glycosylation and proteolytic processing give rise to various isoforms of VEGFs with different biochemical properties and interaction affinities (Baldwin et al., 2001b; Holmes et al., 2005; Künnapuu et al., 2021; Stacker et al., 1999a). Proteolytic processing has been observed in several members of the VEGF family, but in the cases of VEGFD and VEGFC, it serves as a critical maturation mechanism (Künnapuu et al., 2021).

VEGFD and VEGFC are both secreted first as full-length prepropeptides of around 50 kDa containing N-terminal and C-terminal extensions that are proteolytically cleaved in the extracellular space to generate a mature form (Joukov et al., 1997; Künnapuu et al., 2021; Stacker et al., 1999b) (Figure 2). Cleavage can be either partial or full leaving only the VHD of around 21 kDa, which has a higher affinity to its receptors and is considered as the mature form (Joukov et al., 1997; Künnapuu et al., 2021; Stacker et al., 1999b).

Alternative splicing in mice creates six VEGFD isoforms of which the most prominent two ($VEGFD_{358}$ and $VEGFD_{326}$) differ in their C terminal propeptides, which may affect the biochemical properties of VEGFD, but are still proteolytically removed (Baldwin et al., 2001b).

The proteases that execute cleavage of VEGFD and VEGFC include serine proteases, such as the proprotein convertases furin, PC5, and PC7, thrombin, plasmin and prostate-specific antigen, and the aspartic endo-protease cathepsin D (Bui et al., 2016; Jha et al., 2019; Künnapuu et al., 2021; Lim

et al., 2019; McColl et al., 2003; McColl et al., 2007). The metalloproteinase ADAMTS3 is specific for VEGFC during developmental lymphangiogenesis (Bui et al., 2016).

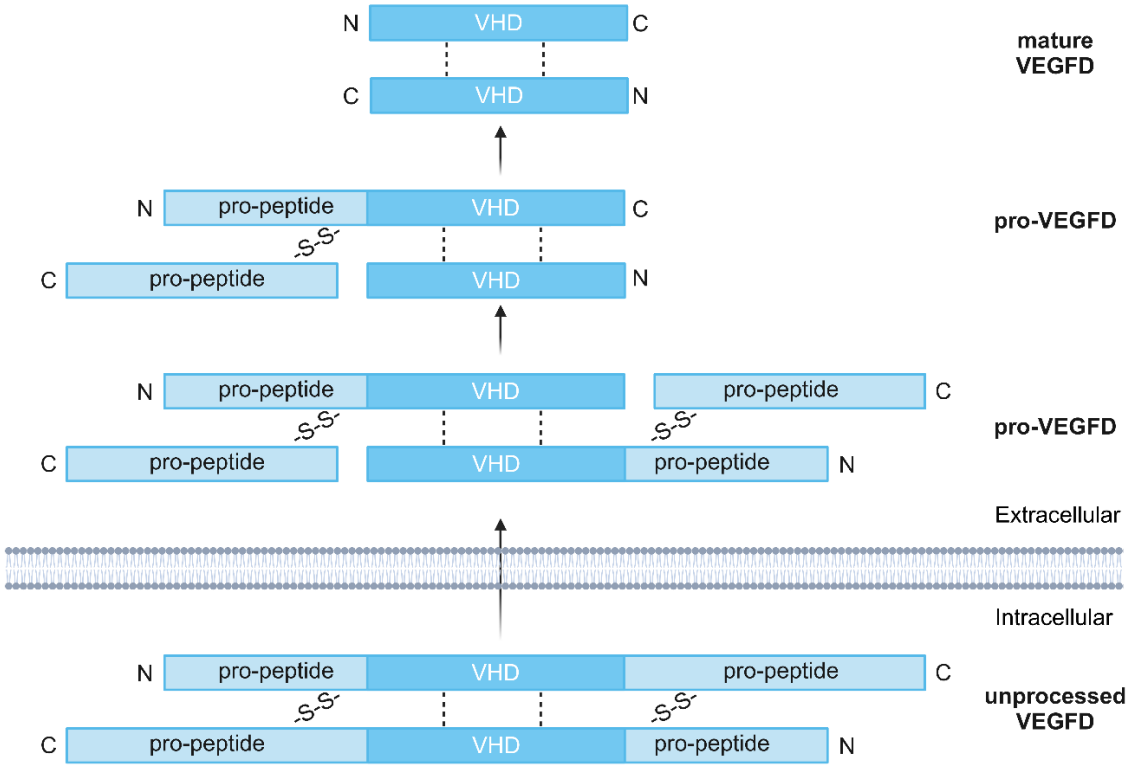

Figure 2. Proteolytic processing of VEGFD. *Unprocessed full-length VEGFD can exist as a monomer or homodimer (as illustrated in this example) stabilized by disulfide bridges. After secretion to the outside of the cell, the C-terminal propeptides are removed, creating pro-VEGFD, followed by the removal of the N-terminal pro-peptides to generate fully mature VEGFD* (Künnapuu et al., 2021). *VHD = VEGF homology domain.*

1.2.3 VEGF receptors

VEGFs are secreted glycoproteins that mediate cellular processes by binding to their cognate VEGF receptors (VEGFRs) at the cell plasma membrane. VEGFRs are receptor tyrosine kinases (RTKs) of which three types are known: VEGFR1 (also known as fms-like tyrosine kinase 1 (flt1)), VEGFR2 (also known as kinase insert domain-containing receptor (kdr), or mouse foetal liver kinase 1 (flk1)) and VEGFR3 (also known as fms-like tyrosine kinase 4 (flt4)). VEGFs and VEGFRs can be additionally bound by non-tyrosine kinase-type co-receptors, such as neuropilin-1 (NRP-1) and neuropilin-2 (NRP-2), extracellular matrix components, integrins, and heparan sulphate proteoglycans (HSPG) which can modulate availability of VEGFs, VEGF/VEGFR interaction and subsequent signaling (Lohela et al., 2009; Olsson et al., 2006). Co-receptors can also present VEGFs to their cognate VEGFRs on the same or neighboring cell (Koch et al., 2011).

All VEGFRs share the same overall structure made up by seven extracellular N-terminal immunoglobulin-like domains, which mediate ligand binding and receptor dimerization, a transmembrane domain, a juxtamembrane domain, a split intracellular tyrosine kinase domain, and a C-terminal tail (Koch et al., 2011; Leppänen et al., 2013) (Figure 3). VEGFR3, however, differs from the other VEGFRs in that its fifth immunoglobulin-like domain is cleaved and connected by a disulfide bridge which may play a role in ligand interaction and receptor stability (Monaghan et al., 2020; Pajusola et al., 1994) (Figure 3).

Upon ligand-binding at the extracellular domain, VEGFRs form homo- or heterodimers of different VEGFR subtypes (Koch et al., 2011; Leppänen et al., 2013). Furthermore, alternative splicing can create soluble forms of these receptors containing only the extracellular domain which can bind and trap their VEGF ligands thereby serving as negative regulators of VEGF signaling (Olsson et al., 2006). In addition, there are two more isoforms of VEGFR3 distinguished by their varying C-terminal tail lengths. The long form is the predominant variant, while the other is 65 amino acids shorter (Galland et al., 1993; Pajusola et al., 1993).

Each VEGF has different receptor affinities depending on its subtype, splice variant, and proteolytic processing (Achen et al., 1998b; Baldwin et al., 2001b; Künnapuu et al., 2021; Lohela et al., 2009; Olsson et al., 2006; Stacker et al., 1999b). Alternative splicing or proteolytic processing can, for example, modify the C-terminal basic heparin-binding domain, which affects the binding of VEGFs to the extracellular matrix, HSPGs and neuropilins and, consequently, govern localization and bioavailability of VEGFs (Harris et al., 2013; Künnapuu et al., 2021; Vempati et al., 2014).

Generally, VEGFA binds to VEGFR1, VEGFR2 and VEGFR1-VEGFR2-heterodimers; VEGFB and PIGF to VEGFR1; VEGFE to VEGFR2; VEGFF to VEGFR1 and VEGFR2; VEGFC and VEGFD to VEGFR3. Proteolytically cleaved mature forms of VEGFC and VEGFD have higher affinity to VEGFR3 than their immature form and can also bind to VEGFR2 or VEGFR2-VEGFR3 heterodimers (Dixelius et al., 2003; Künnapuu et al., 2021; McColl et al., 2007; Stacker et al., 1999b)(Figure 3). In mouse, however, VEGFD was shown to only bind to VEGFR3 (Baldwin et al., 2001a). Leppänen et al. (2011) suggested that mouse-specific changes in the amino acid sequence of the binding surface of VEGFD and not in VEGFR2 are responsible for the inability of VEGFD to bind VEGFR2 in mouse.

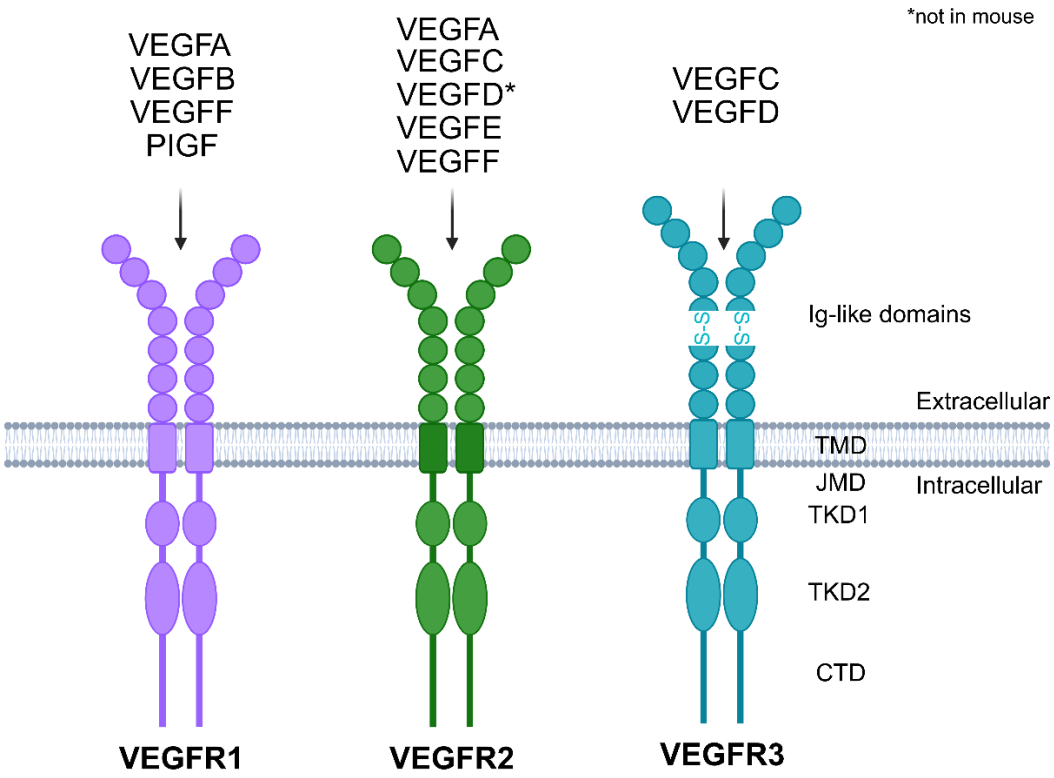

Figure 3. VEGFs and their receptors. *Illustration of the structure of VEGFRs and their binding specificity to different members of the VEGF family. VEGFA also binds to VEGFR1/2 and VEGFC and -D to VEGFR2/3 heterodimers which is not depicted here for the sake of simplification. TMD = transmembrane domain; JMD = juxtamembrane domain; TKD = tyrosine kinase domain; CTD = C-terminal domain.*

1.2.4 Role of VEGFs in the blood vessel and lymphatic system

Variations in VEGF/VEGFR couplings, involvement of co-receptors and the site of expression or secretion enable a wide array of biological functions (Künnapuu et al., 2021; Lohela et al., 2009). In general, VEGFA, VEGFB, and PlGF primarily play a role in the blood vessel system and govern vasculogenesis, the initial formation of a primary capillary plexus from precursor endothelial cells, and angiogenesis, the growth of blood vessels from existing ones (Ferrara et al., 2005; Tammela et al., 2005). Especially, VEGFA is vital for angiogenesis during development. Both homozygous and heterozygous VEGFA knockout mice are embryonically lethal due to defective vascular development (Ferrara et al., 2005), whereas PlGF and VEGFB knockouts show angiogenic defects but are viable (Carmeliet et al., 2001; Tammela et al., 2005).

Although VEGFC and VEGFD are also angiogenic and participate in developmental angiogenesis, they mainly serve as regulators of lymphangiogenesis (Alitalo et al., 2002; Jeltsch et al., 1997; Veikkola et al., 2001). VEGFC is essential for embryonic development of the lymphatics and loss of VEGFC is embryonically lethal (Karkkainen et al., 2004). Even in heterozygous mice, severe defects in their

lymphatic system are observed (Karkkainen et al., 2004). VEGFD, on the other hand, when overexpressed in adult animals, promotes lymphatic vessel growth like VEGFC (Jeltsch et al., 1997; Rissanen et al., 2003; Saaristo et al., 2002). However, it is not required for lymphatic development as lymphatic development is not impeded in VEGFD knockout mice, suggesting a compensation by VEGFC through VEGFR3 (Baldwin et al., 2005; Koch et al., 2009). Nonetheless, dysregulated VEGFD is implicated in several diseases of the lymphatic and angiogenic system, including pulmonary diseases, lymphangioleiomyomatosis, macular degeneration, and diabetic macular edema (Stacker et al., 2018). A mutation in VEGFD that enhances its interaction with the mostly angiogenic VEGFR2, was shown to be involved in pulmonary vasculopathy due to irregular angiogenesis (Bailey et al., 2017). Moreover, elevated levels of VEGFD, originally described as a factor inducible by the proto-oncogene c-fos (Orlandini et al., 1996b), and VEGFC are linked to enhanced tumor angiogenesis and lymphangiogenesis which promotes metastatic spread of tumor cells (Stacker et al., 2018). In addition, ongoing research explores therapeutic approaches involving VEGFD administration to induce angiogenesis or lymphangiogenesis in the context of various medical conditions, such as cardiovascular diseases, inflammation of the skin or adipose tissue in diabetes, secondary lymphedema, wound healing, stenosis of vessels, fetal growth restriction, and peripheral vascular diseases (Stacker et al., 2018). Conversely, inhibiting VEGFD is being investigated as a potential strategy to prevent allograft rejection (Stacker et al., 2018).

The division of VEGFs into primarily angiogenic or lymphangiogenic factors is also reflected in the expression of their receptors on endothelial cells. During early development, all three receptors are broadly expressed on endothelial cells (Alitalo et al., 2002; Kaipainen et al., 1995). However, as development progresses, the expression of VEGFR1 and VEGFR2 becomes primarily confined to blood vascular endothelial cells, while VEGFR3 becomes predominantly expressed on lymphatic endothelial cells (Alitalo et al., 2002; Kaipainen et al., 1995), although VEGFR3 can still be found in a specific group of blood vessels and becomes active again in blood vessels undergoing angiogenesis under pathological circumstances (Partanen et al., 2000; Valtola et al., 1999). VEGFR2-VEGFR3 heterodimers play a role in both lymphatics and blood vessels (Nilsson et al., 2010). Thus, mature VEGFD can act either angiogenic or lymphangiogenic (Bokhari et al., 2023). However, due to the deficient binding of mouse VEGFD to VEGFR2, VEGFD induces angiogenic activity via VEGFR3 (Baldwin et al., 2001a; Bokhari et al., 2023).

The confinement of VEGFRs to primarily blood or lymphatic vessel occurs during the initiation of lymphangiogenesis, which takes place after the establishment of the initial blood vascular system at approximately embryonic day 10.5 (E10.5) (Alitalo et al., 2002; Kaipainen et al., 1995).

Before that, VEGFR3 plays a crucial role in early blood vessel development and knockout of VEGFR3 in mice is embryonically lethal due to cardiovascular failure at E9.5 (Dumont et al., 1998; Haiko et al., 2008). Moreover, its role in early angiogenesis appears to operate independently of its ligands VEGFC and VEGFD or its tyrosine kinase domain, so that the involvement of unidentified ligands, co-receptors, extracellular matrix (ECM) components or interaction with VEGFR2 in initiating VEGFR3-mediated angiogenesis were suggested (Bokhari et al., 2023; Haiko et al., 2008; Zhang et al., 2010). However, after the onset of lymphangiogenesis, VEGFR3 via VEGFC or VEGFD promotes lymphatic growth (Karaman et al., 2018; Veikkola et al., 2001) and inhibition of VEGFR3 at this stage destabilizes newly formed lymphatics during early development (Karpanen et al., 2006; Mäkinen et al., 2001a; Zhang et al., 2010). Interestingly, after the first postnatal weeks, lymphatic growth becomes mostly independent from VEGFR3 signaling and is suggested to be supported by VEGFA signaling, hepatocyte growth factor or angiopoietins (Antila et al., 2017; Karpanen et al., 2006; Mäkinen et al., 2001a; Nurmi et al., 2015).

Similarly, a dysfunctional VEGFR3, like it is the case in Milroy disease due to an autosomal dominant heterozygous missense mutation in the VEGFR3 gene that inactivates its tyrosine kinase domain, leads to impaired lymph drainage and, due to the accumulation of fluids, to hypertrophy, but does not reduce life expectancy (Monaghan et al., 2020; Rockson, 2010).

1.2.5 VEGFD and VEGFC downstream signaling in endothelial cells

VEGFs mainly act via their cognate VEGFRs. VEGFRs, like other RTKs, dimerize upon ligand binding, and are activated by autophosphorylation (Koch et al., 2011; Lemmon et al., 2010). Receptor dimerization leads to the proper alignment and activation of the intracellular tyrosine kinase domains and is believed to initiate a conformational change that exposes a binding site within the kinase domain for adenosine triphosphate (ATP) which delivers the phosphate group for phosphorylation (Koch et al., 2011; Lemmon et al., 2010; Ruch et al., 2007). Upon activation, tyrosine kinases trans-phosphorylate tyrosine residues within the partner receptor's cytoplasmic regions, which serves to control both their kinase activity and their ability to engage with downstream signaling partners (Dixelius et al., 2003; Koch et al., 2011; Lemmon et al., 2010).

Tyrosine phosphorylation patterns differ depending on the VEGFR subtype, the ligand and interactions with co-receptors, accessory proteins, or the ECM, and thus elicit different signaling pathways (Koch et al., 2011; Secker et al., 2021). In VEGFR3, binding of VEGFC and VEGFD results in the phosphorylation of Tyr1230, Tyr1231, Tyr1265, Tyr1337 and Tyr1363 within the cytoplasmic tail and of Tyr1063 and Tyr1068 within the kinase domain (Dixelius et al., 2003; Salameh et al., 2005) (Figure 4). Among them, Tyr1063 and Tyr1068 are essential for receptor kinase activity (Salameh et

al., 2005). Phosphorylated tyrosine residues function as docking sites for downstream signaling molecules (Dixelius et al., 2003; Koch et al., 2011). The specificity of their interactions is determined by the adjacent amino acid sequence proximate to the phosphotyrosine residue (Dixelius et al., 2003). Interacting proteins are typically adaptor molecules equipped with an SH2 (Src homology 2)-domain (Koch et al., 2011; Lemmon et al., 2010). VEGFR2-VEGFR3 heterodimers, however, exhibit a distinct trans-phosphorylation pattern when compared to VEGFR3 homodimers as Tyr1337 and Tyr1363 remain unphosphorylated by the VEGFR2 kinase partner, resulting in an interaction profile distinct from that of VEGFR3 homodimers (Dixelius et al., 2003).

Tyr1230, Tyr1231 and Tyr1337 bind the adaptor proteins SHC (Src homology and collagen homology related adaptor protein) and GRB2 (growth-factor-receptor-bound protein) (Salameh et al., 2005). This leads to the activation of the MAPK ERK1/2 via the GTPases ras (rat sarcoma virus) and c-Raf (proto-oncogene serine/threonine-protein kinase), followed by MEKs (MAPK kinase), or to the activation of PI3K, which phosphorylates the membrane lipid PIP2 (phosphatidylinositol-4,5-bisphosphate) into PIP3 (phosphatidylinositol-3,4,5-trisphosphate) that in turn activates the serine/threonine kinases AKT, also known as protein kinase B (Koch et al., 2011; Salameh et al., 2005) (Figure 4).

Tyr1063 activates the JNK pathway by interacting with adaptor protein CRK I/II (C10 regulator of kinase) (Figure 4). In addition to ligand-induced activation of RTK, VEGFR3 can undergo activation and phosphorylation independently of VEGFC or VEGFD and its kinase activity (Galvagni et al., 2010). Coso et al. (2012) revealed a physical interaction between VEGFR3 and PI3K in lymphatic endothelial cells which occurs regardless of VEGFC presence. Mechanical tension and stretching, due to elevated interstitial fluid levels, was reported to activate VEGFR3 via interactions with mechanosensitive receptors like integrins independently of VEGFC (Planas-Paz et al., 2012; Urner et al., 2019). Interaction between VEGFR3 and integrin triggers Src kinase-induced phosphorylation of the tyrosine residues Tyr830, 833, 853, 1063, 1333, or 1337, leading to the docking of CRKI/II and SHC to VEGFR3 and subsequently, activation of the JNK signaling pathway (Galvagni et al., 2010).

MAPK/ERK1/2, PI3K/Akt and JNK pathways eventually regulate lymphendothelial cell proliferation, migration, and survival to enable growth of vessels (Fournier et al., 1995; Mäkinen et al., 2001b; Salameh et al., 2005). However, their downstream effects, whether involving immediate effects on cell morphology or long-term effects via regulation of gene transcription are poorly understood, particularly regarding VEGFD-VEGFR3 specific signaling (Secker et al., 2021). More extensive research has been conducted on VEGFR3 signaling in the context of VEGFC, primarily due to its crucial role in embryonic lymphangiogenesis (Karkkainen et al., 2004).

It was shown that VEGFC-activated VEGFR3 signaling in lymphatic endothelial cells mainly activates transcription factors or induces their expression (Dieterich et al., 2015; Klein et al., 2016). These include transcription factors that are typically induced by MAPK signaling, such as FosB (FBJ murine osteosarcoma viral oncogene homolog B), ATF3 (Activating Transcription Factor 3) and EGR (Early growth response protein), and transcription factors that are required for lymphatic identity, such as Prox1 (prospero-related homeobox 1), or associated with lymphangiogenesis, such as MAFB (V-maf musculoaponeurotic fibrosarcoma oncogene homolog B) or HOXD10 (Dieterich et al., 2015; Klein et al., 2016). In terms of cell morphology, Durré et al. (2018) demonstrated that the VEGFC-VEGFR3-Tyr1063-Crk-II-JNK pathway regulates lymphatic vasculature via the focal adhesion associated scaffold protein paxillin and the small Rho GTPase Rac1, which are modulators of the cytoskeleton. Furthermore, VEGFC-VEGFR3 signaling in a lung adenocarcinoma cell line was shown to regulate F-actin arrangement via Src-p38-dependent upregulation of the neural cell adhesion molecule contactin-1 (Su et al., 2006).

In neurons, VEGFC-VEGFR3 signaling was shown to play a role in the activation and proliferation of neuronal stem cells through ERK and Akt pathways (Han et al., 2015).

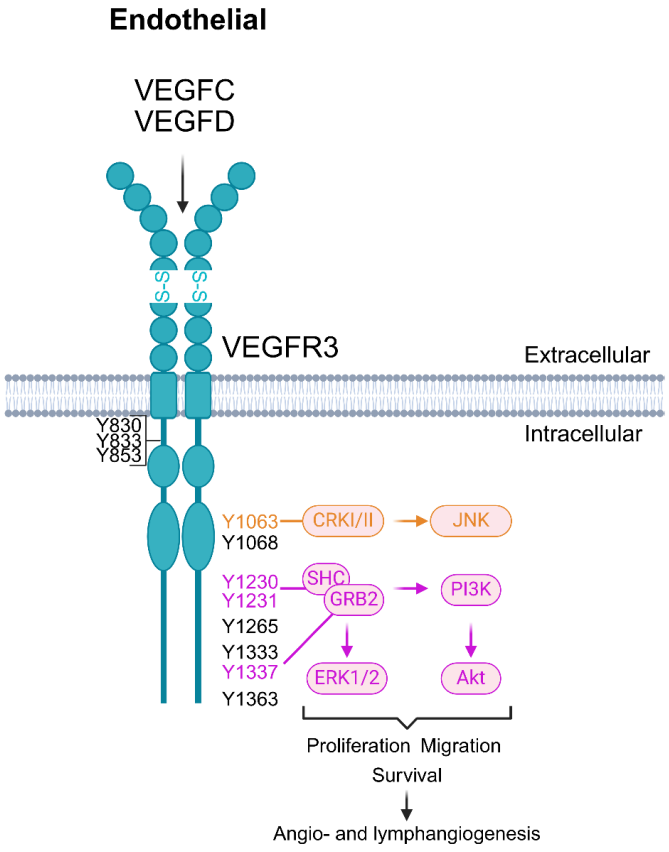

Figure 4. VEGFC- and VEGFD-VEGFR3 downstream signaling in endothelial cells. *Activation of VEGFR3 by VEGFC or VEGFD induces phosphorylation of VEGFR3 at the following tyrosine residues: Y1063, Y1068, Y1230, Y1231, Y1265, Y1337 and Y1363. Phosphorylation at Y1063 causes recruitment*

of the adaptor protein CRKI/II leading to the induction of JNK signaling. Phosphorylation of Y1230, Y1231 or Y1337 recruit SHC and GRB2 inducing ERK1/2 or PI3K/Akt pathways. These pathways eventually induce proliferation, migration and survival of endothelial cells required for angio- and lymphangiogenesis. Tyrosine residues Tyr830, 833, and 853 can be activated independent of ligand binding.

1.2.6 VEGFA downstream signaling in endothelial cells

In contrast, to VEGFR3, VEGFA-VEGFR2-mediated signaling is the most extensively studied pathway within the VEGF family and has revealed a highly complex network of signaling pathways for proliferation, migration, survival and permeability of angiogenic endothelial cells (Wang et al., 2020). Phosphorylated Y1175 or Y801 within VEGFR2 recruit PLCγ, leading to the production of diacylglycerol (DAG) and inositol 1, 4, 5-trisphosphate (IP3) from PIP2 (Wang et al., 2020). IP3 releases calcium ions from the endoplasmatic reticulum which activates in conjunction with DAG the Ca^{2+}-dependent protein kinase C (PKC), which triggers Raf- or Ras-MEK-ERK1/2 signaling (Simons et al., 2016; Wang et al., 2020). Alternatively, PLCγ-PKC induces nitric oxide production to increase vascular permeability (Simons et al., 2016; Wang et al., 2020). PKC via activation of protein kinase D also induces nuclear shuttling of HDACs (histone deacetylase) 5 and 7 and phosphorylation of CREB, leading to transcriptional changes (Koch et al., 2011). PLCγ-mediated elevation of intracellular Ca^{2+} exerts additional transcriptional control via the Ca^{2+} sensor calmodulin (Moccia et al., 2019). Calmodulin activates the Ca^{2+}-dependent serine/threonine phosphatase calcineurin which in turn activates the transcription factor NFAT (nuclear factor of activated T cell). Additionally, calmodulin initiates the phosphorylation of Akt, JNK, and Src through CaMKII, leading to the induction of gene expression (Moccia et al., 2019).

VEGFR2 via Y951 forms a complex with TSAd (T-cell specific adaptor) and Src kinase (Matsumoto et al., 2005). Src signaling leads to the activation of Rho GTPases Rap1, Rac1, Cdc42, and RhoA (Almodovar et al., 2009). Numerous proteins bind to them in a GTP-dependent manner, such as the Rho-associated protein kinase (ROCK) to RhoA, and mediate effects on the actin cytoskeleton, such as cell detachment or filopodia formation (Almodovar et al., 2009). RhoA-ROCK leads among others to the activation of the focal adhesion kinase (FAK), which recruits the scaffold proteins paxillin and vinculin to regulate formation of focal adhesions which connect intracellular actin to the ECM (Almodovar et al., 2009). Src also binds directly to pY1175 and phosphorylates the actin-binding protein IQGAP1 (IQ-motif-containing GTPase-activating protein 1) (Meyer et al., 2008). TSAd-Src or recruitment of the adaptor proteins GRB2 or SHB (SH2-domain-containing adaptor protein B) to pY1175 also activate PI3K-Akt signaling which regulates cell survival by inhibiting apoptotic proteins

but also mTOR signaling and small GTPases, which are involved in cytoskeletal organization (Almodovar et al., 2009; Wang et al., 2020).

pY1214 binds and forms a complex with the adaptor protein NCK (non-catalytic region of tyrosine kinase) and Fyn kinase to induce phosphorylation of cdc42 (cell division cycle 42), which is involved in filopodia formation (Lamarche et al., 1996) and of MAPK p38 which triggers phosphorylation of the actin-binding heat-shock protein 27, which is involved in the reorganization of actin for cell movements (Lamalice et al., 2004; Rousseau et al., 2000; Rousseau et al., 1997). P38 was also shown to be activated by Ca2+-activated protein tyrosine kinase 2β, also known as Pyk2, and Src (McMullen et al., 2004).

1.2.7 VEGFR activation

VEGFRs and RTKs in general, induce similar pathways, but with different intensities, duration, and biological outcomes (Simons et al., 2016). For example, both VEGFA-VEGFR2 and VEGFC-VEGFR3 trigger Akt and ERK signaling pathways, but VEGFR3 induces more pronounced Akt activation, and there are noticeable differences in the activation kinetics of ERK1/2 (Deng et al., 2015). Similarly, VEGFA and VEGFD utilize the same pathways through VEGFR2 in human endothelial cells, but exhibit differences in their kinetics and biological consequences (Jia et al., 2004).

Intensity, duration, and outcome of VEGFR signaling is regulated by the availability of VEGFRs, their ligands, and other interaction partners, such as co-receptors, accessory proteins, or the ECM (Secker et al., 2021; Simons et al., 2016). Moreover, subcellular localization of VEGFRs, such as at lipid rafts, focal adhesions and cell-cell junctions may also affect their output signaling due to interactions with local molecules and pathways (Simons et al., 2016). Crosstalk with other signaling pathways, such as Notch signaling, adds an additional level of regulatory complexity (Simons et al., 2016). In addition, phosphotyrosine phosphatases (PTPs), such as density enhanced phosphatase 1, vascular endothelial PTP, (SH2) domain PTP, and PTP1B, regulate VEGFR phosphorylation (Kappert et al., 2005; Simons et al., 2016). Receptor internalization represents another mechanism governing VEGFR signaling: ligand binding or interaction with accessory proteins or receptors, such as ephrin-B2, induce clathrin-dependent endocytosis, intracellular trafficking and eventually recycling, relocation to specific intracellular compartments or lysosomal degradation of VEGFRs (Lampugnani et al., 2006; Simons, 2012; Wang et al., 2010). This serves to regulate VEGFR presence at the cell surface but is also essential for non-canonical signaling via ERK and Akt pathways as reported for VEGFR2 and VEGFR3 (Koch et al., 2011; Lampugnani et al., 2006; Simons, 2012). VEGFR2-mediated regulation of hippocampal dendritogenesis, for example, requires VEGFR2 internalization (Harde et al., 2019). Even nuclear translocation of VEGFRs, possibly to regulate transcription, was reported, but its

mechanism and role are not fully understood (Domingues et al., 2011; Garces et al., 2006; Silva et al., 2021; Su et al., 2007)

1.2.8 Role of VEGFs in neurons

Given that neurons receive essential nutrients and oxygen through the bloodstream, nerves and blood vessels are intricately connected, exerting mutual influence on each other's growth during both developmental stages and adulthood (Paredes et al., 2018). Neurons, for example, release VEGFA to guide growth of blood vessels, and conversely, VEGFA-mediated blood vessel growth contributes to shaping the nervous system (Adams et al., 2010; Paredes et al., 2018). VEGFA acts as a guidance cue for endothelial cells located at the forefront of vascular sprouts, known as tip cells, as well as for axonal growth cones, which share many structural and functional similarities with endothelial tip cells (Eichmann et al., 2012; Tam et al., 2010). An increasing body of research demonstrates that VEGFA has various other functions in the nervous system (Almodovar et al., 2009; Eichmann et al., 2012; Rosenstein et al., 2010). Similar to endothelial cells, VEGFA acts as a trophic factor that regulates proliferation and migration of neurons or neuronal progenitors and has neuroprotective and neuroregenerative effects (Almodovar et al., 2009; Cao et al., 2004; Cariboni et al., 2011; Jin et al., 2002; Ruiz de Almodovar et al., 2010). VEGFA and/or VEGFR2 was also shown to be required for neurite outgrowth (Khaibullina et al., 2004; Rosenstein et al., 2003), axonal branching (Jin et al., 2006; Luck et al., 2019), and developmental dendrite and spine formation (Harde et al., 2019; Huang et al., 2012; Licht et al., 2010). In addition, neuronal VEGFA signaling via VEGFR2 and/or NRP-1 regulates synaptic transmission and plasticity by enhancing long term potentiation and NMDAR activity, and is required for hippocampal dependent memory (De Rossi et al., 2016; Kim et al., 2008; Licht et al., 2011; Meissirel et al., 2011). A role of VEGFA in synaptic transmission is further corroborated by the finding that VEGFA secretion is dependent on NMDAR or L-type voltage-gated channel activation (Kim et al., 2008) and expression of VEGFR2 at the postsynaptic site (De Rossi et al., 2016; Harde et al., 2019). Dysregulated neuronal VEGFA signaling is also implicated in many neurological disorders (Almodovar et al., 2009; Clark-Raymond et al., 2013; Lange et al., 2016). VEGFC, through VEGFR3 signaling, has been demonstrated to activate and regulate the proliferation of neuronal progenitors and promote neurogenesis (Calvo et al., 2011; Han et al., 2015; Le Bras et al., 2006). VEGFB and PlGF are implicated in neurogenesis, neuronal survival, and neurite outgrowth (Carmeliet et al., 2013).

VEGFD plays a crucial role in dendrite maintenance in adult neurons (Litke et al., 2018; Mauceri et al., 2011; Mauceri et al., 2015), which will be further explained in the section ‘Role of VEGFD in

neurons' below. This role is specific for VEGFD (Litke et al., 2018; Mauceri et al., 2020; Mauceri et al., 2011).

In sum, VEGF family members play crucial roles in the nervous system, despite their initial identification as factors primarily involved in angiogenesis and lymphangiogenesis (Almodovar et al., 2009; Eichmann et al., 2012; Rosenstein et al., 2010). In fact, the VEGF family may have emerged first in the nervous system, as homologues were found in invertebrates that only have a rudimentary vascular system (Popovici et al., 2002).

1.2.9 VEGFA downstream signaling in neurons

Several studies discovered that multiple endothelial VEGFA pathways also play roles in neurons (Almodovar et al., 2009). VEGFA may induce neurite outgrowth via PI3K-Akt and MAPK pathways and Rho and ROCK kinases (Jin et al., 2006; Rosenstein et al., 2003; Sondell et al., 1999). PI3K-Akt-mTOR and PLCγ-Ca^{2+} signaling, followed by CaMKII and CREB activation was discovered as one mechanism through which VEGFA-VEGFR2 regulates synaptic transmission (Kim et al., 2008). PI3K/Akt and MAPK pathways were demonstrated to be involved in VEGFA-mediated neuronal survival (Almodovar et al., 2009). VEGFA was additionally shown to alleviate ischemia-induced Ca^{2+} overload by reducing Ca^{2+} influx through inhibition of voltage-gated Ca^{2+} channels (Ma et al., 2009). VEGFA signaling-activated Src kinases play various roles in neurons (Almodovar et al., 2009). Src-mediated phosphorylation of the actin-binding protein IQGAP1, for example, leads to the recruitment of additional actin- or MT-binding proteins to regulate neuronal migration (Balenci et al., 2007). Src kinase, activated by VEGFA signaling, also contributes to axonal branching (Luck et al., 2019) and, together with Akt signaling, may play a role in VEGFA mediated dendrite development (Harde et al., 2019). However, the exact mechanisms by which these pathways mediate neuronal functions are unclear (Almodovar et al., 2009).

1.2.10 Role of VEGFD in neurons

Synaptic activity via nuclear calcium signaling plays a crucial role in the maintenance of dendrite morphology as described in the previous chapter (Redmond et al., 2005; Redmond et al., 2002). Blocking of nuclear calcium signaling by inhibiting the nuclear calcium/calmodulin complex (Papadia et al., 2005; Zhang et al., 2007; Zhang et al., 2009) with the calmodulin binding-peptide CaMBP4 (Wang et al., 1995) or by overexpressing a catalytically inactive mutant of CaMKIV (CaMKIVK75E) (Anderson et al., 1997; Mauceri et al., 2011) was shown to dramatically reduce length and complexity of the dendritic tree in hippocampal neurons (Mauceri et al., 2011). Among the nuclear calcium/CaMKIV-regulated genes, VEGFD was revealed as the key factor that is responsible for the

observed simplification of the dendritic arbor when nuclear calcium signaling is impaired (Mauceri et al., 2011; Mauceri et al., 2015; Zhang et al., 2009).

It was further demonstrated that shRNA-mediated reduction of VEGFD expression leads to a simplification of the dendritic arbor in cultured hippocampal neurons and in the hippocampus (Hemstedt et al., 2017; Mauceri et al., 2011; Maurer et al., 2020) (Figure 5).

Interestingly, Maurer et al. (2020) revealed that VEGFD knockdown *in vivo* has an asymmetric effect on dendrite morphology: Lack of VEGFD in the hippocampal CA1 layer led to a simplification of basal dendrites. In contrast, apical dendrites, which are characterized by distinct branching patterns and inputs from different layers compared to basal dendrites, exhibited greater dendritic length and complexity. The study by Maurer et al. (2020) proposed regional effects of VEGFD or the presence of a homeostatic mechanism to offset the loss of dendritic structure in basal dendrites.

In line with the simplified dendrite structure and the accompanying reduced plasma membrane surface area induced by VEGFD downregulation, a concurrent reduction in network activity was observed in cultured hippocampal neurons, as evidenced by decreased spike frequencies, reduced neuronal excitability, and lowered membrane capacitance (Mauceri et al., 2011). Furthermore, diminished frequency and amplitudes of miniature excitatory postsynaptic currents (mEPSCs) indicate fewer synapses containing α-amino-3-hydroxy-5-methyl-4-isoxazolepropionic acid receptors (AMPAR), as well as a reduced density of AMPARs within synapses (Mauceri et al., 2011). *In vivo*, on the other hand, membrane capacitance, synaptic potentials, and network oscillations remained unaltered (Hemstedt et al., 2017; Maurer et al., 2020). However, VEGFD downregulation in the hippocampus resulted in a significant impairment of activity-dependent nuclear calcium signaling (Hemstedt et al., 2017).

Reducing VEGFD levels in the hippocampus of mice led to deficits in the formation of spatial and contextual fear memories, both of which are functions associated with the hippocampus (Mauceri et al., 2011). This observed deficit may be attributed to the loss of basal dendrites in CA1 pyramidal cells (Maurer et al., 2020), which receive innervation from the CA2 region (Masurkar, 2018). The CA2 region is responsible for generating sharp wave-ripple complexes, which are linked to long-term memory formation (Oliva et al., 2016). In addition, Hemstedt et al. (2017) demonstrated the significance of VEGFD expression for hippocampus-dependent fear memory consolidation and extinction in mice.

Chakraborty et al. (2021) discovered that VEGFD also reorganizes dendrite structure in neurons that innervate subcutaneous adipose tissue. The involvement of VEGFD in regulating morphological structures other than dendrites, such as axons or spines, is less clear. Previous research demonstrated that knockdown of VEGFD does not impact spine density (Litke et al., 2018; Mauceri

et al., 2011; Mauceri et al., 2015; Maurer et al., 2020), but that administration of VEGFD leads to an increase of axon length, without affecting axon numbers, in developing neurons (Luck et al., 2019). Mouse models of stroke and retina degeneration revealed that VEGFD is downregulated under neurotoxic conditions leading to dendrite loss. Supplementation of VEGFD, however, maintained the structural integrity of dendrites and, consequently, preserved neuronal function (Mauceri et al., 2020; Schlüter et al., 2020) (Figure 5).

In sum, several studies revealed that VEGFD is crucial for the maintenance of mature dendrite morphology, and as a consequence, neuronal and cognitive functions (Hemstedt et al., 2017; Litke et al., 2018; Mauceri et al., 2020; Mauceri et al., 2011; Mauceri et al., 2015; Maurer et al., 2020; Schlüter et al., 2020) (Figure 5).

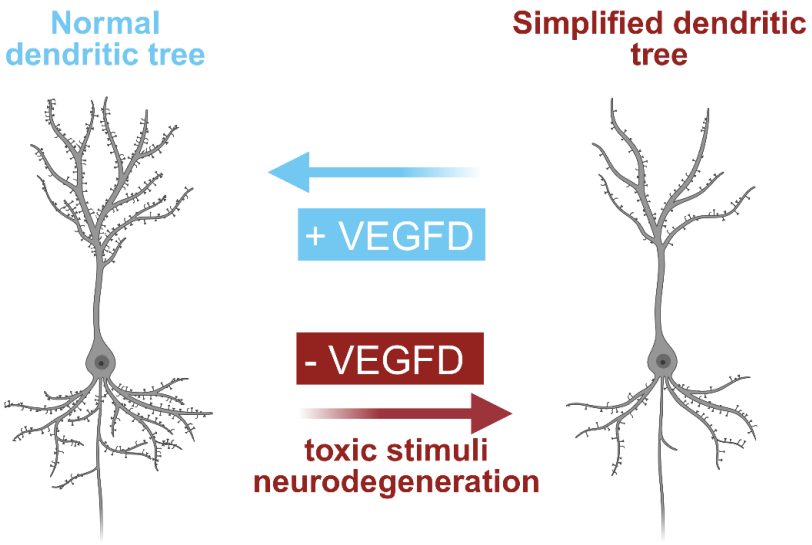

Figure 5. VEGFD is crucial to maintain the structure of the dendritic arbor. *Following toxic stimuli and in neurodegenerative conditions, VEGFD levels are rapidly reduced, leading to the simplification of dendritic trees, cognitive impairments, and neuronal degeneration. The supplementation of VEGFD to counteract downregulation of VEGFD, protects from dendritic simplification, impairments in cognitive function, and neuronal damage.*

1.2.11 Regulation of VEGFD expression and secretion in neurons

Basal levels of synaptic activity in mature neurons maintain VEGFD expression through nuclear calcium CaMKIV signaling (Mauceri et al., 2011). Thus, VEGFD expression also depends on the nuclear calcium buffering capacity of neurons, which is mediated by calcium binding proteins, such as parvalbumin (Mauceri et al., 2015). Computational analysis of transcription regulatory sequences of VEGFD revealed, among others, AP1 (activator protein 1) complex, NFAT (nuclear factor of

activated T-cells), MEF2 (myocyte enhancer factor 2), HiNF (Histone nuclear factor), NF-κB (nuclear factor κ-light-chain-enhancer of activated B cells), POU2-Oct (POU2-domain-octamer transcription factor), and HNF4 (HNF4A hepatocyte nuclear factor 4α) as putative transcription factors (Mauceri et al., 2011). Some of them can interact with the co-activator of CREB, known as CBP (CREB binding protein) (Bedford et al., 2010). CBP, akin to CREB, relies on nuclear calcium and CaMKIV for its activity (Impey et al., 2002) and collaboratively mediates nuclear calcium-induced transcriptional modifications with CREB (Zhang et al., 2009). Although no explicit binding site for CREB, which serves as the principal transcription factor in nuclear calcium signaling, has been identified, the inhibition of CBP has been shown to diminish the transcription of VEGFD (Mauceri et al., 2011).

At an epigenetic level, it has been observed that histone deacetylase 4 (HDAC4) exerts a negative regulatory influence on VEGFD transcription (Litke et al., 2018). In hippocampal neurons, basal synaptic activity, via nuclear calcium signaling, maintains HDAC4 in the cytoplasm (Schlumm et al., 2013). This localization prevents HDAC4 from imposing transcriptional repression on VEGFD (Litke et al., 2018). Disruption of synaptic activity or nuclear calcium signaling results in the accumulation of HDAC4 in the nucleus (Schlumm et al., 2013), leading to the transcriptional suppression of VEGFD (Litke et al., 2018).

VEGFD is a secreted protein (Lohela et al., 2009). However, limited information is available regarding its precise site of secretion and the underlying secretion mechanism in both neuronal and endothelial cell contexts. In contrast, for VEGFA, synaptic activity has been established as a key factor governing its secretion in neurons (De Rossi et al., 2016; Kim et al., 2008). Furthermore, some investigations have observed that the secretion of VEGFA in both endothelial cells and neurons involves extracellular vesicles (Proia et al., 2008; Schiera et al., 2007). Similar mechanisms could potentially be considered for other members of the VEGF family.

1.2.12 VEGFD downstream signaling in neurons

VEGFD signaling is primarily studied in the context of its interaction with its receptors VEGFR2 and VEGFR3, or in the case of mouse VEGFD, only through VEGFR3 (Baldwin et al., 2001a). Full-length VEGFD has also been reported to act intracellularly and independent of its receptors by localizing in fibroblast nuclei and regulating transcription, possibly through interaction with DNA-binding molecules (El-Chemaly et al., 2014).

Mauceri et al. (2011), however, demonstrated that VEGFD maintains dendritic structure through VEGFR3 as knockdown of VEGFR3 leads, similar to knockdown of VEGFD, to dendritic simplification (Mauceri et al., 2011). VEGFD-mediated protection from excitotoxic retinal ganglion cell death due to protection from preceding excitotoxicity-induced dendrite loss, requires VEGFR3 expression

(Schlüter et al., 2020). Furthermore, VEGFD was shown to modulate dendrite morphology of peripheral neurons through VEGFR3 (Chakraborty et al., 2021).

Mauceri et al. (2011) revealed that VEGFD is secreted by neurons and acts mainly in an autocrine manner, whereas both autocrine and paracrine functions are reported for VEGFD in endothelial cells (Bokhari et al., 2023). Little is known on the downstream signal transduction of VEGFD in neurons. The administration of recombinant VEGFD in hippocampal neurons has been observed to activate signaling pathways involving ERK1/2, CREB, and p38 MAP kinase, whereas phosphorylation states of MSK1 (mitogen stress-activated kinase 1), ATF2 (Activating Transcription Factor 2), Akt, MKK4 (Mitogen-activated protein kinase kinase 4), JNK (c-Jun N-terminal kinase), p70, CaMKII, GSKα/β (Glycogen Synthase Kinase 3) remained unaffected by VEGFD (Mauceri et al., 2011). Mauceri et al. (2011) provides further support for the role of p38 as the primary mediator of VEGFD-induced dendrite stabilization, as demonstrated through pharmacological inhibition of p38. Moreover, Mauceri et al. (2020) used phosphorylation levels of p38 or GSK as controls to screen for VEGFD-mimetic peptides.

Nevertheless, the involvement of additional signaling pathways and their translation into alterations in neuronal morphology remains unclear. Given that VEGFD is primarily recognized as an angiogenic and lymphangiogenic factor and is a promising target for a range of angiogenic, lymphangiogenic, and tumor-related conditions, research on VEGFD has predominantly focused on endothelial cells (Stacker et al., 2018), whereas little is known about its signaling in neurons.

1.3 Aim of the project

In an adult organism, the preservation of dendritic structure is essential to ensure the appropriate neural wiring and uphold cognitive function (Koleske, 2013). In many neurological disorders, maintenance of dendrite morphology is disrupted (Arikkath, 2012; Koleske, 2013; Kulkarni et al., 2012; Lin et al., 2010; Parrish et al., 2007). Recent research has unveiled that VEGFD is key for the maintenance of mature dendritic arbor, and, as a result, cognitive functions (Hemstedt et al., 2017; Litke et al., 2018; Mauceri et al., 2011; Mauceri et al., 2015; Maurer et al., 2020). Mouse models of neurodegeneration exhibit decreased VEGFD expression, leading to dendritic atrophy, which can be restored through the administration of VEGFD (Mauceri et al., 2020; Schlüter et al., 2020). This underscores the potential of VEGFD as a promising therapeutic target. However, little is known on VEGFD signaling pathways and the subsequent effects on the neuronal cytoskeleton responsible for executing the VEGFD-induced stabilization of dendrites.

Maintaining established connections in mature neurons is indeed crucial, but during development, structural plasticity plays an essential role (Koleske, 2013). Then, as dendrites transition into

adulthood, they are progressively stabilized; however a certain level of dendritic structural plasticity persists to facilitate adjustments in response to various stimuli and experiences (Koleske, 2013; Simonetti et al., 2021; Tavosanis, 2012; Trabalza et al., 2012). It is unclear what role VEGFD and its downstream signaling plays in structural plasticity during development or in mature dendrites.

The following main questions are addressed in this thesis:

- How does VEGFD impact dendrite morphology during developmental growth of dendrites?
- How does VEGFD impact dendrite morphology and dynamics during synaptic-activity-induced structural remodeling of dendrites?
- Which cytoskeletal elements are targeted and how are they affected by VEGFD signaling?
- What are potential downstream candidates of VEGFD signaling and what role do they play in dendrite maintenance?

Chapter 2. Materials and Methods

2.1 Preparation, maintenance, and treatments of hippocampal cultures

Primary mouse hippocampal cultures were prepared by Iris Bünzli-Ehret in the following way: P0 C57BL/6 mice were decapitated, and hippocampi isolated and cleaned from meningeal tissue in complete dissociation medium (DM), containing DM (Table 1) and Ky/Mg solution (Table 2) in a 1:9 (v/v) ratio. Hippocampi were incubated in 2 x 20 min in 3 ml enzyme solution (10 U/ml Papain latex (Cell Systems GmbH) and 450 µg/ml L-cysteine in complete DM, adjusted with NaOH to pH 7.5-8.0), in a round-bottomed tube containing a slowly stirring magnetic stir bar in a 37°C water bath. Every 5 min, hippocampi were carefully swirled by hand. Enzymatic digestion was stopped by 3 x 1 min washes with careful swirling in 2 ml DM complete, followed by 3 x 5 min incubation in 2 ml trypsin inhibitor solution (10 mg/ml trypsin inhibitor (Sigma Aldrich) in complete DM, adjusted with NaOH to pH 7.5-8.0) at 37°C. Next, hippocampi were washed 3 x 1 min with 2 ml growth medium (GM; Table 3) by careful swirling and removing of DNA slime that developed during the digestion. Then, cells were dissociated three times, by triturating each 40-50 times or 10-20 times in the last step in 2 ml GM using a pipette. After the first two dissociations, 2 ml GM were added, and the mixture let to rest for 5 min before collecting 2 ml of tissue-clump free cell suspension. After the last dissociation, the remaining cell suspension was collected as well to get a final volume of 6 ml. Number of cells was determined using a Neubauer cell counter by diluting 10 µl of cell suspension 1:10 in Trypan Blue. Cells were diluted in OptiMEM-Glucose (Invitrogen) to a final concentration of 0.4 million cells/ml before plating on poly-D-lysine and laminin-coated culture plates with or without ethanol-treated glass coverslips. 1 million cells were plated on 35 mm dishes and 0.18 million cells on 4-or 24-well plates. From then on, cells were kept at 37°C and 5% CO_2. 2.5 h after plating, OptiMEM-Glucose was replaced by GM. At three days in vitro (DIV), cells were treated with 2.8 µM cytosine-D-arabinofuranoside (Ara-C, Sigma Aldrich) to block proliferation of glia cells. Viral infections were done at least 6 h after Ara-C treatment at DIV 3. At DIV 8, GM was replaced by transfection medium (TM, containing salt-glucose-glycine (SGG) solution (Table 4) supplemented with 10% minimum essential medium (Life Technologies) plus sodium selenite (2.9 µM), insulin (72 µM), transferrin (7.2 µM) and penicillin-streptomycin (0.5%)) or cells were transfected using Lipofectamine 2000 (Invitrogen) (Litke et al., 2018; Mauceri et al., 2011; Mauceri et al., 2015). 2.5 µl Lipofectamine 2000 were used to transfect 1 µg DNA. DNA and Lipofectamine were separately mixed each with 50 µl TM in an Eppendorf tube or polystyrene tube, respectively, before combining in the polystyrene tube.

After an incubation of 30 min, mixture was filled up to 500 µl with TM and applied on the cells after removing GM. 2.5-3 h later, medium was replaced with TM. Every other 2 days, medium was half replaced by fresh TM. Experiments were generally performed after a culturing period of 9-14 DIV, when neurons have reached maturity or during development from DIV 0 - DIV3. For live imaging experiments (except neurite length analysis), neurons had to be moved to a different building. This was always done the evening before the experiment to reduce cellular stress on the day of the experiment.

Primary rat hippocampal cultures were prepared in the lab of Prof. Dr. Monica di Luca and Dr. Elena Marcello as described by Gardoni et al. (2002). Treatments were performed at DIV 14.

Table 5 displays an overview of all pharmacological treatments used in this study. Control cells were treated with vehicle only.

Table 1. Dissociation Medium (DM).

Reagent	**Final concentration**
Na_2SO_4	81.8 mM
K_2SO_4	30 mM
$MgCl_2$	5.85 mM
$CaCl_2$	250 µM
Hepes	1 mM
Phenol red	0.2 % (v/v)
Glucose	20 mM
In ddH_2O	

Table 2. Ky/Mg solution.

Reagent	**Final concentration**
Kynurenic acid	10 mM
$MgCl_2$	100 mM
Hepes	5 mM

Phenol red	0.0025 % (v/v)
NaOH	12.5 mM
In ddH_2O	

Table 3. NB-A/Growth Medium (GM).

Reagent	**Final concentration**
Rat serum	1% (v/v)
B-27 supplement (Invitrogen)	2% (v/v)
Penicillin/Streptomycin	0.5% (v/v)
L-glutamine	0.5 mM
in “Neurobasal A” medium (Invitrogen)	

Table 4. Salt-glucose-glycine (SGG).

Reagent	**Final concentration**
NaCl	114 mM
$NaHCO_3$	26 mM
KCl	5.3 mM
$MgCl_2$	1 mM
$CaCl_2$	2 mM
Hepes	10 mM
Glycine	1 mM
Glucose	30 mM
Sodium pyruvate	0.5 mM
Phenol red	0.001% (v/v)
In ddH_2O	

Table 5. Overview of pharmacological treatments.

Drug name	Final concentration	Stock solution	Catalogue Number	Company
Recombinant mouse VEGFD	100 ng/ml	100 ng/µl in PBS	469-VD/CF	R&D Systems
Recombinant mouse VEGFC	100 ng/ml	100 ng/µl in 0.1% acetic acid	4634-10	Biovision
Bicuculline	50 µM	50 mM in DMSO	0130	Tocris Bioscience
TC-2153	1 or 10 µM	10 mM in DMSO	SML-1299	Sigma Aldrich
PP2	1 or 10 µM	10 mM in DMSO	529573	Sigma Aldrich/Merck
BI-0314	100 or 500 µM	500 mM in DMSO	Not commercial, still under testing	Boehringer Ingelheim
Taxol	10 µM	10 mM in DMSO	T7402	Sigma Aldrich
NMDA	20 µM	20 mM in H_2O	BNO385	Biotrend
Nocodazole	10 µM	10 mM in DMSO	M1404	Sigma Aldrich
U0126	10 µM	1 mM in DMSO	BML-E1282-0001	Enzo Life Sciences
Cyclosporin A	1 µM and 5 µM	10 mM in DMSO	30024	Sigma Aldrich

2.2 List of plasmids

Table 6. List of plasmids for shRNA mediated knockdown.

Short name	Construct	Sh sequence 5’ to 3’	Source
Short name	Construct	Sh sequence 5’ to 3’	Source

SCR	pAAV-U6>shSCR-CamKII>mCherry	GTGCCAAGACGGGTAGTCA	Kindly provided by Prof. Dr. Daniela Mauceri (Mauceri et al., 2011).
Sh VEGFD	pAAV-U6>shVEGFD-CamKII>mCherry	GGGCTTCAGGAGCGAACAT	
Sh VEGFR3	pAAV-U6>shVEGFR3-CamKII>mCherry	CCCAGTATTGTGTGGTACAAA	
Sh ezrin 1	pAAV-U6>shezrin1-CamKII>mCherry	GGAAGCAGCTCTTTGATCA	Cloned by me. Sequence derived from commercial siRNA (sc-35350A, SantaCruz).
Sh ezrin 3	pAAV-U6>shezrin3-CamKII>mCherry	CAGAGGCAGAGAAGAATGA	Cloned by me. Sequence derived from commercial siRNA (sc-35350C, SantaCruz).
Sh STEP 1	pAAV-U6>shSTEP1-CamKII>mCherry	GCAGGCGGAATTCTTTGAAAT	Cloned by me. Sequences derived from Yang et al. (2012).
Sh STEP 2	pAAV-U6>shSTEP2-CamKII>mCherry	CCTCTGAGTTCCTACATCAAT	
Sh STEP 3	pAAV-U6>shSTEP3-CamKII>mCherry	GATCCAGACATGCGAACAGTA	
Sh CAP2	pAAV-U6>CamKII-sh-CAP2-CamKII>mCherry	CCAAGTCGTCCGAGATGAATGTCCTGGTC	Kindly provided by Dr. Elena Marcello (Pelucchi et al., 2019).
SCR CAP2	pAAV-U6>CamKII-sh-SCR-CAP2-CamKII>mCherry	GCACTACCAGAGCTAACTCAGATAGTACT	

Table 7. List of plasmids for protein overexpression.

Short name	Construct	Source
hrGFP	pAAV-CMV>hrGFP	Kindly provided by Prof. Dr. Daniela Mauceri (Litke et al., 2018; Mauceri et al., 2011; Mauceri et al., 2015).

VEGFD-HA	pAAV-CMV>VEGFD-HA	Kindly provided by Prof. Dr. Daniela Mauceri (Mauceri et al., 2011; Mauceri et al., 2015; Schlüter et al., 2020).
LacZ-Flag	pAAV-CMV.>LacZ-Flag	
Lenti CMV>VEGFR3-GFP	pLenti6-CMV>VEGFR3-eGFP	Kindly provided by Prof. Dr. Martin Schwartz and Dr. Brian Coon and (Coon et al., 2015).
Lenti hsyn>VEGFR3-GFP	pRRL_hSyn>VEGFR3-eGFP	Cloned by me from VEGFR3-GFP cDNA that was kindly provided by Prof. Dr. Martin Schwartz and Dr. Brian Coon and (Coon et al., 2015).
pAAV VEGFR3-GFP	pAAV-hsyn>VEGFR3-eGFP	Cloned by me from VEGFR3-GFP cDNA that was kindly provided by Prof. Dr. Martin Schwartz and Dr. Brian Coon and (Coon et al., 2015).
Lenti CMV>VEGFR2-GFP	pLenti6-CMV>VEGFR2-eGFP	Kindly provided by Prof. Dr. Martin Schwartz and Dr. Brian Coon and (Coon et al., 2015).
pAAV VEGFR2-GFP	pAAV-hsyn>VEGFR2-eGFP	Cloned by me from VEGFR2-GFP cDNA that was kindly provided by Prof. Dr. Martin Schwartz and Dr. Brian Coon and (Coon et al., 2015).
Hsyn>GFP	pAAV-hsyn>eGFP	Kindly provided by Dr. Annabelle Schlüter.
Ezrin WT	pAAV-hsyn>ezrin WT-Flag	Cloned by me from ezrin WT and mutant cDNA that was kindly provided by Prof. Dr. Peter A. Greer and Prof. Dr. Bruce E. Elliott (Mak et al., 2012).
Ezrin Y478F	pAAV-hsyn>ezrin Y478F-Flag	
Ezrin Y146F	pAAV-hsyn>ezrin Y146F-Flag	
Ezrin Y146F-Y478F	pAAV-hsyn>ezrin Y146F-Y478F-Flag	
LacZ-HA	pAAV-hsyn>LacZ-HA	Cloned by me. Backbone was kindly provided by Dr. Anna M. Hagenston.

cRaf WT	pAAV-hsyn>cRaf WT-Flag	Kindly provided by Dr. Jing Yan.
cRaf S43A	pAAV-hsyn>cRaf S43A-Flag	
cRaf S43D	pAAV-hsyn>cRaf S43D-Flag	
STEP	pAAV-CB7.CI>STEP61-V5	Purchased from Addgene (P3791)
ESARE>STEP	pAAV-ESARE>STEP61-V5-HA-hsyn>tDimer	Cloned by me. Backbone was kindly provided by Prof. Dr. Ana Oliveira (Gulmez Karaca et al., 2020; Kawashima et al., 2013).
ESARE>VEGFD	pAAV-ESARE>VEGFD-HA-hsyn>tDimer	Kindly provided by Prof. Dr. Daniela Mauceri.
ESARE>LacZ	pAAV-ESARE>LacZ-HA-hsyn>tDimer	Kindly provided by Prof. Dr. Ana Oliveira (Gulmez Karaca et al., 2020; Kawashima et al., 2013).
EB3-GFP	CB>EB3-GFP	Kindly provided by Prof. Dr. Casper C. Hoogenraad (Stepanova et al., 2003).
Lifeact-GFP	CMV>lifeact-GFP	Kindly provided by Dr. Silvia Pelucchi and Dr. Elena Marcello (Heinze et al., 2022; Riedl et al., 2008).
LifeAct-TagGFP2	CB>lifeAct-TagGFP2	Kindly provided by Dr. Christian Njoo (Njoo et al., 2015; Riedl et al., 2008).
jRGECO1alpha-NLS	pAAV-CaMKII>jRGECO1alpha-NLS	Kindly provided by Dr. Anna M. Hagenston (Litke et al., 2022).

All constructs that were not cloned by me have been previously characterized (see publications in plasmid tables).

2.3 Molecular cloning

2.3.1 Preparation and ligation of plasmid backbone and insert

Inserts of interest were amplified from template DNA plasmids by polymerase chain reaction (PCR) using 2x Phusion High-Fidelity PCR Master Mix (Thermo Fisher Scientific) in a total reaction of 50 µl using typically 20 – 200 ng template DNA. 2 µl of 10 µM sense and antisense primers (Sigma) were used each. Primers were designed to align with the ends of the insert of interest. An overhang of a few nucleotides was added to generate enzyme restriction sites. General rules for optimal primer design were considered. For long or difficult to amplify sequences, 5-9% DMSO was added to increase efficiency. Negative controls without template DNA were always run in parallel. PCRs were run on a ProFlex PCR system (Applied Biosystems). The PCR program that was generally employed is shown in Table 8. Annealing temperature, elongation time and cycle number were adjusted depending on primer melting temperatures and length of amplicon.

PCR products were checked for the correct size, purity, and yield on agarose gels and purified using the QIAquick® PCR Purification Kit (Qiagen) according to manufacturer's protocol. Briefly, PCR product was mixed with five volumes of buffer PB and centrifuged in a QIAquick column placed on a 2 ml collection tube for 30 s with 20238 g (14680 rpm, in an Eppendorf centrifuge, 5424R rotor). Flow-through was discarded and column was washed with 750 µl buffer PE before repeating centrifugation. Column was spun again with an empty collection tube for 1 min to remove residual wash buffer. DNA was eluted with 50 µl H_2O into a clean 1.5 ml tube by 1 min centrifugation.

Purified PCR products were digested with restriction enzymes at the restriction sites that were generated via PCR and the backbone plasmid was digested to linearize it and to create sticky ends that are compatible with the digested insert. Typically, 15 µg of plasmid or all of PCR product were digested in a total reaction volume of 50 µl using ca. 40 U enzyme at 37°C for 3 h. Buffers and enzyme combinations were chosen based on enzyme compatibility.

Digested insert and backbone were run and purified on an agarose gel using the QIAquick® Gel Extraction Kit (Qiagen) according to manufacturer's protocol. Briefly, DNA band was excised from an agarose gel with a clean scalpel. Gels were dissolved in 300 µl buffer GC per 100 mg gel for 10 min with occasional vortexing in a 50°C water bath. 100 µl isopropanol per 100 mg gel was added and the mixture centrifuged in a QIAquick spin column placed on a 2 ml collection tube for 1 min with 20238 g (14680 rpm, in an Eppendorf centrifuge, 5424R rotor). Flow-through was discarded and column was washed with 750 µl buffer PE before repeating centrifugation. Column was spun again with an empty collection tube for 1 min to remove residual wash buffer. DNA was eluted with 50 µl

H_2O into a clean 1.5 ml tube by 1 min centrifugation. 50 ng plasmid backbone was typically incubated with a typically 2 – 7-fold molar excess of insert using 1 µl T4 DNA ligase in 2x Quick ligation buffer (New England Biolabs) in a total volume of 10 µl for 15 min at RT.

DNA concentrations were always measured at a DeNovix DS-11 spectrophotometer (DeNovix Inc.).

Table 8. PCR program used for molecular cloning.

Step	Temperature	Duration	Cycles
Initialization	50°C	2 min	1 cycle
Denaturation	98°C	30 s	35-40 cycles
Annealing	58-70°C	30 s	
Elongation	72°C	30 s/kb DNA	
Final elongation	72°C	5 min	1 cycle
Final hold	4°C	Forever	1 cycle

2.3.2 Small hairpin RNA (shRNA) oligo annealing

Oligos for small hairpin RNA (shRNA) were designed to harbor a 19 - 21 nucleotides sequence in sense- and antisense orientation from a gene targeted for suppression. Sense- and antisense sequences were separated by a nine nucleotides spacer serving as the hairpin loop that folds back to form a 19 – 21 nucleotides pair stem-loop structure. Oligos were additionally flanked by BamHI and HindIII restriction enzyme sites to create sticky-ends for ligation. A point-mutation in BamHI was introduced for later restriction enzyme screening. Oligos were ordered from Sigma. 3 µl T4 ligase buffer (New England Biolabs) were used to anneal 3 µl sense 3 µl antisense oligos in a reaction volume of 30 µl. Annealing reaction was run on a ProFlex PCR system (Applied Biosystems) using the program shown in Table 9. A small aliquot was checked for the correct size, purity, and yield on a 3% agarose gel. DNA concentration was measured at a DeNovix DS-11 spectrophotometer (DeNovix Inc.).

Table 9. Oligo annealing program.

Step	Temperature	Duration
1	97°C	10 min
2	80°C	5 min
3	75°C	10 min
4	60°C	5 min
5	30°C	5 min
6	4°C	Forever

2.3.3 Agarose gel electrophoresis

Agarose gel electrophoresis was performed to separate DNA by size. Agarose gels were prepared from 0.5% - 3% (0.5% - 1% for low molecular weight, 1% - 3% for higher molecular weight) agarose in TBE buffer (89 mM Tris, 89 mM boric acid, and 2 mM EDTA). A few microliters of Midori Green (NIPPON Genetics) were mixed into the gel to stain DNA. Samples were mixed with 6x loading dye (New England Biolabs) and loaded in individual lanes. GeneRuler 1kb Plus DNA ladder or 100 bp Plus ladder (Thermo Scientific) served as reference. Gels were run at a constant voltage of 120 V in TBE buffer. Midori Green-stained DNA bands were revealed with UV light.

2.3.4 Transformation of competent bacteria

Rubidium Chloride competent E. coli bacteria were used to transform ligation product. Generally, 5 µl ligation product was mixed into 50 µl competent cells and incubated on ice for 30 min, followed by a heatshock of 90 s in a 42°C water bath. Heatshock was stopped by placing cells back on ice for a few min. Bacteria were let to grow for 1 h on a shaker at 37°C after addition of 1 ml LB (Luria-Bertani) medium (10 g tryptone, 5 g yeast extract, 10 g NaCl in 1 l H_2O). Bacteria were pelleted for 5 min at 3500 rpm (Eppendorf centrifuge, 5424R rotor). Bacterial pellets were resuspended in 100 µl of the supernatant and plated evenly using glass beads on LB-agar plates. The plates contained 100 µg/ml ampicillin to prevent growth of non-transformed bacterial colonies, as all plasmids used in this project contained an ampicillin resistance gene. After at least 5 min incubation at RT, bacterial plates were incubated upside down in a 37°C incubator overnight. Single colonies were picked with small

pipette tips the next day and grown in liquid LB medium containing ampicillin overnight. 3 – 5 ml were used for minipreps, 200 – 400 ml for maxipreps.

2.3.5 Plasmid purification from bacteria

Plasmids were purified from overnight liquid bacterial cultures using the QIAprep® Spin Miniprep kit (Qiagen) or PureLink™ HiPure Plasmid-Filter Maxiprep Kit (Thermo Scientific) according to manufacturers' protocols.

For the miniprep, 3 – 4 ml overnight liquid culture were pelleted 3 min at 20238 g (14680 rpm, in an Eppendorf centrifuge, 5424R rotor). Pellets were resuspended vigorously in 250 µl buffer P1, before gently mixing 250 µl lysis buffer P2. After 5 min, lysis was stopped by gently mixing with 350 µl neutralization buffer P3. Mixture was centrifuged for 10 min at 20238 g and 800 µl of the supernatant loaded on QIAprep 2.0 Spin columns placed on 2 ml collection tubes and spun down for 1 min. After washes in 500 µl buffer PB and 700 µl buffer PE, columns were centrifuged without any buffer to remove residual buffer. Plasmid DNA was eluted by incubating the column membrane with 50 µl H_2O and spinning down for 1 min at 20238 g. The eluate was re-eluted to increase yield. All washes were followed by 1 min centrifugation at 20238g and flow-through was always discarded.

For maxipreps, 200 – 400 ml overnight liquid culture were pelleted for 10 min at 6000 rpm (J-14 Beckman Coulter rotor). Pellets were resuspended vigorously in 10 ml resuspension buffer R3, before gently mixing and incubating for 5 min with 10 ml lysis buffer L7. Lysis was neutralized by mixing gently with 10 ml buffer N3 and mixture centrifuged for 10 min at 4000 rpm (#7570E Heraeus Instruments rotor) before loading on HiPure Filter Maxi Columns that were pre-equilibrated with 30 ml equilibration buffer. After lysate flow-through, columns were washed with 60 ml wash buffer W8. Plasmids were eluted with 15ml elution buffer E4. DNA was precipitated by mixing the eluate thoroughly with 10.5 ml isopropanol and centrifuging for 30 min at 11200 rpm (JA-20 Beckman Coulter rotor). Isopropanol was removed and DNA pellets were washed with 5 ml 70% ethanol. Ethanol was removed by spinning for 5 min at 20238 g (14680 rpm, in an Eppendorf centrifuge, 5424R rotor) and DNA pellets were air-dried. DNA was resuspended in 500 µl H_2O.

DNA concentrations were measured at a DeNovix DS-11 spectrophotometer (DeNovix Inc.).

2.4 Production of recombinant adeno-associated viruses (rAAVs)

Recombinant adeno-associated viruses (rAAVs) of serotype 1/2 were produced and purified from a human embryonic kidney (HEK) 293 cell line based on previously published protocols (Klugmann et al., 2005; McClure et al., 2011; Oliveira et al., 2019)

2.4.1 Culturing of Human Embryonic Kidney (HEK) 293 cells

Human Embryonic Kidney (HEK) 293 cells were cultured in Dulbecco's Modified Eagle Medium complete (DMEM complete, Table 10) for a maximum of 35 passages. Cells were propagated by splitting 1:3 to 1:20 depending on the confluency. After a quick wash in 37°C pre-warmed phosphate buffered saline (PBS), cells were detached by incubating in 0.05% Trypsin-EDTA (Gibco™) for 5 min at 37°C. Trypsin incubation was stopped by adding DMEM complete and cells were pelleted in a falcon at 800 g for 5 min at room temperature (RT). Cell pellets were resuspended in fresh DMEM complete and plated in a new flask.

Table 10. DMEM complete.

Solution	Stock	Final	Weight or volume
DMEM (41965-039, gibco)			500 ml
* Heat-inactivated FBS (10270106, gibco)			50 ml
Non-essential amino acids (11140-035, gibco)	100x	1x	5 ml
Sodium pyruvate (11360-039, gibco)	100x	1x	5 ml
Penicillin/Streptomycin	200x	1x	2.5 ml
* Heat-inactivated by incubation for 1 h at 56°C.			

2.4.2 Calcium phosphate transfection of HEK 293 cells

Viral particles were produced by co-transfection of the target AAV plasmid with helper plasmids encoding proteins for viral packaging (pFdelta6, pRV1 and pH21). Five 15-cm dishes with HEK cells at 60-70% confluency were transfected per virus. 2 to 3 hours before transfection, DMEM complete

was replaced by 25 ml Iscove's Modified Dulbecco's Medium (IMDM, 12440-053 gibco) complete (500 ml IMDM containing 25 ml heat-inactivated FBS) per plate. The reagents from Table 11 were mixed and filtered through a 0.2 µm syringe filter. 13 µl 2X HEBS (50 mM Hepes, 280 mM NaCl, 1.5 mM Na_2HPO_4, adjusted to pH 7.05 with NaOH) was quickly added and immediately vortexed for 15 s. Mixture was allowed to sit for at least 90 s to form a fine white precipitate. 5 ml were added drop-wise in a circular motion to each plate. 16-20 hours after transfection, medium was replaced by 25 ml DMEM complete per plate. The same protocol was also used on a smaller scale to transfect HEK cells to test expression of plasmids.

Table 11. HEK 293 transfection mixture for rAAV production.

Solution	Amount
Target AAV plasmid	65 µg
pFdelta6 (helper plasmid) (McClure et al., 2011)	125 µg
pRV1 (helper plasmid) (McClure et al., 2011)	21.25 µg
pH21 (helper plasmid) (McClure et al., 2011)	21.25 µg
1 M $CaCl_2$	4.125 ml
ddH_2O	8.5 ml

2.4.3 rAAV harvesting from HEK 293 cells

60-65 hours after transfection, 18 ml medium from each plate was transferred to a bottle to collect detached cells. The cells on the plates were detached in the remaining medium using cell scrapers and collected in a falcon. Each stack of five plates was additionally washed with 15 ml PBS to collect remaining cells and added to the falcon. Cells were pelleted at 800 g for 5 min at RT. The supernatant was added to the bottle with the medium. The pellet was resuspended in a 30 ml 150 mM NaCl/20 mM Tris buffer (pH 8.0) and frozen at –20°C. 35 ml 40% PEG solution (40% polyethylene glycol 8000 and 411 mM NaCl, pH 7.4) was added to the collected medium in the bottle, stirred for 1 hour at 4°C and then incubated for at least 3 hours or overnight at 4°C. This precipitates the cells from the medium. After PEG incubation, mixture was distributed onto four falcons and cells pelleted at 3000 g for 15 min at 4°C. Each pellet was resuspended in 2.5 ml 150 mM NaCl/20 mM Tris buffer (pH 8.0). Frozen cell suspension was thawed and combined with the four cell suspensions. Cell suspension was vigorously mixed with 2 ml of freshly prepared 10% sodium deoxycholate (0.5% final

concentration) and 8.2 µl Benzonase (Sigma, final concentration 50 U/ml) and incubated for 1 hour in a 37°C water bath, with vigorous shaking every 20 min, to lyse cells and degrade non-viral DNA that is not protected by a viral capsid. Lysates were frozen at -20°C overnight.

2.4.4 Heparin column purification of rAAVs

HiTrap heparin affinity columns (GE Healthcare) were attached to 50 ml syringes and set up on a Harvard infusion pump so that solutions from the syringe flow through the column at a set flow-rate (1 ml/min, 25 mm pump diameter). Columns were first pre-equilibrated with 10 ml 150 mM NaCl/20 mM Tris buffer (pH 8.0). HEK cell lysates were defrosted and spun down at 3000 g for 15 min at 4°C to remove cell debris and supernatant applied onto the columns. Columns were washed with Tris/NaCl buffers (pH 8.0) with increasing NaCl concentration: 20 ml 100 mM NaCl/20 mM Tris, 1 ml 200 mM NaCl/20 mM Tris, 1 ml 300 mM NaCl/20 mM Tris. After the second wash step, columns were washed manually keeping the flow rate of the pump. The last 300-400 µl of flow-through of the last wash step already contain virus eluate and were collected. Virus was further eluted with 1.5 ml 400 mM NaCl/20 mM Tris, then with 3 ml 450 mM NaCl/20 mM Tris, and finally with 1.5 ml 500 mM NaCl/20 mM Tris. rAAVs were filtered though a 13 mm 0.2 µm syringe filter and concentrated using Amicon Ultra-4 centrifugal filter units Amicon (Millipore) at 2000 g for 3 min at RT. PBS was added and centrifugations repeated until viral concentrate had a volume between 200 and 500 µl.

2.4.5 Characterization and titering of rAAVs

2-5 µl of viral solution was mixed with 15-20 µl 2x Laemmli buffer (160 mM Tris HCl, pH 6.8, 4% SDS, 30% glycerol, 0.02% bromophenol blue) with 10 mM dithiothreitol (DTT) and boiled at 95°C for 10 min for SDS gel analysis of rAAV capsid proteins (see chapter 2.8.7).

Viral DNA was extracted by first treating viral solution with DNAse I in ABI buffer (10x ABI buffer: 0.5 M KCl, 0.1 M Tris-HCl pH 8.0, 50 mM $MgCl_2$; pH 8.0-8.3) at 37 °C for 30 min to remove non-viral DNA. DNAse I was inactivated at 70°C for 10 min. Then, 1 µl proteinase K was added, followed by an incubation at 50°C for 60 min. Proteinase K was inactivated at 95°C for 20 min.

Titers of extracted viral DNA were assessed by quantitative real-time polymerase chain reaction (qRT-PCR) on a Step One Plus Real Time PCR System (Applied Biosystems) using Power SYBR Green PCR Master Mix (Applied Biosystems). Reactions were done as triplicates in a 96-well plate (Micro AmpR Fast 96-Well, Applied Biosystems) and contained each 4.5 µl nuclease-free H_2O, 5 µl 2X Power SYBR Green PCR Master Mix, 0.25 µl 10 µM sense WPRE primer (5’ to 3’ sequence:

ACTGTGTTTGCTGAC GCAAC), 0.25 µl 10 µM antisense WPRE primer (5' to 3' sequence: CAACACCACGGAATTGTCAG) and 1 µl DNA (undiluted or 1:10 diluted viral DNA or reference plasmid) or nuclease-free H2O as negative control. A standard curve of a plasmid with the same amplification sequence (WPRE) was used as a reference (starting from 10^7 to 10^{12} molecules/ml). The PCR program used is shown in Table 12.

Infection efficiencies were determined immunocytochemically and by immunoblotting using antibodies to the appropriate tag.

Table 12. PCR program used for rAAV titering.

Step	Temperature	Duration	Cycles
1	95°C	10 min	1 cycle
2	95°C	15 s	46 cycles
3	60°C	1 min	
4	95°C	15 s	1 cycle

2.5 Morphometric analyses

2.5.1 Dendrite analysis of fixed neurons

Cultured neurons were transfected at DIV 8 with humanized *Renilla reniformis* green fluorescent protein (hrGFP) (1 µg/ml) which, from DIV 9 on, is ubiquitously expressed and thus allows visualization of the entire neuronal structure. Depending on the experiment (indicated in figure legends), neurons were co-transfected with another plasmid (1 µg/ml) or transfected just with hrGFP (2 µg/ml in total) as control. Neurons were fixed at DIV 10, for activity-dependent experiments, or DIV 14, when a more mature dendritic network was required, in a solution of 4% paraformaldehyde and 4% sucrose in PBS (pH 7.4) for 20 min at RT, then washed three times in PBS. Transgenes were immunocytochemically stained if neurons were co-transfected with a non-fluorophore gene, and images were acquired at a confocal laser scanning microscope (Leica Sp8) with a 63x oil immersion objective as a z-stack of 0.5 µm intervals at a resolution of 1024 x 1024 pixels with 0.172 µm/pixel. Z-stacks were analyzed as maximum intensity projections. Using the simple neurite tracer (SNT) plugin of Fiji/ImageJ, dendrites of single neurons were traced manually. These traces were used to measure the dendrite lengths. The total dendrite length is defined as the

sum of all dendrite lengths of a neuron. Using the SNT plugin, Sholl analysis with a shell interval of 5 µm was performed to evaluate dendritic complexity (Sholl, 1953). An intersection is defined as the crossing of a dendrite with a shell. The total number of intersections is the sum of all intersections of a neuron up to a radius of 150 µm, unless stated otherwise in the figure legend.

2.5.2 Neurite length time-lapse analysis of adult neurons

Neurons, cultured in 12- or 24-well plates, were transfected at DIV 8 with hrGFP (1 µg/ml) and, depending on the experiment (indicated in figure legends), co-transfected with another plasmid (1 µg/ml) or just with hrGFP (2 µg/ml in total) as control. 24 h after transfection, neurons were treated with 50 µM Bicuculline and imaged in an Incucyte® S3 Live-Cell Analysis System (Sartorius). The first image was acquired around 15 min after treatment and, due to the slow dynamics of neurites, considered as the baseline and referred to as 't0'. The next images were acquired every 4 h for a total of 24 h. Images were taken in the green channel (excitation: 441-481nm, emission: 502-544nm, acquisition time: 300 ms) with a 20x objective. If neurons were cultured in a 24-well plate, 16 images (875x645 µm/image) per well of a size of 1.9 cm^2, containing ca. 0.18 x 10^6 cells, were acquired. Three wells were cultured per condition. If cells were cultivated in 12-well plates, 49 images (875x645 µm/image) per well of a size of 3.8 cm^2 comprising 0.36 x 10^6 cells were acquired. Only one well was cultured per condition. Total neurite length of each well was measured with the Incucyte® Neurotrack Analysis Software Module (Sartorius) using the following parameters: Cell-Body Cluster Segmentation: Top-Hat, radius: 20 µm, threshold: 1.5 GCU, min cell width: 11 µm, neurite course sensitivity: 10, neurite fine sensitivity: 0.5. The total neurite length was normalized per well first to its own t0 and then to the control group. Time-lapse data was analyzed and displayed across time or as area under the curve using Graphpad Prism 8 (GraphPad Software, Inc.).

Neurons were fixed at the end of the time-lapse series, in a solution of 4% paraformaldehyde and 4% sucrose in PBS (pH 7.4) for 20 min at RT, and immunocytochemically stained to confirm expression of non-fluorophore transgenes.

2.5.3 Neurite length time-lapse analysis of developing neurons

As transfection of neurons younger than DIV 8 is not feasible, neurons were plated at lesser density (20%, 40%, 60%, 80% of ca. 0.18 million cells/1.9 cm^2) in 24-well plates to allow distinguishment of individual neurites and imaged in phase contrast. A density of 60% has proven to be the most optimal. Neurons were treated 2 h after the 2.5 h medium change at DIV 0 with 100 ng/ml rVEGFD,

10 µM U0126, or DMSO as control and imaged in an Incucyte® S3 Live-Cell Analysis System (Sartorius). The first image was acquired around 15 min after treatment and, due to the slow dynamics of neurites, considered as the baseline and referred to as 't0'. Every 4 h, an image was taken until DIV6, when the dendritic network was too dense to segment. At DIV3, neurons were treated again with 100 ng/ml rVEGFD. 16 images (875x645 µm/image) per well of a size of 1.9 cm^2, containing ca. 0.18 x 10^6 cells, were acquired in phase contrast with a 20x objective. Two to three wells were cultured per condition. Total neurite length of each well was measured with the Incucyte® Neurotrack Analysis Software Module (Sartorius) using the following parameters: Cell-Body Cluster Segmentation: Brightness mode, segmentation adjustment: 0, min cell width: 12 µm; neurite parameters: 'best' filtering, neurite sensitivity: 0.25, neurite width: 1 µm. The total neurite length was normalized per well first to its own t0 and then to the control group. Time-lapse data was analyzed and displayed across time or as area under the curve using Graphpad Prism 8 (GraphPad Software, Inc.).

2.5.4 Live imaging and analysis of dendrite dynamics

Neurons, cultured in µ-slide 8-well plastic plates (#80821, Ibidi), were transfected at DIV 8 with hrGFP (1 µg/ml) and, depending on the experiment (indicated in figure legends), co-transfected with another plasmid (1 µg/ml) or just with hrGFP (2 µg/ml in total) as control. 24 h after transfection, neurons were treated with 50 µM Bicuculline (Tocris). After around 2 h, when the system was set up, neurons were imaged every hour for a total of 12 h at a Nikon Ti-HCS widefield microscope in a CO_2- and temperature-controlled dark chamber. Due to the slow dynamics of neurites, the first image was still considered as the baseline and referred to as 't0'. Images were taken with a Nikon DS-Qi2 camera in the green channel (emission wavelength: 520 nm) using a 20x objective with 1.5x optical zoom as a z-stack of 1 µm intervals at a resolution of 2424 x 2424 pixels with 0.24 µm/pixel. Perfect focus system prevented focus drift. Neurons were fixed at the end of the time-lapse series, in a solution of 4% paraformaldehyde and 4% sucrose in PBS (pH 7.4) for 20 min at RT, and immunocytochemically stained to confirm expression of non-fluorophore transgenes.

Z-stacks were analyzed as maximum intensity projections. A machine-learning based script developed by KARMENscience® (karmenscience.ai; Croatia, EU) was extensively trained to automatically recognize and trace dendrites of individual neurons, but not axons or protrusions from neighboring neurons, in time lapse videos. At each timepoint, the dendrites marked in the previous timepoint were inherited, and changes in comparison to the previous image were recognized automatically. This allowed to recognize which dendrite is linked to which dendrite across all

timepoints and to track its length changes. Each tracing was manually checked for errors and if required, adjusted manually. KARMENscience® delivered tables with length measurements for each dendrite at every timepoint, as well as the number of all, new or lost dendrites. New dendrite refers to a de novo generation of dendrite. Lost dendrite refers to the disappearance of a dendrite. Using these data, further parameters were computed using Microsoft Excel version 2304, summarized in Table 13. Dendrites that are extending or retracting their length are referred to as growing or retracting dendrites. Time-lapse data was analyzed and displayed across time or as area under the curve using Graphpad Prism 8 (GraphPad Software, Inc.).

Table 13. Explanations of the calculations of dendrite dynamics data.

Parameter name	Calculation	Answers which question?
All dendrites		
Total dendrite length per hour	Sum of all dendrites' lengths per hour	How long is the sum of all dendrites of a neuron at each timepoint?
Total dendrite number (N) per hour	Sum of all dendrites per hour	How many dendrites does a neuron have in total at each timepoint?
New dendrite formations N per hour	Count of all dendrites at tx with dendrite length≠0 at tx and =0 at tx-1. Delivered directly by KARMENscience®	How many dendrites at timepoint tx appeared de novo?
% New dendrite formations N per hour	New dendrite formations N at tx/total dendrite N at tx	What percentage of dendrites at timepoint tx appeared de novo?
Total new dendrite formations N	Sum of all new dendrite formations from all timepoints	How many new dendrites emerged from one neuron throughout the entire imaging time?
Elongating dendrite N per hour	Count of all positive dendrite length changes (between tx-1 and tx) minus number of new dendrite formations at tx.	How many dendrites are longer at timepoint tx compared to the previous timepoint tx-1?
% Elongating dendrite N	Elongating dendrite at tx/total	What percentage of dendrites

per hour	dendrite number at tx-1	from the previous timepoint tx-1 are longer now at tx compared to tx-1?
Rate of elongation and dendrite formation	Average of all positive dendrite length changes per timepoint	How much did dendrites on average grow, regardless of whether it was a new dendrite formation or length extension?
Eliminated dendrite N per hour	Count of all dendrites at tx with dendrite length=0 at tx and ≠0 at tx-1. Delivered directly by KARMENscience®	How many dendrites at timepoint tx disappeared?
% Eliminated dendrite N per hour	Eliminated dendrite N at tx/total dendrite N at tx-1	What percentage of dendrites at timepoint tx-1 did not exist anymore in the next timepoint tx?
Total eliminated dendrite N	Sum of eliminated dendrite N from all timepoints	How many dendrites of a neuron disappeared throughout the entire imaging time?
Shortening dendrite N per hour	Count of all negative dendrite length changes (between tx-1 and tx) minus lost dendrite N at tx.	How many dendrites are shorter at timepoint tx compared to the previous timepoint tx-1 but still exist at tx?
% Shortening dendrite N per hour	Shortening dendrite at tx/total dendrite number at tx-1	What percentage of dendrites from the previous timepoint tx-1 are shorter now at tx compared to tx-1 but still exist at tx?
Rate of shortening and elimination of dendrites	Average of all negative dendrite length changes per timepoint	How much did dendrites on average shorten, regardless of whether the dendrite disappeared as a result of that?
Stable dendrite N per hour	Total dendrite N minus elongating N minus shortening N at tx	How many dendrites had the same length at timepoint tx compared to the previous timepoint tx-1?

% Stable dendrite N per hour	Stable dendrite number at tx/total dendrite number at tx-1	What percentage of dendrites from the previous timepoint tx-1 had the same length as in the previous timepoint tx-1?
New dendrite population		
New dendrite population per hour	Count of all existing dendrites at tx that had a length of 0 at t0.	Which dendrites did not exist at t0 and emerged de novo at any timepoint later?
% New dendrite population per hour	New dendrite population at tx / total number of dendrites at tx	What percentage of dendrites at timepoint tx belong to the population of dendrites that didn't exist yet at timepoint t0?
Elongating new dendrite N per hour	Count of all positive dendrite length changes (between tx-1 and tx) within only the new dendrite population minus new dendrite formations at tx.	How many dendrites of the new dendrite population are longer at timepoint tx compared to the previous timepoint tx-1?
% Elongating new dendrite N per hour	Elongation new dendrite N at tx/ new dendrite population at tx-1	What percentage of dendrites from the previous timepoint tx-1 are longer now at tx compared to tx-1 within the population of new dendrites?
Rate of new dendrite elongation	Average of all positive dendrite length changes within only the new dendrite population per timepoint. Also includes new dendrite formation.	How much did new dendrites on average elongate, regardless of whether it was a new dendrite formation or length extension?
Shortening new dendrite N per hour	Count of all negative dendrite length changes (between tx-1 and tx) within only the new dendrite population. Includes also eliminated new dendrites.	How many new dendrites are shorter or disappeared as a result of that at timepoint tx compared to the previous timepoint tx-1?

% Shortening new dendrite N per hour	Number of shortening new dendrite N at tx (including eliminated new dendrites)/ new dendrite population at tx-1	What percentage of dendrites from the previous timepoint tx-1 are shorter now at tx or disappeared as a result of that compared to tx-1 within the population of new dendrites?
Rate of new dendrite shortening and elimination of dendrites	Average of all negative dendrite length changes within only the new dendrite population per timepoint. Also includes elimination of dendrites.	How much did new dendrites on average shorten, regardless of whether the dendrite disappeared as a result of that?
Stable new dendrite N per hour	Count of all dendrites with length changes = 0 (between tx-1 and tx) within only the new dendrite population.	How many new dendrites had the same length at timepoint tx compared to the previous timepoint tx-1?
% Stable new dendrite N per hour	Number of stable new dendrite N at tx/ new dendrite population at tx-1	What percentage of dendrites from the previous timepoint tx-1 had the same length as in the previous timepoint tx-1 within the population of new dendrites?
Total eliminated new dendrite N	Sum of all dendrites across all timepoints within the new dendrite population with dendrite length=0 at tx and ≠0 at tx-1.	How many new dendrites disappeared again?
% Total eliminated new dendrite N	Total eliminated new dendrite N / total number new dendrite formations N	What percentage of all new dendrites disappeared again?

(tx refers to timepoint x with t0 being the first and t11 the last timepoint after 11 h. tx-1 refers to one hour previous of tx.)

2.5.5 Spine analysis

Cultured neurons were transfected at DIV 8 with hrGFP (1 µg/ml) and another plasmid (1 µg/ml) (indicated in the figure legend) or just with hrGFP (2 µg/ml in total) as control. Neurons were fixed at DIV 14, when spines are typically found in a mature mushroom type, in a solution of 4% paraformaldehyde and 4% sucrose in PBS (pH 7.4) for 20 min at RT, then washed three times in PBS. Non-fluorophore transgenes were immunocytochemically stained, and images were acquired at a confocal laser scanning microscope (Leica Sp8) with a 63x oil immersion objective with 4x optical zoom as a z-stack of 0.01 µm intervals at a resolution of 1024 x 1024 pixels with 0.043 µm/pixel. Z-stacks were analyzed as maximum intensity projections. Spine density was determined by counting spine number over 20 µm dendrite length using the cell counter plugin of ImageJ/Fiji. The straight-line tool of ImageJ/Fiji was used to measure spine length and width.

2.6 Cytoskeleton live imaging

2.6.1 Fluorescence Recovery after Photobleaching (FRAP)

Fluorescence Recovery after Photobleaching (FRAP) was performed based on previously described protocols (Heinze et al., 2022; Koskinen et al., 2014) on actin-GFP transfected cultured neurons that were treated for 5, 15 or 15 min with 100 ng/ml rVEGFD at DIV 14 when spines are typically found in a mature mushroom type shape. Since overexpression of actin itself can affect actin dynamics, transfection was only done the day before FRAP using 1.5 µg/ml plasmid DNA to reduce accumulation of actin overexpression. Image acquisition and bleaching were done at a confocal laser scanning microscope (Leica Sp8) with a 63x water immersion objective and 6x optical zoom at a resolution of 1024 x 1024 pixels with 0.029 µm/pixel. Cells were treated and imaged in HBS containing: 140 mM NaCl, 5.3 mM KCl, 1.0 mM $MgCl_2$, 2.0 mM $CaCl_2$, 10 mM HEPES, 1.0 mM glycine, 35.6 mM D-glucose, and 0.5 mM Na-pyruvate. Images were acquired at a frequency of 1 frame per 1.48 s. Baseline was recorded for three scans before bleaching with five scans (total bleach time: 7.4s) at a laser intensity of 70%. Immediately after bleaching, recording was continued for another 60 frames (total time: 100.64 s). Per neuron, three spines located on different dendrites far from each other to exclude off-target bleach effects were chosen for FRAP. Only mature mushroom type shape spines were considered. Spines with insufficient bleaching were excluded. Images were analyzed using ImageJ. Background was subtracted (rolling ball radius: 50 pixels) and fluorescence intensities in the bleached spine and in a small area of an unrelated dendrite in the same frame were measured using the oval tool. Fluorescence from spines were normalized to the intensities of

dendrites of the same frame and on the average prebleach intensity. Half-time of recovery, stable and mobile fraction were calculated by fitting the normalized intensities to the following equation using Graphpad Prism 8 (GraphPad Software, Inc.) as described by (Koskinen et al., 2014):

$$Y = Y0 + (\text{Plateau} - Y0) \times \left(1 - e(-K \times x)\right)$$

X = time; Y0 = first intensity value of postbleach; Y = percentage of recovery, starts with Y0; K = constant rate.

2.6.2 Actin live imaging

To visualize and examine actin dynamics in dendrites, cultured neurons were transfected with LifeAct-GFP (0.5 µg/ml), that binds to actin (developed by Riedl et al., 2008), at DIV 8. At DIV 10, time lapse imaging was performed at a confocal laser scanning microscope (Leica Sp8) at a frequency of 1 frame per 2.57 s using a 63x water immersion at a resolution of 1024 x 1024 pixels with 0.172 µm/pixel. Imaging was performed in HBS containing: 140 mM NaCl, 2.5 mM KCl, 1.0 mM $MgCl_2$, 2.0 mM $CaCl_2$, 10 mM HEPES, 1.0 mM glycine, 35.6 mM D-glucose, and 0.5 mM Na-pyruvate. After 5 min of baseline recording, neurons were treated with 50 µM bicuculline and/or 100 ng/ml recombinant mouse VEGFD or DMSO as a control. Treatments were carried out by premixing the drugs in additional HBS medium before adding it to the cells. The total time of imaging was 25 min. A frame drift in the time lapse videos was corrected using the 'Align slices in stack' plugin of ImageJ/Fiji with 80%-sized centered rectangle as reference. Images were pre-processed to reduce noise by double standard average subtraction followed by convolution with a 3 × 3 Gauss kernel (1 2 1/2 4 2/1 2 1) in ImageJ/Fiji. Kymographs were created from manually traced individual dendrites using the KymoResliceWide plugin of ImageJ/Fiji. Kymographs were examined qualitatively as only vertical lines were visible on kymographs, indicating no movements of actin along dendrites.

2.6.3 Atomic force microscopy

Atomic force microscopy (AFM) was performed on the soma and proximal dendrites of cultured neurons at DIV 10 using a Nanowizard 3 AFM (JPK Instruments) mounted on an inverted optical microscope (Zeiss), equipped with a 40x objective (Zeiss) in a temperature- and CO_2- controlled chamber. SiO2 colloidal probes with a diameter of 2 µm (sQube) were utilized. The cantilever's spring constant, which ranged from 0.2 to 1.0 N/m, was determined before each experiment using the thermal noise method. The indentation depth remained under 1 µm to prevent interference from the underlying substrate. Around 30 curves were measured for each neuron. Analysis of force-

distance curves was conducted using the Hertz model, which is applicable when a spherical tip indents a flat sample. The force was computed using the following formula:

$$F = \frac{4\ \mathrm{E}}{3\ (1 - v^2)} \sqrt{R} \delta^{\frac{2}{3}}$$

E = Young's modulus; v = Poisson ratio (0.5), R = radius of the sphere; δ = indentation depth. A customized Python script was employed for the analysis, and the force-distance curve was fitted using a least-squares method. All AFM experiments were performed by Dr. Jing Yan. AFM setup was provided by Dr. Dimitris Missirlis.

2.6.4 Microtubule live imaging

To visualize microtubule growth, cultured neurons were transfected with the microtubule plus-end-binding protein 3 (EB3)-GFP (0.25 µg/ml) (developed by Stepanova et al., 2003) at DIV 8. At DIV 10, time lapse imaging was performed at a confocal laser scanning microscope (Leica Sp8) at a frequency of 1 frame per 2.57 s using a 63x water immersion with 4x optical zoom at a resolution of 1024 x 1024 pixels with 0.043 µm/pixel. Imaging was performed in a HEPES-buffered saline solution (HBS) containing: 140 mM NaCl, 2.5 mM KCl, 1.0 mM $MgCl_2$, 2.0 mM $CaCl_2$, 10 mM HEPES, 1.0 mM glycine, 35.6 mM D-glucose, and 0.5 mM Na-pyruvate. After 5 min of baseline recording, neurons were treated with 50 µM bicuculline and/or 100 ng/ml recombinant mouse VEGFD or DMSO as a control. Treatments were carried out by premixing the drugs in additional HBS medium before adding it to the cells. The total time of imaging was 25 min. A frame drift in the time lapse videos was corrected using the 'Align slices in stack' plugin of ImageJ/Fiji with 80%-sized centered rectangle as reference. EB3-GFP appears as fluorescent comets moving inside dendrites in time lapse videos. Images were pre-processed to reduce noise and EB3 comet movements were examined by kymograph analysis as previously described (Schätzle et al., 2016). Briefly, double standard average subtraction followed by convolution with a 3 × 3 Gauss kernel (1 2 1/2 4 2/1 2 1) was done in ImageJ/Fiji. Kymographs were created from manually traced individual dendrites using the KymoResliceWide plugin of ImageJ/Fiji. Comets on kymograph images were manually traced. Only motile (non-vertical) comets visible for at least 10 s in secondary dendrites within similar distance to the soma were analyzed. Data was processed in R 3.6.3 (R Foundation for Statistical Computing) with tidyverse 1.3.0 (Wickham et al., 2019). R script was developed and kindly provided by Javier Sánchez Romero. The speed of EB3 comets was calculated by dividing the distances travelled by time spent traveling (comet lifetime). Number of EB3 comets was counted per 100 µm and min. The direction of EB3 comet movement

was calculated as percentage of anterograde (i.e. away from the soma) movements from all comet movements per dendrite.

2.7 Gene expression analysis

2.7.1 Total RNA extraction and cDNA synthesis

RNA from mouse hippocampus and cortex tissue for time course gene expression experiments was kindly provided by Prof. Dr. Daniela Mauceri. Total RNA from primary mouse hippocampal neurons was extracted using the RNeasy Mini Kit (QIAGEN) according to manufacturer's instructions. Briefly, cells were harvested in RLT buffer (200 µl for a dish of one million cells) containing 1% beta-mercaptoethanol using cell scrapers on ice. The next steps were performed at RT. An equal amount of 70% RNAse-free ethanol was added, and samples transferred to RNeasy spin columns placed on 2 ml collection tubes. Columns were spun for 30 s at 20238 g (14680 rpm, in an Eppendorf centrifuge, 5424R rotor) and flow-through was discarded. DNAse I digestion was performed with 10 µl DNAse I and 70 µl RDD buffer for 10 min at RT. Before and after DNase I digestion, columns were washed with 350 µl RW1 buffer, spun for 30 s at 20238 g and flow-through was discarded. Next, columns were washed twice with 500 µl RPE buffer, spun for 30 s in the first wash and 2 min in the second wash. Flow-throughs were disposed. Using a new 2 ml collection tube, spin columns were spun for 1 min to dry the column membrane. Then, columns were placed on 1.5 ml RNAse-free tubes and 30 µl RNase-free H_2O was added directly to the column membrane. After a 1 min incubation, columns were spun for 1 min at 20238 g to elute the RNA into the collection tube. Eluted RNA was reapplied to the columns and re-eluted to increase yield. RNA concentration was measured at a DeNovix DS-11 spectrophotometer (DeNovix Inc.) and RNA was stored at -80°C for later use.

100 ng RNA was reverse transcribed into first-strand cDNA using a high-capacity cDNA reverse transcription kit (Applied Biosystems). Briefly, 100 ng RNA was diluted in 10 µl RNAse-free water and mixed with 10 µl reverse transcription kit solution (Table 14). The PCR program that was employed at a thermal cycler C1000^{TM} (Bio-Rad) or at a ProFlex PCR system (Applied Biosystems) is shown in Table 15. cDNA was diluted by adding 180 µl RNAse-free H2O and stored at -20°C. All steps were done under RNAse-free conditions.

Table 14. High-capacity cDNA reverse transcription kit solutions.

Reagent	Volume for one reaction
10 x RT buffer	2 µl
10x random primer	2 µl
dNTPs (100 mM)	0.8 µl
Reverse transcriptase (50 U/µl)	1 µl
Rnase out (Rnase inhibiting enzyme) (40 U/µl)	0.5 µl
RNase-free H_2O	3.7 µl
TOTAL	**10 µl**

Table 15. PCR program used for cDNA synthesis.

Step	Temperature	Duration
Annealing	25°C	10 min
Annealing/elongation	37°C	120 min
Denaturation	85°C	5 s
Final hold	4°C	Forever

2.7.2 Quantitative real-time polymerase chain reaction (qRT-PCR)

Quantitative real-time polymerase chain reaction (qRT-PCR) was performed using TaqMan gene expression assays (Applied Biosystems) in 96-well plates (Micro AmpR Fast 96-Well, Applied Biosystems). Each assay was done in duplicates and consisted of 10 µl TaqMan Universal PCR Master Mix (Applied Biosystems), 1 µl FAM (Fluorescein amidite) dye-labelled TaqMan probe (Applied Biosystems) and 9 µl cDNA. See Table 16 for a list of TaqMan probes. Water controls without cDNA served as negative controls. qRT-PCR was run on a StepOne Plus real-time PCR system (Applied Biosystems) using the PCR program listed in Table 17. All steps were done under RNAse-free conditions. Mean cycle times (Ct) and normalizations using the comparative Ct method were calculated by the software StepOne™ (Applied Biosystems). The formula for the comparative Ct

method, is the following: relative expression = 2–ΔΔCt (ΔΔCt = [test(gene of interest) - test(endogenous control)] – [control(gene of interest) – control(endogenous control)]. G*usb* and/or *gapdh* served as endogenous controls.

Table 16. List of TaqMan probes.

Gene	Gene long name	Assay ID
CAP2	adenylyl cyclase-associated protein 2	Mm00482645_m1
cfl	cofilin	Mm03057591_g1
cfos	FBJ osteosarcoma oncogene	Mm00487425_m1
ezn	ezrin	Mm00447761_m1
flt4	FMS-like tyrosine kinase 4	Mm01292618_m1
gapdh	glyceraldehyde-3-phosphate dehydrogenase	Mm99999915_g1
gusb	glucuronidase beta	Mm00446953_m1
STEP	striatal-enriched protein tyrosine phosphatase	Mm00479063_m1
vegfd	vascular endothelial growth factor D	Mm00438963_m1

Table 17. qRT-PCR program.

Step	Temperature	Duration	Cycles
1	50°C	2 min	1 cycle
2	95°C	10 min	1 cycle
3	95°C	15 s	60 cycles
4	60°C	1 min	

2.8 Protein analysis

2.8.1 Phospho-antibody array

An ELISA-based cytoskeleton phospho-antibody array containing 143 different antibodies (FullMoon Biosystems) was employed on cultured neurons following the manufacturer's instructions. For each

antibody, background values were subtracted and normalized on beta-actin protein expression. This experiment was performed by Prof. Dr. Daniela Mauceri.

2.8.2 Immunocytochemistry

Cultured neurons were fixed in a 4% paraformaldehyde and 4% sucrose solution for 20 min at RT and washed three times with PBS. Antibodies were always applied in GDB buffer (16.5 mM phosphate buffer (pH7.4), 0.1% gelatin, 0.3% Triton X-100, and 0.45 M NaCl) using 30-40 µl per coverslip or up to 200 µl in a well of 1.9 cm². Primary antibodies were incubated overnight at 4°C or 4 h at RT, secondary antibodies for 1 h at RT in a humidified chamber. Table 18 shows an overview of all antibodies used. After both antibody incubations, cells were washed with a 500 mM Na_2HPO_4 / 20 mM NaCl buffer. Nuclei were labelled with Hoechst 33258 (1:6000 in PBS, Serva Electrophoresis) for 5 min, followed by three quick washes in PBS and one wash in H_2O. Coverslips were mounted with Mowiol 4-88 (Calbiochem) onto slides. Images were acquired with a Leica DM IRBE inverted fluorescent microscope with a 40x oil immersion objective and a Spot Insight FireWire 2 camera with VisiView software (Visitron Systems) at a resolution of 1392 x 1040 pixels with 0.161 µm/pixel.

Table 18. List of antibodies used for immunocytochemistry.

Antibody	Host species	Type	Dilution	Catalogue number	Company
Primary antibodies					
Flag-M2	mouse	IgG, monoclonal	1:200	F3165	Sigma Aldrich
HA.11	mouse	IgG, monoclonal	1:1000	MMS- 101R	Covance/ BioLegend
V5	mouse	IgG, monoclonal	1:1000	R96025	Thermo Fisher
MAP2	rabbit	IgG, polyclonal	1:200	188002	Synaptic systems
Tubulin	mouse	IgG, monoclonal	1:1000	T9026	Sigma
Flt4	goat	IgG, polyclonal	1:50	AF743-SP	R&D
PSD95	rabbit	IgG, polyclonal	1:200	3450X	Cell Signaling

Secondary antibodies					
anti-mouse	goat	IgG (H+L) Alexa Fluor 488	1:1000	A11001	Life Technologies
anti-mouse	goat	IgG (H+L) Alexa Fluor 594	1:1000	A11005	Life Technologies
anti-mouse	goat	IgG (H+L) Alexa Fluor 633	1:1000	A21052	Life Technologies
anti-mouse	donkey	IgG (H+L) Alexa Fluor 594	1:1000	715-585-150	Dianova
anti-rabbit	goat	IgG (H+L) Alexa Fluor 488	1:1000	A11008	Life Technologies
anti-rabbit	goat	IgG (H+L) Alexa Fluor 594	1:1000	A11037	Life Technologies
anti-rabbit	goat	IgG (H+L) Alexa Fluor 633	1:1000	A21071	Life Technologies
anti-rabbit	donkey	IgG (H+L) Alexa Fluor 594	1:1000	711-585-152	Dianova
anti-goat	donkey	IgG (H+L) Alexa Fluor 594	1:1000	A11058	Life Technologies
anti-goat	donkey	IgG (H+L) Alexa Fluor 633	1:1000	A21082	Life Technologies

2.8.3 Immunohistochemistry

Coronal brain sections of 30 µm thickness were made from mice, stereotaxically injected with rAAV VEGFD-HA or rAAV LacZ-Flag and perfused by Ann-Kristin Kenkel (as described before (Brito et al., 2020)) and blocked in a solution of 8% normal goat serum and 0.3% Triton X-100 in PBS for 1 h at RT. The following primary antibodies were applied overnight at 4 °C in a solution of 2% normal goat

serum and 0.3% Triton X-100 in PBS: mouse anti-HA antibody (1:1000; MMS-101R, Covance), mouse anti-STEP antibody (1:100; 4396, Cell Signaling), and rabbit anti-non-phospho-STEP (Ser221) antibody (1:100; 5659, Cell Signaling). Goat anti-mouse IgG (H+L) Alexa Fluor 488 (1:1000; A11001, Life Technologies) and goat anti-rabbit IgG (H+L) Alexa Fluor 594 (1:1000; A11037, Life Technologies) secondary antibodies were applied the next day for 90 min at RT. Nuclei were visualized with Hoechst (1:6000 in PBS; Serva Electrophoresis) for 5 min. Immunohistochemical stainings were performed by Carmen Leibold. Images were acquired with a Leica DM IRBE inverted fluorescent microscope with a 40x oil immersion objective and a Spot Insight FireWire 2 camera with VisiView software (Visitron Systems) at a resolution of 2560 x 2160 pixels with 0.161 µm/pixel. Background was always subtracted before analysis with the 'subtract background' function (rolling ball radius: 50 pixels). Fluorescence intensity of STEP and non-phospho STEP was measured using ImageJ in six equally sized and distributed rectangles, positioned each within the strata oriens, pyramidale, radiale, and lacunosum moleculare of the hippocampal CA1 and CA2/3 regions.

2.8.4 Protein harvest and Bradford protein assay

Proteins from hippocampal cultures were harvested at DIV 10 in pre-heated 2x Laemmli sample buffer (160 mM Tris HCl, pH 6.8, 4% SDS, 30% glycerol, 0.02% bromophenol blue) containing 10 mM dithiothreitol (DTT) using cell scrapers and boiled for 10 min at 95°C. 200 µl Laemmli buffer were used to harvest cells from a 35 mm dish containing one million cells. Based on previous experience, cells are equally distributed across plates within the same culture. Therefore, protein lysates were employed in equal amounts in Western blotting without prior measurement of protein concentration.

For experiments that require protein concentration measurements (e.g. tissue) or proteins in their native form (e.g. protein fractionation, immunoprecipitation), proteins were harvested in ice-cold homogenization buffer (0.32 M Sucrose, 1 mM Hepes pH 7.4, 1 mM $MgCl_2$, 0.1 mM PMSF, cOmplete™ Mini EDTA-free protease-inhibitor-cocktail (04693159001, Roche), phosphatase inhibitor cocktail 2 (P5726, Sigma Aldrich), 1 mM $NaHCO_3$, 1 mM NaF). The following volumes of buffer were employed: 200 µl for one to two million cultured neurons, 100 – 150 µl for mouse hippocampi younger than 3 months, 200 – 400 µl for mouse cortices younger than 3 months or 900 µl for two hemispheres of a mouse hippocampus or one mouse cortex. Cultured neurons were detached with cell scrapers and homogenized using a glass tissue homogenizer (Wheaton, DWK Life Sciences) on ice. Brain tissue was homogenized with a motorized pestle (Pellet Pestle® Motor, Kontes) before using a glass tissue homogenizer. Tissue lysates were centrifuged for 5 min at 1000 g and

supernatant was kept. All steps were performed on ice or 4°C. Samples meant for mass spectrometry analysis were harvested under keratin-free conditions as much as possible. Protein lysates were stored at -80°C for later use.

Protein concentrations were measured using a Bradford protein assay (Bio-Rad) with BSA as protein standard (0 to 2 µg/ml). Bradford reagent was used diluted 1:4 in H_2O. Absorbance was measured at 595 nm in an Ultrospec® 3000 spectrophotometer (Pharmacia Biotech) or in a CLARIOstar Plus microplate reader (BMG Labtech).

2.8.5 Triton insoluble fractionation (TIF)

Two 35 mm dishes à ca. two million primary hippocampal neurons, two hemispheres of a mouse hippocampus or one mouse cortex were lysed as described in chapter 2.8.2. 30 µl (culture) or 200 µl (tissue) were kept as the homogenate fraction. The rest was subjected to a triton insoluble fractionation (TIF) for the enrichment of postsynaptic proteins as described by (Gardoni et al., 2001). Briefly, samples were centrifuged at 13,000 g for 15 min. The pellet that contains nuclei and crude membrane fractions was resuspended in 150 µl 0.5% Triton-KCl buffer (150 mM KCl, 0.5% Triton X-100, cOmplete™ Mini EDTA-free protease-inhibitor-cocktail (04693159001, Roche)) or 400 µl 1% Triton-KCl buffer (150 mM KCl, 1% Triton X-100, cOmplete™ Mini EDTA-free protease-inhibitor-cocktail (04693159001, Roche)) and transferred into polycarbonate tubes (#343778, Beckmann). After an incubation of 15 min, samples were ultracentrifuged for 1h at 100,000 g. The supernatant (Triton Soluble Fraction, TSF), that primarily contains presynaptic proteins, was transferred to a new tube. The pellet, the triton insoluble fraction, was resuspended in 80 µl (culture) or 200 µl (tissue) Hepes buffer (20 mM Hepes pH 7.4, cOmplete™ Mini EDTA-free protease-inhibitor-cocktail (04693159001, Roche)) and homogenized in a glass tissue homogenizer (Wheaton, DWK Life Sciences). All steps were performed on ice or at 4°C.

2.8.6 Postsynaptic density purification

Postsynaptic densities were purified from four rat complete brain tissue based on a previously described protocol (Gardoni et al., 1998). Brains were first lysed as described in chapter 2.8.2. using 20 ml homogenization buffer. 1 ml was kept of homogenate. The rest was pelleted for 5 min at 1000 g. The pellet (P1), containing the nuclear fraction and which is still in suspension, and 300 µl of the supernatant (S1) were kept. The rest was spun for 15 min at 13800 g. Supernatant (S2) was kept and the pellet (P2), containing the crude synaptosomal fraction, resuspended in 18 ml of buffer A

containing 0.32 M sucrose, 1 mM Hepes pH 7.4, and cOmplete™ Mini EDTA-free protease-inhibitor-cocktail (04693159001, Roche). 300 µl of P2 were kept. The rest of P2 was resuspended into sucrose gradients of 0.85 M, 1.0 M and 1.2 M and centrifuged for 2 h at 24800 rpm (Beckman Coulter SW 41 Ti rotor). The interphase between 1.2 M and 1.0 M sucrose was collected. 300 µl of this was kept as the synaptosome fraction (SYN). The rest was filled up to 70 ml with buffer B containing 0.16 M sucrose, 1mM Hepes pH 7.4 and 0.5% Triton-X100 and incubated for 15 min before spinning down for 45 min at 24800 rpm (Beckman Coulter SW 41 Ti rotor). Supernatant was discarded. The pellet, containing the triton insoluble fraction (TIF), was resuspended in 1800 µl buffer A using a glass tissue homogenizer. 300 µl was kept. The rest of the TIF was resuspended into sucrose gradients of 1.0 M, 1.5 M and 2.1 M and centrifuged for 2 h at 40000 rpm (Beckman Coulter SW 41 Ti rotor). The interphase between 2.1 M and 1.5 M was collected, resuspended in 24 ml buffer C containing 150 mM KCl, 0.5% Triton-X100 and cOmplete™ Mini EDTA-free protease-inhibitor-cocktail (04693159001, Roche) and centrifuged for 30 min at 40000 rpm (Beckman Coulter SW 41 Ti rotor). The pellet contains the postsynaptic density fraction and was resuspended in 2 ml buffer D containing 20 mM Hepes pH 7.4 and cOmplete™ Mini EDTA-free protease-inhibitor-cocktail (04693159001, Roche). All steps were performed on ice or at 4°C. All fractions were stored at -80°C for later use.

2.8.7 Western blotting

Protein homogenates were mixed with 2x Laemmli sample buffer (160 mM Tris HCl, pH 6.8, 4% SDS, 30% glycerol, 0.02% bromophenol blue) containing 1% dithiothreitol (DTT) or were directly harvested in 2x Laemmli buffer and boiled for 10 min at 95°C. Protein samples were loaded in equal quantities in individual lanes on 6-15% polyacrylamide gels (SDS-PAGE, Table 19), depending on protein size (6-10% for > 50 kDa, 10-15% for < 50 kDa), or on Mini-PROTEAN TGX stain-free pre-cast gels (Bio-Rad) and separated at a constant current of 30 mA per gel in running buffer (190 mM glycine, 25 mM Tris, 0.1% SDS and pH 8.8) using a Mini-PROTEAN Tetra Vertical Electrophoresis Cell apparatus (Bio-Rad). As protein amounts are similar across samples within a culture, based on previous experience, protein concentrations were not measured before. Few microliters of the PageRuler™ Prestained Protein Ladder (Thermo Scientific) were loaded alongside as protein molecular weight marker. Proteins were transferred on nitrocellulose membranes (Amersham™ 0.45 µm, GE Healthcare) in transferring buffer (150 mM glycine, 20 mM Tris, 0.1% SDS and 20% methanol) at RT at constant voltage of 18 V for 1.5-2.5h (6-2.5h for > 100 kDa, 2h for 50-100 kDa, 1.5h for < 50 kDa) using an electrophoretic transfer apparatus (Idea Scientific). After the transfer,

membranes were briefly washed with millipore water and proteins stained for at least 5 min with Ponceau S (SERVA Electrophoresis). This allowed evaluation of protein quality and transfer efficiency and cutting the membrane into different sections. After a few more short washes in millipore water, membranes were blocked in 5% milk (m/v, reform instant skimmed milk powder) in PBST (0.1%Tween-20 in PBS: 137 mM NaCl, 2.7 mM KCl, 10 mM Na2HPO4 2H2O, 2 mM KH2PO4, pH 7.4). Then, membranes were incubated overnight at 4°C with primary antibodies diluted either in 5% milk or BSA in PBST (Table 20). The next day, membranes were washed three times for 10 min with PBST, incubated with horseradish peroxidase-conjugated (HRP) secondary antibodies in 5% milk in PBST for 45 min at RT (Table 20), then washed again three times for 10 min with PBST. All incubations and washes were performed on a shaker. Protein bands were revealed by evenly covering the membranes with Clarity and Clarity Max (for weak signal) enhanced chemiluminescence (ECL) solution (Clarity™, Bio-Rad) for 1 min and developing the membranes using a ChemiDoc™ imaging system (Bio-Rad). Membranes were sometimes reprobed with another primary antibody from a different species, by inactivating before the previous secondary antibody with a 1h incubation in 0.1% Natrium Azide in PBS at RT on a shaker.

Protein band densities were measured using the rectangle tool in ImageJ/Fiji. Background was always subtracted before with the 'subtract background' function (rolling ball radius: 50 pixels). Protein densities were normalized to a loading control (typically tubulin) and a control sample.

For fluorescent western blotting, the same procedure was applied with the exception that blocking and antibody incubations were performed in Odyssey blocking buffer (diluted 1:1 in PBS for blocking or PBST for antibody incubations, LI-COR Biosciences), primary antibodies from different species were incubated simultaneously on the same membrane and different secondary antibodies were employed: IRDye 680LT donkey anti-mouse and IRDye 800CW donkey anti-rabbit (LI-COR Biosciences) for 45 min at RT (1:15000). Images of the blots were acquired with the Image Studio Software 4.0 (LI-COR Biosciences). These blots were not quantified and only served to demonstrate co-labeling of two antibodies.

Table 19. SDS-PAGE.

Solution	**Lower/Resolving gel 10ml, 6-15%**	**Upper/Stacking gel 5 ml, 3.7%**
*4x resolving/stacking gel buffer	5 ml	2.5 ml
30%/0.8% Acrylamid/ Bisarcrylamid	Depending on percentage	0.8 ml

10% (w/v) ammonium persulfate (APS)	50 µl	50 µl
N,N,N',N'-Tetramethyl-ethylenediamine (TEMED)	5 µl	5 µl
H_2O	Filled up to 20 ml	Filled up to 5 ml

* Resolving gel buffer: 1.5 M Tris/HCl pH 8.8 and 0.4% SDS

Stacking gel buffer: 0.5 M Tris/HCl pH 6.8 and 0.4% SDS

Table 20. List of antibodies used for Western blotting.

Antibody	Host species	Type	Dilution	Catalogue number	Company
Primary antibodies					
Alpha-Tubulin	mouse	IgG, monoclonal	1:400000 in milk	T9026	Sigma Aldrich
CAP2	rabbit	IgG, polyclonal	1: 1000 in milk	15865-1AP	Proteintech
cFos	rabbit	IgG, polyclonal	1:2000 in milk	sc-52	Santa Cruz
Cofilin	rabbit	IgG, polyclonal	1: 1000 in milk	5175	Cell Signaling
dsRed	mouse	IgG, monoclonal	1:1000 in BSA	632496	Clontech
Ezrin	mouse	IgG, monoclonal	1:1000 in BSA	sc-58758	Santa Cruz
Flag-M2	mouse	IgG, monoclonal	1:5000 in milk	F3165	Sigma Aldrich
Flt4 (N-terminal, Tyr25-	goat	IgG, polyclonal	1:1000 in milk	AF743-SP	R&D

Asp770)					
Flt4 (C-terminal)	rabbit	IgG, polyclonal	1:500 in BSA	sc-321	Santa Cruz
GFP	mouse	IgG, monoclonal	1:1000 in milk	sc-9996	Santa Cruz
H3	rabbit	IgG, polyclonal	1:2000 in BSA	06-755	Millipore
HA.11	mouse	IgG, monoclonal	1:7500 in milk	MMS- 101R	Covance/ BioLegend
Non-phospho-STEP (Ser221) (D74H3)	rabbit	IgG, polyclonal	1:3000 in BSA	5659	Cell Signaling
Phospho-S473 Akt	rabbit	IgG, polyclonal	1:1000 in BSA	9271	Cell Signaling
Phospho-T180/Y182 p38 MAPK	mouse	IgG, monoclonal	1:750 in milk	612288	BD Biosciences
Phospho-T202/Y204) p44/ 42 ERK1/ 2 (MAPK)	mouse	IgG, monoclonal	1:2000 in BSA	9106	Cell Signaling
Phospho-Y-1472 GluN2B	rabbit	IgG, polyclonal	1:1000 in BSA	4208	Cell Signaling
Phospho-Y478 ezrin	rabbit	IgG, polyclonal	1:1000 in BSA	TA326188	Origene/Biocat
PSD95	rabbit	IgG, polyclonal	1:1000 in BSA	3450X	Cell Signaling
STEP	mouse	IgG, monoclonal	1:1000 in milk	4396	Cell Signaling
Synaptophysin	mouse	IgG, monoclonal	1:1000 in	SAB4200544	Sigma Aldrich

			BSA		
V5	mouse	IgG, monoclonal	1:1000 in milk	R96025	Thermo Fisher
Vamp2	rabbit	IgG, polyclonal	1:1000 in BSA	104202	Synaptic Systems
VEGFD	goat	IgG, polyclonal	1:600 in BSA	AF469	R&D
Secondary antibodies					
anti-mouse	goat	hourse radish peroxidase AffiniPure IgG (H+L)	1:5000 in milk	115-035-003	Jackson Immuno Research
anti-rabbit	goat	hourse radish peroxidase AffiniPure IgG (H+L)	1:5000 in milk	111-035-144	Jackson Immuno Research
anti-goat	donkey	hourse radish peroxidase AffiniPure IgG (H+L)	1:5000 in milk	705-035-147	Jackson Immuno Research

2.8.8 Lumit Immunoassay

Lumit™ Immunoassay system with NanoLuc® Binary Technology (Promega) (TM613-2) was tested according to manufacturer's protocol on neuronal lysates harvested in in ice-cold homogenization buffer (0.32 M Sucrose, 1 mM Hepes pH 7.4, 1 mM $MgCl_2$, 0.1 mM PMSF, cOmplete™ Mini EDTA-free protease-inhibitor-cocktail (04693159001, Roche), phosphatase inhibitor cocktail 2 (P5726, Sigma Aldrich), 1 mM $NaHCO_3$, 1 mM NaF). The following antibodies were tested: mouse anti-ezrin (75, 150 or 300 ng/ml; sc-58758, Santa Cruz), rabbit anti-phospho-(Y478) ezrin (75, 150 or 300 ng/ml; TA326188, OriGene Technologies). Luminescence signal was measured at a CLARIOstar Plus microplate reader (BMG Labtech).

2.8.9 Proximity Ligation Assay (PLA)

Proximity ligation assay (PLA) was performed using a Duolink® In Situ Red Starter Kit Mouse/Rabbit (Sigma Aldrich) according to the manufacturer's protocol on neurons cultured on coverslips. Neurons were first fixed in a 4% paraformaldehyde and 4% sucrose solution for 20 min at RT and washed three times with PBS, followed by a one hour blocking in GDB buffer (16.5 mM phosphate buffer (pH7.4), 0.1% gelatin, 0.3% Triton X-100, and 0.45 M NaCl) at RT. Additional blocking was performed with 1 drop of Duolink® blocking solution per coverslip for 1 h at 37°C. Cells were incubated overnight at 4°C with the following two antibodies combined in Duolink® antibody diluent: mouse anti-ezrin (1:50; sc-58758, Santa Cruz), rabbit anti-phospho-(Y478) ezrin (1:50; TA326188, OriGene Technologies). PLA probes were applied 1:5 in Duolink® antibody diluent for 1 h at 37°C. Ligation of probes was done with the Duolink® ligase (1:40 in 1x Duolink® ligation buffer) for 30 min at 37°C. Signal was amplified by the Duolink® polymerase (1:80 in 1x Duolink® amplification buffer) for 100 min at 37°C. Coverslips were washed 2 x 5 min with Duolink® wash buffer A between all incubation times after antibody incubation. After polymerase incubation, cells were washed 2 x 10 min with Duolink® wash buffer B and briefly with 0.01x Duolink® wash buffer B before staining with Hoechst 33258 (1:6000 in PBS, Serva Electrophoresis) for 5 min, followed by three quick washes in PBS and one wash in H_2O. Coverslips were mounted with Mowiol 4-88 (Calbiochem) or with the Duolink® In Situ Mounting Medium with DAPI (in this case, Hoechst staining was not done) onto slides. Always 30 µl were applied per coverslip and solution. All incubation steps were done in a humidified chamber.

Images were acquired with a Leica DM IRBE inverted fluorescent microscope with a 40x oil immersion objective and a Spot Insight FireWire 2 camera with VisiView software (Visitron Systems) at a resolution of 1392 x 1040 pixels with 0.161 µm/pixel or at a confocal laser scanning microscope (Leica Sp8) with a 63x oil immersion objective as a z-stack of 0.1 µm intervals at a resolution of 1024 x 1024 pixels with 0.172 µm/pixel. Within a culture, the same acquisition settings were used. Images were only taken of areas with equal number of Hoechst- or DAPI-labelled cells and were randomly chosen on the coverslip to prevent bias. Five to ten images were taken per coverslip. Z-stacks were analyzed as maximum projections. Images were pre-processed first by subtracting the background (rolling ball radius: 5 pixels) and applying a Gaussian blur (sigma radius: 0.5). Images were converted to binary masks by setting the threshold to a minimum of 2 - 4x of the mean gray value of the entire image (adjusted for each batch of PLA staining) and watershed was applied to split merged objects. PLA signal was segmented and counted using 'Analyze Particles' with the minimum particle size set

to 5 µm. Hoechst- or DAPI-labelled nuclei were counted using the cell counter plugin. PLA signal counts were normalized to cell number counts. All image processing and analysis were done with ImageJ/Fiji.

2.8.10 Immunoprecipitation

Hippocampal neurons infected with hsyn-Flt4-GFP or hsyn-GFP were harvested at DIV 10 as described in chapter 2.8.2. Trap® Magnetic Particles M-270 (Proteintech) were used to target and immunoprecipitate GFP according to manufacturer's protocol. Briefly, 30 µg protein lysate were diluted in 300 µl dilution buffer (150 mM NaCl, 0.5 mM EDTA, 10 mM Tris/Cl pH 7.5) and incubated with 10 µl magnetic particles on a wheel for 1h at 4°C. Magnetic particles were briefly washed three times before and after the incubation with 200 µl wash buffer (150 mM NaCl, 0.5 mM EDTA, 10 mM Tris/Cl pH 7.5, 0.05% NP40). At the last washing step, beads were transferred into a new tube to remove potential contaminants on the tube walls. All steps were performed on ice. 25 µl 2x Laemmli buffer (160 mM Tris HCl, pH 6.8, 4% SDS, 30% glycerol, 0.02% bromophenol blue, 10 mM DTT) followed by 10 min boiling at 95°C were used for elution. Samples were employed in Western blotting or mass spectrometry analysis (see chapter 2.8.11). Beads were removed before loading on a gel. Samples meant for mass spectrometry analysis were handled under keratin-free conditions as much as possible.

2.8.11 Mass spectrometry analysis

Immunoprecipitates (see chapter 2.8.10) were loaded on 10% pre-cast gels and separated by 1 cm in 1x MOPS buffer (50 mM (3-(N-morpholino) propanesulfonic acid (MOPS), 50 mM Tris, 0.1% SDS, 1 mM EDTA) containing 10 mM dithiothreitol (DTT) at the mass spectrometry facility of the ZMBH (Zentrum für Molekulare Biologie der Universität Heidelberg). Gels were briefly washed with deionized water and incubated for 30 min in a fixation solution on a shaker at RT before Coomassie staining. Gel lanes were cut out and employed in mass spectrometry analysis. Samples were handled under keratin-free conditions as much as possible. All steps after the gel run were done by the mass spectrometry facility.

2.9 Calcium Imaging

Nuclear calcium imaging was performed on rAAV-CaMKII.jRGECO1alpha-NLS-infected neurons at DIV 10 in HBS (140 mM NaCl, 2.5 mM KCl, 1.0 mM $MgCl_2$, 2.0 mM $CaCl_2$, 10 mM HEPES, 1.0 mM glycine, 35.6 mM D-glucose, and 0.5 mM Na-pyruvate) as described previously (Litke et al., 2022). Images were acquired at a widefield microscope (BX51W1, Olympus) using the VisiView software (Visitron Systems) with a 20x water-immersion objective with 2 x 2 binning at a resolution of 256 x 256 pixels with 1.6 µm/pixel and a frequency of 1 Hz. Fluorescence excitation was set at 570 ± 10 nm and provided by an LED light source (Cool LED pE-4000). jRGECO1a fluorescence was filtered at 620 ± 30 nm. After 5 min of baseline recording, neurons were treated with 50 µM Bic, 100 ng/ml rVEGFD or both for another 10 min. Treatments were carried out by premixing the drugs in additional HBS medium before adding it to the cells. Just addition of medium without treatment served as another control for rVEGFD treatments.

Calcium signal intensities were quantified by drawing regions of interest around individual cell nuclei overexpressing jRGECO1 and measuring their integrated densities using the oval selection tool of ImageJ/Fiji. Additionally, background levels were measured of three regions of interest drawn in the areas between cells using the free hand selection tool. Measurements were exported to IgorPro (WaveMetrics) and analyzed with a script that was kindly provided by Dr. Anna M. Hagenston. Backgrounds were subtracted the following way: (integrated density cell) - (area cell/area background) x (integrated density background). Calcium signals were quantified as the baseline intensity-normalized change in fluorescence over time, $\Delta F/F = (F - F_{baseline})/F_{baseline}$. Calcium transients were quantified in terms of the mean amplitude size and the peak frequency per min following the start of the treatment.

2.10 Statistical analysis and illustrations

Data was generally normalized to the control group of the respective culture preparation day to correct for any variations between different culture preparations. Normality was assessed with the Shapiro-Wilk test. For the comparison of a condition to a control condition, to which the sample condition was normalized, data was compared to the hypothetical value 1 using a one sample t-test, in the case of normally distributed data or a Wilcoxon signed-rank test for nonparametric data. For the comparison of a condition to a control without prior normalization, an unpaired two-tailed t-test with Welch's correction or an unpaired two-tailed Mann-Whitney test was performed in the case of Gaussian or non-Gaussian distribution, respectively. Multiple groups were compared using one- or

two-way ANOVA, for data with one or two independent variables, respectively, followed by Dunnett's *post hoc* test for comparisons to control or baseline levels (for example t0 in time-lapse experiments) or Tukey's *post hoc* test for comparisons between conditions, respectively, in the case of parametric data. Kruskal-Wallis test followed by Dunn's *post hoc* test was performed for nonparametric data. Results were considered statistically significant in the case of following p values (p): $p<0.05$ (*), $p<0.01$ (**), $p<0.001$ (***), or $p<0.0001$ (****). Each figure legend indicates the sample size, and which statistical test was performed. All data is presented as mean ± SEM. All graphs and statistical analyses were done with Graphpad Prism 8 and 9 (GraphPad Software, Inc.). Figures and schemas were created with Adobe Illustrator 2020, PowerPoint and BioRender.com.

Chapter 3. Results

3.1 VEGFD interferes with structural plasticity of dendrites

In neurons, VEGFD is crucial for dendrite maintenance (Hemstedt et al., 2017; Litke et al., 2018; Mauceri et al., 2020; Mauceri et al., 2011; Mauceri et al., 2015; Maurer et al., 2020; Schlüter et al., 2020). This raises the question of what role VEGFD may have during structural plasticity. This section of the thesis aims to address this question in the context of developmental or activity-dependent structural plasticity.

3.1.1 VEGFD slows down dendrite growth during development

Previous work from Prof. Dr. Daniela Mauceri revealed that expression of *VEGFD* mRNA is very low during development, and rises with increasing age in the murine hippocampus, both *in vitro* (Mauceri et al., 2011) and *in vivo* (Mauceri et al., 2011). Interestingly, in the mouse cortex, *VEGFD* mRNA appears to be stable across age (Mauceri et al., 2011). To investigate whether the presence of VEGFD in developing neurons, when VEGFD expression is almost absent, may interfere with dendrite development, it was taken advantage of the fact that VEGFD is a secreted factor: hippocampal neurons were cultured in medium supplemented with recombinant VEGFD (rVEGFD) starting from day in vitro (DIV) 0. After one week of culture, during which neurons established their overall dendritic arbor, cells were transfected with a plasmid driving expression of humanized *Renilla reniformis* green fluorescent protein (hrGFP) to sparsely label neurons and visualize their morphology. This is necessary due to the high density of neurons, which hinders the distinction of individual dendrites in unlabeled neurons. Neurons were then fixed for subsequent morphometric analysis. VEGFD-supplemented neurons displayed a simpler dendritic architecture than untreated control neurons (Figure 7a-c). In addition to morphometric analysis on fixed samples, I monitored total neurite length changes of cultured neurons over time in an automated imaging system (Figure 7d-f). As transfections are not possible before DIV 8, hrGFP-expression could not be used to visualize neuronal morphology. Instead, neurons were plated at lower densities to allow distinction of neurites in phase contrast images. I tested different densities (20-80% of ca. 0.18 million cells/1.9 cm^2) for their viability and responsiveness to a pharmacological inhibitor of neurite growth (Figure 6a). At densities below 60%, neurons displayed an unhealthy appearance. However, at 60% density, neurons did not differ in their overall morphology from neurons plated as usual and treatments with the MAP kinase inhibitor U0126, known for inhibiting neurite outgrowth (Das et al., 2004; Perron et

al., 1999), decreased total neurite length over time in comparison to DMSO-treated neurons (Figure 6b).

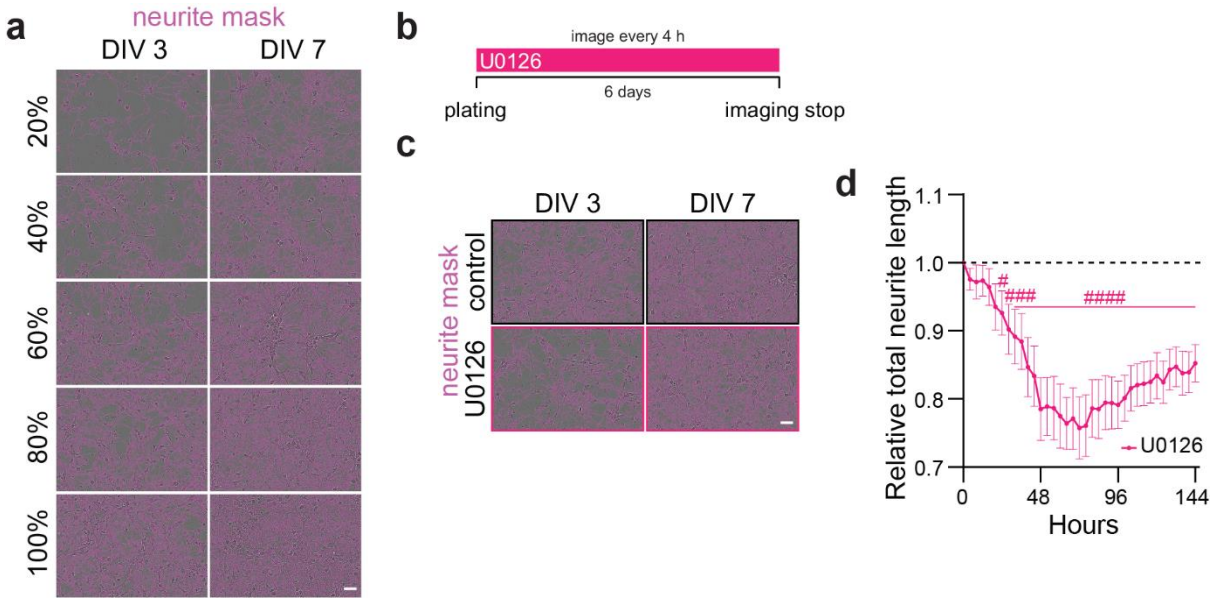

Figure 6. Establishment of a live imaging system for automated monitoring of neurite length in developing neurons. ***a*** *Representative images of cultured mouse hippocampal neurons plated at different densities (100% density is equivalent to ca. 0.18 million cells/1.9 cm²) at specified timepoints overlayed with neurite mask for automated length measurements. Scale bar = 50 µm.* ***b-d*** *Time-lapse monitoring of neurite length of cultured mouse hippocampal neurons supplemented at DIV 0 with U0126 or DMSO (vector) as control for 6 days.* ***b*** *Schema of experiment.* ***c*** *Representative images of neurons at specified timepoints and treatments overlayed with neurite mask for automated length measurements. Scale bar = 50 µm.* ***d*** *Relative total neurite length over time normalized on the first timepoint and untreated control. Multiple unpaired t-test. N = 4 independent culture preparations. Graphs display mean ± SEM. Hashtags (#) indicate significance to baseline value. ####p < 0.0001; ###p < 0.001; #p < 0.05.*

Thus, I used neurons plated at 60% density to assess the effect of VEGFD on neurite growth and demonstrated, consistent with the data from endpoint-based analyses, that neurites of neurons cultured in the presence of rVEGFD displayed slower growth over time compared to untreated controls (Figure 7e, f).

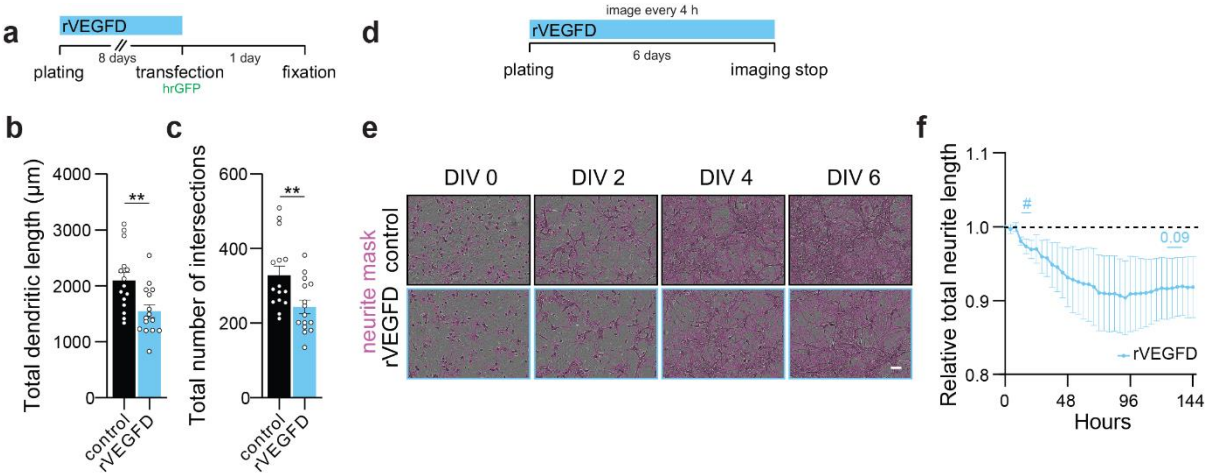

Figure 7. VEGFD slows down dendrite growth in developing neurons. ***a-c*** *Analysis of dendrite morphology of cultured mouse hippocampal neurons with or without recombinant VEGFD (rVEGFD) supplementation for 24 h starting at DIV 0. At DIV 8, neurons were transfected with hrGFP to visualize neuronal morphology.* ***a*** *Schema of experiment.* ***b-c*** *Total dendritic length (**b**) and number of intersections (**c**) of neurons treated as indicated. Two-tailed unpaired Student's t-test. N = 15 neurons from 3 independent culture preparations.* ***d-f*** *Time-lapse monitoring of neurite length of cultured mouse hippocampal neurons supplemented at DIV 0 with or without rVEGFD for 6 days.* ***d*** *Schema of experiment.* ***e*** *Representative images of neurons at specified timepoints and treatments overlayed with neurite mask for automated length measurements. Scale bar = 50 µm.* ***f*** *Relative total neurite length over time normalized on the first timepoint and untreated control. Multiple unpaired t-test (minimal significant p values are displayed). N = 4 independent culture preparations. Graphs display mean ± SEM. Single values are represented as data points. Significance indicators include asterisks (*) for comparisons between conditions and hashtags (#) for comparisons to baseline values within each respective condition. **p < 0.01; #p < 0.05. Experiments in a-c were performed by Prof. Dr. Daniela Mauceri.*

Taken together, these findings indicate that developmental structural remodeling depends on a reduction of VEGFD expression.

3.1.2 VEGFD opposes synaptic activity-dependent dendrite remodeling

Synaptic activity plays a pivotal role in shaping neuronal structure (Kulkarni et al., 2012; McAllister, 2000; Parrish et al., 2007). By employing bicuculline (Bic), which antagonizes the gamma-aminobutyric acid-A receptor, and thereby alleviates inhibition of neuronal activity, it is possible to pharmacologically induce synaptic activity in cultured neurons (Schlumm et al., 2013). Prof. Dr. Daniela Mauceri previously revealed a time-dependent reduction of VEGFD mRNA expression in primary mouse hippocampal neurons treated with Bic (Figure 8a), while elevated mRNA levels of the immediate early gene cFos, a molecular marker of neuronal activity (Chung, 2015), confirmed heightened synaptic activity (data not shown). Furthermore, she demonstrated that the use of BDNF

to enhance synaptic activity (Lau et al., 2015) and dendrite remodeling (Horch et al., 2002; McAllister et al., 1995) independently of Bic also leads to a reduction of *VEGFD* mRNA levels (data not shown).

As VEGFD expression is low during development to allow developmental dendrite growth (chapter 3.1.1), it raises the question whether administering VEGFD during activity-induced downregulation of VEGFD might also hinder activity-dependent dendrite remodeling.

To investigate this, cultured neurons were transfected with plasmids to induce expression of hrGFP for labeling neuronal morphology in morphometric analyses. At DIV 9, when transgenes are expressed, neurons were treated with Bic to stimulate synaptic activity, rVEGFD or both in combination for 24 h (Figure 8b). Bic stimulation resulted in an increase in total dendrite length and complexity (Figure 8c-f). Neurons co-treated with rVEGFD, however, did not produce the same effect (Figure 8c-f). In unstimulated neurons, rVEGFD did not have an apparent impact on the dendritic arbor (Figure 8c-f).

Previously, Prof. Dr. Daniela Mauceri and Dr. Jing Yan showed that dendrite remodeling induced by Bic was also inhibited when VEGFD was overexpressed, either prior to Bic application or at the onset of activity using the synthetic enhanced synaptic activity-regulated element (ESARE) promoter, which drives gene expression upon activity (Gulmez Karaca et al., 2020; Kawashima et al., 2013)(data not shown).

In addition, I monitored total neurite length changes of cultured neurons over time using an automated imaging system (Figure 8g, h). As expected, neurite length of neurons treated with Bic grew with increasing time (Figlia et al., 2022), but not in neurons co-treated with rVEGFD (Figure 8i).

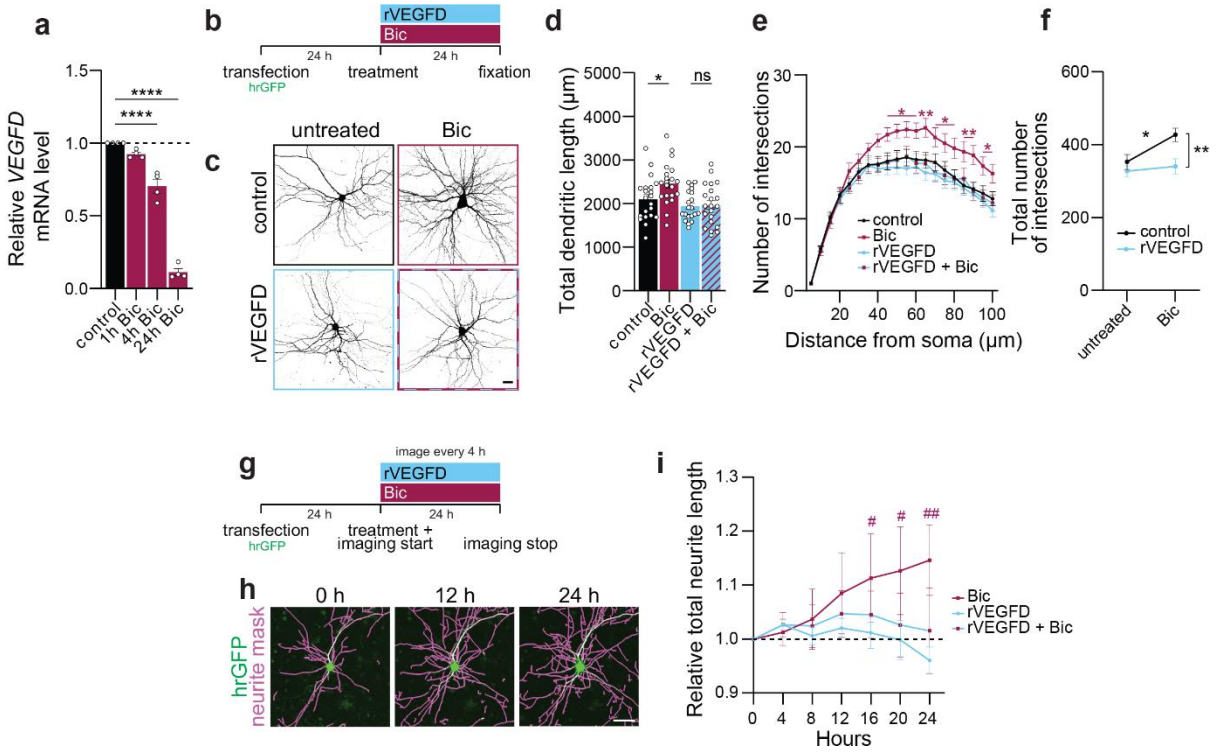

Figure 8. VEGFD counteracts activity-dependent dendrite remodeling in adult neurons. ***a*** *QRT-PCR analysis of VEGFD mRNA expression in cultured mouse hippocampal neurons with or without bicuculline (Bic) administration for 1, 4 or 24 h. Expression was normalized to gusb and control. One-way ANOVA followed by Dunnett's post hoc test. N = 4 independent culture preparations.* ***b-f*** *Analysis of dendrite morphology of hrGFP-transfected cultured mouse hippocampal neurons with or without recombinant VEGFD (rVEGFD) and/or Bic supplementation for 24 h.* ***b*** *Schema of experiment.* ***c*** *Representative images of neurons treated as indicated. hrGFP was used to visualize neuronal morphology. Scale bar = 20 µm.* ***d-f*** *Total dendritic length (**d**), Sholl analysis (**e**) and total number of intersections up to a radius of 150 µm (**f**) of neurons treated as indicated. Two-way ANOVA followed by Bonferroni's post hoc test (**d, f**), or Dunnett's post hoc test (**e**). N = 20-21 neurons from 4 independent culture preparations.* ***g-i*** *Time-lapse monitoring of neurite length for 24 h of hrGFP-transfected cultured mouse hippocampal neurons with or without rVEGFD and/or Bic treatment.* ***g*** *Schema of experiment.* ***h*** *Representative images of neurons at specified timepoints overlayed with neurite mask for automated length measurements. Scale bar = 50 µm.* ***i*** *Relative total neurite length over time normalized on the first timepoint and untreated control. Two-way ANOVA followed by Dunnett's post hoc test or two-way ANOVA with repeated measures followed by Dunnett's post hoc test for comparisons to basal values. N = 3 independent culture preparations. Graphs display mean ± SEM. Single values are represented as data points. Significance indicators include asterisks (*) for comparisons between conditions and hashtags (#) for comparisons to baseline values within each respective condition. ****p < 0.0001; **p < 0.01; *p < 0.05; ##p < 0.01; #p < 0.05; ns p > 0.05. Experiments in a-f were performed by Prof. Dr. Daniela Mauceri and Dr. Jing Yan. This figure is adapted from a first authored manuscript that is currently in revision for submission to Cellular and Molecular Life Sciences (see List of publications).*

This prompts the question as to whether VEGFD may serve a similar role *in vivo* in adult mice. Using a protocol to subject adult mice to contextual and cued fear conditioning (CFC) that induces an increase in basal dendrite length and complexity in CA1 hippocampal neurons (Simonetti et al.,

2021), Prof. Dr. Daniela Mauceri and Ann-Kristin Kenkel showed that *VEGFD* mRNA expression is reduced in the CA1 of mice subjected to CFC (data not shown). Furthermore, they demonstrated that remodeling of basal dendrites is prevented in CA1 neurons that overexpress VEGFD following stereotaxic rAAV delivery (data not shown).

In sum, these findings indicate that VEGFD downregulation is a prerequisite to allow synaptic activity-dependent dendrite remodeling *in vitro* and *in vivo*.

3.1.3 VEGFC does not affect synaptic activity-dependent dendrite remodeling

VEGFC is the closest structural homologue to VEGFD (Achen et al., 1998a; Joukov et al., 1997) and activates the same receptor like VEGFD (Künnapuu et al., 2021). This prompts the question of whether VEGFC might impede activity-dependent structural remodeling similar to VEGFD.

Previously, Dr. Jing Yan treated cultured hippocampal neurons with Bic, recombinant VEGFC (rVEGFC) or both for 24 h and performed morphometric analyses (Figure 9a. Bic-treatment resulted, as expected, in an increase in total dendrite length and complexity, which was also observed when rVEGFC was simultaneously administered (Figure 9b-e).

I repeated this experiment in an automated imaging system to monitor neurite length changes over time. Interestingly, rVEGFC alone exhibited a tendency toward increased neurite length in unstimulated neurons suggesting a role for VEGFC in neuritogenesis (Figure 9f, g). Consistent with the prior observation, Bic induced a time-dependent increase of total neurite length, which was not affected by rVEGFC (Figure 9f, g).

This is in line with previous studies that showed that VEGFC, unlike VEGFD, does not seem to play a role in dendrite maintenance (Litke et al., 2018; Mauceri et al., 2020; Mauceri et al., 2011).

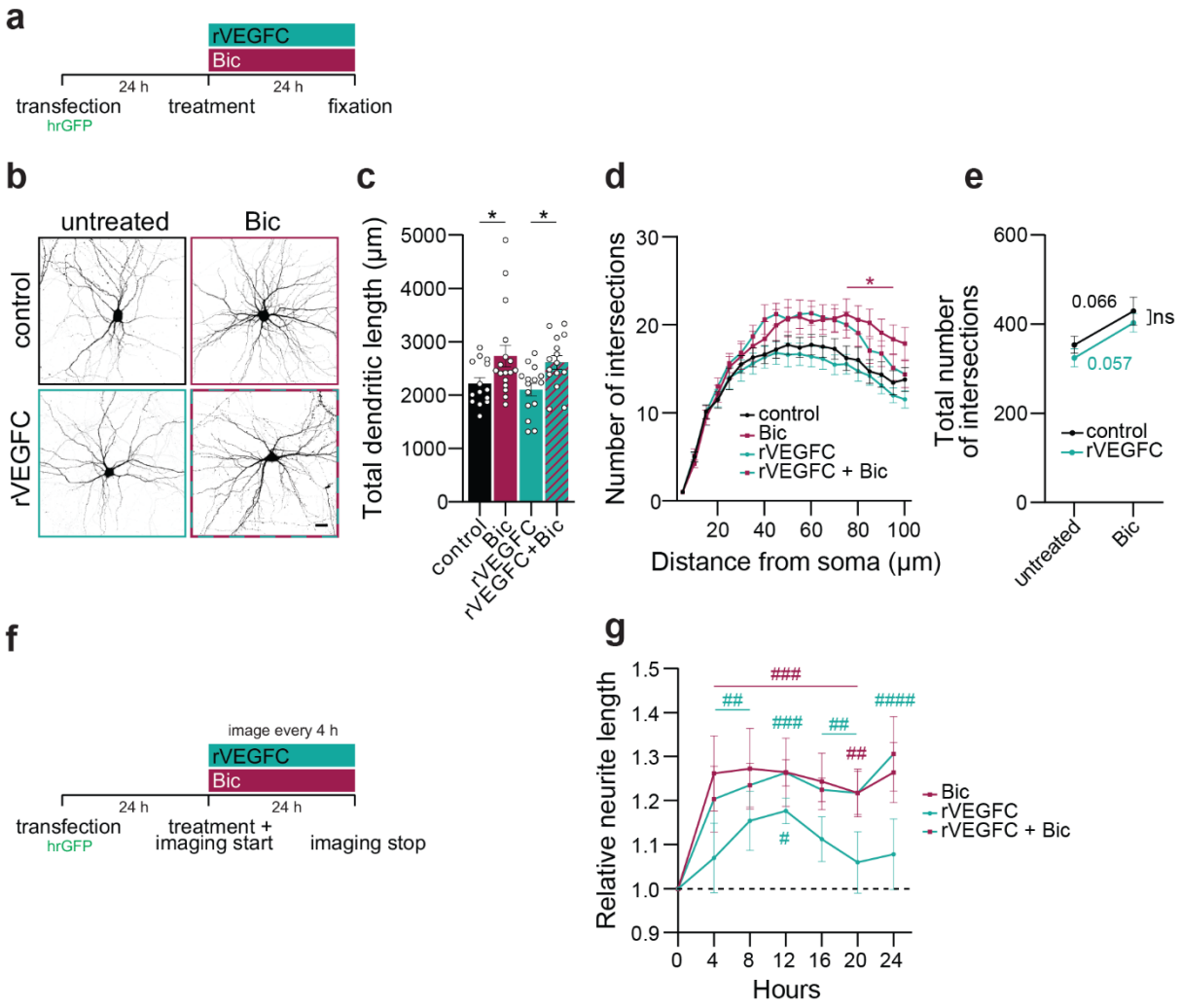

Figure 9. VEGFC does not counteract activity-dependent dendrite remodeling in adult neurons. ***a-e*** *Analysis of dendrite morphology of hrGFP-transfected cultured mouse hippocampal neurons with or without recombinant VEGFC (rVEGFC) and/or Bic supplementation for 24 h.* ***b*** *Schema of experiment.* ***c*** *Representative images of neurons treated as indicated. hrGFP was used to visualize neuronal morphology. Scale bar = 20 µm. c-e Total dendritic length (**c**), Sholl analysis (**d**) and total number of intersections up to a radius of 150 µm (**e**) of neurons treated as indicated. Two-way ANOVA followed by Bonferroni's post hoc test (**c, e**), or Dunnett's post hoc test (**d**). N = 14-17 neurons from 3 independent culture preparations.* ***f, g*** *Time-lapse monitoring of neurite length for 24 h of hrGFP-transfected cultured mouse hippocampal neurons with or without rVEGFD and/or Bic treatment.* ***f*** *Schema of experiment.* ***g*** *Relative total neurite length over time normalized on the first timepoint and untreated control. Two-way ANOVA followed by Dunnett's post hoc test. N = 3 independent cultures. Graphs display mean ± SEM. Single values are represented as data points. Significance indicators include asterisks (*) for comparisons between conditions and hashtags (#) for comparisons to baseline values within each respective condition. *p < 0.05; ####p < 0.0001; ###p < 0.001; ##p < 0.01; #p < 0.05; ns p>0.05. Experiments in a-e were performed by Dr. Jing Yan. This figure is adapted from a first authored manuscript that is currently in revision for submission to Cellular and Molecular Life Sciences (see List of publications).*

3.1.4 VEGFD does not alter neuronal activity

To rule out the potential contribution of non-direct effects of VEGFD on dendrites and instead explore whether the VEGFD-induced modulation of structural rearrangement might be associated with interference in Bic-triggered activity, I performed calcium imaging to assess nuclear calcium transients as an indicator of neuronal activity (Grienberger et al., 2012). Bic stimulation induced repetitive nuclear calcium rises consistent with action potential bursting (Bengtson et al., 2013) (Figure 10a-d). Importantly, these rises persisted and remained comparable in both frequency and amplitude even when rVEGFD was applied to the cultures concurrently or 30 min advance (Figure 10a-d). These findings affirm that VEGFD has a direct impact on dendrite architecture without disrupting neuronal activity.

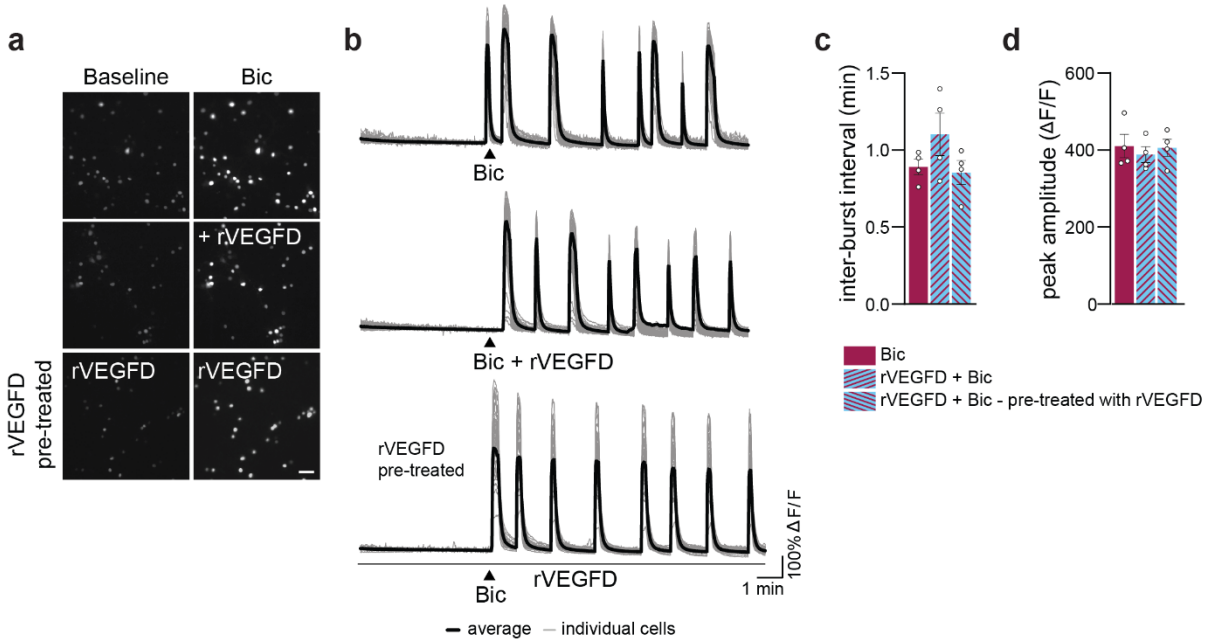

Figure 10. VEGFD does not affect synaptic-activity-induced nuclear calcium transients. *Calcium imaging of jRGECO1alpha-NLS-infected cultured mouse hippocampal neurons pre-treated or not with recombinant VEGFD (rVEGFD) for 30 min followed by a treatment with bicuculline (Bic) or Bic and rVEGFD.* ***a*** *Representative images of jRGECO1alpha-NLS fluorescence at baseline and after Bic or Bic and rVEGFD treatment.* ***b*** *Representative traces showing the time course of evoked Bic-induced nuclear calcium transients in neurons treated as indicated. Scale bar = 100 µm.* ***c, d*** *Mean inter-peak interval (**c**) and mean peak amplitude (**d**) of the first 10 min post treatment. Two-tailed unpaired Student's t-test. N = 6-7 coverslips from 4 independent culture preparations. Graphs display mean ± SEM. Single values are represented as data points. This figure is adapted from a first authored manuscript that is currently in revision for submission to Cellular and Molecular Life Sciences (see List of publications).*

In sum, these data indicate that VEGFD expression hinders structural plasticity of dendrites and is therefore reduced during structural plasticity to enable structural remodeling both during development and in adulthood.

3.2 Effect of VEGFD on dendrite and cytoskeletal dynamics

The previous chapter and studies have shown that VEGFD modulates cellular morphology (Chakraborty et al., 2021; Hemstedt et al., 2017; Litke et al., 2018; Mauceri et al., 2020; Mauceri et al., 2011; Mauceri et al., 2015; Maurer et al., 2020; Orlandini et al., 1996a; Schlüter et al., 2020). However, the cellular mechanism by which VEGFD executes the stabilization of dendritic architecture remains unclear. This section of the thesis aims to investigate the impact of VEGFD on dendrite dynamics and the neuronal cytoskeleton.

3.2.1 VEGFD impacts synaptic activity-induced dendritic dynamics

It is unclear how VEGFD prevents activity-dependent dendrite remodeling. VEGFD might restrict growth or promote the destabilization of growing dendrites. To answer this question, I established time-lapse imaging to monitor dendrite dynamics. Neurons labelled through hrGFP-transfection were treated with Bic to induce synaptic activity, rVEGFD or both and imaged for 11 h. I trained a machine learning-based algorithm to automatically reconstruct the entire dendritic tree in time-lapse videos to allow tracking of all dendrites of a neuron individually over time (Figure 11a-c).

Even though the dendritic arbor of adult neurons is mostly stable, it still undergoes dynamic growth and retraction to a certain extend to allow exploration of the environment for synaptic partners, but the dynamics are at a balance resulting in minimal overall expansion of the dendritic arbor (Cline, 2001; Wong et al., 2002). The dynamic behavior that I observed in untreated neurons is consistent with this pattern (Appendix figure 1).

As expected, Bic-induced synaptic activity triggered an increase of total dendrite length over time, which was prevented by rVEGFD co-application (Figure 11d, e). rVEGFD per se did not affect total dendrite length in unstimulated neurons. Bic stimulation also triggered an increase in the number of dendrites over time (Figure 11f, g). This effect was attenuated by rVEGFD, but surprisingly not fully prevented (Figure 11f, g).

The number of dendrites can increase either by the addition of new dendrites or when fewer dendrites are eliminated compared to control neurons. Assessment of the subpopulation of new

dendrites, i.e. dendrites that did not exist yet in the first imaging timepoint, revealed that Bic-treated neurons had the tendency to not only generate more new dendrites but to also reduce their elimination (Figure 11i, j). While the activity-induced formation of new dendrites was not affected by rVEGFD, newly formed dendrites had the tendency to be eliminated again (Figure 11i, j).

Next, dendrites were classified based on their dynamics: elongated dendrites refer to dendrites that have increased in length; shortened dendrites have decreased in length or were eliminated; stable dendrites have maintained their length (Figure 11h). This was computed for all dendrites (Figure 11l, m). or for just the subpopulation of new dendrites (Figure 11n, o). While Bic did not impact the number of elongated or eliminated dendrites, neither regarding all nor just the subpopulation of new dendrites (Figure 11l-o), fewer dendrites elongated when rVEGFD was co-applied (Figure 11l). However, elimination of dendrites or the dynamics of the subpopulation of new dendrites were also unaffected by rVEGFD (Figure 11m-o). Rate of dendrite elongation or shortening were not affected by any treatment (Appendix figure 1).

These results show that VEGFD has no effect on the formation of new dendrites nor their elongation and shortening. Rather, it amplifies their destabilization and impedes the elongation of pre-existing dendrites driven by synaptic activity. In this way, VEGFD makes up for the synaptic activity-induced formation of new dendrites, preventing the net increase in dendritic length.

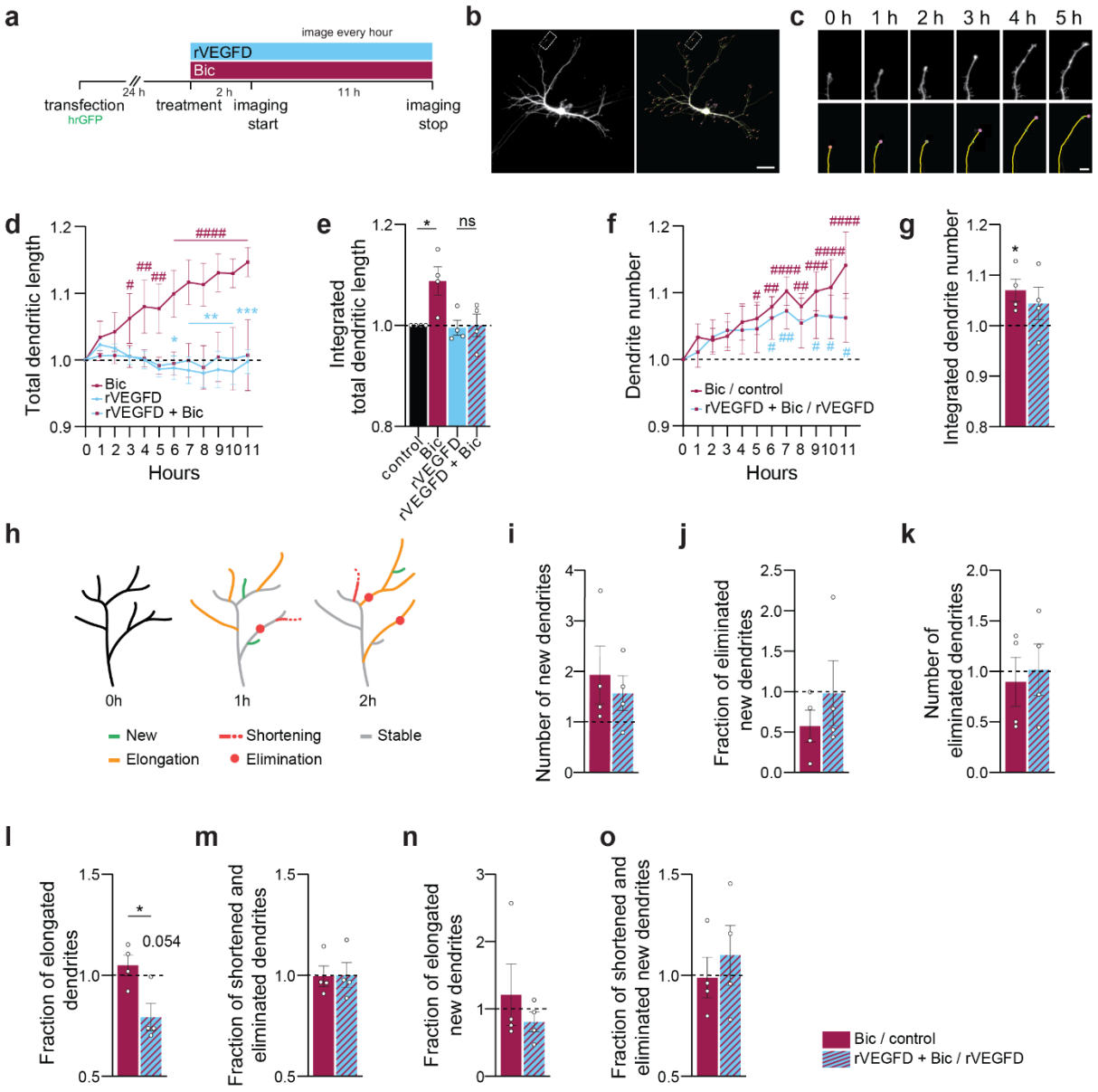

Figure 11. VEGFD modifies synaptic activity-induced dendrite dynamics. *Time-lapse monitoring of dendrites of hrGFP-transfected cultured mouse hippocampal neurons with or without recombinant VEGFD (rVEGFD) and/or bicuculline (Bic) treatment. hrGFP was used to visualize neuronal morphology.* ***a*** *Schema of experiment.* ***b*** *Representative images of an hrGFP-expressing neuron. Image to the right shows an overlay of dendrite traces. Scale bar = 50 µm.* ***c*** *Tracking of an individual dendrite from neuron in (**b**) (marked with a rectangle) at indicated timepoints. Images in the lower row show an overlay of dendrite traces. Scale bar = 10 µm.* ***d*** *Total dendritic length over time normalized on the first timepoint and untreated control.* ***e*** *Integration of data shown in (**d**).* ***f*** *Total dendrite number over time normalized on the first timepoint and respective untreated control.* ***g*** *Integration of data shown in (**f**).* ***h*** *Illustration depicting dendrite dynamics, with dendrites color-coded to represent their respective dynamic properties: elongated dendrite, red: shortened dendrite, red circle: eliminated dendrite, grey: stable dendrite.* ***i*** *Total number of new dendrites normalized on respective untreated control.* ***j*** *Fraction of new dendrites that were then eliminated normalized on respective untreated control.* ***k*** *Total number of eliminated dendrites normalized on respective untreated control.* ***l*** *Fraction of elongated dendrites over time normalized on respective untreated control.* ***m*** *Fraction of shortened and eliminated dendrites over time normalized on respective untreated control.* ***n*** *Fraction of elongated new dendrites over time normalized on respective*

untreated control. ***o*** *Fraction of shortened and eliminated new dendrites over time normalized on respective untreated control. Two-way ANOVA followed by Dunnett's post hoc test for comparisons to basal values (**d, f**), or Tukey's post hoc test for comparisons between conditions (**d, f**); One-way ANOVA followed by Tukey's post hoc test (**e**); one sample t-test for comparisons to respective untreated control (**g, i-o**), or two-tailed unpaired Student's t-test for comparisons between conditions (**g, i-o**). N = 4 independent culture preparations, 14-19 neurons per condition in total. Graphs display mean ± SEM. Single values are represented as data points. Significance indicators include asterisks (*) for comparisons between conditions and hashtags (#) for comparisons to baseline values within each respective condition. ***p < 0.001; **p < 0.01; *p < 0.05; ns p>0.05; ####p < 0.0001; ###p < 0.001; ##p < 0.01; #p < 0.05. This figure is adapted from a first authored manuscript that is currently in revision for submission to Cellular and Molecular Life Sciences (see List of publications).*

A collaboration with Prof. Dr. Gillian Queisser and Madison Shoraka was initiated to develop a mathematical model displaying the contributions of the computed parameters of dendrite dynamics on the total dendritic length. Due to limitations in the sample number, a model incorporating all measured parameters could not be realized. Instead, using the total dendrite number and total length net growth or decay for each timepoint, descriptive models of the changes of total dendrite length were generated for each condition separately (Figure 12). For Bic-treated neurons, which displayed a continuous increase in total dendrite length, a single ordinary differential equation was sufficient to describe the development of the overall dendrite length (Figure 12a). Although total dendrite lengths were not significantly affected by rVEGFD in Bic stimulated or unstimulated neurons, small variations could still be observed compared to control (+/- 2%) (Figure 12b, c). These changes could not be described in a single equation and were instead split into two and three equations for rVEGFD and for rVEGFD with Bic, respectively (Figure 12b, c), indicating that rVEGFD causes dendrite dynamics to undergo different phases.

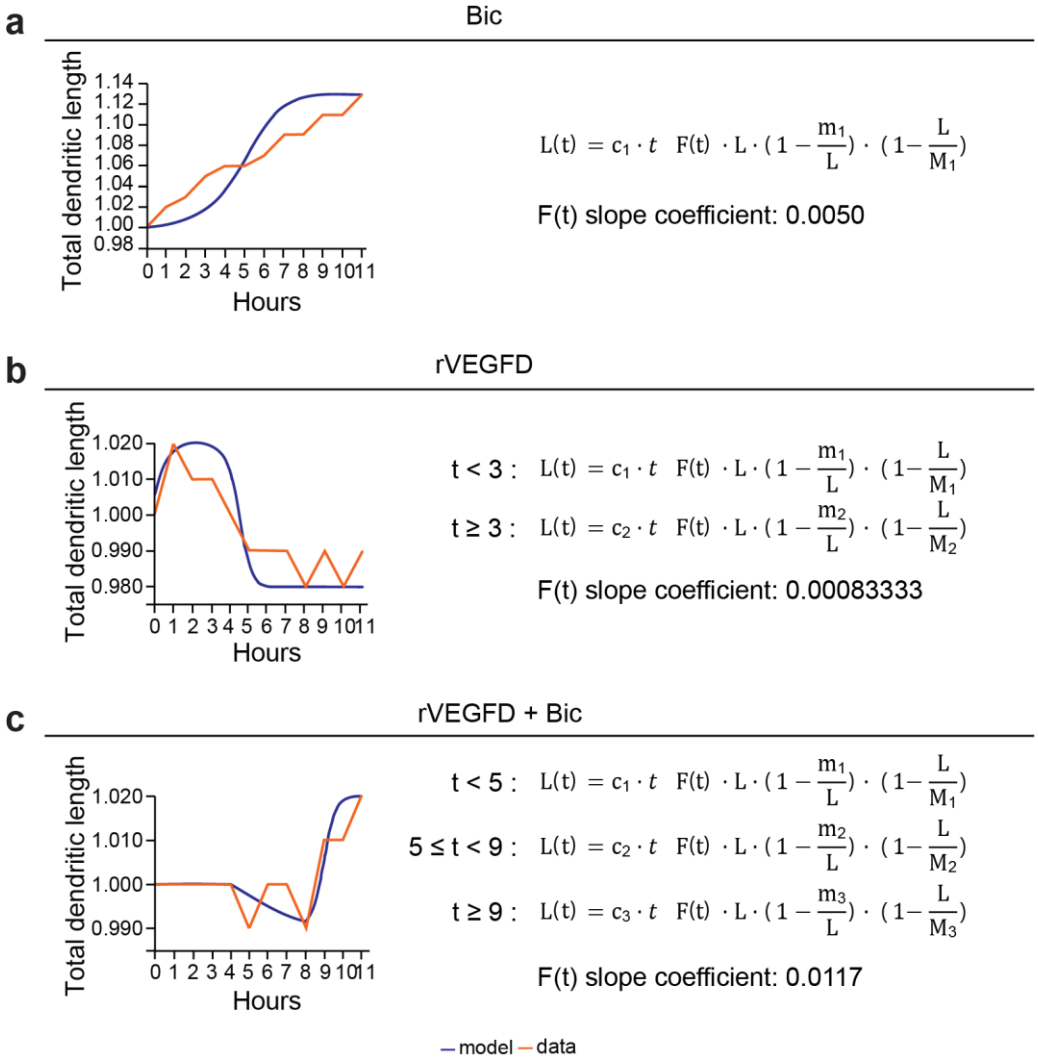

Figure 12. Descriptive mathematical model of the influence of synaptic activity and VEGFD on the dynamics of total dendritic length. *Graphs display actual mean total dendritic length (orange line) and modeled total dendritic length (blue) over time of cultured mouse hippocampal neurons treated with bicuculline (Bic) (**a**), recombinant VEGFD (rVEGFD) (**b**), or both (**c**). Model equations are shown on the right. t = time in hours; L = total dendritic length; L(t) = total dendritic length at t; ci = average total dendritic length change over interval i (calculated from data); mi = minimum total dendritic length value over interval i (calculated from data); Mi = maximum total dendritic length value over interval i (calculated from data); F(t) = number of dendrites at t (linear function interpolated from data). The model is based on data obtained from 14-19 neurons across 4 independent culture preparations per condition and was developed by Madison Shoraka and Dr. Gillian Queisser.*

3.2.2 VEGFD does not affect actin dynamics in dendritic spines

Actin is primarily concentrated in dendritic spines than in the dendritic shaft (Honkura et al., 2008) and plays a major role in the regulation of spine morphology and synaptic plasticity (Cingolani et al., 2008; Koleske, 2013; Yuste et al., 2001). Therefore, to assess the potential effects of VEGFD on actin dynamics, I initially examined it in spines by performing fluorescence recovery after photobleaching (FRAP) (Heinze et al., 2022; Koskinen et al., 2014). For this, primary hippocampal mouse neurons

were transfected to overexpress the peptide Lifeact, which labels actin without interfering with its dynamics, fused to GFP (Riedl et al., 2008). Lifeact-GFP was predominantly localized in spines, exhibiting the same expression pattern as endogenous actin (Figure 13a) (Heinze et al., 2022; Koskinen et al., 2014). After 5, 15 or 30 min with or without rVEGFD treatment, lifeact-GFP expressing spines were bleached with a laser followed by time-lapse imaging to monitor fluorescence recovery (Figure 13a). Fluorescence recovers because bleached GFP-actin is exchanged by new non-bleached GFP-actin molecules that diffuse into the spine (Koskinen et al., 2014). Due to slow and fast exchanging GFP-actin pools, not all GFP-actin molecules in spines are exchanged during the imaging time window. Neither the recovered and non-recovered fractions (referred to as mobile and stable fraction, respectively), nor the time needed to recover half of the GFP-actin fluorescence intensity (half-time) was impacted by rVEGFD when compared to control neurons (Figure 13b).

This indicates that VEGFD does not affect actin turnover and assembly in spines, which is in line with previous findings that VEGFD has no effect on dendritic spine shape or density (Mauceri et al., 2011; Maurer et al., 2020).

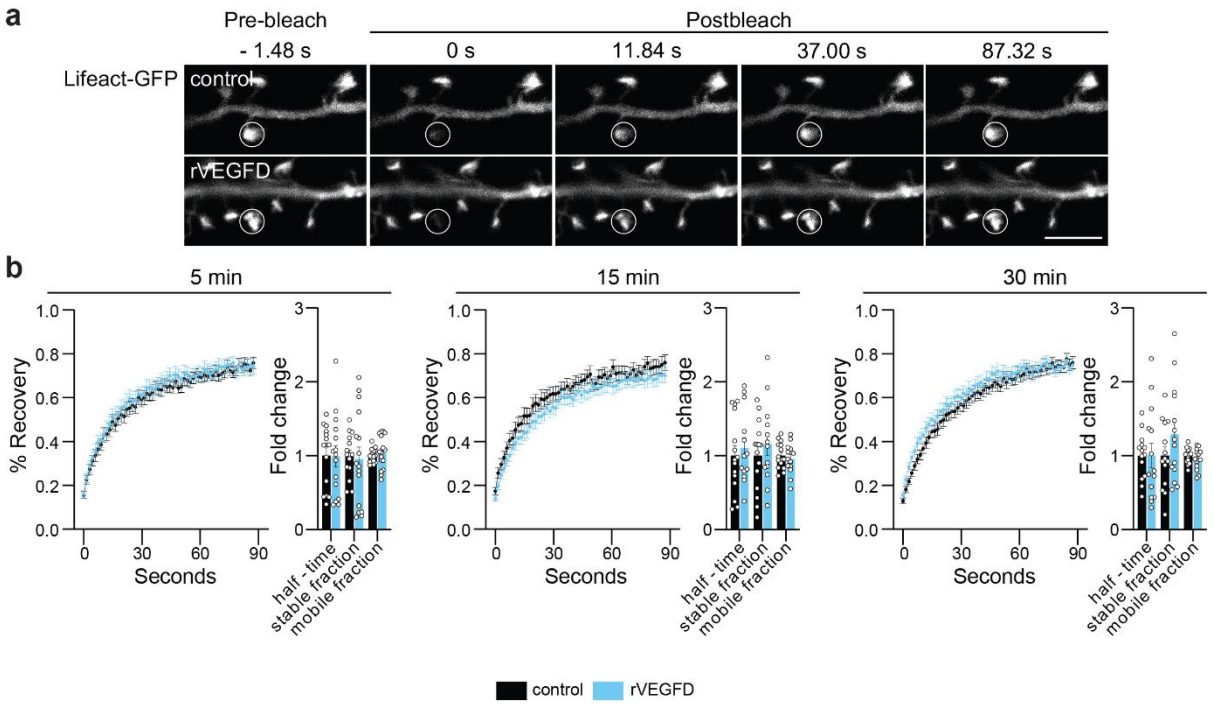

Figure 13. VEGFD does not affect actin turnover in dendritic spines. ***a, b*** *Fluorescence recovery after photobleaching (FRAP) analysis in spines of Lifeact-GFP-transfected cultured mouse hippocampal neurons with or without 5, 15 or 30 min recombinant VEGFD (rVEGFD) treatment.* ***a*** *Representative images of FRAP time-lapse series of neurons with or without 15 min rVEGFD treatment. Bleached spine is marked with a circle. Frames before (-1.48 s) and after bleaching (0 s - 87.32 s) are shown. Scale bar = 5 µm.* ***b*** *GFP-actin FRAP recovery curves from several spines for each condition normalized to average pre-bleach fluorescence and quantifications of half-time, stable and mobile fraction normalized to corresponding untreated control. Two-tailed unpaired Student's t-test or Mann-Whitney test. N = 13-16 neurons from 4 independent culture preparations, 1-3 spines per neuron, 31-*

*36 spines/condition in total. Graphs display mean ± SEM. Single values are represented as data points. **p < 0.01; *p < 0.05. Data presented in this figure are part of a first authored manuscript that is currently in revision for submission to Cellular and Molecular Life Sciences. This figure is adapted from a first authored manuscript that is currently in revision for submission to Cellular and Molecular Life Sciences (see List of publications).*

3.2.3 VEGFD acts on cortical actin

Actin is primarily enriched in spines, yet it also controls the overall architecture of neurons by being a component of the contractile actomyosin network located beneath the cell plasma membrane, commonly referred to as the actin cell cortex (Mikhaylova et al., 2020; Salbreux et al., 2012). This structure is essential for regulating membrane tension, cell shape and elasticity (Mikhaylova et al., 2020; Salbreux et al., 2012). Dr. Jing Yan previously demonstrated an increase in membrane stiffness of primary hippocampal mouse neurons treated with rVEGFD using atomic force microscopy (AFM) (Figure 14a) (Haase et al., 2015; Krieg et al., 2019). As the actin cell cortex and its attachment to the plasma membrane determine cell stiffness (Salbreux et al., 2012; Vahabikashi et al., 2019), this finding indicates an effect of VEGFD on cortical actin. This is consistent with a previous study showing that VEGFD increases cell stiffness in an adenocarcinoma cell line (Wang et al., 2014).

In parallel, it was also tested whether VEGFD retained its ability to enhance cell stiffness in the context of Bic-induced synaptic activity. While Bic did not impact cell stiffness, the co-application of rVEGFD with Bic continued to result in an increase in cell stiffness (Appendix figure 2a).

To complement this discovery with a more direct assessment of actin dynamics in dendrites, I conducted time-lapse imaging of primary hippocampal mouse neurons expressing LifeAct-TagGFP2. The expression pattern, marked by a significant concentration in spines, closely resembled both GFP-actin (see chapter 3.2.2) and the endogenous distribution of actin (Figure 14b) (Heinze et al., 2022; Koskinen et al., 2014). However, time-lapse videos of LifeAct-TagGFP2 revealed no movements of actin along dendrites (Figure 14b, c). Dynamic reorganization of actin dendrites was only recently observed through super resolution imaging (Lavoie-Cardinal et al., 2020). This was also not affected by treatment with rVEGFD for 20 min (Figure 14c).

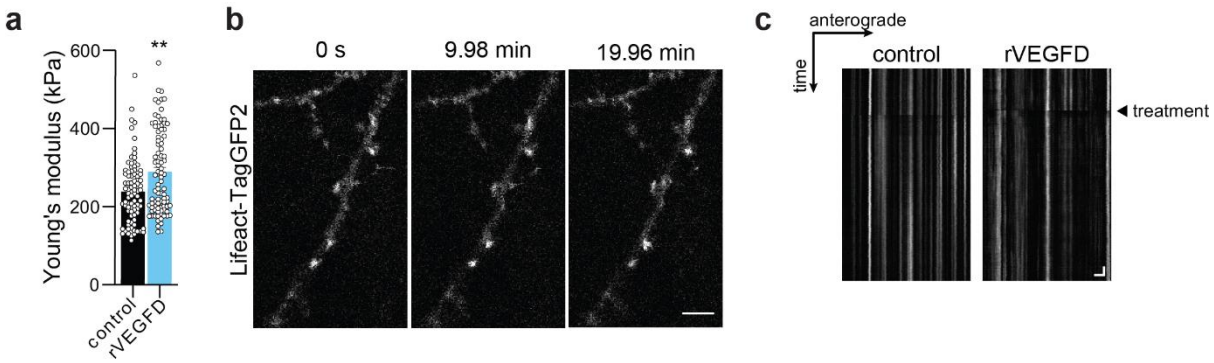

Figure 14. VEGFD modulates cortical actin. ***a*** *Atomic force microscopy measurements on the soma and proximal dendrites of cultured mouse hippocampal neurons with or without recombinant VEGFD (rVEGFD) treatment. Mann-Whitney test. N = 88-90 neurons from 3 independent culture preparations.* ***b-c*** *Time-lapse imaging of actin dynamics in dendrites of LifeAct-TagGFP2-infected cultured mouse hippocampal neurons.* ***b*** *Representative timeseries of LifeAct-TagGFP2-transfected dendrite. Scale bar = 5 µm.* ***c*** *Representative kymograph of LifeAct-TagGFP2-expressing dendrite of a rVEGFD- or vehicle-treated neuron showing no movement of LifeAct-TagGFP2. Arrow on the right indicates treatment start. Scale bar = 5 µm, 60 s. N = 7 neurons from 3 independent culture preparations were imaged. Graphs display mean ± SEM. Single values are represented as data points. **p < 0.01. Parts of this figure are adapted from a first authored manuscript that is currently in revision for submission to Cellular and Molecular Life Sciences (see List of publications).*

3.2.4 VEGFD acts on microtubules

In addition to actin, microtubules (MTs) constitute the predominant cytoskeletal element in dendrites. They provide structural support and exert mechanical force crucial for the growth of dendrites, whether in the formation of new branches or the elongation of existing ones (Georges et al., 2008; Kapitein et al., 2015; Poulain et al., 2010).

Transfection of primary mouse hippocampal neurons with the microtubule plus-end-binding protein 3 (EB3)-GFP, which marks the growing ends of microtubules and manifests as comet-like structures in time-lapse microscopy, allows the visualization and analysis of dynamic changes in microtubules (Figure 15b) (Jaworski et al., 2009; Stepanova et al., 2003). EB3-GFP expression mirrored endogenous expression as it co-localized with immunocytochemically labeled Microtubule Associated Protein 2 (MAP2) and tubulin (Jaworski et al., 2009; Pchitskaya et al., 2017; Stepanova et al., 2003)(Figure 15a). To validate the functioning of EB3-GFP, neurons were treated with drugs that disrupt MT dynamics and are known to eliminate EB3 binding to growing MTs and cause EB3 comets to vanish (Jaworski et al., 2009; Stepanova et al., 2003). Taxol, a microtubule-stabilizing agent, and nocodazole which sequesters tubulin dimers, thereby preventing MT polymerization, were employed (Downing, 2000; Jaworski et al., 2009; Stepanova et al., 2003). Application of both drugs resulted in the disappearance of EB3 comets, confirming the methodology's functionality (Figure 15c).

Next, the potential effect of VEGFD on EB3-GFP dynamics was monitored by supplementing neurons after 5 min of baseline recording with or without rVEGFD (Figure 15d). In the initial 5 min of rVEGFD treatment, there was a decrease in the speed of travel and an increase in the lifetime of EB3-comets, while the density of comets and the direction of microtubule growth remained unaffected when compared to baseline levels and untreated neurons (Figure 15e). When treatment and imaging were maintained for 20 min, this impact was no longer significant (Figure 15f). This implies that VEGFD causes an initial drop in MT dynamics.

In parallel, it was also tested how VEGFD affects MT dynamics in the context of Bic-induced synaptic activity (Appendix figure 2b-d). In contrast to a previous study that found enhanced EB3-comet speed after only 2 min Bic/glycine treatment in rat hippocampal neurons (Ghiretti et al., 2016), 5 min of Bic treatment in mouse hippocampal neurons resulted in a decrease in comet speed at 5 min, similar to rVEGFD (Appendix figure 2c). This variation might be attributable to the duration of exposure to Bic, co-application of Bic with glycine or to differences in the maturity and density of the cultures which might affect network properties and subsequently impact their response to Bic. When rVEGFD was co-applied, the reduction in comet speed remained the same (Appendix figure 2c). However, whereas the drop in comet speed returned to normal values in Bic- or rVEGFD-treated neurons, it remained with rVEGFD co-treatment after 20 min of imaging (Appendix figure 2d). Bic also increased comet lifespan after 20 min of treatment, as previously observed (Ghiretti et al., 2016), which is prevented by rVEGFD (Appendix figure 2d). Comet density and percentage of anterograde movements were not affected by Bic treatment at any timepoint tested (Appendix figure 2c, d), although Ghiretti et al. (2016), previously reported an increase of anterograde movements with Bic treatment. Interestingly, when rVEGFD was delivered for 5 min, percentage of anterograde movements increased marginally (Appendix figure 2c). Moreover, 20 min of rVEGFD reduced comet density even in the presence of Bic (Appendix figure 2d).

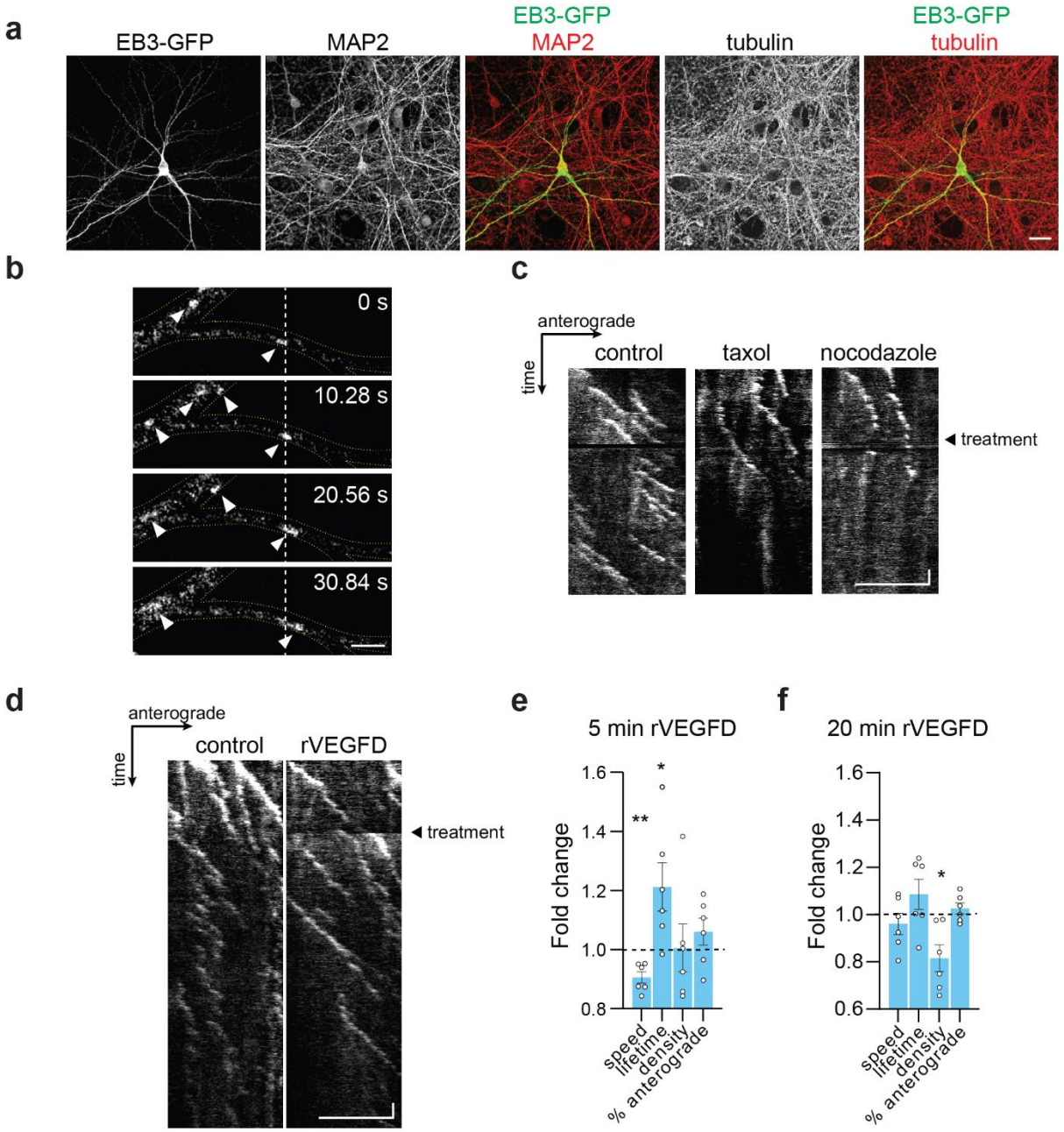

Figure 15. VEGFD modulates microtubule dynamics. ***a-c*** *Validation of time-lapse imaging of microtubule (MT) dynamics in plus-end-binding protein 3 (EB3)-GFP-transfected cultured mouse hippocampal neurons.* ***a*** *Representative images of an EB3-GFP-transfected neuron co-immunostained with microtubule-associated protein 2 (MAP2) and tubulin. Scale bar = 20 µm.* ***b*** *Representative timeseries of EB3-GFP comet (highlighted with arrowheads) movements along a dendrite. Vertical dashed line helps to follow the course of a comet. Scale bar = 2 µm.* ***c*** *Representative kymographs of dendrites from EB3-GFP-transfected neurons treated after 5 min with taxol, nocodazole or vehicle. Arrow on the right indicates treatment start. Scale bar = 5 µm, 60 s.* ***d-f*** *Analysis of MT dynamics in EB3-GFP-transfected neurons treated with recombinant VEGFD (rVEGFD) or not. Treatments were applied after 5 min of baseline recording and the effect monitored for 20 min.* ***d*** *Representative kymographs of dendrites from EB3-GFP-transfected neurons treated as indicated. Arrow on the right indicates treatment start. Scale bar = 5 µm, 60 s.* ***e, f*** *EB3-GFP comet speed, lifetime, density, and percentage of anterograde comet movements normalized on baseline and respective untreated control after 5 min (**e**) or 20 min (**f**) of rVEGFD treatment. One sample t-test. N = 6 independent culture preparations. 10 neurons/condition in total, on average 5-8 dendrites per neuron. Graphs*

*display mean ± SEM. Single values are represented as data points. **p < 0.01; *p < 0.05. Parts of this figure are adapted from a first authored manuscript that is currently in revision for submission to Cellular and Molecular Life Sciences (see List of publications).*

In conclusion, these findings suggest that VEGFD influences cortical actin and MTs to accomplish its structural stabilization role.

3.3 VEGFD signaling in neurons

The previous chapters showed that VEGFD modulates the cytoskeleton and opposes structural plasticity of dendrites. However, little is known about the signaling cascade that VEGFD initiates in order to deliver its stabilization signal to the cytoskeleton and, finally, dendritic structure. This section will focus on VEGFD downstream signaling in neurons.

3.3.1 Phospho-proteomic screening for cytoskeleton-associated proteins regulated by VEGFD signaling

To identify the proteins responsible for transmitting the VEGFD-mediated dendrite stabilization signal to the cytoskeleton, lysates of primary mouse hippocampal neurons treated with rVEGFD for 30 min or 2 h were analyzed using a phospho-antibody array of cytoskeletal regulatory proteins. This array allowed detection of 68 distinct phosphosites and the expression of 55 proteins. This yielded a list of proteins whose phosphorylation was altered as a result of rVEGFD treatment compared to control neurons (Figure 16a, b).

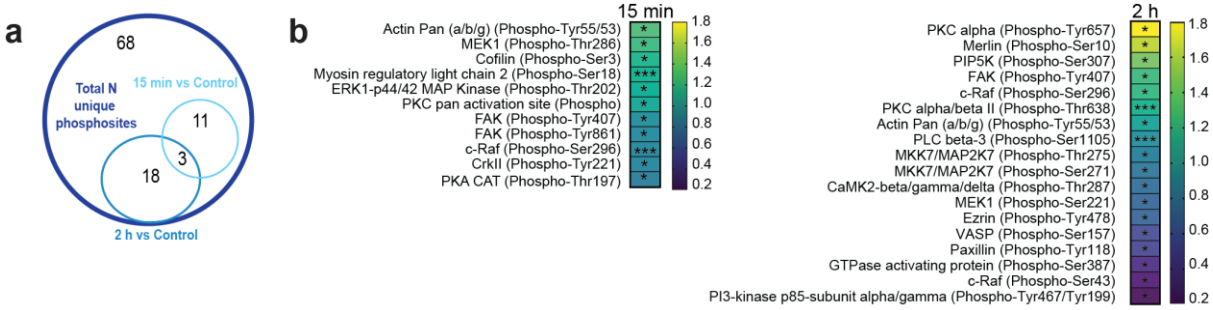

Figure 16. Phospho-proteomic screening for cytoskeleton-associated proteins modulated by VEGFD signaling. ***a, b*** *Phospho-proteomic screening on lysates derived from cultured mouse hippocampal neurons treated for 15 min or 2 h recombinant VEGFD (rVEGFD). Overview of numbers (**a**) and list of identified proteins with heatmap (**b**) showing significantly higher or lower detection in rVEGFD-treated neurons normalized on untreated control. Multiple paired t-test. N = 3 independent*

culture preparations. Experiment was performed by Prof. Dr. Daniela Mauceri. This figure is adapted from a first authored manuscript that is currently in revision for submission to Cellular and Molecular Life Sciences (see List of publications).

3.4 Role of phospho Y478 ezrin as a potential downstream candidate of VEGFD signaling

A noteworthy candidate from the screening conducted in chapter 3.3.1 is ezrin. Ezrin, along with the other two members radixin and moesin of the ERM (ezrin radixin moesin) family, is a protein that functions as a physical bridge connecting the actin cortex with the plasma membrane (Figure 17b), thereby playing a crucial role in regulating membrane tension (Rouven Brückner et al., 2015). ERMs anchor to plasma membrane lipids and transmembrane proteins through their N-terminal FERM domain (Four point one ERM domain), whilst their C-terminal ERMAD domain (ERM-association domain) binds to F-actin (Figure 17a, b) (Fehon et al., 2010; Ponuwei, 2016; Rouven Brückner et al., 2015). In their inactive cytosolic conformation, the FERM and ERMAD domains are linked and hence cannot connect plasma membrane and cortical actin (Figure 17b). Activation of ERMs occurs through the separation of the FERM and ERMAD domains, rendering them available for binding to the plasma membrane and F-actin, respectively. This activation unfolds in a two-step process: initial recruitment to the plasma membrane through attachment to phosphatidylinositol 4,5-bisphosphate (PIP2) via the N-terminal FERM domain, followed by the phosphorylation of a conserved threonine residue (T567 in ezrin) within the now exposed ERMAD domain (Figure 17b) (Fehon et al., 2010; Ponuwei, 2016; Rouven Brückner et al., 2015). Beyond its interaction with actin, ezrin also engages in governing the organization of microtubules at the actin cell cortex (Lasserre et al., 2010; Solinet et al., 2013). In doing so, ezrin functions as a key regulator of cell shape, adhesion, and motility (Buenaventura et al., 2023). Furthermore, ezrin plays an important role in cancer metastasis, and high levels of ezrin are associated with a poor cancer prognosis (Buenaventura et al., 2023).

Following 2 h of rVEGFD treatment, the screening revealed a reduction in the phosphorylation of ezrin at tyrosine 478 (Y478), also known as Y477, which corresponds to the location in chicken where ezrin was originally isolated (Bretscher, 1983) (Figure 17a). Deficient phosphorylation at this tyrosine residue has been linked to decreased actin-rich protrusions in epithelial cancer cells, metastatic spreading (Heiska et al., 2011; Mak et al., 2012) and tumor-induced angio- and lymphangiogenesis (Ghaffari et al., 2014). This chapter aims to uncover the molecular link between VEGFD and ezrin and the role of the dephosphorylation of Y478 ezrin in neuronal morphology.

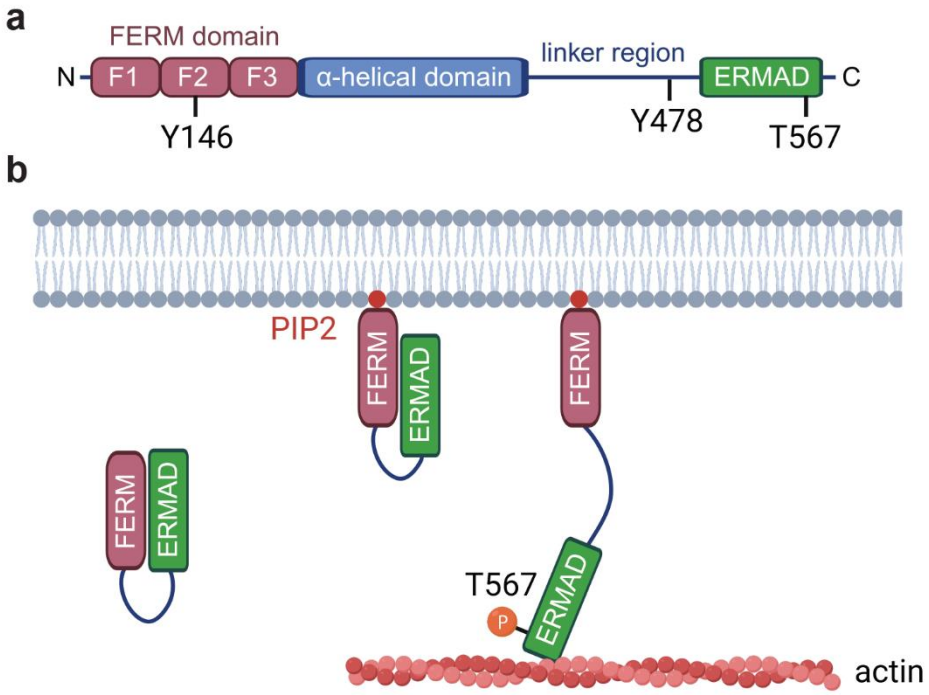

Figure 17. Structure and function of ezrin. ***a*** *Structure of ezrin. Ezrin has an N-terminal FERM domain and a C-terminal ERMAD domain that are connected by an α-helical linker region. The ERMAD domain harbors T567 of which the phosphorylation is crucial for activation of ezrin. Y478 is a phosphosite that is putatively regulated by VEGFD signaling and lies within the linker region. T146 is found within the FERM domain.* ***b*** *Schema illustrating the conversion from inactive to active ezrin. Through an intramolecular interaction between FERM- and ERMAD domains, ezrin is rendered inactive. When the FERM domain interacts with PIP2 at the plasma membrane, the ERMAD domain dissociates from the FERM domain, exposing T567 for phosphorylation. As a result, ezrin's ERMAD domain binds to filamentous actin, allowing it to link the plasma membrane to the actin cytoskeleton. FERM = Four point one ERM domain; ERMAD = ERM-association domain; T567 = Threonine 567; Y478 = Tyrosine 478; Y146 = Tyrosine 146; PIP2 = phosphatidylinositol 4,5-bisphosphate*

3.4.1 VEGFD reduces phosphorylation of Y478 ezrin

In this chapter, the VEGFD-induced reduction in the phosphorylation of ezrin at Y478, as identified in the phospho-proteomic screening (chapter 3.3.1), was further validated through experiments in which phosphorylation of ezrin is measured after enhancing VEGFD levels.

First, similar to the phospho-proteomic screening, primary mouse hippocampal neurons were treated for 2 h with rVEGFD and their homogenates were analyzed by Western blotting. Phosphorylation of ezrin was assessed by immunoblotting using antibodies for total ezrin or specific for pY478 ezrin. Ezrin immunoreactive bands were detected at a molecular weight higher than the predicted 69 kDa (UniProt, 2022). Consistently, in other studies, mouse ezrin is typically observed at approximately 80/85 kDa (Wakayama et al., 2009; Yuan et al., 2018a). PY478 ezrin appeared as

double bands. Fluorescent Western blotting using antibodies from different species against pY478 or total ezrin allowed co-labeling on the same membrane and revealed that the upper band of pY478 corresponds to total ezrin (Figure 18a). Therefore, the upper band was used for all quantifications. 2h rVEGFD treatment significantly reduced pY478 ezrin levels compared to untreated neurons (Figure 18b, c), corroborating the findings of the phospho-proteomic screening.

In parallel with this experiment, some groups received 2 h Bic treatment with or without rVEGFD co-application, to explore whether synaptic activity affects VEGFD-induced dephosphorylation of ezrin. Intriguingly, neurons treated with Bic or rVEGFD and Bic in combination showed much stronger reductions in pY478 ezrin levels (Appendix figure 3a, b).

Next, I attempted to develop a technique for quantifying ezrin phosphorylation using the Lumit™ Immunoassay system that incorporates NanoLuc® Binary Technology (Promega). This method relies on a pair of antibodies from distinct species targeting either total or pY478 ezrin, and the detection is enabled by secondary antibodies labeled with complementary luciferase subunits. When targeting phosphorylated ezrin, the subunits are brought into proximity creating an active enzyme that produces luminescence when exposed to its substrate. Despite its potential, this approach exhibited considerable nonspecific binding and was unreliable for accurate measurement of ezrin phosphorylation (data not shown).

Consequently, I turned to proximity ligation assay (PLA) for immunocytochemical assessment of ezrin phosphorylation. PLA operates similarly to the previous method; however, the secondary antibodies are linked to complementary single-stranded DNA strands, which hybridize when they are in close proximity. Subsequent PCR amplification generates a fluorescent signal, enabling visualization and quantification of phosphorylation (Figure 18d). PLA analysis confirmed the Western blot and screening data, demonstrating a reduction in pY478 ezrin levels in cultured neurons after 2 h rVEGFD treatment (Figure 18e, f).

Additionally, I tested whether rAAV-delivered overexpression of HA-tagged VEGFD driven by a CMV promoter affects pY478 ezrin levels (Figure 18g). CMV>LacZ-Flag served as a control (Figure 18g). Both constructs have been used and validated before in the department. However, pY478 ezrin levels were unaffected in VEGFD-overexpressing neurons (Figure 18h, i). However, it is possible that the putative effects of VEGFD signaling on pY478 ezrin are transient and are not seen when VEGFD is expressed constitutively.

Therefore, in the following experiment, overexpression of VEGFD was restricted to a 24 h time window using the ESARE-inducible system that drives expression of VEGFD-HA upon activity (Figure 18j) (Gulmez Karaca et al., 2020; Kawashima et al., 2013). ESARE>LacZ-HA served as a control (Figure

18j). Both constructs have been used and validated before in the department. As expected, *VEGFD* mRNA expression is reduced in ESARE>LacZ-expressing neurons but induced in ESARE>VEGFD-expressing neurons after Bic treatment (Figure 18k). Nonetheless, activity-induced overexpression of VEGFD did not affect pY478 ezrin levels (Figure 18l, m). 24 h could still be too long. Moreover, *VEGFD* mRNA levels are increased, albeit only slightly, at baseline, thus the real time window may be larger than 24 h. It can also not be ruled out that Bic treatment might have impacted pY478 ezrin levels.

In sum, three independent methods showed that VEGFD signaling leads to an at least transient dephosphorylation of Y478 ezrin.

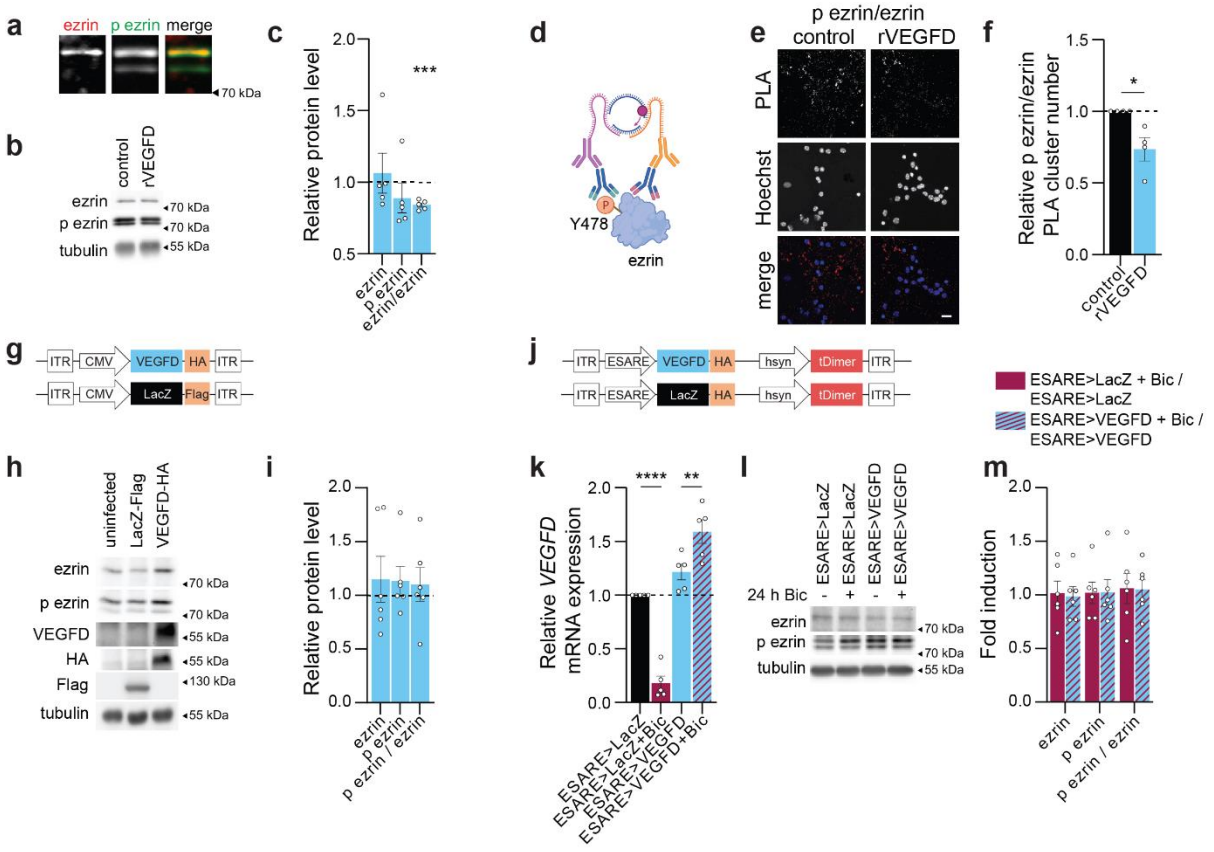

Figure 18. Acute recombinant VEGFD treatment causes dephosphorylation of Y478 ezrin. ***a*** *Two-color infrared fluorescence immunoblot of total ezrin (red) and phospho Y478 ezrin (green) with lysate from cultured hippocampal neurons.* ***b, c*** *Immunoblot analysis of ezrin protein expression and phosphorylation in cultured mouse hippocampal neurons treated or not with recombinant VEGFD (rVEGFD) for 2 h.* ***b*** *Representative immunoblots of ezrin, phospho Y478 ezrin and tubulin.* ***c*** *Quantification of ezrin, phospho Y478 ezrin and its phospho/total protein ratio. Expression was normalized on tubulin and control. One sample t-test (phospho/total ratio) and Wilcoxon signed-rank test (ezrin and phospho-ezrin). N = 5 independent culture preparations.* ***d-f*** *Proximity ligation assay (PLA) with antibodies against ezrin and phosho Y478 ezrin in cultured mouse hippocampal neurons treated or not with rVEGFD for 2 h.* ***d*** *Schema illustrating mechanism of PLA detection of phospho-proteins.* ***e*** *Representative images of PLA signal in neurons treated as indicated. Nuclei were visualized with Hoechst. Scale bar = 20 µm.* ***f*** *PLA cluster number normalized on the number of Hoechst-labelled cells and on control. One sample t-test. N = 4 independent culture preparations.* ***g-i*** *Immunoblot analysis of ezrin protein expression and phosphorylation in cultured mouse hippocampal*

neurons infected with rAAVs to drive overexpression of VEGFD-HA or LacZ-Flag. ***g*** *Schema of rAAV constructs.* ***h*** *Representative immunoblots of ezrin, phospho Y478 ezrin, VEGFD, HA, Flag and tubulin.* ***i*** *Quantification of ezrin, phospho Y478 ezrin and its phospho/total protein ratio. Expression was normalized on tubulin and control. One sample t-test. N = 6 independent culture preparations.* ***j-m*** *Immunoblot analysis of ezrin protein expression in cultured mouse hippocampal neurons infected with rAAVs to drive overexpression under the control of the activity-dependent ESARE promoter of VEGFD-HA or LacZ-HA. Neurons were treated for 24 h with bicuculline (Bic) or not to activate the promoter.* ***j*** *Schema of rAAV constructs.* ***k*** *QRT-PCR analysis of VEGFD mRNA expression to confirm induction of VEGFD expression with Bic treatment. Expression was normalized on gusb and ESARE>LacZ. One-way ANOVA followed by Bonferroni's post hoc test. N = 5 independent culture preparations.* ***l, m*** *Representative immunoblots of ezrin, phospho Y478 ezrin and tubulin. Quantification of ezrin, phospho Y478 ezrin and its phospho/total protein ratio. Expression was normalized on tubulin and respective untreated control. Two-tailed unpaired t-test. N = 6 independent culture preparations. Graphs display mean ± SEM. Single values are represented as data points. ****p < 0.0001; ***p < 0.001; **p < 0.01; *p < 0.05. Experiment in k was jointly performed with Prof. Dr. Daniela Mauceri. Parts of this figure are adapted from a first authored manuscript that is currently in revision for submission to Cellular and Molecular Life Sciences (see List of publications).*

3.4.2 Subcellular expression pattern of ezrin

As the findings suggest a regulation of ezrin by VEGFD, I started to characterize ezrin in neurons and investigated its subcellular expression pattern.

As the antibodies available were inefficient in immunocytochemistry, I performed biochemical fractionations to concentrate proteins from the postsynapse from cultured rat hippocampal neurons (Figure 19a; Figure 38a-e) and from one human cortex sample (Figure 19b) or purified PSD from whole rat brain lysates (Figure 19c; Figure 38f) (Gardoni et al., 1998; Gardoni et al., 2001). Rat cells were used as I performed these experiments as a visiting scientist in the laboratory of Prof. Dr. Monica di Luca and Dr. Elena Marcello (Milano, Italy). Rat and human ezrin appeared at a slightly lower molecular weight (75 kDa) (Figure 19a-c) than mouse ezrin (Figure 18a) and ezrin in the rat brain was observed as a double band (Figure 19c). In rat neurons and in the rat brain, both ezrin and pY478 ezrin were less concentrated in the triton insoluble fraction (TIF), the fraction corresponding to the postsynapse enrichment (TIF), or in the PSD (post synaptic density)-purified fraction, respectively (Figure 19a, c), suggesting a more important role at cortical actin than in spinal actin. In the human cortex sample, on the other side, no difference between the total homogenate and TIF was observed (Figure 19b).

Given the differential distribution of ezrin but also VEGFR3 in spines (chapter 3.7.3), it could be possible that VEGFD signaling has a local effect on ezrin. To test this, I measured pY478 ezrin levels through immunoblotting in TIFs from cultured rat hippocampal neurons treated for 30 min with rVEGFD and observed a tendency toward elevated levels of pY478 ezrin in the TIF (Figure 19d, e).

This suggests that VEGFD signaling may exert a temporal and localization-dependent influence on ezrin phosphorylation. However, species-specific differences cannot be ruled out.

Moreover, phosphorylation of ezrin in TIFs was analyzed in the context of Bic-triggered synaptic activity. Immunoblotting detected a reduction of pY478 ezrin levels in the TIF after 30 min of Bic treatment in rat hippocampal neurons, while no change was observed in the total homogenate (Figure 19f, g). A reduction of pY478 ezrin in whole lysates was, however, detected after 2 h of Bic treatment in cultured mouse hippocampal neurons (Appendix figure 3). This observation suggests that the Bic-induced dephosphorylation of ezrin may be initiated locally at spines and subsequently propagates to other regions with sustained exposure to synaptic activity.

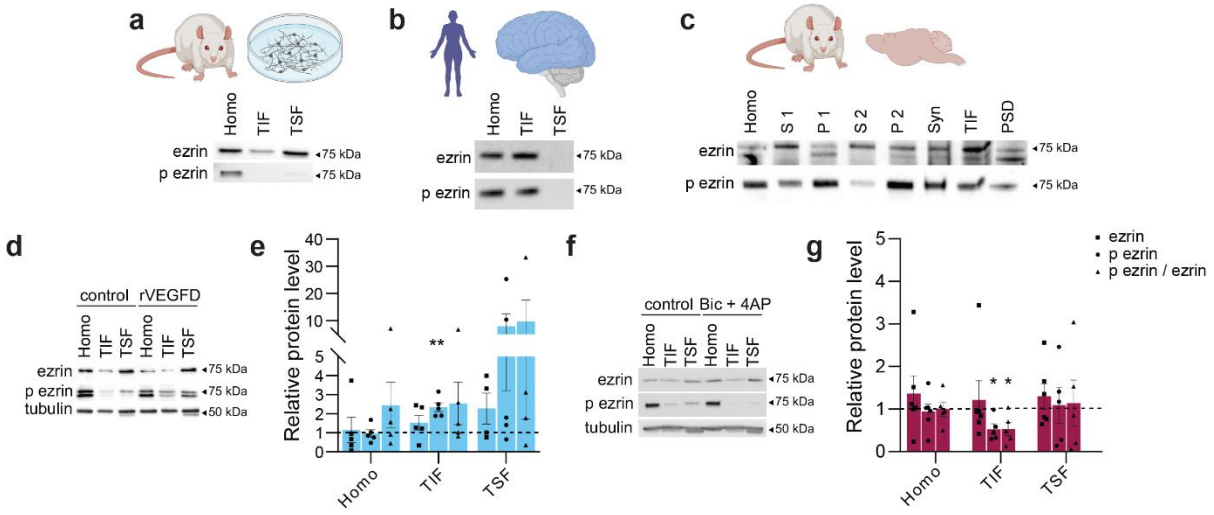

Figure 19. Characterization of the subcellular localization of ezrin. ***a, b*** *Representative immunoblots of total and phospho Y478 ezrin in triton insoluble fractions (TIF) enriched in postsynaptic proteins from lysates derived from rat cultured hippocampal neurons (**a**) or human cortex (**b**).* ***c*** *Representative immunoblots of total and phospho Y478 ezrin in postsynaptic density (PSD) preparations from rat brain lysates.* ***d, e*** *Immunoblot analysis of total and phospho Y478 ezrin protein expression in TIFs derived from cultured rat hippocampal neurons treated with or without rVEGFD for 30 min.* ***d*** *Representative immunoblots of total and phospho Y478 ezrin and tubulin.* ***e*** *Quantification of total and phospho Y478 ezrin and its phospho/total protein ratio normalized to tubulin and control of respective fraction. Wilcoxon signed-rank (**e**, homo ezrin) or one sample t-test N = 4-5 independent culture preparations.* ***f, g*** *Immunoblot analysis of total and phospho Y478 ezrin protein expression in TIFs derived from cultured rat hippocampal neurons treated with or without Bic and 4-aminopyridine (4AP) for 30 min.* ***f*** *Representative immunoblots of total and phospho Y478 ezrin and tubulin.* ***g*** *Quantification of total and phospho Y478 ezrin and its phospho/total protein ratio normalized to tubulin and control of respective fraction. Homo = homogenate; TSF = triton insoluble fraction; S 1/ S 2 = supernatant 1/2; P 1 /P 2 = pellet 1/2; Syn = synaptosomes. One sample t-test N = 5-6 independent culture preparations. Graphs display mean ± SEM. Single values are represented as data points. **p < 0.01; *p < 0.05. PSD was jointly prepared with Elisa Zianni.*

3.4.3 Src does not regulate phosphorylation of Y478 ezrin in neurons

The regulation of Y478 ezrin in neurons is unknown. Previous studies have identified Src as the kinase responsible for Y478 ezrin phosphorylation in human keratinocytes, mouse fibroblasts and HEK 293 cells (Chan et al., 2021; Heiska et al., 2005; Heiska et al., 2011). To investigate whether this holds true in neurons, Src family kinases were pharmacologically inhibited using PP2 at different concentrations and for different timespans (Chan et al., 2021; Heiska et al., 2005; Heiska et al., 2011) in primary mouse hippocampal neurons, and changes in Y478 ezrin phosphorylation were assessed initially through immunoblotting. As expected, the phosphorylation of Akt (p Akt), which is modulated by Src through the PI3K/AKT pathway and known to be reduced by PP2 treatment (Dai et al., 2018), decreased in PP2-treated neurons compared to vector-treated neurons with all treatment concentrations and durations tested (Figure 20a, b). However, pY478 ezrin remained unaffected (Figure 20a, b). Additionally, immunocytochemical analysis using PLA revealed that treatment with PP2, using the condition that induced strongest reduction in p Akt, did not impact the phosphorylation of ezrin (Figure 20c, d). Consequently, these findings suggest that Src may not be responsible for Y478 ezrin phosphorylation in neurons.

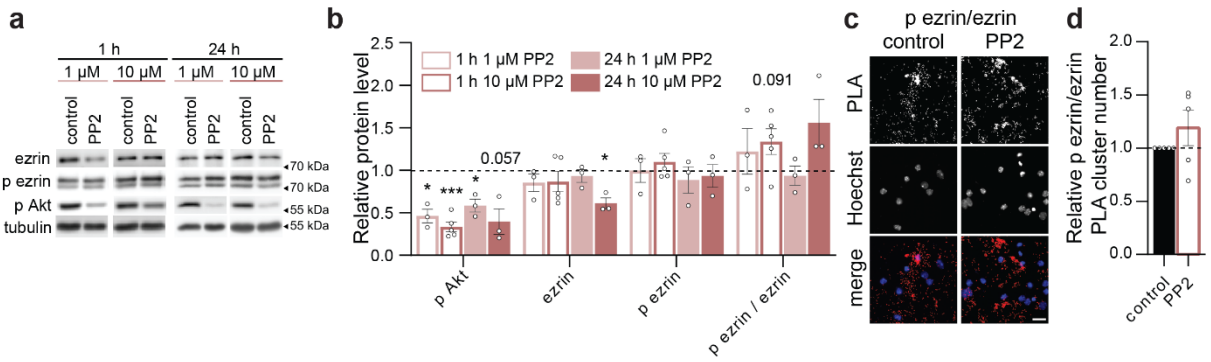

Figure 20. Inhibition of Src does not affect phosphorylation of Y478 ezrin. ***a, b*** *Immunoblot analysis in cultured mouse hippocampal neurons treated with DMSO (vector) or 1 µM or 10 µM PP2 for 1 h or 24 h.* ***a*** *Representative immunoblots of ezrin, phospho Y478 ezrin, phospho Akt and tubulin.* ***b*** *Quantification of phospho Akt, ezrin, phospho Y478 ezrin and its phospho/total protein ratio. Expression was normalized on tubulin and control. One sample t-test. N = 3-5 independent culture preparations.* ***c, d*** *Proximity ligation assay (PLA) with antibodies against ezrin and phosho Y478 ezrin in cultured mouse hippocampal neurons treated or DMSO (vector) or 10 µM PP2 for 1 h.* ***c*** *Representative images of PLA signal in neurons treated as indicated. Nuclei were visualized with Hoechst. Scale bar = 20 µm.* ***d*** *PLA cluster number normalized on the number of Hoechst-labelled cells and on control. One sample t-test. N = 5 independent culture preparations. Graphs display mean ± SEM. Single values are represented as data points. ***p < 0.001; *p < 0.05.*

3.4.4 STEP phosphatase dephosphorylates Y478 ezrin

A recent interactome analysis revealed an interaction between ezrin and the striatal-enriched protein tyrosine phosphatase (STEP) in the mouse brain (Won et al., 2019) suggesting STEP as a potential regulator of ezrin phosphorylation. STEP is a brain-specific phosphatase that regulates phosphorylation and activation levels of key plasticity-related proteins (Mahaman et al., 2021). These proteins include the (N-methyl-D-aspartate receptor) NMDAR and (α-amino-3-hydroxy-5-methyl-4-isoxazolepropionic acid receptor) AMPAR subunits GluN2B and GluA2, as well as Fyn, Pyk2, ERK and p38 (Mahaman et al., 2021). By doing so, STEP regulates multiple signaling pathways relevant to synaptic and neurological function, as well as dendrite and spine morphology (Chatterjee et al., 2021; Karasawa et al., 2014; Mahaman et al., 2021). As a result, deregulations of STEP expression, whether too much or too little, can have a detrimental impact on brain function and are a feature of many neurological diseases (Chatterjee et al., 2021; Karasawa et al., 2014; Mahaman et al., 2021).

To test whether STEP also dephosphorylates Y478 ezrin, I pharmacologically inhibited its activity by treating primary mouse hippocampal neurons for 1 h with 10 µM TC-2153, that forms a reversible covalent bond with the catalytic cysteine residue of STEP (Castonguay et al., 2018; Chatterjee et al., 2021; Xu et al., 2014) and assessed phosphorylation changes of ezrin through immunoblotting and PLA. Phosphorylation of known targets of STEP - ERK, GluN2B and p38 (Castonguay et al., 2018; Xu et al., 2014) – went up in immunoblotting compared to vector-treated neurons, as expected (Figure 21a, b). Furthermore, pY478 ezrin levels were increased as shown in immunoblots and PLA (Figure 21-d). I also tested other TC-2153 concentrations and treatment durations; however, it was only under this specific condition that the induction of phosphorylation of STEP targets was observed (Appendix figure 4).

STEP is active when it is not phosphorylated at S221 (Castonguay et al., 2018; Paul et al., 2000). As this phosphorylation site is regulated by the phosphatase calcineurin (Paul et al., 2003), I tested whether inhibition of STEP activity through pharmacological inhibition of calcineurin with cyclosporin A (CsA) may be sufficient to induce phosphorylation of Y478 ezrin. To assess phosphorylation of STEP, I used an antibody specifically designed to detect the non-phosphorylated form at S221 (non p STEP) of the predominant splice variant of STEP (STEP61) (Figure 21e) (Castonguay et al., 2018; Paul et al., 2000). I could confirm that CsA at different concentrations and treatment durations reduces levels of non p STEP compared to control neurons, indicative of less active STEP (Figure 21f, g) (Paul et al., 2003). Nevertheless, not all the tested known targets of STEP

exhibited a reduction in their phosphorylation levels in immunoblots compared to control treated neurons, making it challenging to draw conclusions (Figure 21f, g).

In an alternative approach to attenuate STEP activity, I employed short-hairpin RNA (shRNA)-mediated knockdown of STEP. Three recombinant adeno-associated viruses (rAAVs) were generated, each expressing shRNAs targeting distinct sequences of STEP (Figure 21h). A scrambled sh sequence (SCR) served as a control. Both constructs additionally drive expression of mCherry, serving as a marker for successful vector delivery and expression in neurons, driven by the calcium-calmodulin-dependent protein kinase II (CamKII) promoter (Figure 21h, j). As expected, STEP mRNA and protein were nearly undetectable in primary mouse hippocampal neurons infected with any of the three shSTEP constructs, in contrast to shSCR-infected neurons (Figure 21i-k). While phosphorylation of STEP targets was assessed in only one set of samples, initial data indicated no change in p GluN2B and a reduction in p ERK (Figure 21i-k). However, total GluN2B levels were also reduced. Considering p GluN2B in relation to its total expression levels, the initial data suggested increased phosphorylation with two of the shSTEP constructs (Figure 21i-k). A similar trend may be observed for ERK. Interestingly, total levels of ezrin significantly decreased upon STEP knockdown, whereas its phosphorylation at Y478 showed a clear trend toward an increase when compared to its total expression levels (Figure 21i-k).

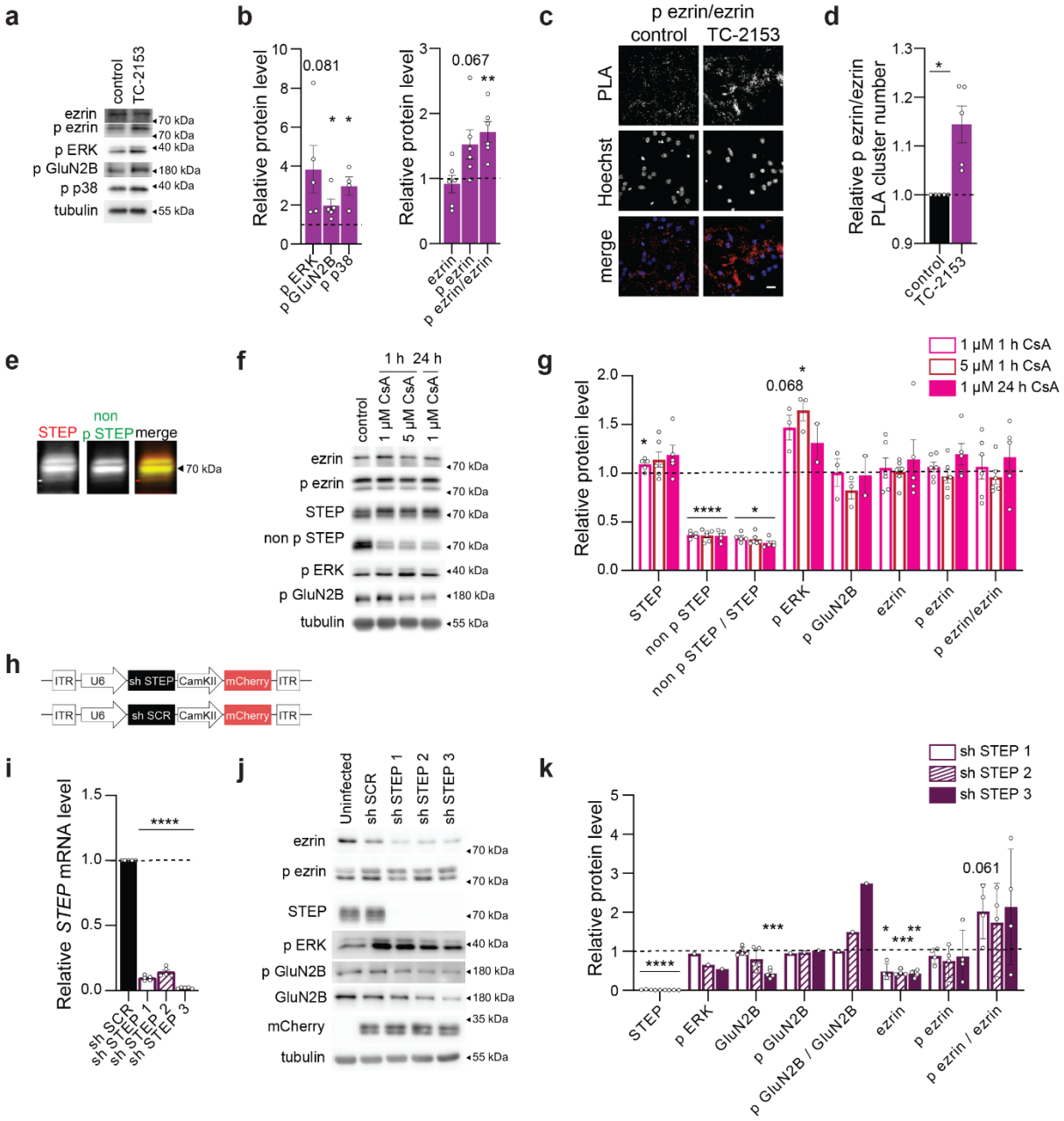

Figure 21. Effect of STEP inhibition on phosphorylation of Y478 ezrin. ***a, b*** *Immunoblot analysis in cultured mouse hippocampal neurons treated with DMSO (vector) or 10 µM TC-2153 for 1 h.* ***a*** *Representative immunoblots of ezrin, phospho Y478 ezrin, phospho ERK, phospho GluN2B, phospho p38 and tubulin.* ***b*** *Quantification of phospho ERK, phospho GluN2B, phospho p38, ezrin, phospho Y478 ezrin and the phospho Y478 ezrin/total ezrin protein ratio. Expression was normalized on tubulin and control. One sample t-test. N = 4-5 independent culture preparations.* ***c, d*** *Proximity ligation assay (PLA) with antibodies against ezrin and phosho Y478 ezrin in cultured mouse hippocampal neurons treated with DMSO (vector) or 10 µM TC-2153 for 1 h.* ***c*** *Representative images of PLA signal in neurons treated as indicated. Nuclei were visualized with Hoechst. Scale bar = 20 µm.* ***d*** *PLA cluster number normalized on the number of Hoechst-labelled cells and on control. One sample t-test. N = 5 independent culture preparations.* ***e*** *Two-color infrared fluorescence immunoblot of total STEP (red) and non-phospho STEP (green) with lysate from cultured hippocampal neurons.* ***f, g*** *Immunoblot analysis in cultured mouse hippocampal neurons treated with DMSO (vector) or 1 µM or 5 µM Cyclosporin A (CsA) for 1 h or 24 h.* ***f*** *Representative immunoblots of ezrin, phospho Y478 ezrin, STEP, non-phospho STEP, phospho ERK, phospho GluN2B, and tubulin.* ***g*** *Quantification of STEP, non-*

phospho STEP, non-phospho STEP/total STEP ratio, phospho ERK, phospho GluN2B, ezrin, phospho Y478 ezrin and phospho Y478 ezrin/total ezrin ratio. Expression was normalized on tubulin and control. Wilcoxon signed rank test (non-phospho STEP, 1 h 5 µM) or one sample t-test (minimal significant p value is displayed for non-phospho STEP/STEP ratio). N = 2-6 independent culture preparations. ***h-k*** *rAAV infection of shRNAs for downregulation of STEP expression in cultured mouse hippocampal neurons. Three different shRNA sequences were used (sh STEP 1-3).* ***h*** *Schema of rAAV constructs.* ***i*** *QRT-PCR analysis of STEP mRNA expression in cultured mouse hippocampal neurons infected as indicated. Expression was normalized on gusb and control. One sample t-test. N = 5 independent culture preparations.* ***j, k*** *Immunoblot analysis in cultured mouse hippocampal neurons infected as indicated.* ***j*** *Representative immunoblots of ezrin, phospho Y478 ezrin, STEP, phospho ERK, phospho GluN2B, GluN2B, mCherry, and tubulin.* ***k*** *Quantification of STEP, phospho ERK, GluN2B, phospho GluN2B, phospho GluN2B/GluN2B ratio, ezrin, phospho Y478 ezrin, phospho Y478 ezrin/ezrin ratio. Expression was normalized on tubulin and control. One sample t-test. N = 1-5 independent culture preparations. Graphs display mean ± SEM. Single values are represented as data points. ****p < 0.0001; ***p < 0.001; **p < 0.01; *p < 0.05. Parts of this figure are adapted from a first authored manuscript that is currently in revision for submission to Cellular and Molecular Life Sciences (see List of publications).*

I proceeded to modulate STEP in the opposite direction by enhancing its activity. Initially, I tested an alleged but not yet validated allosteric activator of STEP, BI-0314 (Boehringer Ingelheim; Tautermann et al. (2019)). At 500 µM for 24 h, phosphorylation levels of known STEP targets, ERK and p38, exhibited a trend toward reduction compared to vector-treated neurons (Figure 22a, b). However, when employed at different concentrations and durations, a trend toward increased phosphorylation levels of ERK and p38 emerged (Figure 22a, b), suggesting that this drug did not exhibit the intended effect.

Consequently, I opted for STEP overexpression. To this end, I generated rAAVs from a commercially purchased construct to drive expression of STEP61, tagged with V5, under the control of a chicken beta actin (CB7) promoter (Figure 22c). CMV>LacZ-Flag served as control (Figure 22c). As expected, STEP mRNA and protein levels were strongly increased in STEP-V5-infected cultured mouse hippocampal neurons compared to LacZ-infected neurons (Figure 22d, f, g). Flag and V5 tags were exclusively detected in LacZ-Flag and STEP-V5-infected cells, respectively (Figure 22e, f). While p ERK was significantly reduced in STEP-V5-expressing cells compared to LacZ-expressing cells, p GluN2B was not (Figure 22f, g). Phosphorylation of ezrin was unaffected (Figure 22f, g). This experiment cannot be used to make conclusions about whether STEP modulates pY478 ezrin since not all of the investigated STEP targets were impacted.

In addition, considering that increased STEP expression has been linked to a variety of neurodegenerative diseases (Karasawa et al., 2014; Mahaman et al., 2021) and overexpression of STEP causes memory deficits in mice (Castonguay et al., 2018), I generated constructs that drive expression of STEP - tagged with HA - under the control of the activity-inducible ESARE promoter

(Gulmez Karaca et al., 2020; Kawashima et al., 2013) to restrict the duration of STEP overexpression (Figure 22h). ESARE>LacZ-HA served as control. 24 h treatment with Bic of cultured neurons infected with ESARE>LacZ or ESARE>STEP successfully triggered an increase in cFos mRNA levels (Figure 22I) a well-established marker for neuronal activity (Chung, 2015). Both constructs additionally drive constitutive expression of tDimer as a marker for vector delivery, which was confirmed by immunocytochemistry and immunoblotting (Figure 22j, k). HA expression was induced upon activity (Figure 22j, k). In ESARE>STEP expressing neurons, activity led to an increase in STEP mRNA and protein levels compared to ESARE>LacZ expressing neurons (Figure 22i, k, l). Immunoblotting confirmed downregulation of p ERK, GluN2B and p38, as well as of pY478 ezrin in ESARE>STEP-expressing neurons after Bic-induced activity compared to ESARE>LacZ expressing neurons (Figure 22k, l).

In sum, these data suggest that STEP controls pY478 ezrin.

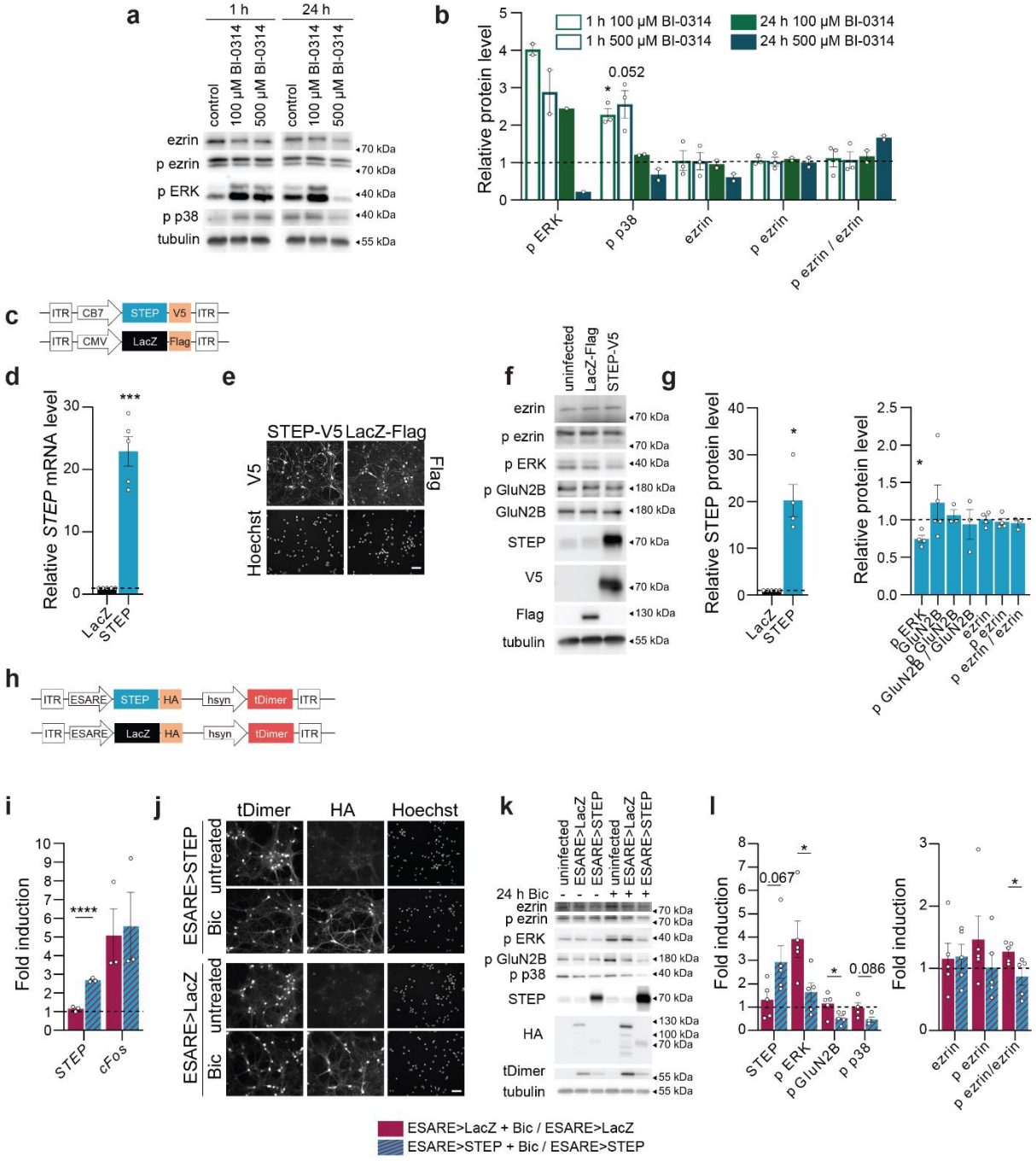

Figure 22. Effect of STEP upregulation on phosphorylation of Y478 ezrin. ***a, b*** *Immunoblot analysis in cultured mouse hippocampal neurons treated with DMSO (vector) or 100 µM or 500 µM BI-0314 for 1 h or 24 h.* ***a*** *Representative immunoblots of ezrin, phospho Y478 ezrin, phospho ERK, phospho p38 and tubulin.* ***b*** *Quantification of phospho ERK, phospho p38, ezrin, phospho Y478 ezrin and the phospho Y478 ezrin/total ezrin protein ratio. Expression was normalized on tubulin and control. One sample t-test. N = 1-3 independent culture preparations.* ***c-g*** *rAAV infection of STEP-V5 or LacZ-Flag in cultured mouse hippocampal neurons.* ***c*** *Schema of rAAV constructs.* ***d*** *QRT-PCR analysis of STEP mRNA expression in cultured mouse hippocampal neurons infected as indicated. Expression was normalized on gusb and control. One sample t-test. N = 5 independent culture preparations.* ***f, g*** *Immunoblot analysis in cultured mouse hippocampal neurons infected as indicated.* ***f*** *Representative immunoblots of ezrin, phospho Y478 ezrin, phospho ERK, phospho GluN2B, GluN2B, STEP, V5, Flag, and tubulin.* ***g*** *Quantification of STEP, phospho ERK, GluN2B, phospho GluN2B, phospho GluN2B/GluN2B ratio, ezrin, phospho Y478 ezrin, phospho Y478 ezrin/ezrin ratio. Expression was*

normalized on tubulin and control. One sample t-test. N = 3-5 independent culture preparations. ***h-l*** *rAAV infection of ESARE>STEP-HA or ESARE>LacZ-HA in cultured mouse hippocampal neurons to drive overexpression of STEP or LacZ under the control of the activity-dependent ESARE promoter. Neurons were treated for 24 h with bicuculline (Bic) or not to activate the promoter.* ***h*** *Schema of rAAV constructs.* ***i*** *QRT-PCR analysis of STEP and cFos mRNA expression in cultured mouse hippocampal neurons infected and treated as indicated. Expression was normalized on gusb and respective untreated control. Wilcoxon signed rank test (cFos) or one sample t-test. N = 3 independent culture preparations.* ***j*** *Representative images of tDimer- and HA- immunocytochemistry in cultured mouse hippocampal neurons infected and treated as indicated. Nuclei were visualized with Hoechst. Scale bar = 50 µm.* ***k, l*** *Immunoblot analysis in cultured mouse hippocampal neurons infected and treated as indicated.* ***k*** *Representative immunoblots of ezrin, phospho Y478 ezrin, phospho ERK, phospho GluN2B, phospho p38, STEP, HA, tDimer, and tubulin.* ***g*** *Quantification of STEP, phospho ERK, phospho GluN2B, phospho p38, ezrin, phospho Y478 ezrin, and phospho Y478 ezrin/ezrin ratio. Expression was normalized on tubulin and respective untreated control. Two-tailed unpaired Student's t-test. N = 4-5 independent culture preparations. Graphs display mean ± SEM. Single values are represented as data points. ****p < 0.0001; ***p < 0.001; *p < 0.05. Parts of this figure are adapted from a first authored manuscript that is currently in revision for submission to Cellular and Molecular Life Sciences (see List of publications).*

3.4.5 VEGFD dephosphorylates Y478 ezrin via activation of STEP phosphatase

As the previous chapter showed that pY478 ezrin is regulated by STEP phosphatase, I investigated the potential involvement of STEP in the VEGFD-induced dephosphorylation of Y478 ezrin, through evaluation of the levels of non-phosphorylated STEP, indicative of active STEP (Castonguay et al., 2018; Paul et al., 2000).

First, I measured non p STEP levels in primary mouse hippocampal neurons that were infected to overexpress VEGFD-HA or LacZ-Flag as a control (Figure 23a-c). While total STEP levels were lower in VEGFD-HA-expressing cells than in LacZ controls, non p STEP levels were enhanced (Figure 23b, c), indicative of active STEP.

Next, I tested whether VEGFD overexpression for a shorter time window of 24 h through usage of the inducible ESARE promoter might be sufficient to reduce STEP phosphorylation in cultured mouse hippocampal neurons, but no significant effect was observed (Figure 23d-f).

As Y478 ezrin is phosphorylated by VEGFD within 2 h, a potential activation of STEP by VEGFD should happen at least within this time frame. Therefore, I assessed non p STEP levels in cultured hippocampal neurons treated with rVEGFD for 2 h. Although rVEGFD exhibited a tendency to reduce total STEP expression, levels of non p STEP were increased following rVEGFD treatment (Figure 23g, h), suggesting that VEGFD signaling induces activation of STEP.

In parallel with this experiment, some groups received 2 h Bic treatment with or without rVEGFD co-application, to explore whether synaptic activity affects VEGFD-induced dephosphorylation of STEP.

As expected, total protein expression of STEP declines by almost 50% after 2 h Bic treatment, as Bic has been shown to cause ubiquitination and proteasomal degradation of STEP (Appendix figure 3a, b) (Xu et al., 2018). This effect was still observable when rVEGFD was co-applied (Appendix figure 3a, b). Non p STEP levels, on the other hand, were strongly increased with Bic and even more so with rVEGFD and Bic combined (Appendix figure 3a, b).

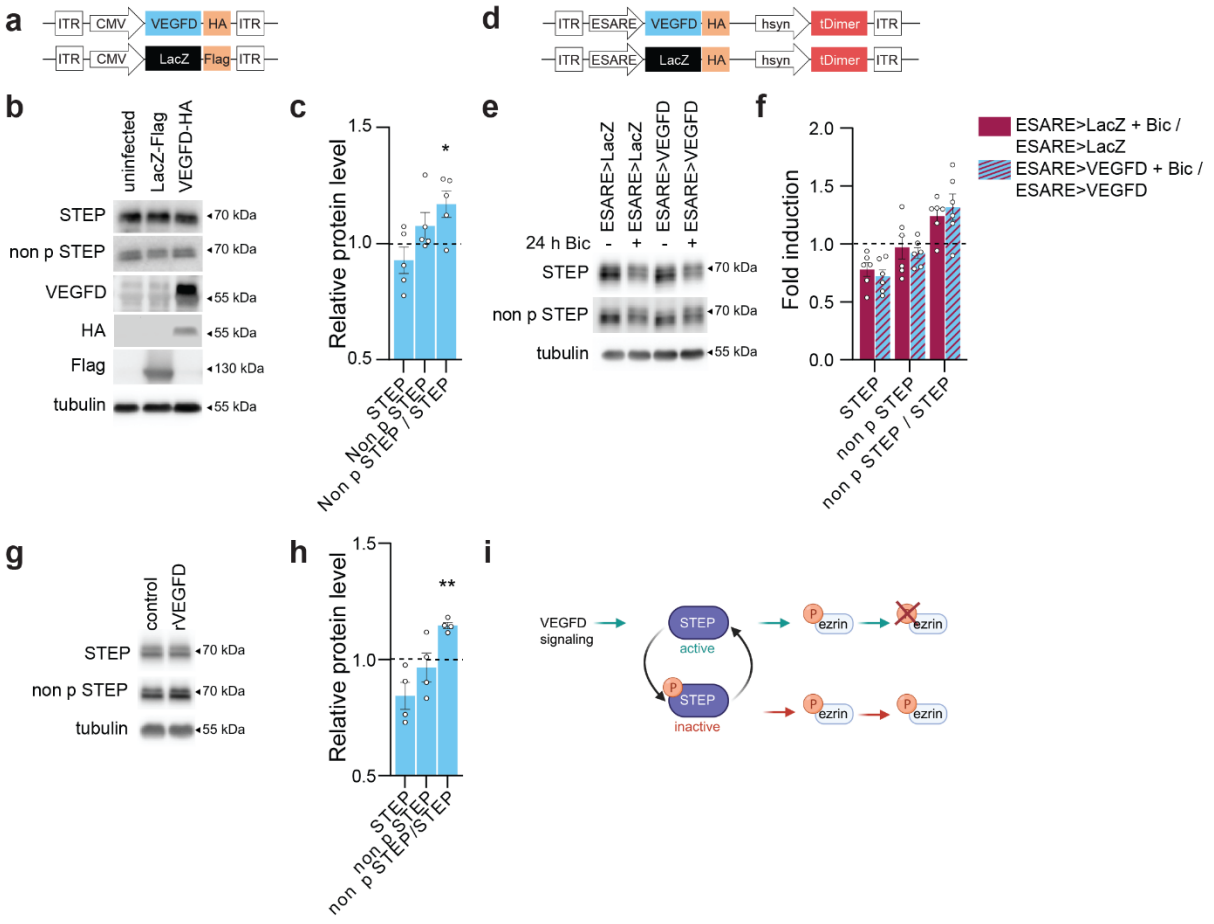

Figure 23. VEGFD induces dephosphorylation of STEP. ***a-c*** *rAAV infection of VEGFD-HA or LacZ-Flag in cultured mouse hippocampal neurons.* ***a*** *Schema of rAAV constructs.* ***b, c*** *Immunoblot analysis in cultured mouse hippocampal neurons infected as indicated.* ***b*** *Representative immunoblots of STEP, non-phospho STEP, VEGFD, HA, Flag, and tubulin.* ***c*** *Quantification of STEP, non-phospho STEP, non-phospho STEP/STEP ratio. Expression was normalized on tubulin and control. One sample t-test. N = 5 independent culture preparations.* ***d-f*** *rAAV infection of ESARE>VEGFD-HA or ESARE>LacZ-HA in cultured mouse hippocampal neurons to drive overexpression of VEGFD or LacZ under the control of the activity-dependent ESARE promoter. Neurons were treated for 24 h with bicuculline (Bic) or not to activate the promoter.* ***d*** *Schema of rAAV constructs.* ***e, f*** *Immunoblot analysis in cultured mouse hippocampal neurons infected and treated as indicated.* ***e*** *Representative immunoblots of STEP, non-phospho STEP, and tubulin.* ***f*** *Quantification of STEP, non-phospho STEP, and non-phospho STEP/STEP ratio. Expression was normalized on tubulin and respective untreated control. Two-tailed unpaired Student's t-test. N = 6 independent culture preparations.* ***g, h*** *Immunoblot analysis of STEP protein expression and phosphorylation in cultured mouse hippocampal neurons treated or not with recombinant VEGFD (rVEGFD) for 2 h.* ***g*** *Representative immunoblots of STEP, non-phospho STEP, and*

tubulin. ***h*** *Quantification of STEP, non-phospho STEP and its phospho/total protein ratio. Expression was normalized on tubulin and control. One sample t-test. N = 4 independent culture preparations.* ***i*** *Schema illustrating the proposed mechanism of VEGFD-mediated dephosphorylation of ezrin. VEGFD signaling induces the dephosphorylation STEP. Consequently, STEP is active and dephosphorylates Y478 ezrin. Graphs display mean ± SEM. Single values are represented as data points. **p < 0.01; *p < 0.05. Parts of this figure are adapted from a first authored manuscript that is currently in revision for submission to Cellular and Molecular Life Sciences (see List of publications).*

In addition, I had the opportunity to assess expression and phosphorylation of STEP through immunohistochemistry in vivo in the hippocampal CA1 and CA2/3 regions of mice overexpressing VEGFD-HA or LacZ-Flag through viral delivery into the hippocampus (Figure 24). Successful delivery and expression of VEGFD and LacZ was previously validated (data not shown). Although STEP antibodies labelled the entire brain, the strongest labeling was observed in the hippocampal CA2 region (Figure 24b, c, e, f), consistent with its typical use as a CA2 marker (Radzicki et al., 2023). STEP expression and phosphorylation was measured in the different layers of each CA1 and CA2/3. In the stratum lacunosum moleculare of the CA1, mice infected with VEGFD-HA displayed a tendency toward increased STEP phosphorylation compared to LacZ-Flag-infected mice (Figure 24b-d). However, no effect was observed in the other regions (Figure 24d, g). Phosphorylation of STEP could be a transient effect that is not detectable anymore after long-term overexpression of VEGFD.

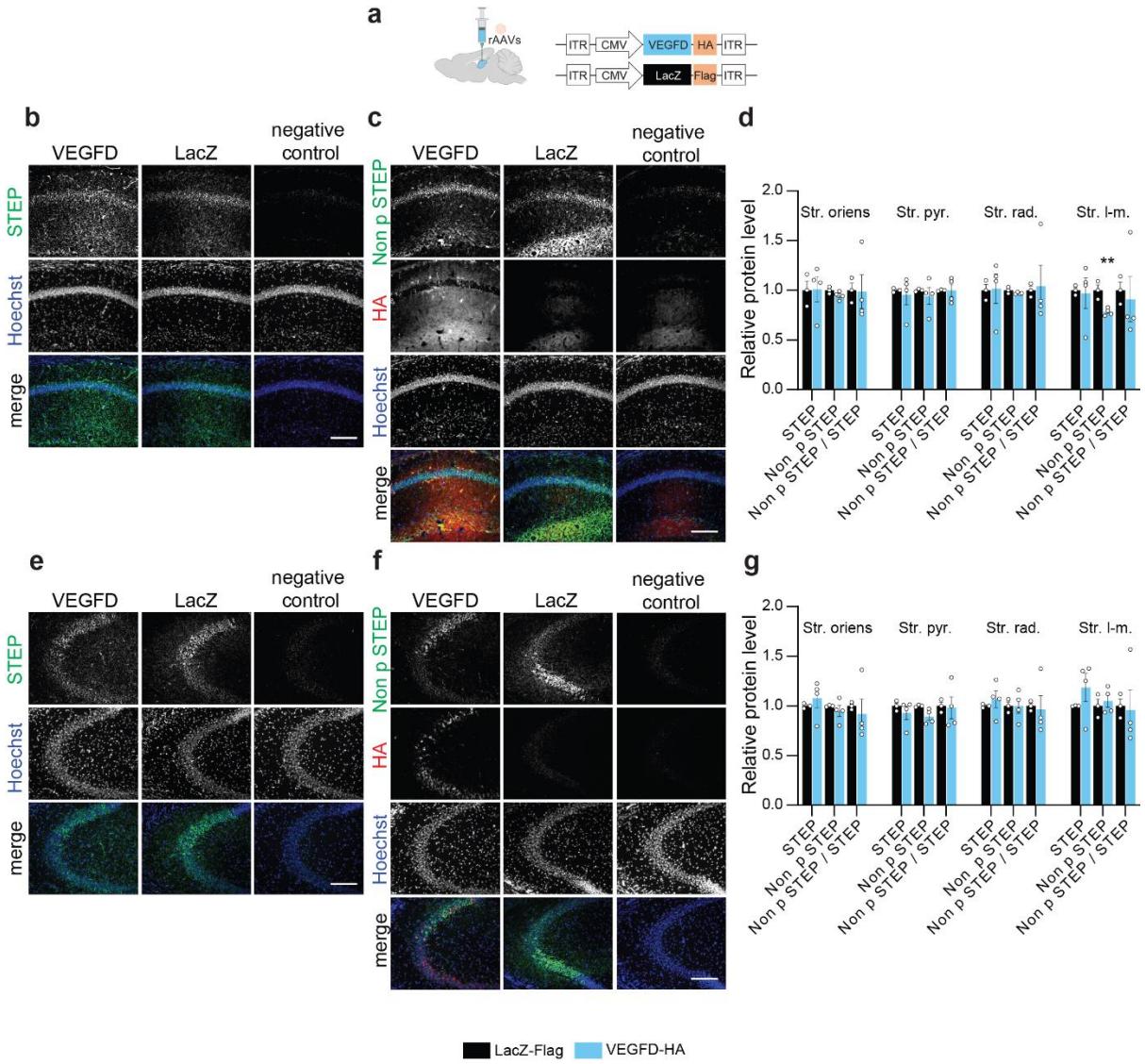

Figure 24. Overexpression of VEGFD in the hippocampus does not affect phosphorylation of STEP. *Immunohistochemical analysis of STEP protein expression and phosphorylation in the hippocampal CA1 (**b-d**) and CA2/3 (**e-g**) regions in mice stereotaxically-injected with rAAV-VEGFD-HA or rAAV-LacZ-Flag. **a** Schema of rAAV constructs. **b, c** Representative images of STEP (**b**) or non-phospho-STEP- and HA- (**c**) immunostained CA1 regions from the dorsal hippocampi of mice injected as indicated. Nuclei were visualized with Hoechst. Negative controls were only stained with the secondary antibody. Scale bar = 100 µm. **d** Quantification of STEP, non-phospho-STEP and its phospho/total protein ratio in different layers of the CA1 as indicated in VEGFD-HA injected mice normalized on LacZ-Flag- injected mice. Two-tailed unpaired Student's t-test. N = 3-4 mice. **e, f** Representative images of STEP (**e**) or non-phospho-STEP- and HA- (**f**) immunostained CA2/3 regions from the dorsal hippocampi of mice injected as indicated. Nuclei were visualized with Hoechst. Negative controls were only stained with the secondary antibody. Scale bar = 100 µm. **d** Quantification of STEP, non-phospho-STEP and its phospho/total protein ratio in different layers of the CA2/3 as indicated in VEGFD-HA injected mice normalized on LacZ-Flag- injected mice. Two-tailed unpaired Student's t-test. N = 3-4 mice. Graphs display mean ± SEM. Single values are represented as data points. **p < 0.01. Injections were performed by Ann-Kristin Kenkel, stainings by Carmen Leibold.*

In conclusion, these findings indicate that VEGFD signaling results in the dephosphorylation of Y478 ezrin through activation of STEP (Figure 23i).

3.4.6 Inhibition of STEP activity does not affect neurite length

According to a recent study (Chatterjee et al., 2021) dendritic complexity is increased by pharmacologically inhibiting STEP with TC-2153. As the previous chapter indicates a potential role for STEP in VEGFD signaling, I tested whether inhibition of STEP with TC-2153 would also cause cultured hippocampus neurons' neurite length to increase. Prior to this, I had investigated TC-2153 at 1 and 10 µM on cultured hippocampus neurons (Figure 21a, b; Appendix figure 4a, b). Only 10 µM for 1 h resulted in a robust phosphorylation of STEP targets (Figure 21a, b; Appendix figure 4a, b); however, this concentration was toxic when administered for 24 h.

Since Chatterjee et al. (2021) employed 1 µM and as neurite dynamics are slow and require analysis over an extended period of time, I opted to use the same concentration. Using an automated imaging system to track changes in the total neurite length (see chapter 3.1.2) of neurons treated with TC-2153 over time (Figure 25a)., I found the reverse of what Chatterjee et al. (2021) reported: neurite lengths were reduced with TC-2153 administration (Figure 25b). Next, I tested whether co-treatment with rVEGFD might interfere with this effect (Figure 25c). Intriguingly, neurite length increased when rVEGFD and TC-2153 were applied in combination (Figure 25d). However, in this experiment, neurite length was also no longer decreased by TC-2153 alone (Figure 25d). This makes it impossible to interpret the data.

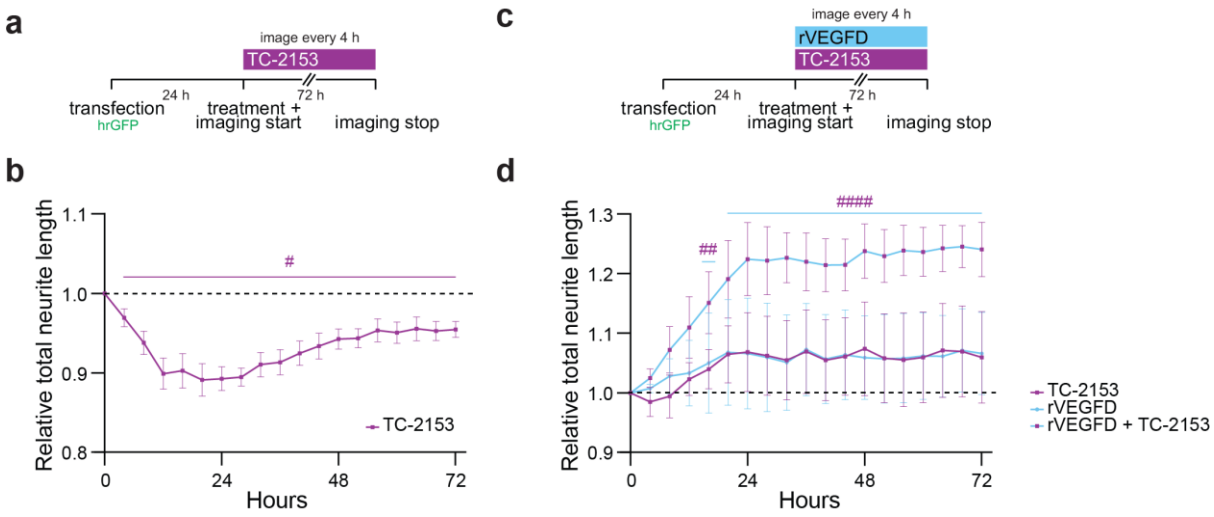

Figure 25. Effect of STEP inhibition on neurite length. ***a, b*** *Time-lapse monitoring of neurite length for 72 h of hrGFP-transfected cultured mouse hippocampal neurons with or without TC-2153 treatment. hrGFP was used to visualize neuronal morphology.* ***a*** *Schema of experiment.* ***b*** *Relative total neurite length over time normalized on the first timepoint and untreated control. Multiple*

unpaired t-test (minimal significant p value is displayed). N = 4 independent culture preparations. ***c, d*** *Time-lapse monitoring of neurite length for 72 h of hrGFP-transfected cultured mouse hippocampal neurons with or without TC-2153, recombinant VEGFD (rVEGFD) or both.* ***c*** *Schema of experiment.* ***d*** *Relative total neurite length over time normalized on the first timepoint and untreated control. Two-way ANOVA followed by Dunnett's or Tukey's post hoc test. N = 4-5 independent culture preparations. Graphs display mean ± SEM. Hashtags (#) indicate statistical significance in comparisons to baseline values. ####p < 0.0001; ##p < 0.01; #p < 0.05.*

3.4.7 Ezrin during NMDA-induced excitotoxicity

Given that NMDA-induced excitotoxicity causes a reduction in VEGFD levels (Mauceri et al., 2020; Schlüter et al., 2020), I explored whether ezrin and its phosphorylation may also be affected. To this end, ezrin expression was measured in cultured hippocampal neurons treated with NMDA for 1, 2 or 4 h. However, ezrin mRNA and protein levels as well as phosphorylation of ezrin were unaffected by NMDA (Figure 26a-c).

I had the opportunity to test if this holds true *in vivo*, in retinal lysates from mouse eyes injected with NMDA, a well-established in vivo model for excitotoxicity in which VEGFD expression is reduced (Schlüter et al., 2020). While ezrin mRNA levels were elevated at 1 d and 7 d after NMDA-injection (Figure 26d), there was no evident trend in protein levels (Figure 26e, f). It is important to acknowledge that the protein samples used in the study were old. Although no apparent degradation was observed, as indicated by stable levels of tubulin or GAPDH, the quality of the ezrin blots was compromised. Further investigation with fresh samples is necessary to draw a definitive conclusion on whether excitotoxicity modulates ezrin.

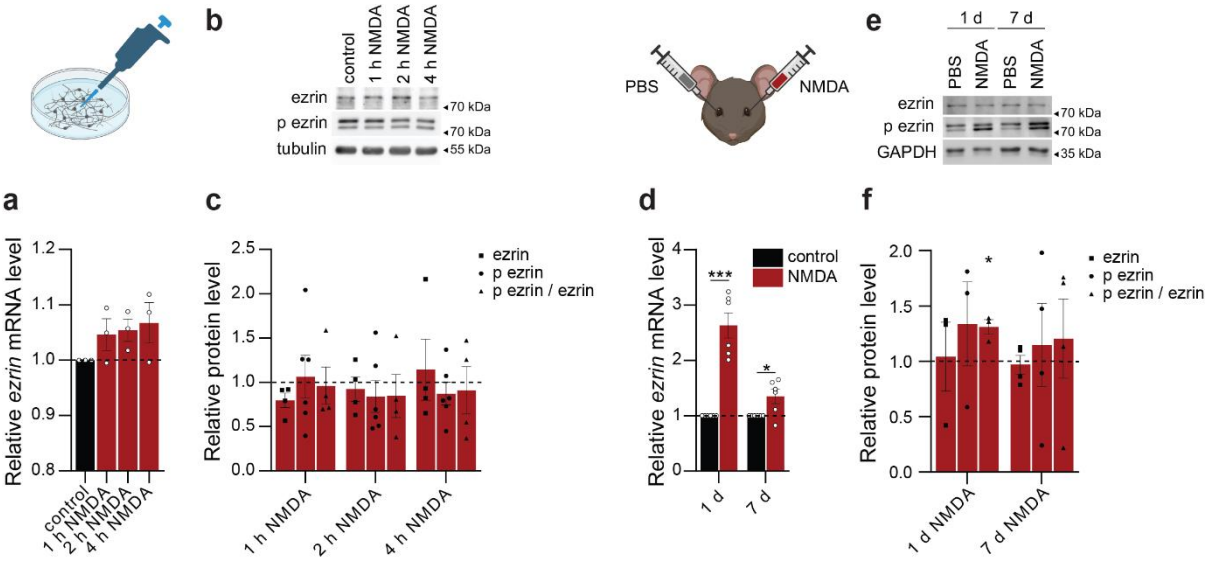

Figure 26. Characterization of ezrin expression and phosphorylation in NMDA-induced excitotoxicity. ***a-c*** *QRT-PCR (**a**) and immunoblot analysis (**b, c**) of ezrin expression in cultured mouse hippocampal neurons treated with or without NMDA for 1, 2 or 4 h.* ***a*** *Relative ezrin mRNA levels normalized on gusb and control. One-way ANOVA followed by Dunnett's post hoc test. N = 3 independent culture preparations.* ***b*** *Representative immunoblots of ezrin, phospho Y478 ezrin and tubulin.* ***c*** *Quantification of ezrin, phospho Y478 ezrin and its phospho/total protein ratio normalized on tubulin and control. One-way ANOVA followed by Dunnett's post hoc test. N = 4-6 independent culture preparations.* ***e-f*** *QRT-PCR (**e**) and immunoblot analysis (**d, f**) of ezrin expression in retinas of mice following 1 or 7 d after intravitreal injection with NMDA or PBS in the contralateral eye as a control.* ***d*** *Relative ezrin mRNA levels normalized on gapdh and control. One sample t-test. N = 6 mice.* ***d*** *Representative immunoblots of ezrin, phospho Y478 ezrin and GAPDH.* ***f*** *Quantification of ezrin, phospho Y478 ezrin and its phospho/total protein ratio normalized on GAPDH and control. One sample t-test. N = 3-4 mice. Graphs display mean ± SEM. Single values are represented as data points. ***p < 0.001; *p < 0.05. NMDA treatments in a-c were performed by Lisa Ruff and Netta Ussyshkin. NMDA injections in d-e were done by Dr. Annabelle Schlüter. QRT-PCR in d was conducted by Prof. Dr. Daniela Mauceri.*

3.4.8 Developmental expression pattern of ezrin

As the findings suggest a regulation of ezrin by VEGFD, I investigated the function of ezrin in neurons by characterizing its developmental expression pattern.

In the mouse hippocampus, mRNA levels of *ezrin* peak in young animals and decreased with age (Figure 27a). A similar trend was observed in the mouse cortex, although *ezrin* levels appear to slightly increase again in aged animals (Figure 27b). This expression pattern is reflected at the protein level in cultured mouse hippocampal neurons, where ezrin gradually decreased with age (Figure 27c, d), aligning with its known role in developmental neuritogenesis (Matsumoto et al., 2014). In contrast, levels of pY478 ezrin mostly remained unchanged and even exhibited a trend to increase with age (Figure 27c, d). Preliminary data also indicate a similar expression and phosphorylation pattern *in vivo* in the mouse hippocampus (Figure 27e, f). This implies that

sustained phosphorylation of pY478 ezrin may be necessary throughout development and could potentially play an even more crucial role in the adult brain. However, in the mouse cortex, developmental expression and phosphorylation pattern of ezrin was less clear (Figure 27g, h).

In addition, I assessed ezrin phosphorylation at T567 at various developmental time points in primary mouse hippocampal neurons. Intriguingly, the levels of pT567 ezrin exhibited a similar trend to pY478 (Appendix figure 5a, b), suggesting that despite a decrease in ezrin expression with age, it remains predominantly active, as phosphorylation of T567 is essential for transitioning ezrin into its active open conformation (Ponuwei, 2016).

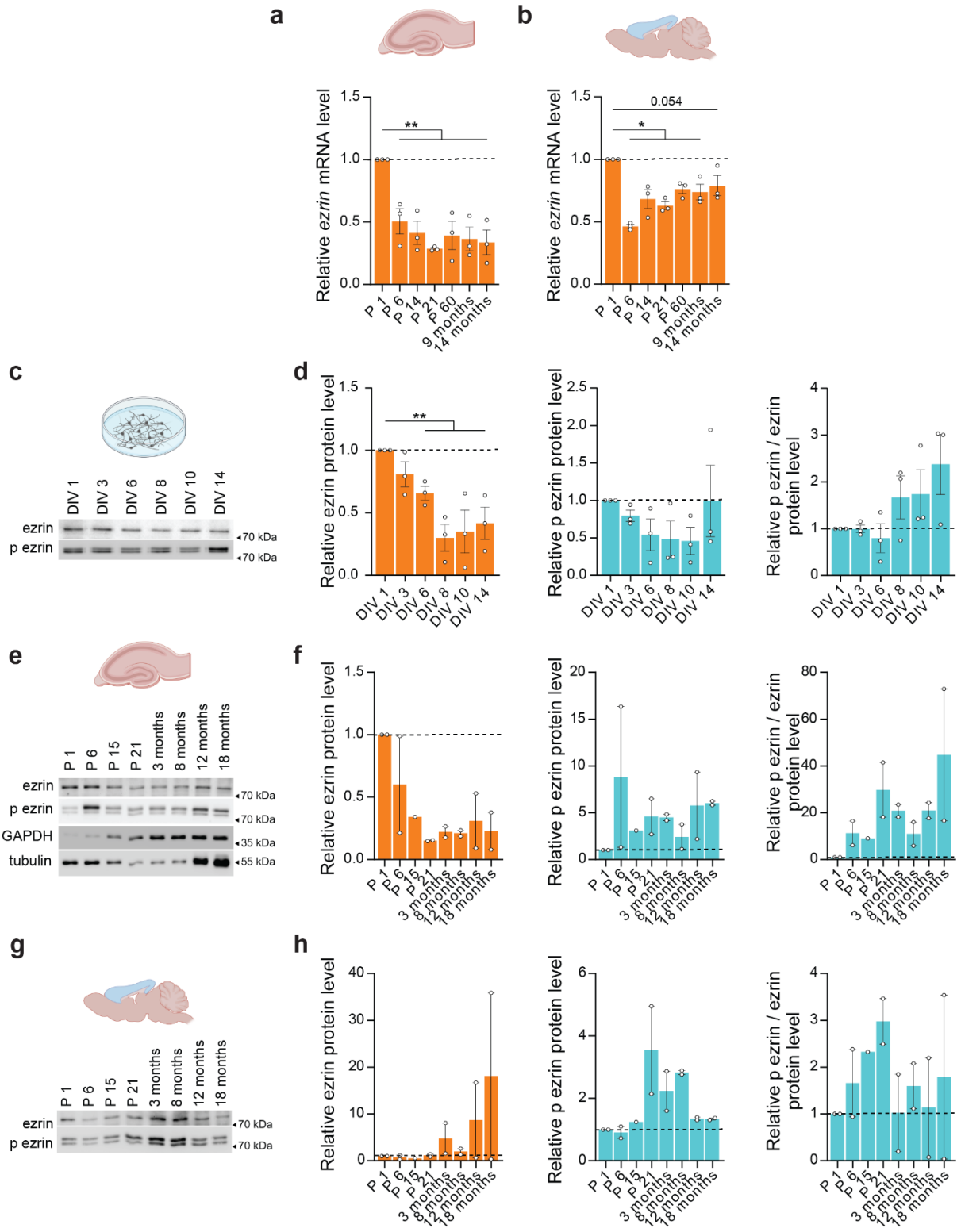

Figure 27. Characterization of ezrin expression throughout development. ***a, b*** *QRT-PCR analysis of ezrin mRNA expression in hippocampus (**a**) or cortex (**b**) lysates derived from mice at indicated ages (P 1-60 = postnatal day 1-60). Expression was normalized to GAPDH, gusb and P 1. One-way ANOVA followed by Dunnett's post hoc test. N = 3 mice.* ***c, d*** *Immunoblot analysis of ezrin protein expression in cultured mouse hippocampal neurons at different days in vitro (DIV).* ***c*** *Representative immunoblots of ezrin and phospho Y478 ezrin.* ***d*** *Quantification of ezrin, phospho Y478 ezrin and its phospho/total protein ratio. Expression was only normalized to DIV 1 due to DIV-related fluctuations*

in GAPDH and tubulin expression (see Figure 32). One-way ANOVA followed by Dunnett's post hoc test. N = 3 independent culture preparations. ***e-h*** *Immunoblot analysis of ezrin protein expression in hippocampal (**e, f**) and cortex (**g, h**) lysates derived from mice at indicated ages.* ***e*** *Representative immunoblots of ezrin, phospho Y478 ezrin, GAPDH and tubulin.* ***f*** *Quantification of ezrin, phospho Y478 ezrin and its phospho/total protein ratio. Expression was only normalized to P 1 due to age-related fluctuations in GAPDH and tubulin expression. N = 2 mice.* ***g*** *Representative immunoblots of ezrin and phospho Y478.* ***h*** *Quantification of ezrin, phospho Y478 ezrin and its phospho/total protein ratio. Expression was only normalized to P 1 due to age-related fluctuations in β actin and tubulin expression (see Figure 36). N = 2 mice. Graphs display mean ± SEM. Single values are represented as data points. **p < 0.01; *p < 0.05.*

3.4.9 Ezrin overexpression induces dendrite remodeling and affects spine morphology

Given that VEGFD modulates the phosphorylation of ezrin, I explored whether modulating ezrin expression and phosphorylation would affect neuronal morphology. To this end, I generated constructs to drive via a human synapsin promoter (hsyn) neuron-specific overexpression of either wildtype (WT) or a mutant version of ezrin in which the tyrosine at residue 478 has been replaced with a phenylalanine (Y478F; Figure 28a) (Chan et al., 2021; Ghaffari et al., 2014; Heiska et al., 2005; Heiska et al., 2011; Mak et al., 2012; Murchie et al., 2014; Naba et al., 2008). Phenylalanine, structurally similar to tyrosine but lacking the hydroxyl group crucial for phosphorylation, serves as a non-phosphorylatable version of Y478 ezrin. As an additional control, I cloned a construct in which Y146 (often also referred to as Y145), another tyrosine phosphosite in ezrin that was also examined in the phospho-proteomic screening (chapter 3.3.1) but showed no response to VEGFD, was replaced with phenylalanine (Y146F; Figure 28a) (Saygideğer-Kont et al., 2016; Srivastava et al., 2005).

All constructs were C-terminally tagged with Flag to facilitate detection, which could be successfully expressed and detected in primary mouse hippocampal neurons (Figure 28a, b). Flag-stained ezrin was found distributed within the cytoplasmic compartment along the plasma membrane throughout the entire neuron (Figure 28b).

To evaluate potential effects of ezrin overexpression on neuronal morphology, neuronal structure was visualized in primary mouse hippocampal neurons through hrGFP transfection with or without ezrin constructs (Figure 28c). First, I examined dendrite morphology. Dendrite length and complexity was increased in WT ezrin-overexpressing neurons which was even more pronounced when Y478F ezrin was expressed (Figure 28d-g). Intriguingly, dendrite morphology was unaffected by Y146F ezrin overexpression (Figure 28d-g).

During the analysis of dendrite morphology, it was evident to the naked eye that not only was there a difference in dendritic structure, but also in spine number and morphology compared to control neurons. Indeed, spine density was significantly higher in neurons expressing WT or Y146F ezrin, but not in neurons expressing Y478F ezrin (Figure 28h, i). Spine diameter was also larger in WT ezrin-expressing neurons (Figure 28j, k) which may suggest maturation and stability of spines (Bourne et al., 2007; Runge et al., 2020). Neurons expressing Y478F ezrin, on the other hand, displayed filopodia-like structures or immature spines characterized by longer spine length compared to control neurons (Figure 28l, m). Spine morphology for Y146F ezrin was not analyzed.

In summary, overexpression of ezrin influences both dendrite and spine morphology. However, while ezrin overexpression induces dendrite remodeling regardless of the phosphorylation state at Y478, Y478F ezrin has a differential impact on spine morphology.

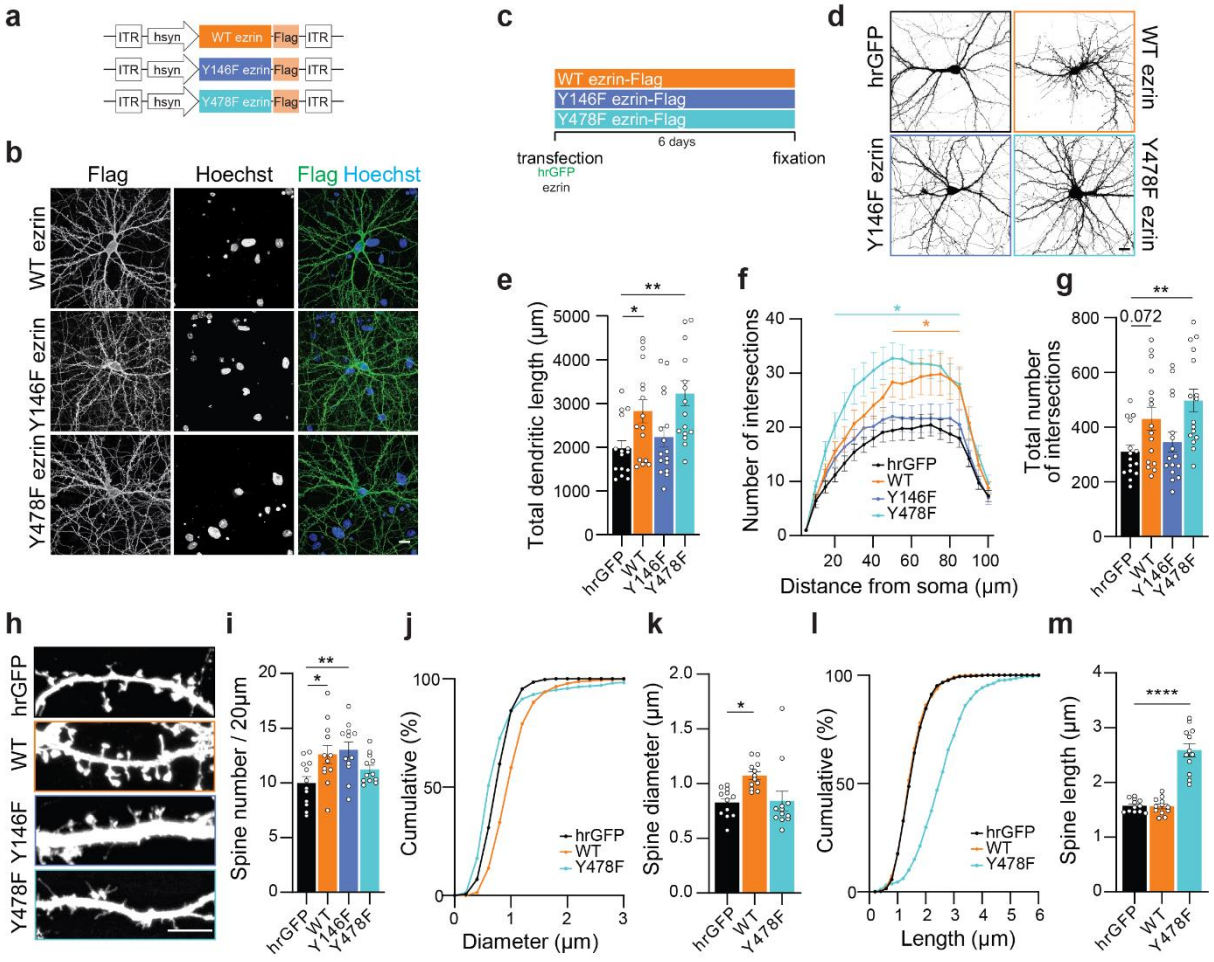

Figure 28. Overexpression of ezrin modulates neuronal morphology. *Analysis of neuronal morphology of hrGFP (vector) and/or WT, Y146F or Y478F ezrin-transfected cultured mouse hippocampal neurons.* ***a*** *Schema of constructs.* ***b*** *Representative Flag-immunostained neuron at DIV 14 transfected as indicated. Nuclei were visualized with Hoechst. Scale bar = 20 µm.* ***c*** *Schema of experiment.* ***d-g*** *Analysis of dendrite morphology.* ***d*** *Representative images of neurons transfected as*

indicated. hrGFP was used to visualize neuronal morphology. Scale bar = 20 µm. ***e*****-****g*** *Total dendritic length (****e****), Sholl analysis (****f****) and total number of intersections up to a radius of 150 µm (****g****) of neurons transfected as indicated. One-way (****e, g****) or Two-way ANOVA followed by Dunnett's post hoc test (****f****). N = 15-16 neurons from 3 independent culture preparations.* ***h*****-****m*** *Analysis of spine density and morphology.* ***h*** *Representative images of dendritic spines of neurons transfected as indicated. Scale bar = 5 µm.* ***i*****-****m*** *spine number per 20 µm dendrite length (****i****), diameter (****j, k****) and length (****l, m****) of neurons transfected as indicated. N = 12 neurons from 3 independent culture preparations. One-way ANOVA followed by Dunnett's post hoc test. Graphs display mean ± SEM. Single values are represented as data points. ****p < 0.0001; **p < 0.01; *p < 0.05. Analysis of i-m was done by Prof. Dr. Daniela Mauceri. Parts of this figure are adapted from a first authored manuscript that is currently in revision for submission to Cellular and Molecular Life Sciences (see List of publications).*

3.4.10 Phospho-mutant Y478F ezrin opposes synaptic activity-dependent dendrite remodeling

As overexpression of ezrin induces dendrite remodeling, I explored what role ezrin and its phosphorylation state might play in the context of synaptic activity.

Neuronal morphology in primary mouse hippocampal neurons was visualized through hrGFP transfection, with or without constructs for overexpressing WT, Y146F and Y478F ezrin (Figure 29a). Due to the different effects that Y146F and Y478F ezrin had on neuronal morphology (chapter 3.4.9), I additionally employed a double-mutant ezrin harboring both Y146F and Y478F (Y146F-Y478F) to explore the combined actions of both phosphorylation sites (Figure 29a). The successful expression of the double-mutant was verified through immunocytochemical labeling of its Flag-tag (Figure 29b). Its distribution pattern was similar to that of the other ezrin constructs (Figure 29b; Figure 28b)

Bic treatment, employed to induce synaptic activity, led to increased dendrite length and complexity in neurons expressing only hrGFP, as anticipated (Figure 29c-g). As expected, under baseline conditions, dendritic arborization was already elevated in both WT and Y478F ezrin-expressing neurons (Figure 29c-g). A similar trend was observed for neurons expressing Y146F or Y146F-Y478F ezrin (Figure 29c-g), although this was not the case for Y146F when dendrite morphology was analyzed at a more mature stage (Figure 28c, g). Bic treatment did not lead to further dendrite growth in WT, Y146F or Y146F-Y478F-ezrin-expressing neurons, potentially as a result of exceeding physiological growth limits. Surprisingly, dendrite length and complexity of Bic-treated Y478F ezrin-expressing neurons was comparable to untreated control neurons (Figure 29c-g).

Thus, these findings indicate that dephosphorylation of ezrin at Y478 prevents activity-dependent dendrite remodeling, as long as Y146 remains phosphorylatable.

To assess whether these observations hold true *in vivo* in adult mice, rAAV delivery to introduce constructs for overexpressing LacZ, WT ezrin, or Y478F ezrin into the dorsal hippocampus was employed. The successful expression of these constructs was validated through histochemistry. CFC served as the stimulus for inducing activity-dependent dendrite remodeling *in vivo* (chapter 3.1.2). As anticipated, the basal dendrites of LacZ-expressing neurons in the CA1 region displayed greater and more complex architecture in mice subjected to CFC compared to control mice. In alignment with the *in vitro* results, overexpression of WT or Y478F ezrin was sufficient to elevate basal dendritic arborization in control mice and CFC did not trigger further dendrite sprouting in WT ezrin-expressing neurons, hinting at a potential growth limitation. Intriguingly, Y478F ezrin-expressing neurons mirrored the *in vitro* findings, exhibiting a reversal to control values following CFC. These *in vivo* experiments were conducted by Prof. Dr. Daniela Mauceri and Ann-Kristin Kenkel (data not shown).

In summary, elevated levels of ezrin drive dendritic growth, while the phosphorylation status of Y478 instructs neurons on how to adapt their morphology in response to remodeling stimuli both *in vitro* and *in vivo*.

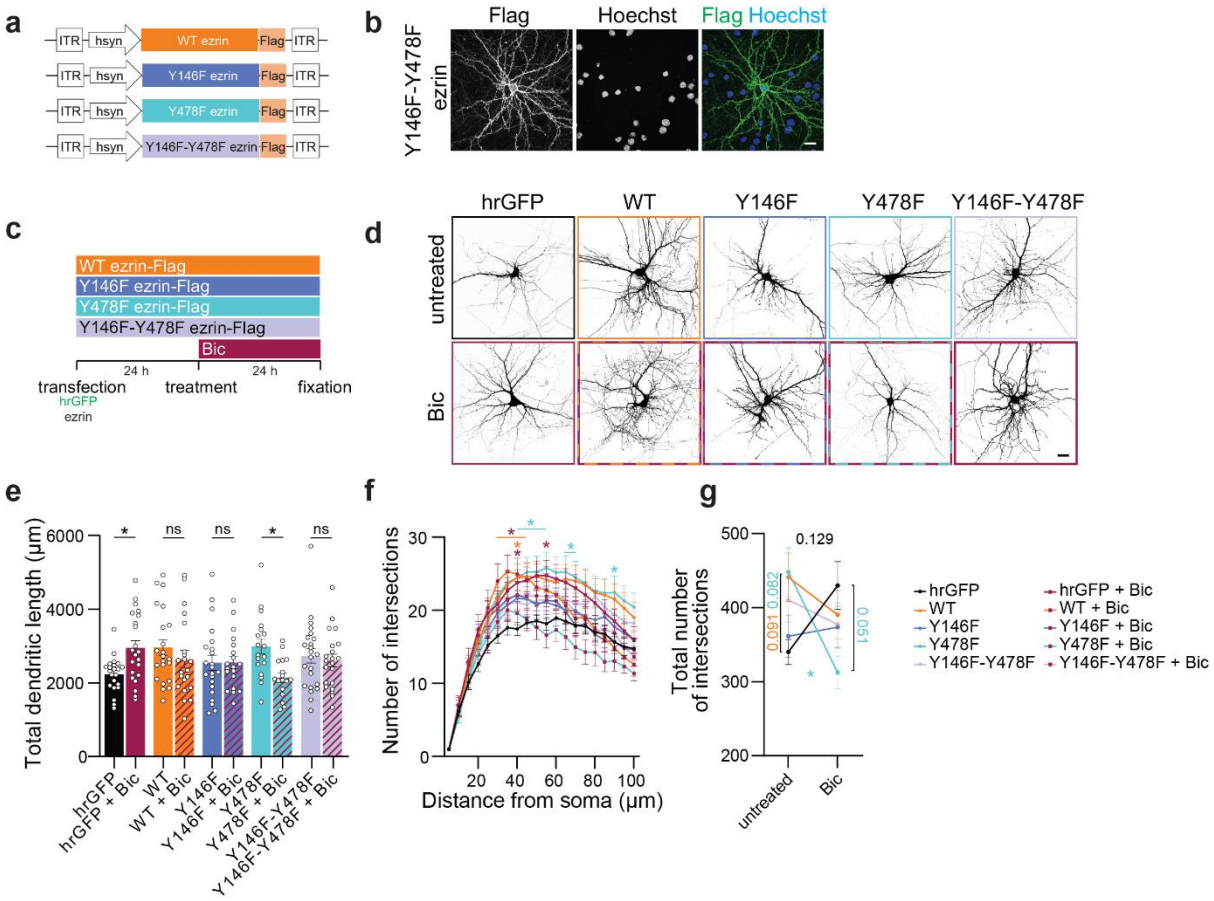

Figure 29. Overexpression of phospho-mutant Y478F ezrin blocks activity-dependent dendrite remodeling. *Analysis of dendrite morphology of hrGFP (vector) and/or WT, Y146F, Y478F or Y146F-Y478F ezrin-transfected cultured mouse hippocampal neurons with or without bicuculline (Bic) treatment.* ***a*** *Schema of constructs.* ***b*** *Representative Flag-immunostained Y146F-Y478F ezrin-transfected neuron at DIV 10. Nuclei were visualized with Hoechst. Scale bar = 20 µm.* ***c*** *Schema of experiment.* ***d*** *Representative images of neurons transfected and treated as indicated. hrGFP was used to visualize neuronal morphology. Scale bar = 20 µm.* ***e-g*** *Total dendritic length (**e**), Sholl analysis (minimal significant p values are displayed; WT vs hrGFP, p = 0.040; WT + Bic vs hrGFP, p = 0.530; Y146F vs hrGFP, p = 0.806; Y146F + Bic vs hrGFP, p = 0.801; Y478F vs hrGFP, p = 0.042; Y478F + Bic vs hrGFP, p = 0.999; Y146F-Y478F vs hrGFP, p = 0.279; Y146F-Y478F + Bic vs hrGFP, p = 0.649) (**f**) and total number of intersections up to a radius of 150 µm (**g**) of neurons transfected and treated as indicated. One- and Two-way ANOVA followed by Bonferroni's or Tukey's post hoc test (**e, g**) or Dunnett's post hoc test (**e, f**). N = 17-22 neurons from 5 independent culture preparations. *p < 0.05; ns p > 0.05. Parts of this figure are adapted from a first authored manuscript that is currently in revision for submission to Cellular and Molecular Life Sciences (see List of publications).*

3.4.11 Phospho-mutant Y478F ezrin impacts synaptic activity-induced dendritic dynamics

In order to understand how phospho-mutant Y478F ezrin modulates dendrite dynamics to counteract activity-dependent dendrite remodeling, I performed time-lapse imaging to monitor dendrite dynamics in primary mouse hippocampal neurons transfected with hrGFP for the

visualization of neuronal morphology, and with or without WT and Y478F ezrin and treated with Bic to induce synaptic activity (Figure 30a). Consistent with the findings in chapter 3.4.10, overexpression of both WT and Y478F ezrin resulted in a notable increase in total dendritic length (Figure 30b). Bic treatment increased total dendritic length in control neurons but failed to induce a similar response in neurons expressing WT ezrin and even led to a reduction in total dendritic length in neurons expressing Y478F ezrin (Figure 30b-d). Bic also increased dendrite number in control neurons, as expected (Figure 30e, f). This effect was smaller in WT ezrin-expressing neurons (Figure 30e, f). Surprisingly, there was a reduction in dendrite number in the mutant compared to their respective untreated controls (Figure 30e, f). Dendrite number is increased in Bic-treated control neurons, because of a higher tendency to form new dendrites, which are at the same time less eliminated (Figure 30g, h). Bic failed to increase the formation of new dendrites in WT and Y478F ezrin-expressing neurons (Figure 30g, h). However, new dendrites still exhibited increased stabilization with Bic in WT ezrin-expressing neurons (Figure 30g, h). Conversely, this stabilization effect was not observed Y478F-expressing neurons (Figure 30g, h). Dendrite elimination in general but also elongation, shortening and elimination of dendrites, whether of all dendrites or just new dendrites, was not affected (Figure 30i-m; Appendix figure 6).

In conclusion, these results indicate that Bic treatment is ineffective in inducing additional dendrite remodeling in neurons expressing WT ezrin, as WT ezrin hinders the Bic-induced formation of new dendrites. On the other hand, the Y478F mutant not only prevents the Bic-induced formation of new dendrites but also results in the destabilization of any newly formed dendrites, leading to a reversal of total dendrite length to control values. This suggests that dephosphorylated ezrin at Y478 may be responsible for mediating the observed VEGFD-induced destabilization of new dendrites that emerged in response to Bic.

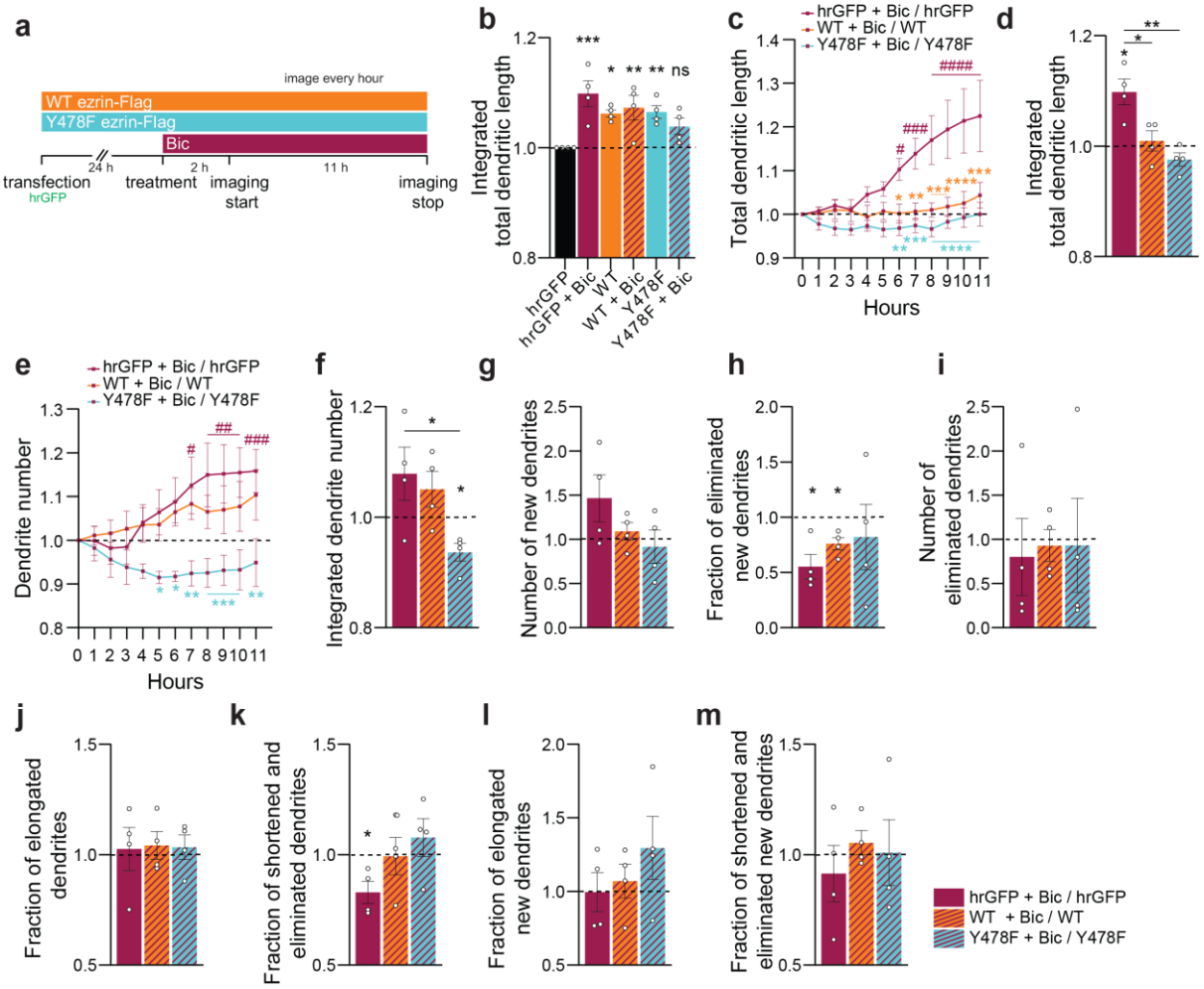

Figure 30. Y478F ezrin modifies synaptic activity-induced dendrite dynamics. *Time-lapse monitoring of dendrites of hrGFP (vector) and/or WT or Y478F ezrin-transfected cultured mouse hippocampal neurons with or without bicuculline (Bic) treatment. hrGFP was used to visualize neuronal morphology.* ***a*** *Schema of experiment.* ***b*** *Integration of total dendritic length over time normalized on the first timepoint and untreated control.* ***c*** *Total dendritic length over time normalized on the first timepoint and respective untreated control.* ***d*** *Integration of data shown in (**c**).* ***e*** *Total dendrite number over time normalized on the first timepoint and respective untreated control.* ***f*** *Integration of data shown in (**e**).* ***g*** *Total number of new dendrites normalized on respective untreated control.* ***h*** *Fraction of new dendrites that were then eliminated normalized on respective untreated control.* ***i*** *Total number of eliminated dendrites normalized on respective untreated control.* ***j*** *Fraction of elongated dendrites over time normalized on respective untreated control.* ***k*** *Fraction of shortened and eliminated dendrites over time normalized on respective untreated control.* ***l*** *Fraction of elongated new dendrites over time normalized on respective untreated control.* ***m*** *Fraction of shortened and eliminated new dendrites over time normalized on respective untreated control. Two-way ANOVA followed by Dunnett's post hoc test for comparisons to basal values (**c, e**), or Tukey's post hoc test for comparisons between conditions (**c, e**); One-way ANOVA followed by Dunnett's post hoc test (**b**) or Tukey's post hoc test (**d, f-m**); one sample t-test for comparisons to respective untreated control (**d, f-m**). N = 4 independent culture preparations, 13-16 neurons/condition in total. Graphs display mean ± SEM. Single values are represented as data points. Significance indicators include asterisks (*) for comparisons between conditions and hashtags (#) for comparisons to baseline values within each respective condition. ****p < 0.0001; ***p < 0.001; **p < 0.01; *p < 0.05; ns p>0.05; ####p < 0.0001; ###p < 0.001; ##p < 0.01; #p < 0.05. This figure is adapted from a first*

authored manuscript that is currently in revision for submission to Cellular and Molecular Life Sciences (see List of publications).

In sum, chapters 3.1, 3.2, 3.3 and 3.4 show that VEGFD signaling modulates the cytoskeleton by acting on cortical actin and MTs and that VEGFD needs to be downregulated to allow alterations in dendrite morphology both during development and in adulthood. Moreover, it uncovered that VEGFD prevents dendrite elongation and destabilizes newly formed dendrites in response to synaptic activity, which is partially mediated through STEP-induced dephosphorylation of Y478 ezrin.

Parts of this work have been submitted as a first authored manuscript that is currently in revision to Cellular and Molecular Life Sciences (see List of publications).

3.5 Role of phospho S43 cRaf as potential downstream candidate of VEGFD signaling

The serine/threonine-protein kinase c-Raf (rapidly accelerated fibrosarcoma), also known as Raf-1 (Zebisch et al., 2006), was identified as one of the VEGFD signaling downstream candidate proteins during the phospho-proteomic screening (chapter 3.3.1). It was found first among the other Raf isoforms, a-Raf and b-Raf (Rapp et al., 1983). Promoted by RTK signaling, c-Raf acts as a mitogen-activated protein kinase kinase kinase (MAP3K) to induce MEK/ERK signaling (Figure 31) (Wellbrock et al., 2004). As a result, it triggers many cellular functions, including cell proliferation, differentiation, and survival (Wellbrock et al., 2004). As part of RTK-MAPK signaling, c-Raf also plays a role in VEGFA signaling (Alavi et al., 2003; Hood et al., 2003). Since MAPK signalling may also be part of VEGFD signalling (Mauceri et al., 2011), which is further supported by the phospho-proteomic screening that revealed several MAPKs (chapter 3.3.1), c-Raf may also be part of VEGFD signalling. However, independently of MEK/ERK signalling, c-Raf also modulates cortical actin and cell migration via Rho signaling (Ehrenreiter et al., 2005). Moreover, Rafs play a role in sensory otic neuron expansion (Magariños et al., 2011) and axon growth of dorsal root ganglion neurons (Zhong et al., 2007).

C-Raf has numerous phosphorylation sites that regulate its activation or inactivation (Leicht et al., 2007). 15 min and 2h rVEGFD treatment reduced c-Raf phosphorylation at Serine 296 (S296) and Serine 43 (S43), respectively (chapter 3.3.1). Phosphorylation at S296, however, was found increased again after 2 h rVEGFD treatment. S296 is phosphorylated by ERK as part of a negative feedback loop although it has also been linked to activation (Leicht et al., 2007; Zhao et al., 2022).

GTPase Ras (Rat sarcoma virus) interacts and activates c-Raf by recruiting it to the plasma membrane (Figure 31) (Wellbrock et al., 2004). However, when S43, which is positioned near the Ras-binding domain (Figure 31), is phosphorylated by the cyclic AMP (cAMP)-dependent protein kinase (PKA), its affinity for Ras is diminished due to steric hindrance, reducing Ras-dependent activation of c-Raf (Wellbrock et al., 2004).

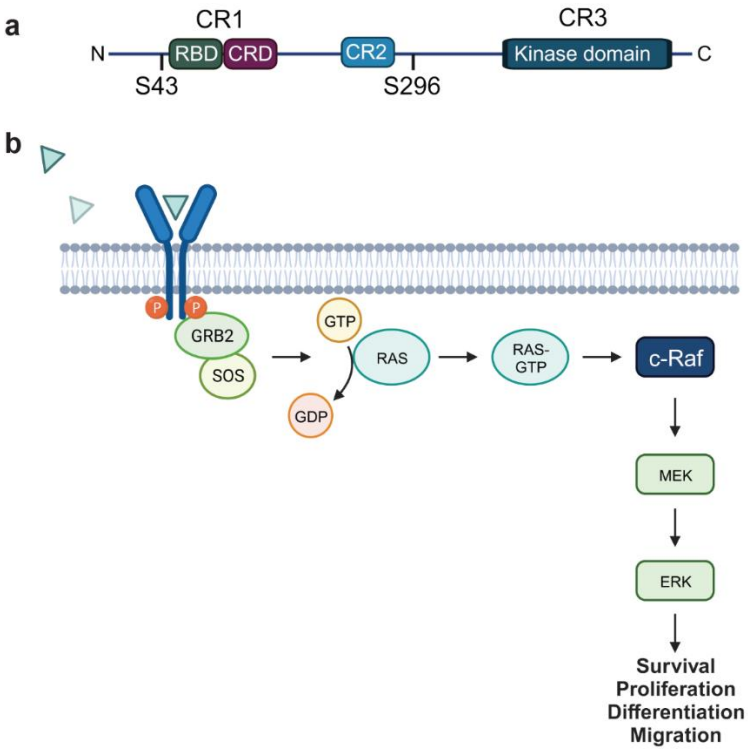

Figure 31. Structure and function of c-Raf. ***a*** *Structure of c-Raf. C-Raf has three conserved regions (CR1-3). CR1 contains the Ras-binding domain (RBD) and the cysteine-rich domain (CRD), required for membrane recruitment. CR3 harbors the kinase catalytic domain. Serine 43 (S43) and serine 296 (S296) are phosphosites putatively regulated by VEGFD signaling.* ***b*** *Schema showing function of c-Raf in receptor tyrosine kinase (RTK)-mitogen-activated protein kinase (MAPK)-signaling. Ligand-bound and phosphorylated RTK recruits via GRB2 the guanine nucleotide exchange factor SOS which induces exchange of GDP with GTP at the Ras. Active GTP-bound Ras then actives c-Raf leading to activation of MEK and ERK signaling. GRB2 = growth factor receptor-bound protein 2; SOS = son of sevenless; GTP = guanosine triphosphate; GDP = guanosine diphosphate; Ras = Rat sarcoma virus; MEK = mitogen-activated protein kinase kinase; ERK = extracellular signal-regulated kinases.*

3.5.1 Characterization of c-Raf expression

VEGFD-induced c-Raf phosphorylation was not further validated by other methods, but I tested whether 2 h of rVEGFD treatment might affect overall c-Raf expression through immunoblotting. Increased levels of phospho p38 (p p38) confirmed successful rVEGFD treatment (Figure 32a) (Mauceri et al., 2011). Expression of c-Raf was unaffected by rVEGFD (Figure 32a, b). In parallel with this experiment, some groups received 2 h Bic treatment with or without rVEGFD co-application, to

explore whether synaptic activity or VEGFD in the context of synaptic activity might affect c-Raf expression. A statistically non-significant trend toward a reduction of c-Raf levels after 2 h Bic treatment, but not when co-treated with rVEGFD, was observed (Appendix figure 3a, b).

Next, I examined the developmental expression of c-Raf. In cultured mouse hippocampal neurons, protein expression of c-Raf gradually decreases with increasing DIV (Figure 32c, d), which suggests a developmental role for c-Raf. This is consistent with its role in early organogenesis of the inner chicken ear (Magariños et al., 2011; Sanz et al., 1999).

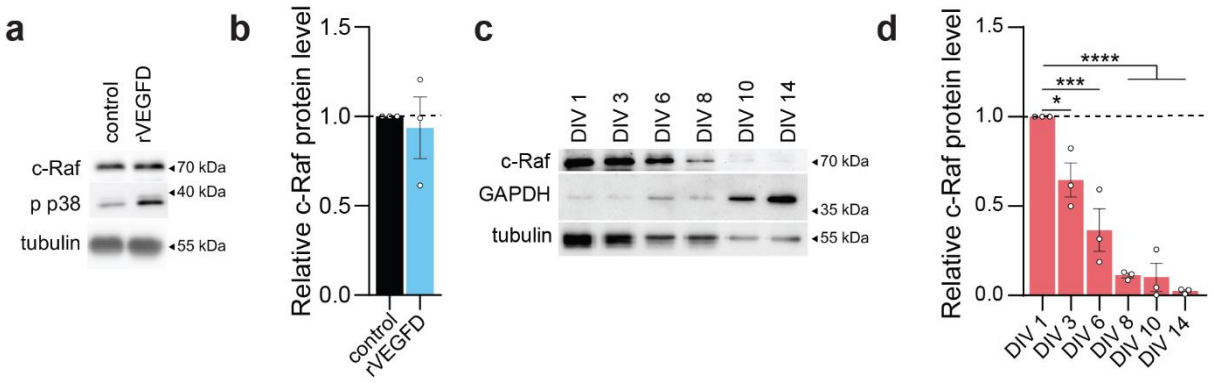

Figure 32. C-Raf is strongly expressed in developing neurons. ***a, b*** *Immunoblot analysis of c-Raf protein expression in cultured mouse hippocampal neurons treated or not with recombinant VEGFD (rVEGFD) for 2 h.* ***a*** *Representative immunoblots of c-Raf, phospho p38 (p p38) and tubulin.* **b** Quantification of c-Raf protein expression normalized to tubulin and control. One sample t-test. N = 3 independent culture preparations. ***c, d*** *Immunoblot analysis of c-Raf protein expression in cultured mouse hippocampal neurons at different days in vitro (DIV).* ***c*** *Representative immunoblots of c-Raf, GAPDH and tubulin.* ***d*** *Quantification of c-Raf protein expression. Expression was only normalized to DIV 1 due to DIV-related fluctuations in GAPDH and tubulin expression. One-way ANOVA followed by Dunnett's post hoc test. N = 3 independent culture preparations. Graphs display mean ± SEM. Single values are represented as data points. ****p < 0.0001; ***p < 0.001; *p < 0.05.*

3.5.2 Overexpression of phospho-mutant c-Raf does not affect dendrite morphology

I proceeded to characterize the role of c-Raf and its phosphorylation at S43 on dendrite morphology. To this end, I employed constructs to drive neuron-specific overexpression through the use of a hsyn promoter of either WT or mutant versions of c-Raf in which the serine at residue 43 has been replaced with an alanine (S43A) (Dhillon et al., 2002; Dumaz et al., 2006; Kamemura et al., 2017; Sidovar et al., 2000) or aspartic acid (S43D) (Kamemura et al., 2017). Alanine is structurally similar to serine but lacks the hydroxyl group crucial for phosphorylation and thereby serves as a non-phosphorylatable and active version of S43 c-Raf (Dhillon et al., 2002; Dumaz et al., 2006; Kamemura

et al., 2017; Sidovar et al., 2000). Aspartic acid, on the other hand, structurally mimics phosphorylated serine and thereby prevents interaction of c-Raf with Ras (Kamemura et al., 2017). All constructs contain a C-terminal Flag-tag to enable immunocytochemical detection (Figure 33a). When transfected into primary mouse hippocampal neurons, all three versions of c-Raf were ubiquitously distributed in the cytoplasm, with more pronounced expression in the soma and primary dendrites (Figure 33b). This distribution aligns with a previous study that reported reduced c-Raf presence in neural processes of chicken acoustic-vestibular ganglia (Magariños et al., 2011).

I examined dendrite morphology through co-transfection with hrGFP to visualize neuronal structure (Figure 33c-g). Control neurons were only transfected with hrGFP. Morphology was analyzed at DIV 14, a stage at which the cultures are mature, and dendrite morphology is largely established. Dendrite length and complexity was increased in WT c-Raf-overexpressing neurons (Figure 33e-g). S43A follows a similar trend, but it is not statistically significant (Figure 33e-g). No difference in dendrite morphology was measured for S43D (Figure 33e-g).

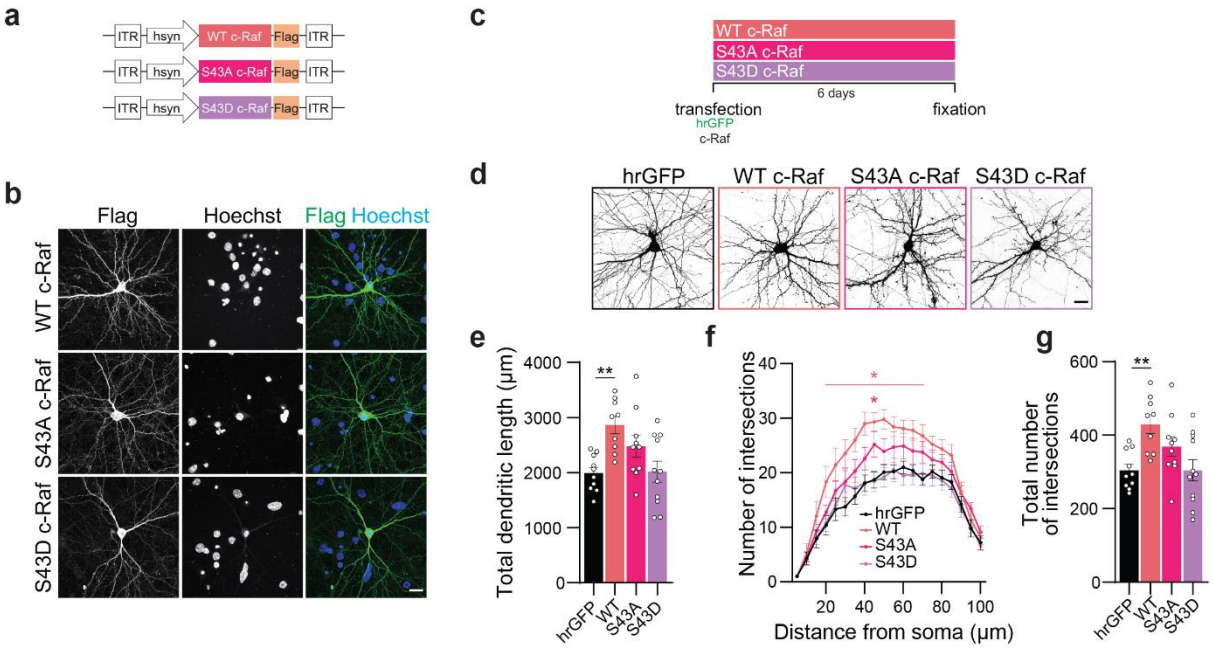

Figure 33. Overexpression of WT but not phospho-mutant c-Raf induces dendrite remodeling. *Analysis of dendrite morphology of hrGFP (vector) and/or WT, S43A or S43D c-Raf-transfected cultured mouse hippocampal neurons.* ***a*** *Schema of constructs.* ***b*** *Representative images of Flag-immunostained WT, S43A or S43D c-Raf-expressing neurons. Nuclei were visualized with Hoechst. Scale bar = 20 µm.* ***c*** *Schema of experiment.* ***d*** *Representative images of neurons transfected as indicated. hrGFP was used to visualize neuronal morphology. Scale bar = 20 µm.* ***e-g*** *Total dendritic length (**e**), Sholl analysis (minimal significant p values are displayed) (**f**) and total number of intersections up to a radius of 150 µm (**g**) of neurons transfected as indicated. One- (**e, g**) and Two-way ANOVA (**f**) followed by Dunnett's post hoc test. N = 9-11 neurons from 3 independent culture preparations. Graphs display mean ± SEM. Single values are represented as data points. **p < 0.01; *p < 0.05.*

3.5.3 Overexpression and inactivation of c-Raf interferes with activity-dependent dendrite remodeling

Next, the role of c-Raf and its phosphorylation state at S43 in the context of synaptic activity was explored. For this, c-Raf- and hrGFP-transfected neurons were treated with Bic at DIV 9 for 24 h to induce synaptic activity-induced dendrite remodeling (Figure 34a-e). As expected, this resulted in an increase in dendrite length and complexity in Bic treated control neurons (Figure 34c-e). Although WT c-Raf overexpression induced dendrite growth under baseline conditions when morphology was analyzed at DIV 14 (Figure 33e-g), it did not at DIV 10 (Figure 34c-e). The phospho-mutants also did not differ from untreated control neurons (Figure 34c-e). Intriguingly, Bic-induced dendrite remodeling did not take place when c-Raf was overexpressed, regardless of which construct (Figure 34c-e). This suggests that high levels of c-Raf interfere with activity-dependent dendrite remodeling, independent of its phosphorylation at S43.

Therefore, Dr. Jing Yan tested whether pharmacological inhibition of c-Raf using the drug GW5074 might interfere with Bic-induced activity-dependent dendrite remodeling in cultured hippocampal mouse neurons (Figure 34f) (Chin et al., 2004; Lei et al., 2008). While GW5074 treatment by itself did not affect dendrite morphology, its co-administration with Bic not only prevented activity-induced increase in dendrite length and complexity, but even resulted in a simplification of the dendritic tree compared to control neurons (Figure 34g-j).

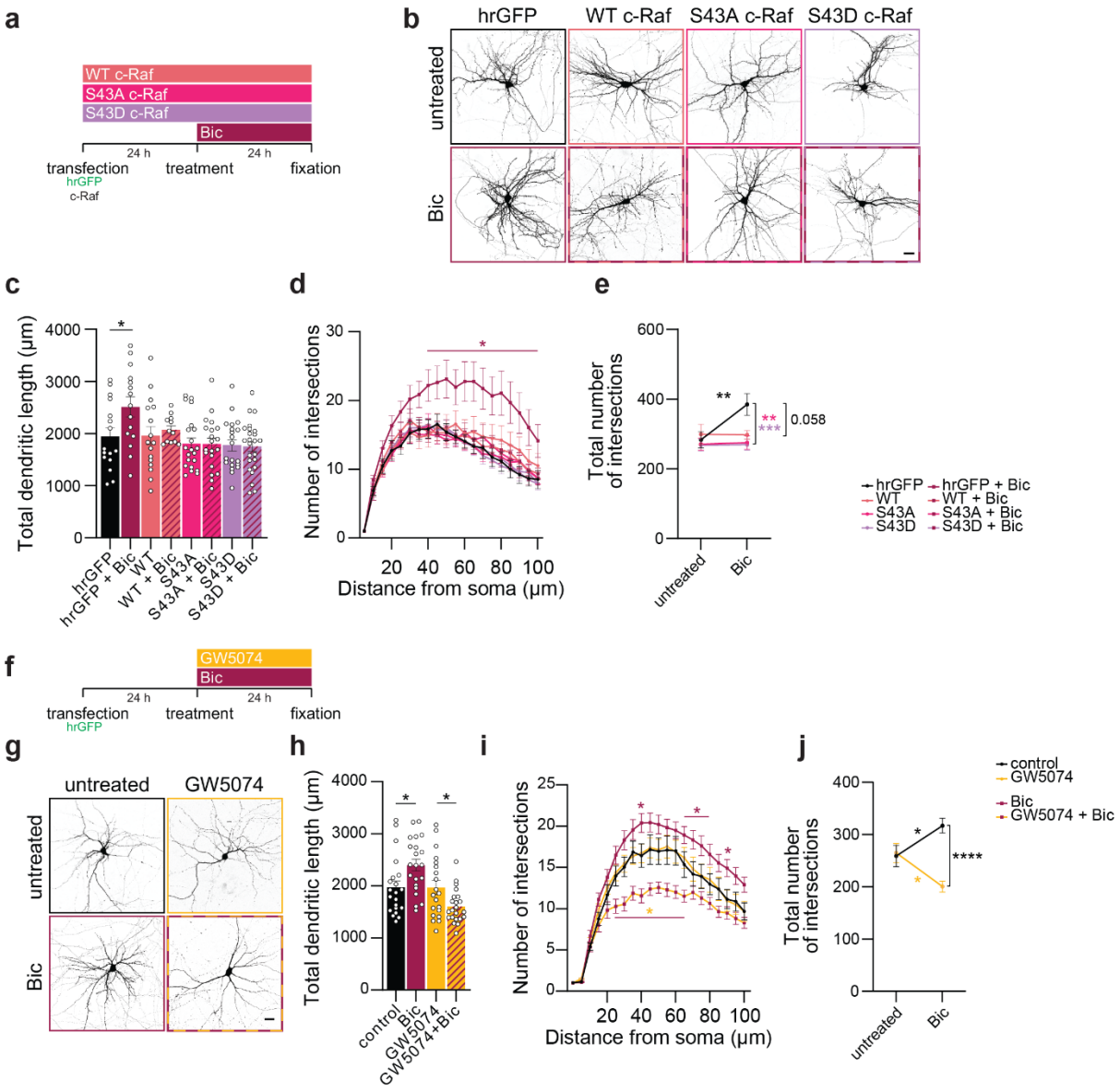

Figure 34. Both overexpression and inhibition of c-Raf block activity-dependent dendrite remodeling. ***a-e*** *Analysis of dendrite morphology of hrGFP (vector) and/or WT, S43A or S43D c-Raf-transfected cultured mouse hippocampal neurons with or without bicuculline (Bic) treatment.* ***a*** *Schema of experiment.* ***b*** *Representative images of neurons transfected and treated as indicated. hrGFP was used to visualize neuronal morphology. Scale bar = 20 µm.* ***c-e*** *Total dendritic length (**c**), Sholl analysis (minimal significant p values are displayed) (**d**) and total number of intersections up to a radius of 100 µm (**e**) of neurons transfected and treated as indicated. One- and Two-way ANOVA followed by Bonferroni's or Tukey's post hoc test (**c, e**) or Dunnett's post hoc test (**d**). N = 12-23 neurons from 3-4 independent culture preparations.* ***f-j*** *Analysis of dendrite morphology of hrGFP-transfected cultured mouse hippocampal neurons with or without GW5074 treatment.* ***f*** *Schema of experiment.* ***g*** *Representative images of neurons treated as indicated. Scale bar = 20 µm.* ***h-j*** *Total dendritic length (**h**), Sholl analysis (minimal significant p values are displayed) (**i**) and total number of intersections up to a radius of 100 µm (**j**) of neurons transfected and treated as indicated. One- and Two-way ANOVA followed by Bonferroni's or Tukey's post hoc test (**h, j**) or Dunnett's post hoc test (**i**). N = 20-23 neurons from 3 independent culture preparations. Graphs display mean ± SEM. Single values are represented as data points. ****p < 0.0001; ***p < 0.001; **p < 0.01; *p < 0.05. Experiments in a-e were jointly performed with Dr. Jing Yan. Experiments in f-j were all performed by Dr. Jing Yan.*

In sum, these data show that expression and activity levels of c-Raf, potentially independent of its phosphorylation at S43, seems to play a role in dendrite morphology, particularly in response to activity-dependent dendrite remodeling.

3.6 Acute VEGFD treatment does not induce nuclear calcium transients

As VEGFA-VEGFR2 signaling is known to induce PLCγ-Ca^{2+} signaling in neurons (Kim et al., 2008), I tested if VEGFD may also induce calcium transients by performing nuclear calcium imaging on primary mouse hippocampus neurons. After a 5 min baseline recording, neurons underwent a 5 min treatment with imaging medium (vector) as a control, followed by an additional 10 minutes with rVEGFD. Both the introduction of the control medium and rVEGFD led to initial or spontaneous calcium rises (Figure 35), which were, however, unlike the robust and repetitive nuclear calcium rises observed with Bic (Figure 10) (Bengtson et al., 2013). This suggests that an acute increase of VEGFD levels does not induce calcium signaling in neurons.

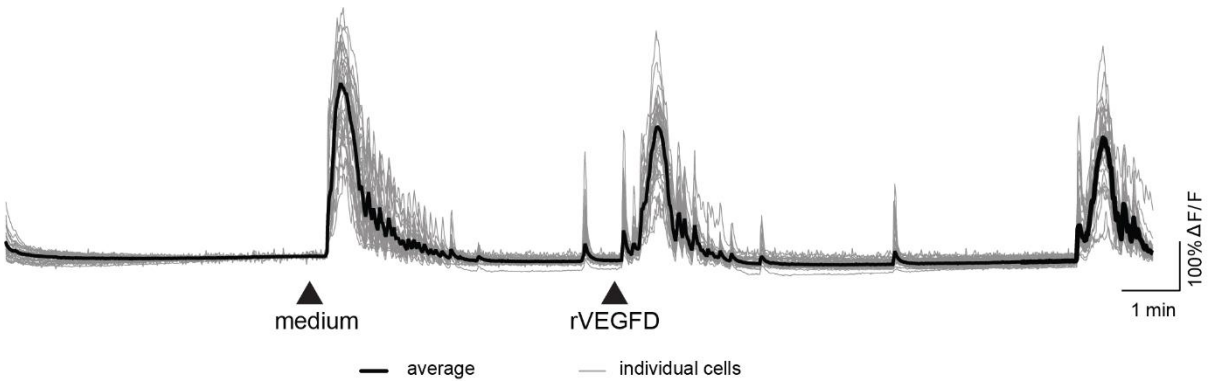

Figure 35. Acute recombinant VEGFD treatment does not elicit calcium transients. *Calcium imaging of jRGECO1alpha-NLS-infected cultured mouse hippocampal neurons treated after 5 min of baseline recording with imaging medium for 5 min, followed by a 10 min treatment with recombinant VEGFD (rVEGFD). Treatment with medium served as control. N = 12 coverslips from 5 independent culture preparations. Graphs display mean ± SEM. Single values are represented as data points.*

3.7 Characterization of VEGFR3 in neurons

3.7.1 Developmental expression pattern of VEGFR3

VEGFD is a secreted factor that mediates its dendrite stabilization signal in an autocrine manner through its receptor VEGFR3 (Mauceri et al., 2011). Given the low expression of VEGFD during

development to allow dendritogenesis, I explored whether VEGFR3 may follow a similar expression pattern. Surprisingly, in contrast to *VEGFD*, *VEGFR3* mRNA expression peaked in the hippocampi and cortices of young mice (Figure 36a, b). Due to limited availability of protein samples, analysis of VEGFR3 expression on protein level is only preliminary. Nevertheless, immunoblot analysis indicates an age-related increase in VEGFR3 expression, mirroring the observed pattern for VEGFD (Figure 36c, d). It should be noted, however, that the antibody employed for measuring VEGFR3 protein levels, may not be effective for endogenous VEGFR3 expression, as it failed to detect a reduction of VEGFR3 through immunoblotting in homogenates from cultured neurons in which VEGFR3 was downregulated through infection with shVEGFR3 (Appendix figure 7a).

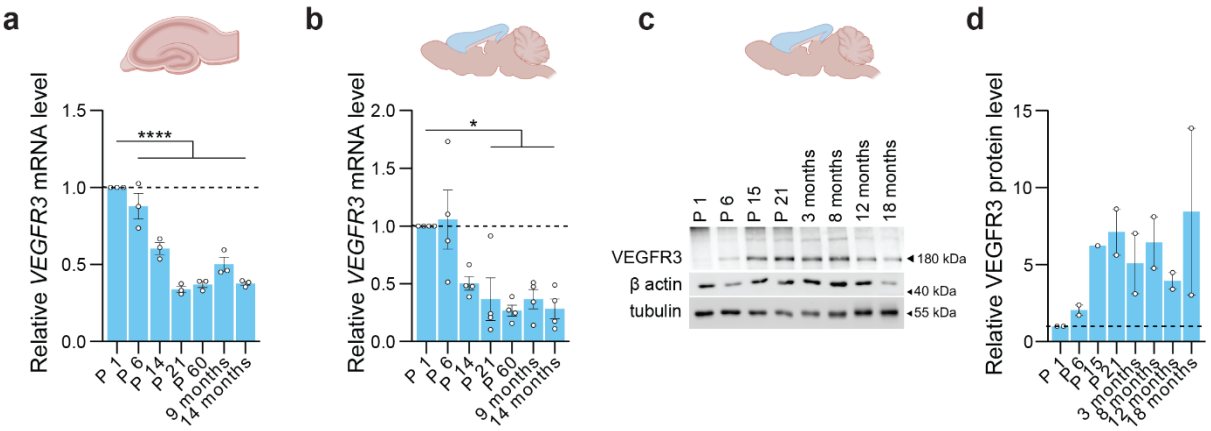

Figure 36. Characterization of VEGFR3 expression throughout development. ***a, b*** *QRT-PCR analysis of VEGFR3 mRNA expression in hippocampus (**a**) or cortex (**b**) lysates derived from mice at indicated ages (P 1-60 = postnatal day 1-60). Expression was normalized to GAPDH, gusb and P 1. One-way ANOVA followed by Dunnett's post hoc test. N = 3 mice.* ***c, d*** *Immunoblot analysis of VEGFR3 protein expression in cortex lysates derived from mice at indicated ages.* ***c*** *Representative immunoblots of VEGFR3, β actin and tubulin.* ***d*** *Quantification of VEGFR3 protein expression. Expression was only normalized to P 1 due to age-related fluctuations in β actin and tubulin expression. N = 2 mice. Graphs display mean ± SEM. Single values are represented as data points. ****p < 0.0001; *p < 0.05.*

3.7.2 Synaptic activity affects VEGFR3 expression

As the previous chapters showed that VEGFD expression is reduced during synaptic activity, it raises the question whether expression of the receptor of VEGFD is affected as well. Prof. Dr. Daniela Mauceri had previously measured *VEGFR3* mRNA levels in primary mouse hippocampal neurons treated with Bic for different durations and observed an increase after 24 h of Bic treatment, while expression was unaffected by shorter treatment times (Figure 37a). This opposite observation might be due to a compensatory effect in response to decreased availability of its ligand.

I additionally tested the effect of synaptic activity on VEGFR3 protein expression both in whole lysates as well as in protein fractions enriched in postsynaptic proteins (TIF, see chapter 3.7.3). As these experiments were performed during my time as a visiting scientist in the laboratory of Prof. Dr. Monica di Luca and Dr. Elena Marcello (Milano, Italy), cultured rat hippocampal neurons were employed. Synaptic activity was induced by Bic in combination with the K+-channel blocker 4-aminopyridine (4AP) (Hardingham et al., 2001) for 30 min. A significant reduction in VEGFR3 levels was detected only in the homogenate but not in the TIF, although a similar trend was visible (Figure 37a), indicating that short induction of activity decreases overall expression of VEGFR3 which may be compensated for in spines by enhanced localization to spines. It should be noted, however, that the antibody employed for measuring VEGFR3 protein levels, may not be effective for endogenous VEGFR3 expression, as it failed to detect a shRNA-mediated reduction of VEGFR3 (Appendix figure 7a).

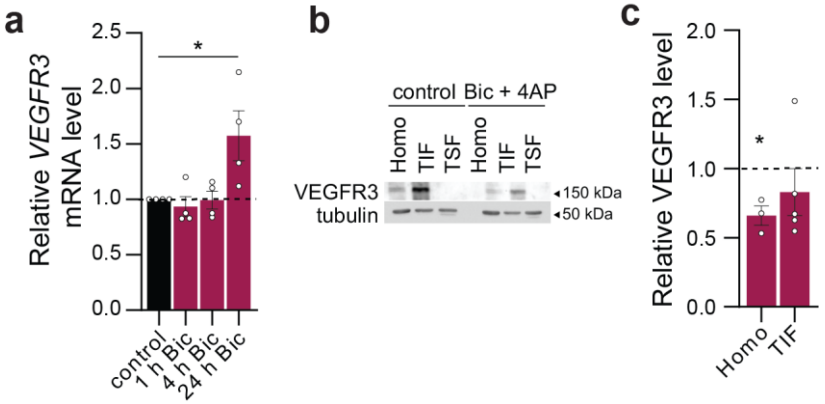

Figure 37. Synaptic activity influences expression of VEGFR3. ***a*** *QRT-PCR analysis of VEGFR3 mRNA expression in cultured mouse hippocampal neurons with or without bicuculline (Bic) administration for 1, 4 or 24 h. Expression was normalized to gusb and control. One-way ANOVA followed by Dunnett's post hoc test. N = 4 independent culture preparations.* ***b, c*** *Immunoblot analysis of VEGFR3 protein expression in triton insoluble fractions (TIF) derived from cultured rat hippocampal neurons treated with or without Bic and 4-aminopyridine (4AP) for 30 min.* ***b*** *Representative immunoblots of VEGFR3 and tubulin.* ***c*** *Quantification of VEGFR3 protein expression normalized to tubulin and control of respective fraction. Homo = homogenate; TSF = triton insoluble fraction. One sample t-test N = 3-6 independent culture preparations. Graphs display mean ± SEM. Single values are represented as data points. *p < 0.05. Experiment in a was performed by Prof. Dr. Daniela Mauceri.*

3.7.3 Subcellular localization of VEGFR3

VEGFD is a secreted factor that mediates its dendrite stabilization signal in an autocrine manner through its receptor VEGFR3 (Mauceri et al., 2011). Nevertheless, the precise subcellular localization of VEGFD or its receptor VEGFR3 within neurons remains unknown. Given the intricately compartmentalized morphology of neurons and the reported divergent effects of VEGFD on basal

and apical dendrites (Maurer et al., 2020), it is possible that VEGFD signaling operates in a localized fashion. Therefore, determining the subcellular localization of the receptor is crucial for gaining insights into the specific site of VEGFD action.

So far, the lack of effective antibodies for immunocyto- or histochemical labeling has made the visualization of the subcellular localization of VEGFR3 challenging. Consequently, I opted for an alternative approach, conducting biochemical fractionation to concentrate proteins from the postsynapse and analyzed VEGFR3 protein levels in this fraction (Figure 38a-e). This was done on lysates of cultured mouse (Figure 38a) or rat (Figure 38d) hippocampal cells as well as *in vivo* with lysates of the mouse hippocampus (Figure 38b) and cortex (Figure 38c) or rat hippocampus (Figure 38e). Additionally, I purified the postsynaptic density (PSD) from whole rat brain lysates (Figure 38f). The postsynaptic protein postsynaptic density 95 (PSD95) appeared at a higher quantity and the presynaptic protein synaptophysine and tubulin, which are mostly absent at the postsynapse, were less or even missing in the triton insoluble fraction (TIF), the fraction corresponding to the postsynapse enrichment (Figure 38a-e), and in the PSD fraction (Figure 38f), demonstrating correct enrichment of the postsynapse. An antibody against VEGFR3 detected a band around 180 kDa in the TIFs of cultured mouse hippocampal neurons and of the mouse hippocampus and cortex, which was almost absent in the homogenates (Figure 38a-c), indicating a potential localization of VEGFR3 at the postsynaptic compartment. It should, however, be noted that the antibody employed for measuring VEGFR3 protein levels, may not be effective for endogenous VEGFR3 expression, as it failed to detect VEGFR3 knockout (Appendix figure 7).

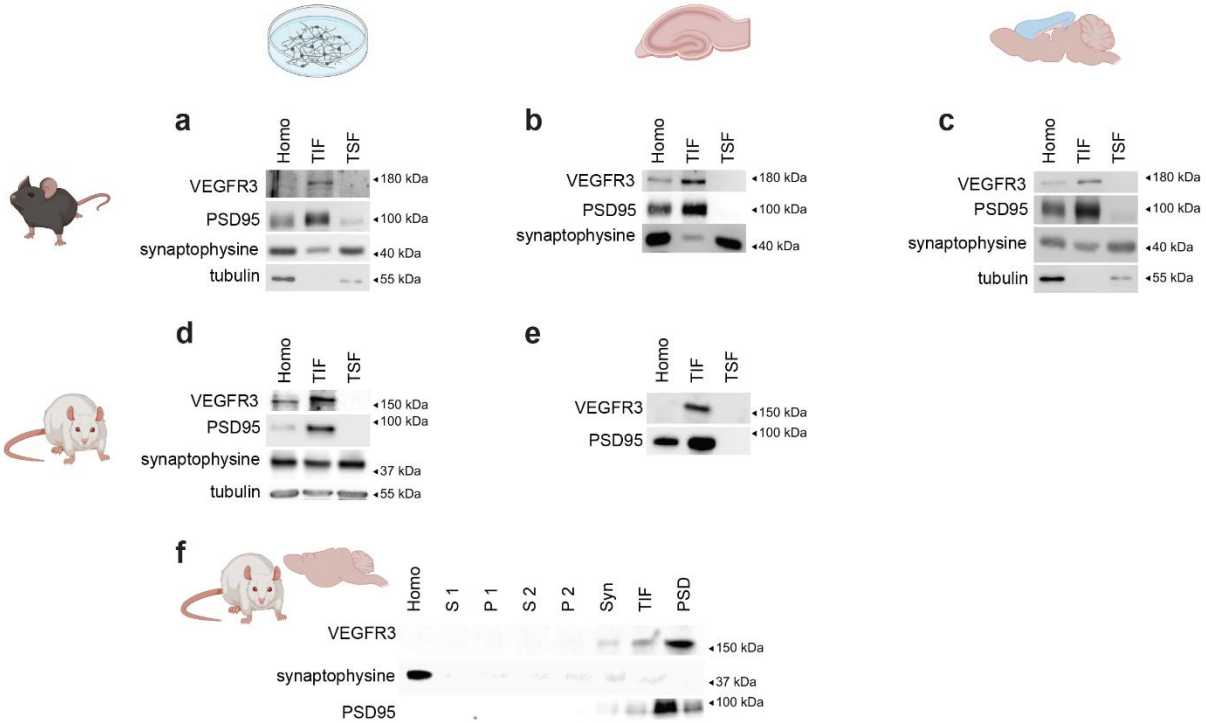

Figure 38. VEGFR3 is predominantly present in protein fractions that are enriched with postsynaptic proteins. ***a-e*** *Representative immunoblots of VEGFR3, PSD95, synaptophysine and tubulin in triton insoluble fractions (TIF) enriched in postsynaptic proteins from lysates derived from mouse (**a**: cultured hippocampal neurons; **b**: hippocampus; **c**: cortex) or rat (**d**: cultured hippocampal neurons; **e**: hippocampus). Homo = homogenate; TSF = triton insoluble fraction.* ***f*** *Representative immunoblots of VEGFR3, PSD95 and synaptophysine in postsynaptic density (PSD) preparations from rat brain lysates. S 1/ S 2 = supernatant 1/2; P 1 /P 2 = pellet 1/2; Syn = synaptosomes. PSD was jointly prepared with Elisa Zianni.*

Another approach that I pursued to determine the subcellular localization of VEGFR3 was through overexpression of VEGFR3. I was kindly provided by Prof. Dr. Martin Schwartz and Dr. Brian Coon with pLenti plasmids that drive VEGFR3 or, as a comparison to another member of the VEGF family, VEGFR2 expression under the control of a CMV (cytomegalovirus) promoter (Coon et al., 2015) (Figure 39a). Transfection efficiency of these plasmids was very low in cultured neurons. This may be due to the large size of VEGFRs. Therefore, I tested whether different backbones might improve transfection yield. For this, I subcloned VEGFR3 into another pLenti vector and a pAAV vector, respectively (Figure 39a). Additionally, a hsyn promoter was selected to allow neuron-specific expression of VEGFR3 (Figure 39a). VEGFR2 was only cloned into a pAAV vector (Figure 39a). Transfection efficiency, however, remained low in cultured neurons. Therefore, I tested transfection in Human Embryonic Kidney (HEK) 293FT cells, which are typically used for transfection with pLenti vectors and where transfection is generally more efficient than in cultured neurons. All constructs induced GFP fluorescence in HEK 293FT cells, even the ones containing a hsyn promoter (Figure 39b). Some of the constructs were also assessed by immunoblotting. A pLenti construct driving expression of CMV>GFP served as transfection control (Figure 39a) and resulted in a strong expression of GFP that was detectable by immunoblotting at 27 kDa (Figure 39c). Among all constructs tested, only pLenti-CMV>VEGFR3-GFP-transfected cells showed a strong GFP band at a size significantly higher than 180 kDa, that was also identified by a VEGFR3 antibody (Figure 39c), which may correspond to VEGFR3-GFP. However, with high exposures, this band formed in untransfected HEK cells as well. Furthermore, a GFP band of 27 kDa was observed in pAAV-hsyn>VEGFR2-GFP- and pLenti-CMV>VEGFR3-GFP-transfected cells (Figure 39c), indicating that GFP may be cleaved from VEGFR2 and VEGFR3. Using the GFP-tag, I also attempted to pull down VEGFR3-GFP with magnetic beads coupled to nanobodies that target GFP to concentrate VEGFR3-GFP and facilitate its detection via immunoblotting. While the band significantly above 180 kDa was still detected by a GFP antibody in the immunoprecipitate (IP), IPs from cells transfected with the other constructs showed the same pattern as the untransfected control, suggesting the precipitation of unspecific proteins (Figure 39d).

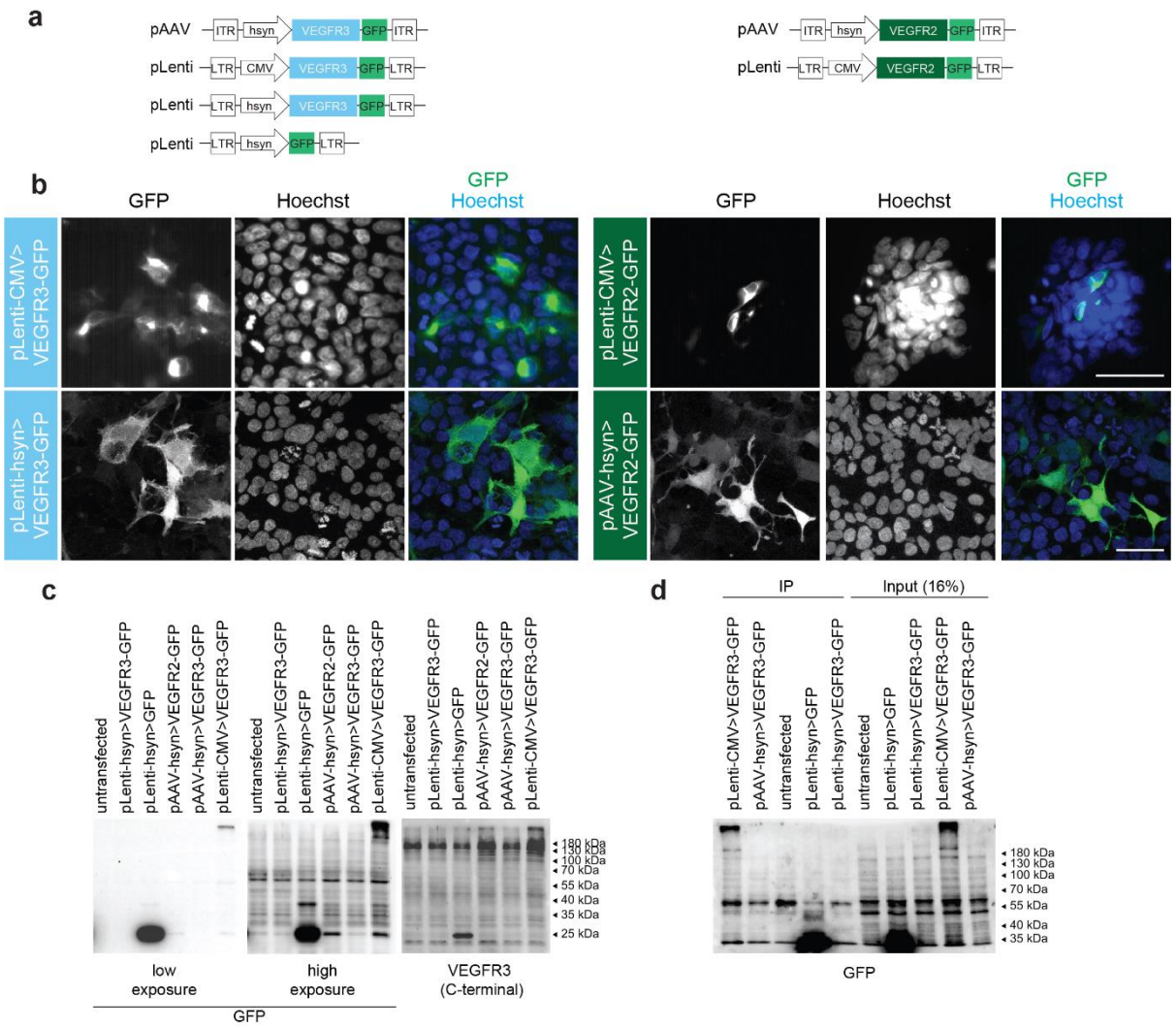

Figure 39. Establishment of tools for VEGFR3 overexpression in human embryonic kidney cells. ***a*** *Schema of constructs used to overexpress VEGFR3-GFP, VEGFR2-GFP or GFP as control.* ***b*** *Representative images of GFP fluorescence in HEK293FT cells transfected with indicated constructs. Nuclei were visualized with Hoechst. Scale bar = 50 µm.* ***c*** *Representative immunoblots of GFP (at low or high exposure) and VEGFR3 (antibody labels VEGFR3 C-terminally; sc-321; Santa Cruz) in lysates of HEK293FT cells transfected as indicated.* ***d*** *Representative immunoblot of immunoprecipitated (IP) GFP from lysates of HEK293FT cells transfected as indicated. ITR = Inverted terminal repeat; LTR = long terminal repeat.*

Despite the poor transfection efficiency of VEGFR2- and VEGFR3-GFP, few pLenti-CMV>VEGFR2-GFP- and pLenti-CMV>VEGFR2-GFP-transfected cultured mouse hippocampal neurons could still be detected. The majority of them were dead, but in those that were alive, GFP signal was ubiquitously expressed, although with punctae-like expression on branches (Figure 40a-d). To test the hypothesis that VEGFR3 may be localized at the postsynapse, I used immunocytochemistry to look for co-localization of VEGFR2- or VEGFR3-GFP with PSD95, but there was no apparent overlap (Figure 40c, d). However, it cannot be ruled out that overexpressed VEGFR2 and VEGFR3 are misfolded,

aggregated and/or distributed differently than the endogenous version, especially given that transfection was ineffective and toxic. It should also be noted that stainings were performed at DIV 10, when spines are less mature, as fewer transfected neurons remained until DIV 14.

As the delivery of plasmids through infection typically introduces a lower copy number per cell, which might facilitate expression and minimize toxicity, and infects a larger number of cells compared to transfection, I generated rAAVs from pAAV-hsyn>VEGFR3-GFP and pAAV-hsyn>GFP as a control (Figure 40e). Immunocytochemistry confirmed successful GFP expression with both constructs in cultured mouse hippocampal neurons (Figure 40f). In contrast to neurons expressing GFP alone, those expressing VEGFR3-GFP exhibited less pronounced nuclear localization. Immunoblotting for GFP revealed a band at 27 kDa corresponding to GFP in GFP-expressing neurons (Figure 40g). Notably, the 27 kDa band appeared in both VEGFR3-GFP-infected and uninfected cells at high exposure, suggesting potential non-specificity. A band at 180 kDa appeared in VEGFR3-GFP-infected neurons, potentially corresponding to VEGFR3-GFP (VEGFR3: 153 kDa; GFP: 27 kDa) and which was not present in uninfected or GFP-only expressing neurons (Figure 40g). Additionally, VEGFR3 overexpression was assessed with an antibody against VEGFR3 through immunocytochemistry and immunoblotting (Figure 40f, g). VEGFR3-GFP expressing cells exhibited significantly more VEGFR3 fluorescence than GFP-expressing cells (Figure 40f). Intriguingly, VEGFR3 staining in neurons expressing only GFP was predominantly nuclear, while in VEGFR3-GFP-expressing neurons, it was primarily cytoplasmic (Figure 40f). This observation may signify distinct distributions of overexpressed VEGFR3 or, considering the antibody's ineffectiveness in detecting VEGFR3 knockout (Appendix figure 7), unspecific labeling of endogenous VEGFR3. Immunoblotting revealed a band at 180 kDa, but also additional non-specific bands that were exclusively observed in VEGFR3-GFP-expressing cells, which hint at possible cleavage or posttranslational modifications of VEGFR3 (Figure 40g).

Because overexpression of VEGFR3-GFP appears to be effective, I examined co-localization with PSD95 using immunocytochemistry (Figure 40f). There appears to be overlap between VEGFR3/GFP and PSD95 in both VEGFR3-GFP and GFP-expressing neurons. To reach more certain conclusions, higher magnification and quantitative analysis are required. It should also be noted that stainings were performed at DIV 10, when spines are less mature.

As the VEGFR3 antibodies seem to detect overexpressed VEGFR3, I repeated biochemical fractionation to enrich postsynaptic proteins on VEGFR3-GFP overexpressing neurons. Using VEGFR3 antibodies against the C-terminal or N-terminal ends of VEGFR3 to exclude potential overlooking of

cleaved VEGFR3, I detected not exclusive but higher levels of VEGFR3 in the TIFs (Figure 40h). This suggests that VEGFR3 may be localized in spines.

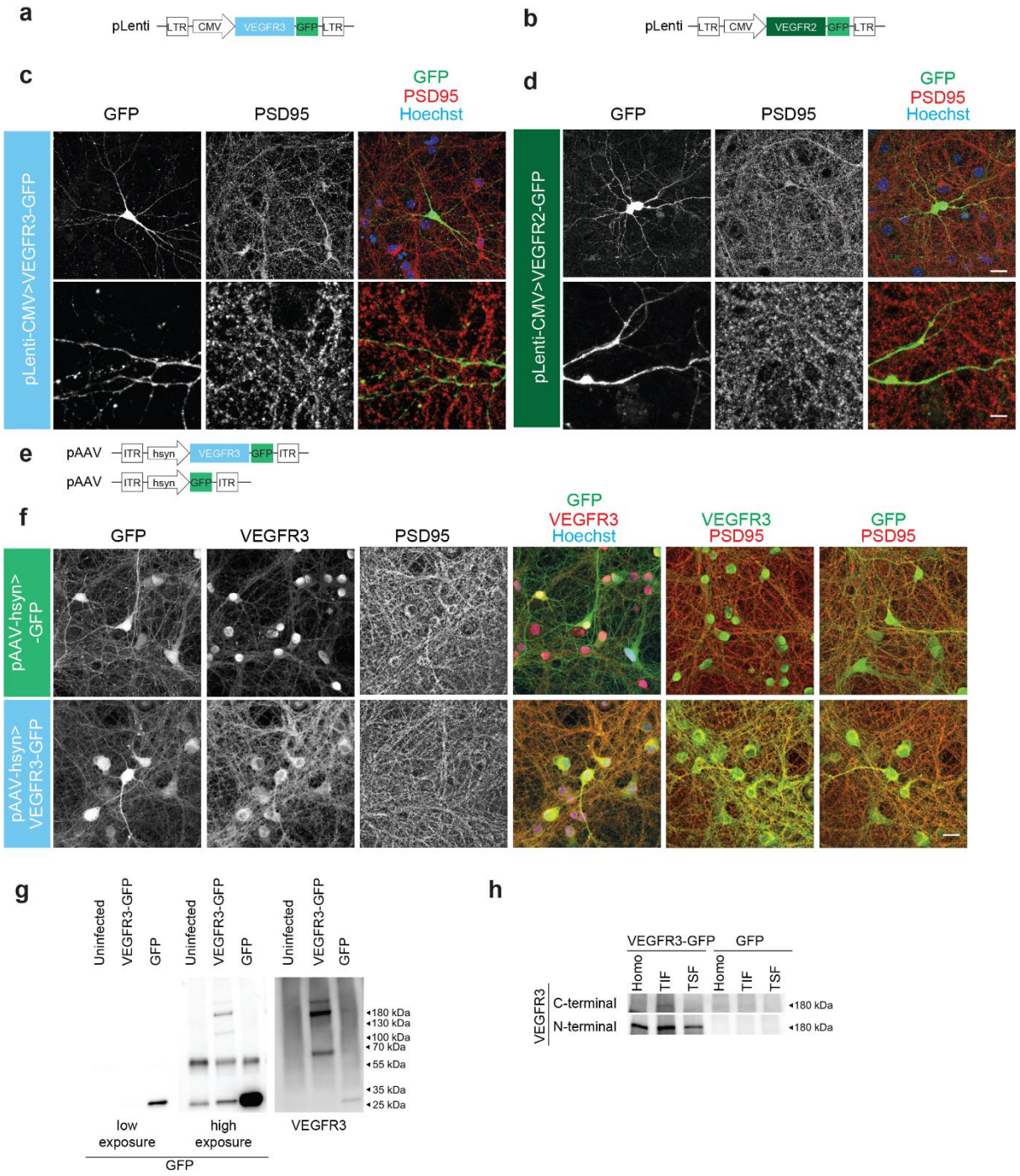

Figure 40. Establishment of tools for VEGFR3 overexpression in cultured neurons. ***a, b*** *Schema of constructs used to overexpress VEGFR3-GFP (**a**) or VEGFR2-GFP (**b**) under the control of a CMV promoter.* ***c, d*** *Representative images of GFP fluorescence and PSD95-immunostaining in cultured mouse hippocampal neurons at DIV 10 transfected with construct in a (**c**) or in b (**d**) as indicated. Lower image shows magnification of dendrites from upper image. Nuclei were visualized with Hoechst. Scale bars = 20 µm (upper image); 5 µm (lower image).* ***e-h*** *Characterization of VEGFR3-GFP expression in cultured mouse hippocampal neurons infected with rAAVs to drive neuronal expression of VEGFR3-GFP or GFP as control.* ***e*** *Schema of constructs.* ***f*** *Representative images of GFP*

fluorescence and PSD95-and VEGFR3-co-immunostaining in cultured mouse hippocampal neurons at DIV 10 infected with indicated construct. Nuclei were visualized with Hoechst. Scale bar = 20 µm. ***g*** *Representative immunoblots of GFP (at low or high exposure) and VEGFR3 (antibody labels VEGFR3 N-terminally; AF743; R&D) in lysates of neurons infected or not as indicated.* ***h*** *Representative immunoblots of VEGFR3 (using antibodies to label VEGFR3 N-terminally (AF743; R&D) or C-terminally (sc-321; Santa Cruz)) in triton insoluble fractions (TIF) enriched in postsynaptic proteins from lysates derived from neurons infected as indicated. Homo = homogenate; TSF = triton insoluble fraction. ITR = Inverted terminal repeat; LTR = long terminal repeat.*

Overall, some evidence indicates that VEGFR3 is localized and even enriched in dendritic spines, while other findings are less conclusive.

3.7.4 Mass spectrometry-based screening for interaction partners of VEGFR3

Since VEGFD preserves dendritic structure through its receptor VEGFR3 (Mauceri et al., 2011), discovering the interaction partners of VEGFR3 can provide valuable insights into the downstream signaling pathway of VEGFD. Co-immunoprecipitation followed by quantitative mass spectrometry analysis was performed to identify interaction partners of VEGFR3. However, due to the lack of antibodies that effectively label endogenous VEGFR3 (Appendix figure 7), I opted instead for rAAV-delivered overexpression of VEGFR3-GFP or GFP as a control in primary mouse hippocampal neurons and immunoprecipitated VEGFR3 with its interacting proteins using nanobodies against GFP (Figure 41; chapter 3.7.3). Immunoblotting confirmed GFP expression at 180 kDa and 27 kDa in GFP-immunoprecipitated samples of VEGFR3-GFP- and GFP-expressing neurons, corresponding to VEGFR3-GFP and GFP, respectively (Figure 41a). Interestingly, there was also a 27 kDa band in the GFP-labelled blots of VEGFR3-GFP suggesting that some of the GFP tag of VEGFR3 might have been cleaved. It might also be unspecific as it also appeared in the uninfected sample (Figure 41a; Figure 40). Membranes were reprobed with antibodies recognizing either the N-terminal or C-terminal ends of VEGFR3 (Figure 41a), indicating that both ends of VEGFR3 are expressed and precipitated. Even though several viral titers were tested, increasing VEGFR3-GFP expression proved challenging. As a result, the GFP control had substantially greater GFP expression, which could not fully be removed by reprobing (Figure 41a).

Subsequent mass spectrometry analysis of GFP-immunoprecipitated samples (Figure 41b) detected GFP expression in samples from both VEGFR3-GFP- and GFP-expressing neurons. Due to the low expression of VEGFR3-GFP, the detected peptides did not cover the entire amino acid sequence. However, the detected VEGFR3-peptides were evenly distributed along the VEGFR3 sequence and did not appear in samples of GFP-expressing neurons (Appendix figure 8).

Mass spectrometry identified eight proteins that were only present or highly enriched in immunoprecipitated samples of VEGFR3-GFP-expressing neurons compared to GFP-expressing neurons (Figure 41c). The majority is involved in RNA processing, transport or translation: neuro-oncological ventral antigen 2 (nova2), U2 small nuclear RNA auxiliary factor 1 (u2af1), small nuclear ribonucleoprotein Sm D3 (snrpd3), forty-two-three domain-containing protein 1 (fyttd1) and large ribosomal subunit protein P2 (rplp2); or play a role at lipid rafts of the endoplasmic reticulum (erlin2), at mitochondria (voltage-dependent anion-selective channel protein 3 (vdac3)), or in clathrin-dependent endocytosis (adaptor related protein complex 2 subunit mu 1 (ap2m1)) (Figure 41c) (Artero-Castro et al., 2011; Baek et al., 2019; Koscielny et al., 2018; Nian et al., 2024; Reina et al., 2021; Reina et al., 2016; Salib et al., 2024; Zhang et al., 2015).

Ap2m1 is a component of the adaptor protein complex 2 (AP2) (Koscielny et al., 2018) which is involved in the clathrin-dependent endocytosis of VEGFR2 (Ewan et al., 2006). Other AP2 components were also detected by mass spectrometry; these components, however, were not enriched in every independent culture preparation. Given that VEGFR3 is also known to undergo clathrin-dependent endocytosis (Simons, 2012; Wang et al., 2010), the identification of ap2m1 indicates that VEGFR3-immunoprecipitation was effective.

Erlin2 is crucial for the endoplasmic reticulum-associated degradation (ERAD) pathway and mutations of erlin2 are associated with motor neuron diseases (Al-Saif et al., 2012; Yıldırım et al., 2011). It was also shown to interact with microtubules in the context of cell cycle progression (Zhang et al., 2015), making it a promising target for VEGFD signaling. The mitochondrial porin vdac3 was also suggested to be associated with microtubular organization (Sampson et al., 2001).

The most promising candidate that the screening identified may be nova2. Through regulation of alternative splicing, nova2 is reported to play a role in dendrite arborization-associated cytoskeletal organization (Yuan et al., 2018b) as well as in axonal outgrowth and guidance (Leggere et al., 2016; Saito et al., 2016). Additionally, studies have shown that knockdown of nova2, akin to the knockdown of VEGFD (Mauceri et al., 2011; Maurer et al., 2020), leads to a simplification of the dendritic arbor while leaving spines unaffected (Yuan et al., 2018b). Furthermore, it has been reported that nova2, through alternative splicing, negatively regulates VEGFC-VEGFR3-induced MAPK/ERK signaling to restrict lymphatic endothelial cell fate specification (Baek et al., 2019).

There was also one candidate, heat shock protein family A member 8 (hspa8; also known as heat shock cognate protein 70 (hsc70))(Bonam et al., 2019), identified by mass spectrometry that almost but not fully met the criteria (criteria: ≥3 peptides, ≥ 1.5-fold enrichment or only detected in VEGFR3-GFP in all three sample preparations; hpsa8: 31 peptides, ≥1.5-fold enrichment in two

cultures, 1.2-fold enrichment in one sample preparation) that were chosen for the final list (Table 21). Interaction between hspa8 and VEGFR3 and VEGFR2 has been demonstrated before through co-immunoprecipitation in a human gastric adenocarcinoma cell line (Park et al., 2008). As part of the heat shock protein 70 (hsp70) family, hsp8a is involved in various cellular processes but most importantly, it plays a role in the uncoating of clathrin vesicles (Chappell et al., 1986) and regulation of dendritic spine elongation (Yagi et al., 2017), is localized to the plasma membrane through ezrin (Watanabe et al., 2009) and serves as a regulator of endothelial cell migration and tube formation via the VEGFA-PI3K/Akt pathway (Shiota et al., 2010).

In summary, several putative VEGFR3 interaction partners were discovered, with some being involved in the regulation of cytoskeletal and neuronal morphology.

a

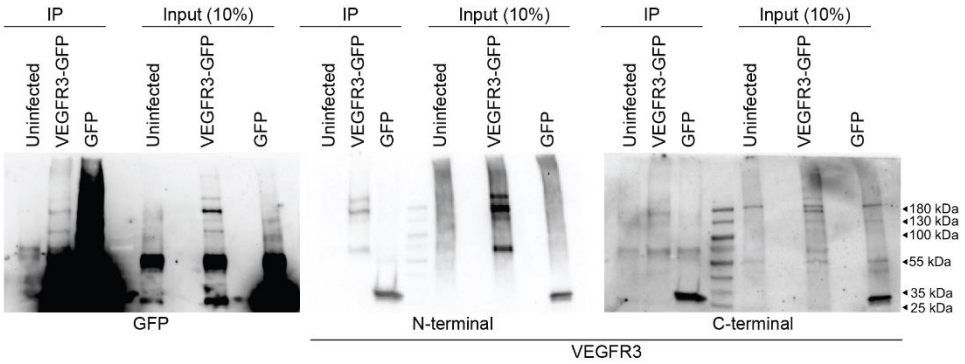

b

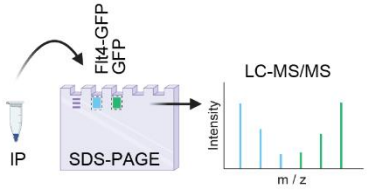

c

Biological category	Accession number	Protein name	Protein name (long)	Detected peptides number
Splicing	D3YVV7	nova2	alternative-splicing regulator 2	8
	Q9D883	u2af1	U2 small nuclear RNA auxiliary factor 1	6
	P62320	snrpd3	small nuclear ribonucleoprotein Sm D3	3
Nulcear mRNA export	Q91Z49	fyttd1	forty-two-three domain-containing protein 1	6
Ribosomal	P99027	rplp2	large ribosomal subunit protein P2	4
Lipid metabolism, ERAD	Q8BFZ9	erlin2	erlin2	3
Mitochondrial	Q60931	vdac3	voltage-dependent anion-selective channel protein 3	4
Endocytosis	P84091	ap2m1	adaptor related protein complex 2 subunit mu 1	15

Figure 41. Co-immunoprecipitation/mass spectrometry analysis of VEGFR3 interaction partners. ***a-b*** *GFP-immunoprecipitation (IP) followed by liquid chromatography mass spectrometry (LC-MS) analysis of lysates derived from cultured mouse hippocampal neurons at DIV 10 that were infected with rAAVs to drive neuron specific expression of VEGFR3-GFP or GFP.* ***a*** *Representative immunoblots of GFP and VEGFR3 (using antibodies to label VEGFR3 N-terminally (AF743; R&D) or C-terminally (sc-*

321; Santa Cruz)). ***b*** *Schema of experiment.* ***c*** *List of co-immunoprecipitated proteins of which ≥3 unique peptides were detected and which were ≥ 1.5-fold enriched or only detected in VEGFR3-GFP-infected neurons compared to GFP-infected neurons in all sample preparations. N = 3 independent culture preparations.*

3.8 Role of VEGFD signaling in Alzheimer's Disease

Alzheimer's Disease (AD) is characterized by neurodegeneration, but emerging studies indicate that dendritic aberrations may precede neurodegeneration (Adlard et al., 2002; Falke et al., 2003; Grutzendler et al., 2007; Moolman et al., 2004; Spires et al., 2004; Tsai et al., 2004). Furthermore, excitotoxicity, a process involving cell death resulting from the toxic effects of glutamate overload, is implicated in various neurodegenerative diseases, including AD (Bading, 2017).

Given that excitotoxicity has been demonstrated to decrease VEGFD levels, leading to dendrite loss (Mauceri et al., 2020; Schlüter et al., 2020), it raises the possibility that VEGFD may also be altered in AD. Indeed, Prof. Dr. Daniela Mauceri previously revealed diminished *VEGFD* mRNA levels in the hippocampus of an AD mouse model (6 months old APP/PS1) as well as in the hippocampi of human AD patients (data not shown, unpublished observation).

Recently, Dr. Elena Marcello demonstrated that cyclase-associated protein 2 (CAP2), through its association with cofilin, regulates actin dynamics and structural plasticity (Pelucchi et al., 2020). They found that this regulatory process is disrupted in AD due to reduced CAP2 expression and its diminished association with cofilin. Moreover, shRNA-mediated knockdown of CAP2 resulted in a simplified dendritic arbor (Pelucchi et al., 2020). Intriguingly, *VEGFD* and *VEGFR3* mRNA levels were also found to be reduced after knockdown of CAP2 and supplementation of rVEGFD rescued the shCAP2-induced simplification of dendrite morphology (data not shown, unpublished observation). These findings hint at a potential connection between VEGFD and CAP2 signaling pathways, which might play a role in AD.

During my thesis, I had the opportunity to be part of a collaborative project with Dr. Elena Marcello, supported by the Alzheimer Forschung Initiative. In this project, I characterized expression of VEGFR3 and ezrin on protein level in primary hippocampal cultures treated with β-amyloid peptide and in the brains of human AD patients. Furthermore, I generated rAAVs to achieve gain- or loss-of-function of proteins involved in VEGFD and CAP2 signaling in cultured hippocampal neurons to uncover how modulation of one signaling pathway affects the expression of components of the other pathway. As this was a side project, it will not be further presented and discussed here. The data can be found in the Appendix (Appendix figure 11 - Appendix figure 15).

Chapter 4. Discussion

4.1 VEGFD governs the balance between structural stability and plasticity of dendrites

Numerous studies have focused on and uncovered the mechanisms behind the development of the dendritic arbor. After the formation of the overall dendritic arbor at the onset of adolescence in mice (P21-P60), dendrites are increasingly stabilized to preserve the established structure (Koleske, 2013). This is crucial to maintain proper neuronal wiring and cognitive function (Koleske, 2013). However, a certain level of dendritic structural plasticity persists in adult neurons allowing for modifications in response to diverse stimuli and experiences (Koleske, 2013; Simonetti et al., 2021; Tavosanis, 2012; Trabalza et al., 2012). Recent research has revealed that the preservation of the adult dendritic arbor depends on VEGFD expression and that absence of VEGFD leads to dendrite loss (Hemstedt et al., 2017; Litke et al., 2018; Mauceri et al., 2011; Mauceri et al., 2015; Maurer et al., 2020). This study revealed that VEGFD does not only protect dendrite morphology from simplification but also prevents structural plasticity.

4.1.1 VEGFD slows down dendritogenesis

It was shown previously that VEGFD expression in hippocampal neurons is low throughout neural development but rises with age both *in vitro* and *in vivo* (Mauceri et al., 2011). This suggests that VEGFD expression may not be essential for neural development. This is also reflected in the finding that knockdown of VEGFD impairs neuronal network activity only after DIV 10, when neurons start to mature and increase VEGFD expression (Mauceri et al., 2011). It is highly probable that the upregulation of VEGFD expression is associated with the formation of synaptic connections due to the increased need to maintain recently established connections.

Prof. Dr. Daniela Mauceri discovered that hippocampal neurons formed less complex dendritic arbors when supplemented with rVEGFD throughout their development when endogenous VEGFD is almost absent. This discovery indicated that VEGFD disrupts the development of dendrites; however, the mechanism underlying this interference remained unclear. It is uncertain whether dendrites undergo normal growth but are destabilized later on at a specific age, exhibit slower or later growth, or possibly undergo a cyclical pattern of growth and destabilization.

By employing time-lapse tracking of neurites, I demonstrated that total neurite length continues to increase in the presence of rVEGFD in the culture medium. However, the extent of growth is noticeably smaller compared to control neurons. In sum, the findings show that rVEGFD-treatment causes neurons to lag behind in their neurite development. It should be noted, however, that this analysis could not differentiate between axons and dendrites. Therefore, these results might even underestimate the effect that VEGFD has on dendrite development as Luck et al. (2019) previously revealed that administration of rVEGFD in developing cultured hippocampal neurons causes an increase in the length of axons.

Interestingly, Mauceri et al. (2011) demonstrated a constant VEGFD expression in the mouse cortex throughout its lifetime. However, it is imperative to acknowledge that the involvement of brain endothelial cells could mask the precise neuronal expression of VEGFD when analyzing entire brain lysates. As the effect of VEGFD on developmental dendritogenesis has only been shown in hippocampal neurons, it is unknown if it might have a comparable role in the cortex. Nevertheless, given the pivotal role of VEGFD in dendritic maintenance in the cortex (Mauceri et al., 2020), such a hypothesis does not appear implausible.

Differences in the expression pattern may be attributed to a potentially different development of circuits in the cortex and hippocampus, resulting in diverse requirements for dendrite maintenance and plasticity. It is conceivable that the necessity for dendritic maintenance could manifest at an earlier stage, with VEGFD expression being low during embryonic cortical development and potentially reaching a plateau at birth. As VEGFD expression was assessed only from P1 onward, exploring VEGFD prenatal expression could provide valuable insights.

4.1.2 VEGFD blocks activity-dependent structural plasticity

This study shows that not only developmental structural plasticity requires low VEGFD levels but also synaptic activity-induced dendrite remodeling. This was also additionally proven *in vivo* in the mouse hippocampus by Prof. Dr. Daniela Mauceri and Ann-Kristin Kenkel.

It was unexpected that structural plasticity requires a reduction in VEGFD expression, as VEGFD expression depends on basal levels of synaptic activity and is crucial for maintaining dendritic shape in adult neurons (Litke et al., 2018; Mauceri et al., 2011). Moreover, the activation of extrasynaptic NMDARs by elevated glutamate levels, a characteristic step in many neurodegenerative conditions, causes a fast drop in VEGFD resulting in dendritic atrophy (Mauceri et al., 2020; Schlüter et al., 2020). At first glance, it seems paradoxical that a reduction in VEGFD expression is both damaging in degenerative conditions and necessary for physiological dendrite growth.

However, there is a difference in the kinetics of VEGFD reduction after a toxic insult or synaptic activity. Basal synaptic activity is necessary to maintain VEGFD expression and one to two hours of Bic treatment does not lead to a reduction in VEGFD expression (Mauceri et al., 2011). Only after sustained enhanced synaptic activity, VEGFD expression was found to be gradually reduced.

NMDA treatments, on the other side, activate extrasynaptic NMDARs causing a toxic insult and VEGFD is dramatically reduced after 10 min and almost completely shutdown after only 30 minutes (Mauceri et al., 2020). It is well known that synaptic and extrasynaptic NMDAR signaling activated by Bic or NMDA treatment, respectively induce opposing pathways (Hagenston et al., 2011). This provides an explanation for the different kinetics of VEGFD reduction and the associated differences in biological outcomes. It is also worth noting that synaptic or extrasynaptic pathways exert differential effects on the cytoskeleton, promoting either dendritic growth or atrophy (Gonzalez et al., 2016; Koleske, 2013; Van Aelst et al., 2004).

It is not unusual that neuronal morphology is regulated in different directions by the same molecule. The RNA-binding protein pumilio, for example, exerts a similar dualistic behavior. Its absence is associated with dendritic growth and branching in developing neurons but in mature neurons leads to a reduction in the number of dendritic spines while increasing the number of elongated dendritic filopodia (Vessey et al., 2010). Other examples include semaphorin 3A, acting as a chemoattractant for dendrites but a chemorepellent for axons (Polleux et al., 2000), and VEGFA whose inactivation results in either decreased or increased spine density in developing or adult olfactory bulb granule cells, respectively (Licht et al., 2011). These instances demonstrate the intricate and multifaceted nature of the regulatory mechanisms governing neuronal structure.

In conclusion, it seems that VEGFD serves as a regulatory constraint on dendritic morphological alterations regardless of whether these involve loss or growth of dendrites. In the context of physiologically regulated morphological changes, this constraint must be removed gradually and in a controlled manner, whereas sudden removal due to toxic stimuli causes dendritic loss.

Although diminished after completion of neuronal development, a certain degree of structural plasticity remains indispensable for fundamental brain functions, including learning, memory, and the capacity to adapt to dynamic environmental, stress-related, or injury-induced challenges (Simonetti et al., 2021; Tavosanis, 2012; Trabalza et al., 2012). However, it is imperative that such plasticity occurs in a regulated manner to prevent adverse effects on existing neural structures. Maladaptive plasticity and aberrant morphology represent pathological conditions. For instance, uncontrolled dendritic sprouting resulting from deregulated neuronal activity is a hallmark of

epilepsy (Ribak et al., 2002), while maladaptive dendrite remodeling has been associated with neuropathic pain and addiction (Ehlinger et al., 2012; Lu et al., 2012; Metz et al., 2009).

Hence, it is imperative for neurons to establish and maintain an optimal morphology, while also possessing the capacity to adjust it in a controlled manner, when necessary, without exceeding thresholds. This delicate balance between structural stability and plasticity is crucial, as deviations from this equilibrium are associated with various neurological disorders. Previous research revealed the importance of VEGFD in sustaining established dendritic structure (Litke et al., 2018; Mauceri et al., 2020; Mauceri et al., 2011; Mauceri et al., 2015). This current study demonstrated that structural plasticity necessitates a downregulation of VEGFD as well. Consequently, this study proposes that VEGFD is a key molecule that governs the equilibrium between structural maintenance and plasticity.

Supplementation of VEGFD in neurodegeneration has emerged as a promising therapeutic target (Mauceri et al., 2020; Schlüter et al., 2020). Its application, facilitated by its nature as a secreted factor, through means such as nasal spray or intravitreal injections, offers practical advantages. However, the findings of this study raise concerns regarding potential long-term harm associated with VEGFD application, given that failure to downregulate VEGFD interferes with structural plasticity. At the same time, this prompts future investigations into whether pathologies characterized by maladaptive plasticity exhibit diminished levels of VEGFD, and whether the application of VEGFD could potentially serve as a beneficial approach for controlling maladaptive plasticity in neurological disorders.

4.2 VEGFD has a homeostatic effect on activity-induced dendrite dynamics

The mechanism behind how VEGFD prevents activity-dependent dendrite remodeling has so far remained elusive. There is a possibility that VEGFD restricts dendritic growth or facilitates the destabilization of growing dendrites. To address this question, I employed time-lapse imaging to observe dendrite dynamics in neurons subjected to Bic-induced synaptic activity and how this is impacted by rVEGFD supplementation.

This revealed that synaptic activity primarily stimulates the formation of new dendrites and exhibited a tendency toward their stabilization. The co-administration of rVEGFD did not impede the activity-induced emergence of new dendrites; rather, it manifested a trend toward increased elimination of activity-induced new dendrites. Nevertheless, it is essential to note that this

destabilization effect lacked statistical significance, potentially attributed to the generally low count of new dendrites, with only a fraction undergoing elimination, resulting in higher variability.

Unexpectedly, when rVEGFD is co-applied, the most significant outcome is a reduction in dendrite elongation, surpassing both untreated neurons and those treated solely with rVEGFD under basal conditions. This observation is surprising, considering that treating with rVEGFD alone does not lead to discernible changes in dendrite dynamics compared to control neurons. It is striking that the impact of rVEGFD manifests only in conjunction with synaptic activity resulting in reduced dendrite elongation, which is not elicited by rVEGFD or synaptic activity in isolation. It is possible that synaptic activity-induced pathways may interplay with VEGFD signaling, causing different outcomes, given that signaling within the VEGFD family is commonly controlled by numerous co-receptors, accessory proteins, or alternative signaling pathways (Secker et al., 2021; Simons et al., 2016).

In conclusion, these findings suggest that VEGFD hinders activity-dependent dendrite remodeling by exerting homeostatic control over dendrite dynamics, achieved through inhibiting dendrite elongation and destabilizing newly formed dendrites. Essentially, VEGFD appears to preserve the neurons' original morphological state.

The extent to which specific parameters in dendrite dynamics, such as dendrite elongation and elimination, contribute to alterations in total dendrite length and their modulation by synaptic activity and rVEGFD remains unexplored and could be elucidated through a mathematical model. A collaboration with Prof. Dr. Gillian Queisser and Madison Shoraka aimed to address these questions mathematically. However, constraints in sample size limited the model to descriptive representations for each condition. These models revealed a pattern of continuous growth of total dendrite length induced by synaptic activity, whereas neurons treated with rVEGFD displayed distinctive phases of both growth, reduction and stabilization.

It would be interesting to explore whether VEGFD influences developmental dendrite dynamics in a similar manner. Despite conducting time-lapse imaging of neurite development, the experiment measured only the total neurite length of neuronal populations and did not provide insights into rVEGFD's impact on individual neurite dynamics during development. Tracking individual neurites or dendrites over time necessitates clear visual separation of branches, achievable through sparse labeling of neurons. However, transfection-induced labeling is restricted to adult neurons. Although attempts were made with hippocampal cultures from Thy1-GFP mice, in which neurons exhibit sparse GFP labeling (Feng et al., 2000), GFP expression did not manifest until DIV 8. Exploring electroporation on dissociated primary neurons before plating could be a promising approach for future experiments.

4.3 VEGFD acts on the actin cell cortex and microtubules

This section of the thesis revealed that VEGFD influences cortical actin and microtubules (MTs) and represents the first characterization of the impact of VEGFD on cytoskeletal elements in neurons.

In line with a previous study demonstrating that VEGFD enhances membrane stiffness in an adenocarcinoma cell line (Wang et al., 2014), AFM recordings in this study revealed that VEGFD similarly elevates cell membrane stiffness in neurons. Cell shape and elasticity are defined by membrane tension, a phenomenon regulated by the actin network beneath the cell membrane, commonly known as the actin cell cortex, and its attachment to the cell membrane (Mikhaylova et al., 2020; Salbreux et al., 2012). Hence, this finding suggests that VEGFD influences cortical actin. Additionally, phospho-proteomic screening data corroborated this by demonstrating modulation of proteins associated with cortical actin.

However, due to technical limitations, these AFM recordings were confined to the soma and proximal dendrites. Considering the distinct subcellular organization of cortical actin, leading to a generally higher membrane rigidity in dendrites compared to the soma (Zhang et al., 2017), the possibility of a divergent effect of VEGFD on dendrites is conceivable. The initiation of de novo dendritic filopodia, for instance, may necessitate a localized destabilization of membrane tension (Bisaria et al., 2020; Welf et al., 2020). This raises the question about potential local effects of VEGFD on membrane tension, particularly considering VEGFD's inability to prevent the activity-induced formation of new dendrites.

Nevertheless, dendrites harbor diverse actin populations with distinct functions, with cortical actin representing just one component (Konietzny et al., 2017). F-actin patches play a crucial role in triggering the initiation of de novo dendritic filopodia, achieved through the polymerization of F-actin, which generates a force to propel the membrane forward (Kessels et al., 2011; Korobova et al., 2010; Sainath et al., 2015; Svitkina, 2018). It is conceivable that F-actin patches may not be affected by VEGFD, considering the observed inability of VEGFD to hinder the activity-induced formation of new dendrites.

Moreover, I found that actin dynamics in spines were not impacted by acute 5-30 min treatments of rVEGFD. This observation aligns with prior studies demonstrating that VEGFD does not exert any influence on the structure or density of dendritic spines (Mauceri et al., 2011; Maurer et al., 2020).

In sum, these findings indicate that VEGFD signaling-induced modulation of the actin cytoskeleton may be specific for the actin cell cortex.

Nonetheless, it cannot be excluded that the increase in membrane stiffness is due to other reasons, as for example the formation of stable MT bundles may also contribute to higher membrane stiffness in neurons (Spedden et al., 2012). I demonstrated that acute treatment with rVEGFD increases the lifespan of EB3 comets while decreasing the speed of MT growth. A longer lifetime indicates that MT development is not constantly interrupted or dismantled (catastrophe), reducing MT dynamics and increasing MT stability. Neurite remodeling, including neurite loss, is associated with increased MT dynamics (Kleele et al., 2014; Rolls et al., 2021; Sweet et al., 2011; Tao et al., 2016). As a result, one of the mechanisms that contribute to VEGFD-mediated dendritic maintenance might be VEGFD-induced MT stabilization.

The present findings are derived from the acute administration of rVEGFD. Given the continuous and dynamic nature of cytoskeletal remodeling (Koleske, 2013) and the aim to discern effects specific for VEGFD signaling, it was imperative to assess the immediate impact of VEGFD. However, considering the possibility of time-dependent changes, particularly given the considerably slower pace of dendritic dynamics compared to the cytoskeleton (Koleske, 2013) it becomes essential to acknowledge potential temporal variations.. Furthermore, my observations indicate a temporal variation in the rVEGFD-induced modulation of MTs with prolonged treatment duration. Previous studies have also reported time-dependent alterations in the impact of Bic on MT dynamics (Ghiretti et al., 2016; Kapitein et al., 2011b). Consequently, future investigations should explore the prolonged influence of VEGFD on the underlying cytoskeleton across extended time intervals.

Furthermore, it is essential to acknowledge that the untreated control, strictly speaking, is not devoid of VEGFD, as healthy adult neurons naturally express and secrete VEGFD to uphold their morphology. Consequently, even in control neurons, VEGFD exerts an influence on the cytoskeleton. Therefore, investigating the impact of VEGFD level reduction on the cytoskeleton and elucidating the effects of VEGFD supplementation on these neurons would be of particular interest.

It is also noteworthy that the observed impacts of acute rVEGFD on the cytoskeleton did not cause observable effects on the total dendrite length or dendrite dynamics. This raises the possibility that these effects might instead render dendrites more resistant to inputs that typically induce changes in dendrite morphology. Understanding the role of these observed cytoskeletal effects in VEGFD-mediated dendrite maintenance, and whether VEGFD modulates the cytoskeleton differently in the context of remodeling inputs, presents an intriguing avenue for exploration. A similar consideration applies to spines, as VEGFD itself did not influence actin spine dynamics under baseline conditions. However, it remains to be explored whether VEGFD may play a role in influencing the activity-induced remodeling of spines.

Here, experiments were conducted in parallel in which neurons were co-treated acutely with Bic and rVEGFD providing initial insights into the potential interactions between VEGFD and Bic-induced dynamic changes in the dendritic cytoskeleton.

AFM recordings revealed that membrane stiffness is still increased when rVEGFD is applied in conjunction with Bic, while Bic treatment alone did not exhibit any impact on membrane stiffness. Given that the elongation or shortening of neurites and non-neuronal filopodia is linked to cortical actin and membrane tension (Ahmad et al., 2000; Bornschlögl et al., 2013; Lan et al., 2008; Sheetz et al., 1996; Spedden et al., 2012) and considering that VEGFD inhibits activity-dependent dendrite remodeling primarily by reducing dendrite elongations, this finding suggests that VEGFD-induced reduction in dendrite elongation may be mediated through VEGFD's impact on cortical actin.

In dendrites, Lavoie-Cardinal et al. (2020) observed that actin ring structures have the potential to transition into longitudinal actin fibers in response to synaptic activity and calcium signaling. Although the precise function of these structures remains unclear, there is speculation that they may be involved in the transport of proteins relevant to plasticity (Lavoie-Cardinal et al., 2020). It would be intriguing to investigate whether VEGFD has any influence on this phenomenon.

Similarly, I investigated the impact of acute Bic treatment on MT dynamics and its modulation when co-administered with rVEGFD. Bic exhibited partially comparable stabilizing effects on MT dynamics as rVEGFD, albeit primarily manifesting at a later duration of treatment. This finding aligns with existing literature suggesting that Bic induces MT stabilization to facilitate MT-based transport (Ghiretti et al., 2016; Kapitein et al., 2011b; Nirschl et al., 2017). Morphological alterations in neurites are, however, also linked to enhanced MT dynamics (Kleele et al., 2014; Rolls et al., 2021; Sweet et al., 2011; Tao et al., 2016). For instance, microtubules play a pivotal role in generating a mechanical force through polymerization, thereby contributing to the growth and stabilization of newly formed or elongating branches (Georges et al., 2008; Kapitein et al., 2015; Poulain et al., 2010; Roossien et al., 2014).

Interestingly, certain stabilizing effects of Bic on MT dynamics were negated in the presence of co-applied rVEGFD. For instance, while Bic increased MT comet lifetime at 20 min, this effect was not observed in the concurrent presence of rVEGFD. This observation leads to the hypothesis that activity-induced dendrite remodeling might necessitate a combination of both MT stabilization and enhanced dynamics, depending on timing and localization. Moreover, it suggests that the presence of VEGFD may disrupt this delicate balance in the regulation of MT dynamics during dendrite remodeling.

All of these findings underscore the importance of meticulously unraveling the long-term effects and interactions between signals that induce dendrite remodeling and VEGFD in the modulation of the cytoskeleton. Furthermore, it is crucial to consider local effects, for example at branching points.

Moreover, it is essential to acknowledge that these experiments were conducted on neurons subjected to Bic treatment for less than 20 min. Notably, Bic-induced reduction in VEGFD expression occurs only after 4 h (Figure 8)(Mauceri et al., 2020; Mauceri et al., 2011). Exploring the impact of Bic on the cytoskeleton under conditions of reduced VEGFD expression and understanding how preventing VEGFD downregulation might influence cytoskeletal dynamics would be intriguing avenues for further investigation.

4.4 Phospho Y478 ezrin plays a role in VEGFD signaling

4.4.1 VEGFD dephosphorylates Y478 ezrin via STEP phosphatase

The phospho-screening revealed a potential reduction in phospho Y478 ezrin in response to VEGFD signaling in neurons. I verified the VEGFD-induced dephosphorylation of Y478 ezrin through Western blotting and PLA. Only acute 2 h treatments of rVEGFD but not overexpression impacted phospho Y478 ezrin, suggesting a potentially transient nature of this effect. Conversely, I observed a trend toward elevated phosphorylation of Y478 ezrin in the spines of rat hippocampal neurons treated for 30 min with rVEGFD, as determined by protein fractionation. While acknowledging the possibility of species-specific differences, this finding implies that VEGFD signaling may exert a temporal and location-dependent influence on ezrin phosphorylation, particularly considering that localization of ezrin determines formation of cellular protrusions (Welf et al., 2020). Additionally, it is important to note that ezrin is also highly expressed in glial cells, especially astrocytes (Derouiche et al., 2019). Since the neuronal cultures used were not entirely devoid of glial cells, potential masking of effects through glia cells cannot be ruled out. Therefore, future experiments should further investigate the local and neuron-specific effects of VEGFD signaling on ezrin.

The regulation of Y478 ezrin in neurons was previously unexplored. Previous studies in human keratinocytes, mouse fibroblasts, and HEK 293 cells have identified Src as the kinase responsible for Y478 ezrin phosphorylation (Chan et al., 2021; Heiska et al., 2005; Heiska et al., 2011). However, utilizing a selective inhibitor of Src family kinases, I demonstrated that this may not be the case in neurons. Additionally, the phospho-screening results indicated that the phosphorylation of Src at various sites, including its activation site Y418 (or Y416 in chicken) (Salter et al., 2004), was not impacted by rVEGFD treatment. Instead, I identified STEP phosphatase as a regulator of phospho

Y478 ezrin using pharmacological and genetic tools. Notably, short-term modulation of up to 24 h of STEP activity or expression led to a modulation of ezrin phosphorylation, while constitutive overexpression or knockdown did not. This discrepancy could be attributed to the potentially transient effects or the possibility that long-term modulation of STEP might have off-target negative effects on neuronal health.

Furthermore, I demonstrated that acute treatment with rVEGFD or overexpression of VEGFD induces the dephosphorylation of S221 STEP, indicative of its activation (Castonguay et al., 2018; Paul et al., 2000). Notably, this effect was not observed when VEGFD overexpression was limited to 24 h using an activity-dependent promoter. However, it is essential to consider that Bic treatment, employed to activate the promoter, might have influenced STEP and obscured potential effects of VEGFD, as Bic is known to induce ubiquitination and proteasomal degradation of STEP (Xu et al., 2018).

These findings indicate that VEGFD signaling may induce the dephosphorylation of Y478 ezrin via activation of STEP phosphatase.

The specific enzymes regulated by VEGFD that induce the dephosphorylation of STEP remain to be elucidated. The phospho-screening identified a VEGFD-induced reduction in the phosphorylation of protein kinase A (PKA), suggesting lower PKA activity (Cheng et al., 1998). Considering that PKA is a known regulator of pS221 STEP (Paul et al., 2000), PKA may represent one of the links between the VEGFD signaling cascade and STEP. Additionally, the calcineurin-dopamine/adenosine-3',5'-monophosphate-regulated phosphoprotein 32 (DARPP-32)-protein phosphatase 1 (PP1) pathway also regulates pS221 STEP (Fitzpatrick et al., 2011; Paul et al., 2003; Snyder et al., 2005; Valjent et al., 2005). Subsequent studies should explore the involvement of these enzymes in the VEGFD signaling pathway.

4.4.2 Phosphorylation of Y478 ezrin plays a role in VEGFD-mediated blocking of activity-dependent dendrite remodeling

I showed that ezrin mRNA and protein expression is predominant during development in the hippocampus both *in vitro* and *in vivo*, in line with its role as a mediator of developmental neuritogenesis, dendritic filopodia formation and axonal growth (Antoine-Bertrand et al., 2011; Furutani et al., 2007; Matsumoto et al., 2014). Phosphorylation at Y478, on the other hand, remained stable throughout development or even exhibited an increase in adulthood within the mouse hippocampus *in vitro* and *in vivo*, suggesting a potential role of Y478 phosphorylation in adult neurons. Conversely, ezrin expression and phosphorylation in the mouse cortex remained stable

during development or displayed a trend toward an increase in adult mice. It is important to note that some of the *in vivo* data presented here are preliminary and to be cautious about the potential contribution of ezrin expression in other cell types, such as glia cells (Derouiche et al., 2019).

Consistent with my observation of a predominantly developmental expression pattern of ezrin and its role as a mediator of developmental neuritogenesis, dendritic filopodia formation, axonal growth and urokinase-type plasminogen activator-induced dendrite branching (Antoine-Bertrand et al., 2011; Furutani et al., 2007; Matsumoto et al., 2014; Merino et al., 2018), I have demonstrated that ezrin promotes an increase in dendrite length and complexity in hippocampal neurons. This was also the case, when phospho-deficient mutant Y478F ezrin was overexpressed. However, the overexpression of Y478F ezrin, as opposed to WT ezrin, prevented activity-dependent dendrite remodeling, indicating that the phosphorylation state of Y478F ezrin renders neurons resistant to activity-dependent dendritogenesis. In addition, this discovery was corroborated *in vivo* within the mouse hippocampus as shown by Prof. Dr. Daniela Mauceri and Ann-Kristin Kenkel. This observation aligns with the reported impact of Y478F ezrin on impeding the development of actin-rich protrusions in epithelial and endothelial cells during tumor-induced invasion, angiogenesis, and lymphangiogenesis (Ghaffari et al., 2014; Heiska et al., 2011; Mak et al., 2012). However, a recent observation has reported a contrary finding, indicating that keratinocytes expressing Y478F exhibited an increase in myosin light chain bundles, suggesting heightened cell protrusions (Chan et al., 2021).

I discovered that Y478F ezrin interferes with the activity-induced increase in the number of dendrites by intensifying the elimination of newly formed dendrites similar to VEGFD. These findings suggest that a reduction in the phosphorylation of Y478 ezrin through VEGFD signaling may constitute one of the mechanisms by which VEGFD signaling maintains dendritic morphology in the context of activity-dependent dendritogenesis. Nonetheless, unlike VEGFD, Y478F ezrin did not decrease the elongation of existing dendrites in response to persistent synaptic activity. This suggests that other proteins may be implicated in the VEGFD stabilization signal. It is essential to note that the overexpression of both WT and Y478F ezrin significantly enhances dendrite arborization even in the absence of remodeling-inducing signals. Consequently, certain aspects of dendritic dynamics, such as dendrite elongation and formation, may have achieved a plateau, preventing neurons from increasing them further.

The mechanism by which the phosphorylation of Y478 ezrin may confer instability to newly formed dendrites remains unknown. As a membrane-actin-linker, ezrin regulates the attachment of cortical actin to the plasma membrane and membrane tension (Rouven Brückner et al., 2015). Recent studies suggest that the development of cellular protrusions may require the localized separation of

cortical actin from the plasma membrane to alleviate tension, possibly achieved through the localized detachment of ezrin (Welf et al., 2020). Additionally, ezrin may act as a docking site for other cytoskeleton-associated proteins or signaling molecules influencing the cytoskeleton (Arpin et al., 2011; Mak et al., 2012). For example, pY478 ezrin is implicated in the regulation of mammalian target of rapamycin (mTOR) targets 4E-BP1 and p70S6K (Heiska et al., 2011), which contribute to dendrite arborization through translational control (Jaworski et al., 2005). PY478 ezrin and Fes kinase have been shown to interact, altering the actin cytoskeleton at cell-cell interactions to initiate cell scattering (Naba et al., 2008). Fes contributes to neurite outgrowth in PC12 cells (Laurent et al., 2004b; Shibata et al., 2003), phosphorylates actin-regulatory proteins (Greer, 2002), and has been shown to interact with and modulate MT dynamics (Laurent et al., 2004a; Takahashi et al., 2003). Consequently, the mechanisms by which Y478 ezrin modulates cytoskeletal elements to mediate structural stability in neurons remain to be elucidated.

In parallel to Y478F, I employed another mutant form of ezrin that is phospho-deficient at another site (Y146F), which is unaffected by VEGFD signaling based on the phospho-screening. In contrast to neurons expressing WT or Y478F, those expressing Y146F did not display an augmented total dendrite length or complexity. Moreover, synaptic activity failed to induce dendrite remodeling in Y146F-expressing neurons. However, overexpression of the double-mutant Y146F-Y478F ezrin did lead to dendrite remodeling per se, with no additional enhancement upon synaptic activity, potentially due to physiological constraints similar to those expressing WT ezrin. It is intriguing that the two phospho-sites, when acting individually, yield different effects, yet their combination leads to a completely distinct outcome. Particularly interesting is the observation that while Y478F prevents activity-dependent dendrite remodeling, this effect is mitigated when Y146 remains unphosphorylatable. Notably, this is not the first instance reported where phosphorylation at one site in ezrin affects another. For example, Srivastava et al. (2005) found that binding of Src to phosphorylate Y146 depends on the phosphorylation of Y190 within ezrin's FERM domain. Moreover, Y146 remains unphosphorylated when ezrin is in its closed conformation, which is partially dependent on T567 phosphorylation (Srivastava et al., 2005). The interplay between the phosphorylation of Y146 and Y478 is yet to be elucidated. Despite being at opposite ends of ezrin, in its closed conformation, Y146 and Y478 are positioned in close proximity to each other (Fehon et al., 2010), raising the possibility of potential interference. Furthermore, both phosphorylation sites could potentially initiate downstream effects that interfere with or counteract each other. Phosphorylation of Y146 in ezrin within epithelial cells facilitates interaction with various proteins, including Src kinases and EGFR, thereby enabling pivotal cellular processes such as cell proliferation, F-actin assembly, focal adhesion assembly, cell spreading, and tubule formation (Saygideğer-Kont et

al., 2016; Srivastava et al., 2005). It remains speculative whether any of these mechanisms could underlie the interference of Y146F with Y478F-induced blocking of activity-dependent dendrite remodeling. These findings highlight the complexity involved in regulating ezrin function, emphasizing the importance of considering the combined effects of phosphorylation at various sites. Consequently, it becomes imperative to explore additional phospho-sites of ezrin and their respective functions, particularly concerning their roles in VEGFD signaling.

Since Y478F impedes activity-dependent dendrite remodeling, it raises the question how this phospho-site might be influenced by neuronal activity. Intriguingly, I observed a more pronounced reduction in ezrin phosphorylation after a 2 h Bic treatment, and this reduction persisted even when co-applied with rVEGFD. Corresponding with diminished pY478 ezrin, the pS221 STEP was also reduced, indicative of active STEP (Paul et al., 2003). This suggests that synaptic activity induces dephosphorylation of ezrin via STEP. This finding seems paradoxical, particularly in light of my earlier discovery that the dephosphorylation of Y478 ezrin is involved in mediating the VEGFD-induced blockade of activity-dependent dendrite remodeling.

However, as discussed above, the potential contribution of ezrin expression in other cell types, such as glia cells (Derouiche et al., 2019), might distort the picture. Potentially distinct kinetics, timing, and localization of ezrin dephosphorylation induced by synaptic activity or VEGFD treatment may also result in diverse biological outcomes. For instance, I observed that a 30 min exposure to Bic/4AP in rat hippocampal cells led to a downregulation of pY478 ezrin, specifically in spines, suggesting that synaptic activity might induce a more rapid and initially spine-specific dephosphorylation. Conversely, a 30 min treatment with rVEGFD in the same cell type did not affect pY478 ezrin or even showed a tendency toward increased phosphorylation at spines. Furthermore, other phospho-sites in ezrin might be regulated differently by synaptic activity or VEGFD, potentially leading to distinct outcomes, as seen in the case of the Y146F-Y478F double-mutant, even if both synaptic activity and VEGFD induce dephosphorylation of Y478 ezrin. Temporal and subcellular monitoring of the effects of VEGFD and/or synaptic activity on various phosphorylation sites of ezrin, along with its phosphatase STEP, would contribute to a more comprehensive understanding of the underlying mechanisms.

Given that these findings suggest that ezrin serves as one of the downstream mediators in preventing VEGFD-induced activity-dependent dendrite remodeling, it would be intriguing to investigate in the future whether ezrin is also implicated in VEGFD-dependent maintenance of dendrites in baseline conditions in adult neurons. In my preliminary data, I observed that the activation of extrasynaptic NMDARs, leading to a rapid decrease in VEGFD levels and dendritic

atrophy (Mauceri et al., 2020; Schlüter et al., 2020), might potentially result in an upregulation of ezrin expression, though this requires further investigation.

4.4.3 Phosphorylation of Y478 ezrin plays a role in spine morphology

Ezrin is also present in spines and has been identified as a contributor to the formation of dendritic filopodia in cultured hippocampal neurons (Furutani et al., 2007). Furutani et al. (2007) demonstrated that a constitutively active form of ezrin, one that continuously links actin and the plasma membrane, induces the generation of dendritic filopodia. In alignment with this, my observations revealed that the overexpression of ezrin led to an increase in spine density. This phenomenon was also observed when Y146F was overexpressed. However, in contrast to the findings of Furutani et al. (2007) my results indicated that the overexpression of WT ezrin induced the formation of more mushroom-like spines, suggesting potential spine maturation and stability (Bourne et al., 2007; Runge et al., 2020). WT ezrin exists in both its cytosolic closed conformation and active membrane-bound conformation (Welf et al., 2020), implying that spine maturation may necessitate a balanced and dynamic presence of ezrin at the membrane.

On the other hand, Y478F overexpression did not increase the number of spines but instead facilitated the generation of immature filopodia. Furutani et al. (2007) proposed that membrane-bound active ezrin interacts with the adhesion molecule telencephalin to induce filopodia formation and elongation, which in turn decelerates spine maturation. Spine maturation initiates when ezrin is predominantly inactive and ceases its interaction with the plasma membrane and telencephalin (Furutani et al., 2007). This raises the possibility that the phosphorylation of Y478 ezrin may also regulate the binding of ezrin to telencephalin. Additionally, my findings indicated that both WT and Y478F ezrin overexpression resulted in reduced expression of CAP2 and cofilin, two proteins involved in the actin dynamics of spines (Pelucchi et al., 2020) (Appendix figure 15), suggesting a potential involvement of ezrin in modulating spine structure through its impact on these proteins.

4.5 C-Raf modulates dendrite morphology

The phospho-screening revealed that VEGFD signaling in neurons leads to a potential reduction of phospho S43 c-Raf. I demonstrated predominant c-Raf expression in developing neurons, aligning with its recognized developmental function in various cell types (Magariños et al., 2011; Sanz et al., 1999). This implies a developmental role for c-Raf in neurons as well. In fact, overexpression of WT c-Raf in adult neurons resulted in dendritic remodeling, indicating a potential involvement in

developmental dendritogenesis. Intriguingly, this effect was absent when either the phospho-deficient S43A or phospho-mimicking S43D mutant was expressed, implying that the phosphorylation state at S43 may contribute to c-Raf's function as a dendritogenic inducer. However, the precise phosphorylation state required remains unclear, raising the possibility of a dynamic regulation or a specific threshold of phosphorylation necessary for c-Raf function.

Phosphorylation at S43, regulated by PKA, is conventionally considered a regulatory site for the inhibition of c-Raf (Dumaz et al., 2003; Ramstad et al., 2000; Sidovar et al., 2000). This phosphorylation, through steric hindrance, is thought to prevent c-Raf association with Ras. However, the role of S43 in c-Raf inactivation is controversial, as studies have shown that the unphosphorylatable mutant S43A c-Raf can still be inhibited by PKA, indicating that dephosphorylation at this site alone is insufficient for c-Raf inactivation (Dhillon et al., 2002; Sidovar et al., 2000). Moreover, in the presence of mitogenic factors, c-Raf phosphorylated on S43 can bind Ras, suggesting that this site might not regulate c-Raf activity in such circumstances (Dhillon et al., 2002). The complexity of c-Raf regulation is further highlighted by the involvement of other phosphorylation sites and negative feedback loops, and S43 might be part of a complex activation mechanism (Dhillon et al., 2002; Zhao et al., 2022). Dhillon et al. (2002). also pointed out that c-Raf might be differentially phosphorylated and regulated, leading to different pools of differentially phosphorylated c-Raf, depending on its subcellular localization.

The screening identified another regulatory phosphosite, S296 (Leicht et al., 2007; Zhao et al., 2022), suggesting that the potential regulation of c-Raf through VEGFD signaling might be more intricate. Future investigations should include S296 and other phospho-sites for a comprehensive understanding.

Additionally, the phospho-screening implied a potential activation of PKA in neurons treated with rVEGFD for 15 min. Further validation and characterization of VEGFD-induced dephosphorylation of c-Raf phosphorylation are imperative for conclusive insights.

However, limitations in discerning the activation state of phospho-mutants used in the experiment and potential compensatory effects through other Raf family members (Camarero et al., 2006; Wellbrock et al., 2004) introduce complexity to the interpretation. Additionally, the possibility cannot be excluded that, beyond its involvement in the canonical regulatory mechanism of c-Raf activation, S43 may harbor non-canonical roles that are involved in the regulation of dendritic morphology.

Interestingly, both WT and phospho-mutant c-Raf overexpression impeded activity-dependent dendrite remodeling. Moreover, I identified a trend, albeit not significant, indicating a decrease in

endogenous c-Raf expression following treatment with Bic, which was not observed when rVEGFD was co-applied. From these findings, one could hypothesize that low levels of c-Raf expression is crucial for facilitating activity-dependent dendrite remodeling independent of its phosphorylation at S43 and that VEGFD might interfere with a potential activity-induced downregulation of c-Raf. However, it is intriguing that c-Raf, capable of inducing dendrite remodeling through sustained overexpression, might paradoxically need to be downregulated to facilitate activity-induced dendrite remodeling. Conversely, pharmacological inhibition of c-Raf, although having no discernible effect on dendrite morphology under baseline conditions, resulted in a simplification of the dendritic arbor following synaptic activity. It is plausible that the inhibition of c-Raf rendered neurons more unstable, impeding their proper response to signals inducing structural plasticity. These findings suggest that achieving a balance in c-Raf levels and activity is crucial for structural dendritic plasticity.

Although the prevention of activity-dependent dendrite remodeling through c-Raf overexpression appeared independent of S43 phosphorylation, it cannot be excluded that overexpression itself may obscure potential influences of the phospho-site. Additionally, it is conceivable that WT c-Raf inhibits Bic-induced dendrite remodeling by influencing dendrite dynamics differently than the phospho-mutants.

In conclusion, while challenges persist in elucidating the specific role of S43 phosphorylation of c-Raf in VEGFD signaling, the findings suggest that c-Raf may play a role in the regulation of neuronal morphology.

4.6 VEGFD does not induce nuclear calcium signaling in neurons

I have demonstrated that the inhibition of activity-dependent dendrite remodeling by VEGFD is likely not attributable to interference with neuronal activity, as neither acute treatment with rVEGFD nor 30 min pre-treatment with rVEGFD interfered with activity-induced calcium rises. Moreover, in his doctoral thesis, Freitag (2009) conducted MEA recordings to investigate the impact of 24 h or longer rVEGFD treatments on network activity. The results showed that overall network activity was not significantly affected, though some noteworthy trends were observed. Specifically, at DIV 7 following a 24 h rVEGFD treatment, burst duration and interval exhibited slight increases, although not reaching statistical significance. Moreover, treatments with rVEGFD for 24 h or longer starting at DIV 10, but not at DIV 6, led to a slight reduction in spike activity, albeit not statistically significant. Freitag's data suggests that prolonged exposure to VEGFD may have modest effects on network electrical properties, dependent on the timing and duration of administration. Nevertheless, these

effects were minimal, statistically insignificant, and discernible only when rVEGFD was applied at later timepoints and for longer durations than those employed in the morphometric experiments. Therefore, these findings imply that VEGFD directly influences the dendrite remodeling process rather than impacting neuronal activity.

Calcium signaling plays a crucial role in neuronal activity (Hagenston et al., 2011) but is also key in numerous other pathways regulating various cellular functions, including the regulation of the cytoskeleton (Gasperini et al., 2017; Tsai et al., 2015). VEGFA signaling through VEGFR2, for instance, induces calcium signaling in both endothelial cells and neurons (Kim et al., 2008; Simons et al., 2016; Wang et al., 2020). VEGFR2 has also been demonstrated to induce calcium signaling in human endothelial cells when activated by VEGFD (Jia et al., 2004). However, VEGFD-VEGFR2-induced calcium rises exhibit a delayed onset, are weaker, and more transient compared to VEGFA-induced responses. Nevertheless, murine VEGFD does not bind and activate VEGFR2 (Baldwin et al., 2001a), raising uncertainty about whether VEGFD would induce calcium signaling in mice, particularly in mouse neurons.

In this thesis, I showed that no immediate rise in nuclear calcium transients was observed within the initial 10 min of rVEGFD treatment in cultured mouse hippocampal neurons. However, definitive conclusions regarding the ability of VEGFD to induce calcium signaling in neurons cannot be drawn. The calcium indicator employed in this thesis was nuclear, chosen as part of a side experiment originally utilizing a nuclear indicator. It is conceivable that if VEGFD induces calcium signaling, it may remain localized and not enter the nucleus. Additionally, while Jia et al. (2004) detected calcium rises starting at 200 s, it cannot be ruled out that a potential calcium increase in neurons may occur beyond the initial 10 min of rVEGFD application. Future experiments should involve more prolonged treatments and employ cytoplasmic calcium indicators to provide clarity.

4.7 Role of VEGFR3 in neurons

VEGFD can bind and activate VEGFR2 and VEGFR3 (Stacker et al., 1999a) but maintenance of dendritic structure through VEGFD has been demonstrated to occur through VEGFR3 (Mauceri et al., 2011; Schlüter et al., 2020): Suppression of VEGFR3 expression leads to a reduction in dendrite structure similar to that observed with VEGFD. Also, Schlüter et al. (2020) demonstrated that VEGFD preserves the structural integrity and function of retinal ganglion cells in a mouse model of retina degeneration. This effect is prevented when VEGFR3 expression is suppressed in neurons. Moreover, dendrite maintenance was shown to be specific for VEGFD and not VEGFA (Mauceri et al., 2020; Mauceri et al., 2011), which activates VEGFR1 and -2 (Stacker et al., 1999a). As murine VEGFD was

only shown to activate VEGFR3 and not VEGFR2 (Baldwin et al., 2001a), one might infer that the hindrance of structural plasticity induced by VEGFD could also be mediated by VEGFR3. However, experimental confirmation of this assumption is still pending.

Interestingly, both this thesis and previous studies show that VEGFD's closest homologue VEGFC which is also capable of activating VEGFR3 (Joukov et al., 1997), does not mediate dendrite stabilization (Litke et al., 2018; Mauceri et al., 2011). While seemingly paradoxical, the existence of differential signaling pathways or similar pathways with varying intensities, durations, and biological outcomes through the same receptor, especially within the VEGF family, is not uncommon (Simons et al., 2016). For instance, VEGFA, acting via VEGFR2, was shown to induce axon branching and dendritogenesis through distinct mechanisms (Harde et al., 2019; Luck et al., 2019). And even VEGFD and VEGFA employ the same pathways through VEGFR2 in human endothelial cells, yet they exhibit differences in their activation kinetics and biological consequences (Jia et al., 2004).

4.7.1 Expression and localization of VEGFR3 in neurons

Given that dendrite remodeling necessitates low VEGFD expression, I assessed whether VEGFR3 follows a comparable expression pattern. In contrast to VEGFD, I detected lower *VEGFR3* mRNA expression in adult neurons or aged mouse brains compared to those from young mice. Interestingly, there was no discernible effect or even an increase in VEGFR3 expression upon synaptic activity, indicating that structural plasticity-inducing signals downregulate VEGFD signaling through the modulation of VEGFD itself and not via its receptor. This may serve to ensure specific regulation of VEGFD signaling, as VEGFR3 is also activated by VEGFC (Joukov et al., 1997). However, it is possible that a compensatory mechanism exists, in which the reduction in VEGFD expression is counteracted by modification of VEGFR3 expression. On the protein level, preliminary data suggest that VEGFR3 expression may mirror the low expression of VEGFD during development and structural plasticity. Nonetheless, it is unclear as the data are either preliminary or were collected during my stay as a visiting scientist in a lab working with rat hippocampal cells. Moreover, the antibody employed for assessing VEGFR3 protein levels failed to detect shRNA-mediated downregulation of VEGFR3 (Appendix figure 7a), although it successfully detected overexpressed VEGFR3. It is noteworthy that canonical mouse, rat and human VEGFR3 have a molecular weight of approximately 153 kDa, and other known isoforms are typically smaller (UniProt, 2022). However, in immunoblots of both the mouse brain endothelial cell line bEND.3 and primary mouse hippocampal cultures, a band corresponding to the size of mouse VEGFR3 at 153 kDa (UniProt, 2022) did not appear using this antibody (Appendix figure 7b). Instead, the identified protein band using this antibody exhibited

a molecular weight of around 180 kDa in bEND.3 cells, in the mouse hippocampus and cortex, as well as in cultured hippocampal cells, while it appeared at 150 kDa in the rat hippocampus, both *in vitro* and *in vivo*. Overexpressed VEGFR3-GFP, however, was detected at 180 kDa as expected when considering the additional weight of the GFP fusion. On the other side, bands at 170/180 kDa have been reported before for VEGFR3 in HUVECs (Tammela et al., 2011). Posttranslational modifications, similar to VEGFR2, where glycosylation is known to cause size shifts (Wang et al., 2020), or alternative splicing may be a possible explanation for the differences in the observed sizes. Consequently, it is difficult to draw definitive conclusions about the protein expression pattern of VEGFR3 during development and synaptic activity in adult neurons.

Considering the intricately compartmentalized morphology of neurons and the distinct impact of VEGFD on basal and apical dendrites (Maurer et al., 2020), it is conceivable that VEGFD signaling operates in a localized fashion. Through biochemical fractionation aimed at enriching or isolating postsynaptic proteins, I observed predominant VEGFR3 expression at the postsynapse. This pattern was consistent for both endogenous and overexpressed VEGFR3. This observation is noteworthy, considering that the antibodies employed for VEGFR3 detection may not effectively capture endogenous VEGFR3 levels but rather overexpressed VEGFR3, as discussed above.

Intriguingly, the expression of VEGFR3 exhibited a reduction after a 30 min exposure to Bic/4AP-induced synaptic activity in total homogenates of rat hippocampal cells, while its expression in spines remained unaffected. This suggests that synaptic activity might induce a global reduction in VEGFR3 expression, which could be compensated in spines through an enhanced localization to these structures. This underscores the importance of evaluating the local roles of VEGFR3.

This is the first time that localization of VEGFR3 in neurons was characterized, to the best of my knowledge. Subsequent investigations are imperative to validate its localization at spines and to unravel its significance for VEGFD signaling. It would be particularly intriguing if VEGFD were to mediate its signaling through VEGFR3 at dendritic spines, given the pivotal role of spines in neuronal function.

4.7.2 Nova2 is a potential interaction partner of VEGFR3

In this thesis, I identified potential direct or indirect interaction partners of VEGFR3 through co-immunoprecipitation of overexpressed VEGFR3-GFP and subsequent mass spectrometry analysis. Due to the uncertainty regarding the antibodies' capability to detect endogenous VEGFR3, this experiment was conducted using overexpressed VEGFR3. The analysis identified eight potential interaction partners of VEGFR3 in neurons, with roles primarily associated with RNA processing,

transport or translation, at lipid rafts of the endoplasmic reticulum, at mitochondria, or in clathrin-dependent endocytosis but also with implications in the regulation of the cytoskeleton and neuronal morphology. However, achieving overexpression in neurons proved challenging, resulting in only a modest increase in VEGFR3 levels. This challenge may stem from the construct's large size or the inherent difficulty in incorporating a transmembrane protein into the membrane. Consequently, potential issues such as incorrect localization, protein misfolding, aggregation, or cleavage must be considered. Notably, immunocytochemical labeling of VEGFR3 in neurons expressing only GFP appeared predominantly nuclear, while in VEGFR3-GFP-expressing neurons, it was primarily cytoplasmic. This discrepancy could indicate distinct distributions of overexpressed VEGFR3 or potentially reflect the true localization of VEGFR3 that the antibody may fail to detect on the endogenous protein.

Furthermore, immunoblotting of neurons overexpressing VEGFR3 revealed additional GFP- or VEGFR3-immunoreactive bands, exclusively observed in VEGFR3-GFP-expressing cells. This could simply be due to unspecific antibody labeling but could also indicate potential cleavage of VEGFR3. These challenges resulted in a low abundance of immunoprecipitated VEGFR3-GFP, although it was successfully detected through immunoblotting and mass spectrometry. Consequently, only a limited number of interaction partners could be identified. Therefore, it is crucial to interpret the results with caution. Nonetheless, this approach, while limiting in the number of partners identified, may provide a more accurate representation, as VEGFR3 expression might have been closer to endogenous VEGFR3 expression, thereby reducing the likelihood of overestimating interactions and encountering potential false positives. In addition, overexpression had the advantage of being neuron-specific, excluding glial cells from the results.

Nova2 emerged as the most promising candidate among those identified. Through its role as a regulator of alternative splicing, it plays a role in the regulation of neuronal morphology, most importantly in the cytoskeletal organization of dendrites (Leggere et al., 2016; Saito et al., 2016; Yuan et al., 2018b). Notably, nova2 knockdown was shown to cause dendritic arbor simplification while sparing spines (Yuan et al., 2018b), reminiscent of the impact observed with VEGFD knockdown (Mauceri et al., 2011; Maurer et al., 2020). Additionally, nova2-mediated alternative splicing has been reported to negatively modulate VEGFC-VEGFR3-induced MAPK/ERK signaling, limiting lymphatic endothelial cell fate specification (Baek et al., 2019).

Future studies should validate and characterize its potential interaction with VEGFR3 and assess how this is impacted by VEGFD binding to VEGFR3 and eventually characterize its role in VEGFD signaling.

4.8 Conclusion and outlook

In summary, this study demonstrates that VEGFD exerts an inhibitory influence on morphological alterations in dendrites, irrespective of whether they involve dendrite atrophy, developmental dendritogenesis, or activity-dependent dendrite remodeling. Consequently, it proposes VEGFD as a pivotal regulator governing the equilibrium between dendritic maintenance and plasticity. Furthermore, this work suggests that VEGFD achieves this regulatory role through modulating cortical actin and MTs and by destabilizing dendrite elongation and formation, thereby maintaining the morphological status quo. Moreover, it revealed that VEGFD imparts stabilization to dendrites when encountering remodeling-inducing inputs, partly through the dephosphorylation—and subsequently, activation—of STEP. This, in turn, leads to the dephosphorylation of the cytoskeletal-associated protein ezrin at Y478. Additionally, nova2 was identified as a potential interaction partner of VEGFD's receptor VEGFR3 and as a promising downstream mediator of VEGFD signaling, providing an interesting path for future investigations.

These findings are of importance, as many neurological disorders are associated with structural aberrations stemming from an imbalance between structural plasticity and stability. The elucidated mechanisms in this thesis hold promise for potential therapeutic interventions in the treatment of neurological disorders.

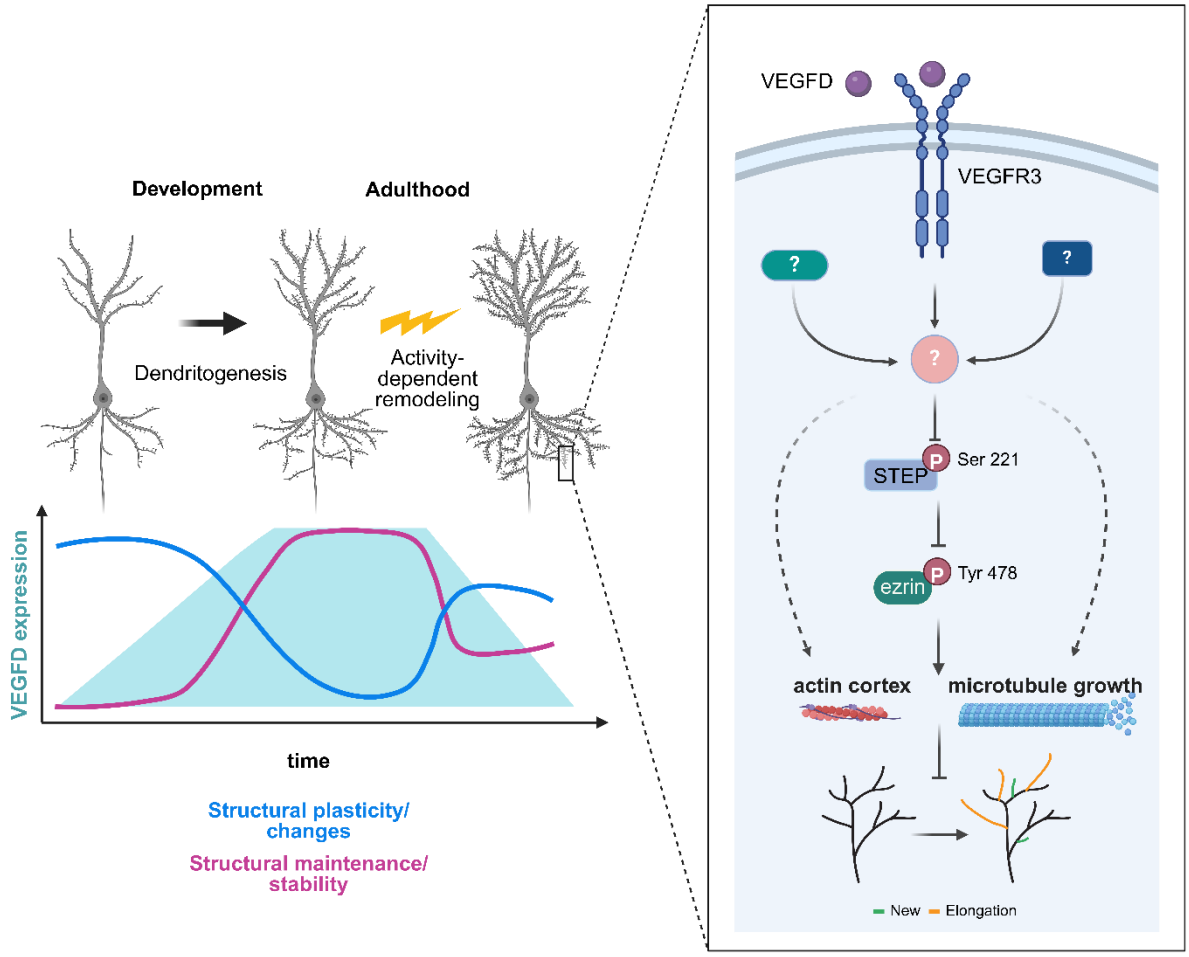

Figure 42. Schema of main findings: VEGFD governs the balance between dendritic maintenance and plasticity. *Structural maintenance and plasticity are two competing morphological requirements. Structural maintenance in adult neurons requires VEGFD expression, whereas structural plasticity during developmental dendritogenesis or activity-dependent dendrite remodeling require low VEGFD expression. VEGFD maintains the original morphological state of neurons by modulating the actin cell cortex and microtubule growth, thereby hindering dendrite elongation, and destabilizing de novo dendrite formation. VEGFD signaling triggers activation of STEP through dephosphorylation at S221. Consequently, STEP dephosphorylates the cytoskeleton-associated protein ezrin at Y478. This figure is adapted from a first authored manuscript that is currently in revision for submission to Cellular and Molecular Life Sciences (see List of publications).*

In conclusion, despite the advancements made in this study, several questions remain unresolved, as discussed above. In the context of future research, I have pinpointed follow-up questions that, in my perspective, hold significant interest for future investigations:

- What upstream mechanisms regulate the levels of VEGFD to adjust the balance between structural stabilization or plasticity?

- How do neurons ensure the targeted remodeling of specific dendrites while preserving others? Could this process be regulated through the localized action of VEGFD, and if so, what mechanisms govern this regulation?
- What are the molecular links between VEGFD signaling and STEP?
- How does the dephosphorylation of Y478 ezrin affect neuronal cytoskeleton, and by what means does it mediate this effect?
- Are the pathways and mechanisms underlying VEGFD-induced dendrite stabilization that were identified here in the context of activity-dependent dendrite remodeling in adult neurons, the same in developing neurons?
- Does nova2 play a role in VEGFD-dependent dendrite maintenance?

References

Achen MG, Jeltsch M, Kukk E, Mäkinen T, Vitali A, Wilks AF, . . . Stacker SA (1998a). Vascular endothelial growth factor D (VEGF-D) is a ligand for the tyrosine kinases VEGF receptor 2 (Flk1) and VEGF receptor 3 (Flt4). Proc Natl Acad Sci U S A 95:548-553. https://doi.org/10.1073/pnas.95.2.548

Achen MG, Stacker SA (1998b). The vascular endothelial growth factor family; proteins which guide the development of the vasculature. Int J Exp Pathol 79:255-265. https://doi.org/10.1046/j.1365-2613.1998.700404.x

Adams RH, Eichmann A (2010). Axon guidance molecules in vascular patterning. Cold Spring Harb Perspect Biol 2:a001875. https://doi.org/10.1101/cshperspect.a001875

Adlard PA, Vickers JC (2002). Morphologically distinct plaque types differentially affect dendritic structure and organisation in the early and late stages of Alzheimer's disease. Acta Neuropathol 103:377-383. https://doi.org/10.1007/s00401-001-0476-6

Ahmad FJ, Hughey J, Wittmann T, Hyman A, Greaser M, Baas PW (2000). Motor proteins regulate force interactions between microtubules and microfilaments in the axon. Nat Cell Biol 2:276-280. https://doi.org/10.1038/35010544

Al-Saif A, Bohlega S, Al-Mohanna F (2012). Loss of ERLIN2 function leads to juvenile primary lateral sclerosis. Ann Neurol 72:510-516. https://doi.org/10.1002/ana.23641

Alavi A, Hood JD, Frausto R, Stupack DG, Cheresh DA (2003). Role of Raf in Vascular Protection from Distinct Apoptotic Stimuli. Science 301:94-96. https://doi.org/10.1126/science.1082015

Alitalo K, Carmeliet P (2002). Molecular mechanisms of lymphangiogenesis in health and disease. Cancer Cell 1:219-227

Almodovar CRd, Lambrechts D, Mazzone M, Carmeliet P (2009). Role and Therapeutic Potential of VEGF in the Nervous System. Physiol Rev 89:607-648. https://doi.org/10.1152/physrev.00031.2008

Amann KJ, Pollard TD (2000). Cellular regulation of actin network assembly. Curr Biol 10:R728-R730. https://doi.org/10.1016/S0960-9822(00)00751-X

Anderson KA, Ribar TJ, Illario M, Means AR (1997). Defective survival and activation of thymocytes in transgenic mice expressing a catalytically inactive form of Ca2+/calmodulin-dependent protein kinase IV. Mol Endocrinol 11:725-737. https://doi.org/10.1210/mend.11.6.0011

Anderton BH, Callahan L, Coleman P, Davies P, Flood D, Jicha GA, . . . Weaver C (1998). Dendritic changes in Alzheimer's disease and factors that may underlie these changes. Prog Neurobiol 55:595-609

Antila S, Karaman S, Nurmi H, Airavaara M, Voutilainen MH, Mathivet T, . . . Alitalo K (2017). Development and plasticity of meningeal lymphatic vessels. J Exp Med 214:3645-3667. https://doi.org/10.1084/jem.20170391

Antoine-Bertrand J, Ghogha A, Luangrath V, Bedford FK, Lamarche-Vane N (2011). The activation of ezrin-radixin-moesin proteins is regulated by netrin-1 through Src kinase and RhoA/Rho kinase activities and mediates netrin-1-induced axon outgrowth. Mol Biol Cell 22:3734-3746. https://doi.org/10.1091/mbc.E10-11-0917

Arikkath J (2012). Molecular mechanisms of dendrite morphogenesis. Front Cell Neurosci 6. https://doi.org/10.3389/fncel.2012.00061

Armstrong D, Dunn JK, Antalffy B, Trivedi R (1995). Selective dendritic alterations in the cortex of Rett syndrome. J Neuropathol Exp Neurol 54:195-201

Armstrong DD, Dunn K, Antalffy B (1998). Decreased dendritic branching in frontal, motor and limbic cortex in Rett syndrome compared with trisomy 21. J Neuropathol Exp Neurol 57:1013-1017

Arpin M, Chirivino D, Naba A, Zwaenepoel I (2011). Emerging role for ERM proteins in cell adhesion and migration. Cell Adh Migr 5:199-206. https://doi.org/10.4161/cam.5.2.15081

Artero-Castro A, Castellvi J, García A, Hernández J, Cajal SRy, Lleonart ME (2011). Expression of the ribosomal proteins Rplp0, Rplp1, and Rplp2 in gynecologic tumors. Hum Pathol 42:194-203. https://doi.org/10.1016/j.humpath.2010.04.020

Avantaggiato V, Orlandini M, Acampora D, Oliviero S, Simeone A (1998). Embryonic expression pattern of the murine figf gene, a growth factor belonging to platelet-derived growth factor/vascular endothelial growth factor family. Mech Dev 73:221-224. https://doi.org/10.1016/s0925-4773(98)00049-5

Baas PW, Lin S (2011). Hooks and comets: The story of microtubule polarity orientation in the neuron. Dev Neurobiol 71:403-418. https://doi.org/10.1002/dneu.20818

Baas PW, Rao AN, Matamoros AJ, Leo L (2016). Stability properties of neuronal microtubules. Cytoskeleton 73:442-460. https://doi.org/10.1002/cm.21286

Bading H (2017). Therapeutic targeting of the pathological triad of extrasynaptic NMDA receptor signaling in neurodegenerations. J Exp Med 214:569-578. https://doi.org/10.1084/jem.20161673

Baek S, Oh TG, Secker G, Sutton DL, Okuda KS, Paterson S, . . . Hogan BM (2019). The Alternative Splicing Regulator Nova2 Constrains Vascular Erk Signaling to Limit Specification of the Lymphatic Lineage. Dev Cell 49:279-292.e275. https://doi.org/10.1016/j.devcel.2019.03.017

Bailey E, Cui Y, Casey A, Stoler JM, Ai X, Ma D, . . . El-Chemaly SY (2017). Pulmonary Vasculopathy Associated with FIGF Gene Mutation. Am J Pathol 187:25-32. https://doi.org/10.1016/j.ajpath.2016.09.008

Baldwin ME, Catimel B, Nice EC, Roufail S, Hall NE, Stenvers KL, . . . Achen MG (2001a). The specificity of receptor binding by vascular endothelial growth factor-d is different in mouse and man. J Biol Chem 276:19166-19171. https://doi.org/10.1074/jbc.M100097200

Baldwin ME, Halford MM, Roufail S, Williams RA, Hibbs ML, Grail D, . . . Achen MG (2005). Vascular endothelial growth factor D is dispensable for development of the lymphatic system. Mol Cell Biol 25:2441-2449. https://doi.org/10.1128/mcb.25.6.2441-2449.2005

Baldwin ME, Roufail S, Halford MM, Alitalo K, Stacker SA, Achen MG (2001b). Multiple forms of mouse vascular endothelial growth factor-D are generated by RNA splicing and proteolysis. J Biol Chem 276:44307-44314. https://doi.org/10.1074/jbc.M106188200

Balenci L, Saoudi Y, Grunwald D, Deloulme JC, Bouron A, Bernards A, Baudier J (2007). IQGAP1 regulates adult neural progenitors in vivo and vascular endothelial growth factor-triggered neural progenitor migration in vitro. J Neurosci 27:4716-4724. https://doi.org/10.1523/jneurosci.0830-07.2007

Bär J, Kobler O, van Bommel B, Mikhaylova M (2016). Periodic F-actin structures shape the neck of dendritic spines. Sci Rep 6:37136. https://doi.org/10.1038/srep37136

Becker L, Armstrong D, Chan F (1986). Dendritic atrophy in children with Down's syndrome. Annals of Neurology: Official Journal of the American Neurological Association and the Child Neurology Society 20:520-526

Bedford DC, Kasper LH, Fukuyama T, Brindle PK (2010). Target gene context influences the transcriptional requirement for the KAT3 family of CBP and p300 histone acetyltransferases. Epigenetics 5:9-15. https://doi.org/10.4161/epi.5.1.10449

Bengtson CP, Kaiser M, Obermayer J, Bading H (2013). Calcium responses to synaptically activated bursts of action potentials and their synapse-independent replay in cultured networks of hippocampal neurons. Biochim Biophys Acta 1833:1672-1679. https://doi.org/10.1016/j.bbamcr.2013.01.022

Bianchi M, Hagan J, Heidbreder C (2005). Neuronal plasticity, stress and depression: involvement of the cytoskeletal microtubular system? Current Drug Targets-CNS & Neurological Disorders 4:597-611

Bisaria A, Hayer A, Garbett D, Cohen D, Meyer T (2020). Membrane-proximal F-actin restricts local membrane protrusions and directs cell migration. Science 368:1205-1210. https://doi.org/10.1126/science.aay7794

Blanchoin L, Boujemaa-Paterski R, Sykes C, Plastino J (2014). Actin Dynamics, Architecture, and Mechanics in Cell Motility. Physiol Rev 94:235-263. https://doi.org/10.1152/physrev.00018.2013

Bloss E, Morrison J, Hof P, Dickstein D (2011). Influence of aging and neurodegeneration on dendritic spine morphology. Transl Neurosci 2:49-60. https://doi.org/10.2478/s13380-011-0008-3

Bokhari SMZ, Hamar P (2023). Vascular Endothelial Growth Factor-D (VEGF-D): An Angiogenesis Bypass in Malignant Tumors. Int J Mol Sci 24. https://doi.org/10.3390/ijms241713317

Bonam SR, Ruff M, Muller S (2019). HSPA8/HSC70 in Immune Disorders: A Molecular Rheostat that Adjusts Chaperone-Mediated Autophagy Substrates. Cells 8. https://doi.org/10.3390/cells8080849

Bongmba OY, Martinez LA, Elhardt ME, Butler K, Tejada-Simon MV (2011). Modulation of dendritic spines and synaptic function by Rac1: a possible link to Fragile X syndrome pathology. Brain Res 1399:79-95

Bornschlögl T, Romero S, Vestergaard CL, Joanny J-F, Van Nhieu GT, Bassereau P (2013). Filopodial retraction force is generated by cortical actin dynamics and controlled by reversible tethering at the tip. Proc Natl Acad Sci U S A 110:18928-18933. https://doi.org/10.1073/pnas.1316572110

Bourne J, Harris KM (2007). Do thin spines learn to be mushroom spines that remember? Curr Opin Neurobiol 17:381-386. https://doi.org/10.1016/j.conb.2007.04.009

Bourne JN, Harris KM (2008). Balancing structure and function at hippocampal dendritic spines. Annu Rev Neurosci 31:47-67. https://doi.org/10.1146/annurev.neuro.31.060407.125646

Bretscher A (1983). Purification of an 80,000-dalton protein that is a component of the isolated microvillus cytoskeleton, and its localization in nonmuscle cells. J Cell Biol 97:425-432. https://doi.org/10.1083/jcb.97.2.425

Brito DVC, Kupke J, Gulmez Karaca K, Zeuch B, Oliveira AMM (2020). Mimicking Age-Associated Gadd45γ Dysregulation Results in Memory Impairments in Young Adult Mice. J Neurosci 40:1197-1210. https://doi.org/10.1523/jneurosci.1621-19.2019

Broadbelt K, Byne W, Jones LB (2002). Evidence for a decrease in basilar dendrites of pyramidal cells in schizophrenic medial prefrontal cortex. Schizophr Res 58:75-81

Buenaventura RGM, Merlino G, Yu Y (2023). Ez-Metastasizing: The Crucial Roles of Ezrin in Metastasis. Cells 12:1620

Bui HM, Enis D, Robciuc MR, Nurmi HJ, Cohen J, Chen M, . . . Kahn ML (2016). Proteolytic activation defines distinct lymphangiogenic mechanisms for VEGFC and VEGFD. The Journal of Clinical Investigation 126:2167-2180. https://doi.org/10.1172/JCI83967

Burnette DT, Ji L, Schaefer AW, Medeiros NA, Danuser G, Forscher P (2008). Myosin II activity facilitates microtubule bundling in the neuronal growth cone neck. Dev Cell 15:163-169. https://doi.org/10.1016/j.devcel.2008.05.016

Calvo CF, Fontaine RH, Soueid J, Tammela T, Makinen T, Alfaro-Cervello C, . . . Thomas JL (2011). Vascular endothelial growth factor receptor 3 directly regulates murine neurogenesis. Genes Dev 25:831-844. https://doi.org/10.1101/gad.615311

Camarero G, Tyrsin OY, Xiang C, Pfeiffer V, Pleiser S, Wiese S, . . . Rapp UR (2006). Cortical migration defects in mice expressing A-RAF from the B-RAF locus. Mol Cell Biol 26:7103-7115. https://doi.org/10.1128/MCB.00424-06

Cao L, Jiao X, Zuzga DS, Liu Y, Fong DM, Young D, During MJ (2004). VEGF links hippocampal activity with neurogenesis, learning and memory. Nat Genet 36:827-835. https://doi.org/10.1038/ng1395

Cariboni A, Davidson K, Dozio E, Memi F, Schwarz Q, Stossi F, . . . Ruhrberg C (2011). VEGF signalling controls GnRH neuron survival via NRP1 independently of KDR and blood vessels. Development 138:3723-3733. https://doi.org/10.1242/dev.063362

Carmeliet P, de Almodovar CR (2013). VEGF ligands and receptors: implications in neurodevelopment and neurodegeneration. Cell Mol Life Sci 70:1763-1778. https://doi.org/10.1007/s00018-013-1283-7

Carmeliet P, Moons L, Luttun A, Vincenti V, Compernolle V, De Mol M, . . . Persico MG (2001). Synergism between vascular endothelial growth factor and placental growth factor contributes to angiogenesis and plasma extravasation in pathological conditions. Nat Med 7:575-583. https://doi.org/10.1038/87904

Castonguay D, Dufort-Gervais J, Ménard C, Chatterjee M, Quirion R, Bontempi B, . . . Brouillette J (2018). The Tyrosine Phosphatase STEP Is Involved in Age-Related Memory Decline. Curr Biol 28:1079-1089.e1074. https://doi.org/10.1016/j.cub.2018.02.047

Chakraborty A, Upadhya R, Usman TA, Shetty AK, Rutkowski JM (2021). Chronic VEGFR-3 signaling preserves dendritic arborization and sensitization under stress. Brain Behav Immun 98:219-233. https://doi.org/10.1016/j.bbi.2021.08.007

Chan GK, McGrath JA, Parsons M (2021). Spatial activation of ezrin by epidermal growth factor receptor and focal adhesion kinase co-ordinates epithelial cell migration. Open Biol 11:210166. https://doi.org/10.1098/rsob.210166

Chappell TG, Welch WJ, Schlossman DM, Palter KB, Schlesinger MJ, Rothman JE (1986). Uncoating ATPase is a member of the 70 kilodalton family of stress proteins. Cell 45:3-13. https://doi.org/10.1016/0092-8674(86)90532-5

Chatterjee M, Kwon J, Benedict J, Kamceva M, Kurup P, Lombroso PJ (2021). STEP inhibition prevents Aβ-mediated damage in dendritic complexity and spine density in Alzheimer's disease. Exp Brain Res 239:881-890. https://doi.org/10.1007/s00221-020-06028-x

Cheng X, Ma Y, Moore M, Hemmings BA, Taylor SS (1998). Phosphorylation and activation of cAMP-dependent protein kinase by phosphoinositide-dependent protein kinase. Proc Natl Acad Sci U S A 95:9849-9854. https://doi.org/10.1073/pnas.95.17.9849

Chin PC, Liu L, Morrison BE, Siddiq A, Ratan RR, Bottiglieri T, D'Mello SR (2004). The c-Raf inhibitor GW5074 provides neuroprotection in vitro and in an animal model of neurodegeneration through a MEK-ERK and Akt-independent mechanism. J Neurochem 90:595-608. https://doi.org/10.1111/j.1471-4159.2004.02530.x

Chung L (2015). A Brief Introduction to the Transduction of Neural Activity into Fos Signal. Dev Reprod 19:61-67. https://doi.org/10.12717/dr.2015.19.2.061

Cingolani LA, Goda Y (2008). Actin in action: the interplay between the actin cytoskeleton and synaptic efficacy. Nature Reviews Neuroscience 9:344-356. https://doi.org/10.1038/nrn2373

Clark-Raymond A, Halaris A (2013). VEGF and depression: a comprehensive assessment of clinical data. J Psychiatr Res 47:1080-1087. https://doi.org/10.1016/j.jpsychires.2013.04.008

Cline H, Haas K (2008). The regulation of dendritic arbor development and plasticity by glutamatergic synaptic input: a review of the synaptotrophic hypothesis. J Physiol 586:1509-1517. https://doi.org/10.1113/jphysiol.2007.150029

Cline HT (2001). Dendritic arbor development and synaptogenesis. Curr Opin Neurobiol 11:118-126. https://doi.org/10.1016/s0959-4388(00)00182-3

Coles Charlotte H, Bradke F (2015). Coordinating Neuronal Actin–Microtubule Dynamics. Curr Biol 25:R677-R691. https://doi.org/10.1016/j.cub.2015.06.020

Coon BG, Baeyens N, Han J, Budatha M, Ross TD, Fang JS, . . . Schwartz MA (2015). Intramembrane binding of VE-cadherin to VEGFR2 and VEGFR3 assembles the endothelial mechanosensory complex. J Cell Biol 208:975-986. https://doi.org/10.1083/jcb.201408103

Coso S, Zeng Y, Opeskin K, Williams ED (2012). Vascular endothelial growth factor receptor-3 directly interacts with phosphatidylinositol 3-kinase to regulate lymphangiogenesis. PLoS One 7:e39558. https://doi.org/10.1371/journal.pone.0039558

Costa AR, Sousa MM (2021). The role of the membrane-associated periodic skeleton in axons. Cell Mol Life Sci 78:5371-5379. https://doi.org/10.1007/s00018-021-03867-x

Craig AM, Banker G (1994). Neuronal polarity. Annu Rev Neurosci 17:267-310

D'Este E, Kamin D, Göttfert F, El-Hady A, Hell SW (2015). STED nanoscopy reveals the ubiquity of subcortical cytoskeleton periodicity in living neurons. Cell Rep 10:1246-1251. https://doi.org/10.1016/j.celrep.2015.02.007

Dahlhaus R, El-Husseini A (2010). Altered neuroligin expression is involved in social deficits in a mouse model of the fragile X syndrome. Behav Brain Res 208:96-105. https://doi.org/10.1016/j.bbr.2009.11.019

Dai X, Wang LJ, Wu J, Shi YX, Li GP, Yang XQ (2018). Src kinase inhibitor PP2 regulates the biological characteristics of A549 cells via the PI3K/Akt signaling pathway. Oncol Lett 16:5059-5065. https://doi.org/10.3892/ol.2018.9282

Das KP, Freudenrich TM, Mundy WR (2004). Assessment of PC12 cell differentiation and neurite growth: a comparison of morphological and neurochemical measures. Neurotoxicol Teratol 26:397-406. https://doi.org/10.1016/j.ntt.2004.02.006

De Rossi P, Harde E, Dupuis JP, Martin L, Chounlamountri N, Bardin M, . . . Meissirel C (2016). A critical role for VEGF and VEGFR2 in NMDA receptor synaptic function and fear-related behavior. Mol Psychiatry 21:1768-1780. https://doi.org/10.1038/mp.2015.195

Delandre C, Amikura R, Moore AW (2016). Microtubule nucleation and organization in dendrites. Cell Cycle 15:1685-1692. https://doi.org/10.1080/15384101.2016.1172158

Deng Y, Zhang X, Simons M (2015). Molecular controls of lymphatic VEGFR3 signaling. Arterioscler Thromb Vasc Biol 35:421-429. https://doi.org/10.1161/atvbaha.114.304881

Derouiche A, Geiger KD (2019). Perspectives for Ezrin and Radixin in Astrocytes: Kinases, Functions and Pathology. Int J Mol Sci 20. https://doi.org/10.3390/ijms20153776

Desai A, Mitchison TJ (1997). Microtubule polymerization dynamics. Annu Rev Cell Dev Biol 13:83-117

Dhillon AS, Pollock C, Steen H, Shaw PE, Mischak H, Kolch W (2002). Cyclic AMP-dependent kinase regulates Raf-1 kinase mainly by phosphorylation of serine 259. Mol Cell Biol 22:3237-3246. https://doi.org/10.1128/mcb.22.10.3237-3246.2002

Dickstein DL, Kabaso D, Rocher AB, Luebke JI, Wearne SL, Hof PR (2007). Changes in the structural complexity of the aged brain. Aging Cell 6:275-284. https://doi.org/10.1111/j.1474-9726.2007.00289.x

Dieterich LC, Klein S, Mathelier A, Sliwa-Primorac A, Ma Q, Hong Y-K, . . . Detmar M (2015). DeepCAGE Transcriptomics Reveal an Important Role of the Transcription Factor MAFB in the Lymphatic Endothelium. Cell Rep 13:1493-1504. https://doi.org/10.1016/j.celrep.2015.10.002

Dixelius J, Makinen T, Wirzenius M, Karkkainen MJ, Wernstedt C, Alitalo K, Claesson-Welsh L (2003). Ligand-induced vascular endothelial growth factor receptor-3 (VEGFR-3) heterodimerization with VEGFR-2 in primary lymphatic endothelial cells regulates tyrosine phosphorylation sites. J Biol Chem 278:40973-40979. https://doi.org/10.1074/jbc.M304499200

Domingues I, Rino J, Demmers JAA, de Lanerolle P, Santos SCR (2011). VEGFR2 Translocates to the Nucleus to Regulate Its Own Transcription. PLoS One 6:e25668. https://doi.org/10.1371/journal.pone.0025668

Dong X, Shen K, Bülow HE (2015). Intrinsic and extrinsic mechanisms of dendritic morphogenesis. Annu Rev Physiol 77:271-300. https://doi.org/10.1146/annurev-physiol-021014-071746

Doussau F, Augustine GJ (2000). The actin cytoskeleton and neurotransmitter release: An overview. Biochimie 82:353-363. https://doi.org/10.1016/S0300-9084(00)00217-0

Downing KH (2000). Structural basis for the interaction of tubulin with proteins and drugs that affect microtubule dynamics. Annu Rev Cell Dev Biol 16:89-111. https://doi.org/10.1146/annurev.cellbio.16.1.89

Dumaz N, Hayward R, Martin J, Ogilvie L, Hedley D, Curtin JA, . . . Marais R (2006). In Melanoma, RAS Mutations Are Accompanied by Switching Signaling from BRAF to CRAF and Disrupted Cyclic AMP Signaling. Cancer Res 66:9483-9491. https://doi.org/10.1158/0008-5472.Can-05-4227

Dumaz N, Marais R (2003). Protein kinase A blocks Raf-1 activity by stimulating 14-3-3 binding and blocking Raf-1 interaction with Ras. J Biol Chem 278:29819-29823. https://doi.org/10.1074/jbc.C300182200

Dumont DJ, Jussila L, Taipale J, Lymboussaki A, Mustonen T, Pajusola K, . . . Alitalo K (1998). Cardiovascular failure in mouse embryos deficient in VEGF receptor-3. Science 282:946-949. https://doi.org/10.1126/science.282.5390.946

Durand CM, Betancur C, Boeckers TM, Bockmann J, Chaste P, Fauchereau F, . . . Anckarsäter H (2007). Mutations in the gene encoding the synaptic scaffolding protein SHANK3 are associated with autism spectrum disorders. Nat Genet 39:25-27

Durré T, Morfoisse F, Erpicum C, Ebroin M, Blacher S, García-Caballero M, . . . Noel A (2018). uPARAP/Endo180 receptor is a gatekeeper of VEGFR-2/VEGFR-3 heterodimerisation during pathological lymphangiogenesis. Nat Commun 9:5178. https://doi.org/10.1038/s41467-018-07514-1

Ehlinger DG, Bergstrom HC, McDonald CG, Smith RF (2012). Nicotine-induced dendritic remodeling in the insular cortex. Neurosci Lett 516:89-93. https://doi.org/10.1016/j.neulet.2012.03.064

Ehrenreiter K, Piazzolla D, Velamoor V, Sobczak I, Small JV, Takeda J, . . . Baccarini M (2005). Raf-1 regulates Rho signaling and cell migration. J Cell Biol 168:955-964. https://doi.org/10.1083/jcb.200409162

Eichmann A, Simons M (2012). VEGF signaling inside vascular endothelial cells and beyond. Curr Opin Cell Biol 24:188-193. https://doi.org/10.1016/j.ceb.2012.02.002

El-Chemaly S, Pacheco-Rodriguez G, Malide D, Meza-Carmen V, Kato J, Cui Y, . . . Moss J (2014). Nuclear localization of vascular endothelial growth factor-D and regulation of c-Myc-dependent transcripts in human lung fibroblasts. Am J Respir Cell Mol Biol 51:34-42. https://doi.org/10.1165/rcmb.2013-0417OC

El Hachimi K, Foncin J (1990). Loss of dendritic spines in Alzheimer's disease. Comptes rendus de l'Academie des sciences Serie III, Sciences de la vie 311:397-402

Ewan LC, Jopling HM, Jia H, Mittar S, Bagherzadeh A, Howell GJ, . . . Ponnambalam S (2006). Intrinsic Tyrosine Kinase Activity is Required for Vascular Endothelial Growth Factor Receptor 2 Ubiquitination, Sorting and Degradation in Endothelial Cells. Traffic 7:1270-1282. https://doi.org/10.1111/j.1600-0854.2006.00462.x

Falke E, Nissanov J, Mitchell TW, Bennett DA, Trojanowski JQ, Arnold SE (2003). Subicular dendritic arborization in Alzheimer's disease correlates with neurofibrillary tangle density. Am J Pathol 163:1615-1621. https://doi.org/10.1016/s0002-9440(10)63518-3

Fehon RG, McClatchey AI, Bretscher A (2010). Organizing the cell cortex: the role of ERM proteins. Nat Rev Mol Cell Biol 11:276-287. https://doi.org/10.1038/nrm2866

Feng G, Mellor RH, Bernstein M, Keller-Peck C, Nguyen QT, Wallace M, . . . Sanes JR (2000). Imaging Neuronal Subsets in Transgenic Mice Expressing Multiple Spectral Variants of GFP. Neuron 28:41-51. https://doi.org/10.1016/S0896-6273(00)00084-2

Ferrante RJ, Kowall NW, Richardson EP, Jr. (1991). Proliferative and degenerative changes in striatal spiny neurons in Huntington's disease: a combined study using the section-Golgi method and calbindin D28k immunocytochemistry. J Neurosci 11:3877-3887. https://doi.org/10.1523/jneurosci.11-12-03877.1991

Ferrara N, Kerbel RS (2005). Angiogenesis as a therapeutic target. Nature 438:967-974

Figlia G, Müller S, Hagenston AM, Kleber S, Roiuk M, Quast J-P, . . . Teleman AA (2022). Brain-enriched RagB isoforms regulate the dynamics of mTORC1 activity through GATOR1 inhibition. Nat Cell Biol 24:1407-1421. https://doi.org/10.1038/s41556-022-00977-x

Fitzpatrick C, Lombroso P (2011). The Role of Striatal-Enriched Protein Tyrosine Phosphatase (STEP) in Cognition. Front Neuroanat 5. https://doi.org/10.3389/fnana.2011.00047

Fournier E, Dubreuil P, Birnbaum D, Borg JP (1995). Mutation at tyrosine residue 1337 abrogates ligand-dependent transforming capacity of the FLT4 receptor. Oncogene 11:921-931

Freitag HE (2009). Micro-Electrode-Array recordings: a tool to study calcium signaling pathways involved in neuronal network plasticity and late phase long-term potentiation (Doctoral dissertation, Heidelberg University) heiDOK. https://doi.org/10.11588/heidok.00012436

Fukuda T, Itoh M, Ichikawa T, Washiyama K, Goto Y-i (2005). Delayed maturation of neuronal architecture and synaptogenesis in cerebral cortex of Mecp2-deficient mice. J Neuropathol Exp Neurol 64:537-544

Furutani Y, Matsuno H, Kawasaki M, Sasaki T, Mori K, Yoshihara Y (2007). Interaction between Telencephalin and ERM Family Proteins Mediates Dendritic Filopodia Formation. J Neurosci 27:8866-8876. https://doi.org/10.1523/jneurosci.1047-07.2007

Galland F, Karamysheva A, Pebusque MJ, Borg JP, Rottapel R, Dubreuil P, . . . Birnbaum D (1993). The FLT4 gene encodes a transmembrane tyrosine kinase related to the vascular endothelial growth factor receptor. Oncogene 8:1233-1240

Galvagni F, Pennacchini S, Salameh A, Rocchigiani M, Neri F, Orlandini M, . . . Oliviero S (2010). Endothelial cell adhesion to the extracellular matrix induces c-Src-dependent VEGFR-3 phosphorylation without the activation of the receptor intrinsic kinase activity. Circ Res 106:1839-1848. https://doi.org/10.1161/circresaha.109.206326

Gao X, Deng P, Xu ZC, Chen J (2011). Moderate traumatic brain injury causes acute dendritic and synaptic degeneration in the hippocampal dentate gyrus. PLoS One 6:e24566. https://doi.org/10.1371/journal.pone.0024566

Garces CA, Kurenova EV, Golubovskaya VM, Cance WG (2006). Vascular Endothelial Growth Factor Receptor-3 and Focal Adhesion Kinase Bind and Suppress Apoptosis in Breast Cancer Cells. Cancer Res 66:1446-1454. https://doi.org/10.1158/0008-5472.CAN-05-1661

Gardoni F, Bellone C, Viviani B, Marinovich M, Meli E, Pellegrini-Giampietro DE, . . . Di Luca M (2002). Lack of PSD-95 drives hippocampal neuronal cell death through activation of an αCaMKII transduction pathway. Eur J Neurosci 16:777-786. https://doi.org/10.1046/j.1460-9568.2002.02141.x

Gardoni F, Caputi A, Cimino M, Pastorino L, Cattabeni F, Di Luca M (1998). Calcium/calmodulin-dependent protein kinase II is associated with NR2A/B subunits of NMDA receptor in postsynaptic densities. J Neurochem 71:1733-1741. https://doi.org/10.1046/j.1471-4159.1998.71041733.x

Gardoni F, Schrama LH, Kamal A, Gispen WH, Cattabeni F, Di Luca M (2001). Hippocampal synaptic plasticity involves competition between Ca2+/calmodulin-dependent protein kinase II and postsynaptic density 95 for binding to the NR2A subunit of the NMDA receptor. J Neurosci 21:1501-1509. https://doi.org/10.1523/jneurosci.21-05-01501.2001

Gasperini RJ, Pavez M, Thompson AC, Mitchell CB, Hardy H, Young KM, . . . Foa L (2017). How does calcium interact with the cytoskeleton to regulate growth cone motility during axon pathfinding? Mol Cell Neurosci 84:29-35. https://doi.org/10.1016/j.mcn.2017.07.006

Gentile JE, Carrizales MG, Koleske AJ (2022). Control of Synapse Structure and Function by Actin and Its Regulators. Cells 11. https://doi.org/10.3390/cells11040603

Georges PC, Hadzimichalis NM, Sweet ES, Firestein BL (2008). The Yin–Yang of Dendrite Morphology: Unity of Actin and Microtubules. Mol Neurobiol 38:270-284. https://doi.org/10.1007/s12035-008-8046-8

Ghaffari A, Hoskin V, Szeto A, Hum M, Liaghati N, Nakatsu K, . . . Elliott BE (2014). A novel role for ezrin in breast cancer angio/lymphangiogenesis. Breast Cancer Res 16:438. https://doi.org/10.1186/s13058-014-0438-2

Ghiretti AE, Thies E, Tokito MK, Lin T, Ostap EM, Kneussel M, Holzbaur ELF (2016). Activity-Dependent Regulation of Distinct Transport and Cytoskeletal Remodeling Functions of the Dendritic Kinesin KIF21B. Neuron 92:857-872. https://doi.org/10.1016/j.neuron.2016.10.003

Glantz LA, Lewis DA (2000). Decreased dendritic spine density on prefrontal cortical pyramidal neurons in schizophrenia. Arch Gen Psychiatry 57:65-73

Gomez TM, Letourneau PC (2014). Actin dynamics in growth cone motility and navigation. J Neurochem 129:221-234. https://doi.org/10.1111/jnc.12506

Gonzalez A, Moya-Alvarado G, Gonzalez-Billaut C, Bronfman FC (2016). Cellular and molecular mechanisms regulating neuronal growth by brain-derived neurotrophic factor. Cytoskeleton 73:612-628. https://doi.org/10.1002/cm.21312

Greer P (2002). Closing in on the biological functions of fps/fes and fer. Nat Rev Mol Cell Biol 3:278-289. https://doi.org/10.1038/nrm783

Grienberger C, Konnerth A (2012). Imaging Calcium in Neurons. Neuron 73:862-885. https://doi.org/10.1016/j.neuron.2012.02.011

Grutzendler J, Helmin K, Tsai J, Gan WB (2007). Various dendritic abnormalities are associated with fibrillar amyloid deposits in Alzheimer's disease. Ann N Y Acad Sci 1097:30-39. https://doi.org/10.1196/annals.1379.003

Guidetti P, Charles V, Chen E-Y, Reddy PH, Kordower JH, Whetsell WO, . . . Tagle DA (2001). Early Degenerative Changes in Transgenic Mice Expressing Mutant Huntingtin Involve Dendritic Abnormalities but No Impairment of Mitochondrial Energy Production. Exp Neurol 169:340-350. https://doi.org/10.1006/exnr.2000.7626

Gulino R (2023). Synaptic Dysfunction and Plasticity in Amyotrophic Lateral Sclerosis. Int J Mol Sci 24:4613

Gulmez Karaca K, Kupke J, Brito DVC, Zeuch B, Thome C, Weichenhan D, . . . Oliveira AMM (2020). Neuronal ensemble-specific DNA methylation strengthens engram stability. Nat Commun 11:639. https://doi.org/10.1038/s41467-020-14498-4

Gürth C-M, do Rego Barros Fernandes Lima MA, Macarrón Palacios V, Cereceda Delgado AR, Hubrich J, D'Este E (2023). Neurofilament Levels in Dendritic Spines Associate with Synaptic Status. Cells 12:909

Haase K, Pelling AE (2015). Investigating cell mechanics with atomic force microscopy. J R Soc Interface 12:20140970. https://doi.org/10.1098/rsif.2014.0970

Hagenston AM, Bading H (2011). Calcium signaling in synapse-to-nucleus communication. Cold Spring Harb Perspect Biol 3:a004564. https://doi.org/10.1101/cshperspect.a004564

Haiko P, Makinen T, Keskitalo S, Taipale J, Karkkainen MJ, Baldwin ME, . . . Alitalo K (2008). Deletion of vascular endothelial growth factor C (VEGF-C) and VEGF-D is not equivalent to VEGF receptor 3 deletion in mouse embryos. Mol Cell Biol 28:4843-4850. https://doi.org/10.1128/mcb.02214-07

Han B, Zhou R, Xia C, Zhuang X (2017). Structural organization of the actin-spectrin-based membrane skeleton in dendrites and soma of neurons. Proc Natl Acad Sci U S A 114:E6678-e6685. https://doi.org/10.1073/pnas.1705043114

Han J, Calvo C-F, Kang Tae H, Baker Kasey L, Park J-H, Parras C, . . . Thomas J-L (2015). Vascular Endothelial Growth Factor Receptor 3 Controls Neural Stem Cell Activation in Mice and Humans. Cell Rep 10:1158-1172. https://doi.org/10.1016/j.celrep.2015.01.049

Harde E, Nicholson L, Furones Cuadrado B, Bissen D, Wigge S, Urban S, . . . Acker-Palmer A (2019). EphrinB2 regulates VEGFR2 during dendritogenesis and hippocampal circuitry development. eLife 8:e49819. https://doi.org/10.7554/eLife.49819

Hardingham GE, Arnold FJL, Bading H (2001). Nuclear calcium signaling controls CREB-mediated gene expression triggered by synaptic activity. Nat Neurosci 4:261-267. https://doi.org/10.1038/85109

Harris NC, Davydova N, Roufail S, Paquet-Fifield S, Paavonen K, Karnezis T, . . . Achen MG (2013). The propeptides of VEGF-D determine heparin binding, receptor heterodimerization, and effects on tumor biology. J Biol Chem 288:8176-8186. https://doi.org/10.1074/jbc.M112.439299

Häusser M, Spruston N, Stuart GJ (2000). Diversity and dynamics of dendritic signaling. Science 290:739-744. https://doi.org/10.1126/science.290.5492.739

Heiman MG, Shaham S (2010). Twigs into branches: how a filopodium becomes a dendrite. Curr Opin Neurobiol 20:86-91. https://doi.org/10.1016/j.conb.2009.10.016

Heinze A, Schuldt C, Khudayberdiev S, van Bommel B, Hacker D, Schulz TG, . . . Rust MB (2022). Functional interdependence of the actin regulators CAP1 and cofilin1 in control of dendritic spine morphology. Cell Mol Life Sci 79:558. https://doi.org/10.1007/s00018-022-04593-8

Heiska L, Carpén O (2005). Src phosphorylates ezrin at tyrosine 477 and induces a phosphospecific association between ezrin and a kelch-repeat protein family member. J Biol Chem 280:10244-10252. https://doi.org/10.1074/jbc.M411353200

Heiska L, Melikova M, Zhao F, Saotome I, McClatchey AI, Carpén O (2011). Ezrin is key regulator of Src-induced malignant phenotype in three-dimensional environment. Oncogene 30:4953-4962. https://doi.org/10.1038/onc.2011.207

Hemstedt TJ, Bengtson CP, Ramírez O, Oliveira AMM, Bading H (2017). Reciprocal Interaction of Dendrite Geometry and Nuclear Calcium–VEGFD Signaling Gates Memory Consolidation and Extinction. J Neurosci 37:6946-6955. https://doi.org/10.1523/jneurosci.2345-16.2017

Hill J, Hashimoto T, Lewis D (2006). Molecular mechanisms contributing to dendritic spine alterations in the prefrontal cortex of subjects with schizophrenia. Mol Psychiatry 11:557-566

Holmes DI, Zachary I (2005). The vascular endothelial growth factor (VEGF) family: angiogenic factors in health and disease. Genome Biol 6:209. https://doi.org/10.1186/gb-2005-6-2-209

Honkura N, Matsuzaki M, Noguchi J, Ellis-Davies GCR, Kasai H (2008). The Subspine Organization of Actin Fibers Regulates the Structure and Plasticity of Dendritic Spines. Neuron 57:719-729. https://doi.org/10.1016/j.neuron.2008.01.013

Hood JD, Frausto R, Kiosses WB, Schwartz MA, Cheresh DA (2003). Differential αv integrin–mediated Ras-ERK signaling during two pathways of angiogenesis. J Cell Biol 162:933-943. https://doi.org/10.1083/jcb.200304105

Horch HW, Katz LC (2002). BDNF release from single cells elicits local dendritic growth in nearby neurons. Nat Neurosci 5:1177-1184. https://doi.org/10.1038/nn927

Howes OD, Onwordi EC (2023). The synaptic hypothesis of schizophrenia version III: a master mechanism. Mol Psychiatry. https://doi.org/10.1038/s41380-023-02043-w

Huang YF, Yang CH, Huang CC, Hsu KS (2012). Vascular endothelial growth factor-dependent spinogenesis underlies antidepressant-like effects of enriched environment. J Biol Chem 287:40938-40955. https://doi.org/10.1074/jbc.M112.392076

Hutsler JJ, Zhang H (2010). Increased dendritic spine densities on cortical projection neurons in autism spectrum disorders. Brain Res 1309:83-94

Impey S, Fong AL, Wang Y, Cardinaux J-R, Fass DM, Obrietan K, . . . Goodman RH (2002). Phosphorylation of CBP Mediates Transcriptional Activation by Neural Activity and CaM Kinase IV. Neuron 34:235-244. https://doi.org/10.1016/S0896-6273(02)00654-2

Jan Y-N, Jan LY (2003). The Control of Dendrite Development. Neuron 40:229-242. https://doi.org/10.1016/S0896-6273(03)00631-7

Jan YN, Jan LY (2010). Branching out: mechanisms of dendritic arborization. Nat Rev Neurosci 11:316-328. https://doi.org/10.1038/nrn2836

Jaworski J, Kapitein LC, Gouveia SM, Dortland BR, Wulf PS, Grigoriev I, . . . Hoogenraad CC (2009). Dynamic Microtubules Regulate Dendritic Spine Morphology and Synaptic Plasticity. Neuron 61:85-100. https://doi.org/10.1016/j.neuron.2008.11.013

Jaworski J, Spangler S, Seeburg DP, Hoogenraad CC, Sheng M (2005). Control of Dendritic Arborization by the Phosphoinositide-3'-Kinase–Akt–Mammalian Target of Rapamycin Pathway. J Neurosci 25:11300-11312. https://doi.org/10.1523/jneurosci.2270-05.2005

Jeltsch M, Kaipainen A, Joukov V, Meng X, Lakso M, Rauvala H, . . . Alitalo K (1997). Hyperplasia of lymphatic vessels in VEGF-C transgenic mice. Science 276:1423-1425. https://doi.org/10.1126/science.276.5317.1423

Jha SK, Rauniyar K, Chronowska E, Mattonet K, Maina EW, Koistinen H, . . . Jeltsch M (2019). KLK3/PSA and cathepsin D activate VEGF-C and VEGF-D. eLife 8:e44478. https://doi.org/10.7554/eLife.44478

Jia H, Bagherzadeh A, Bicknell R, Duchen MR, Liu D, Zachary I (2004). Vascular Endothelial Growth Factor (VEGF)-D and VEGF-A Differentially Regulate KDR-mediated Signaling and Biological Function in Vascular Endothelial Cells*. J Biol Chem 279:36148-36157. https://doi.org/10.1074/jbc.M401538200

Jin K, Mao XO, Greenberg DA (2006). Vascular endothelial growth factor stimulates neurite outgrowth from cerebral cortical neurons via Rho kinase signaling. J Neurobiol 66:236-242. https://doi.org/10.1002/neu.20215

Jin K, Zhu Y, Sun Y, Mao XO, Xie L, Greenberg DA (2002). Vascular endothelial growth factor (VEGF) stimulates neurogenesis in vitro and in vivo. Proc Natl Acad Sci U S A 99:11946-11950. https://doi.org/10.1073/pnas.182296499

Joukov V, Sorsa T, Kumar V, Jeltsch M, Claesson-Welsh L, Cao Y, . . . Alitalo K (1997). Proteolytic processing regulates receptor specificity and activity of VEGF-C. EMBO J 16:3898-3911. https://doi.org/10.1093/emboj/16.13.3898

Kaipainen A, Korhonen J, Mustonen T, van Hinsbergh VW, Fang GH, Dumont D, . . . Alitalo K (1995). Expression of the fms-like tyrosine kinase 4 gene becomes restricted to lymphatic endothelium during development. Proc Natl Acad Sci U S A 92:3566-3570. https://doi.org/10.1073/pnas.92.8.3566

Kamemura N, Murakami S, Komatsu H, Sawanoi M, Miyamoto K, Ishidoh K, . . . Yuasa K (2017). Type II cGMP-dependent protein kinase negatively regulates fibroblast growth factor signaling by phosphorylating Raf-1 at serine 43 in rat chondrosarcoma cells. Biochem Biophys Res Commun 483:82-87. https://doi.org/10.1016/j.bbrc.2017.01.001

Kapitein LC, Hoogenraad CC (2011a). Which way to go? Cytoskeletal organization and polarized transport in neurons. Mol Cell Neurosci 46:9-20. https://doi.org/10.1016/j.mcn.2010.08.015

Kapitein Lukas C, Hoogenraad Casper C (2015). Building the Neuronal Microtubule Cytoskeleton. Neuron 87:492-506. https://doi.org/10.1016/j.neuron.2015.05.046

Kapitein LC, Yau KW, Gouveia SM, van der Zwan WA, Wulf PS, Keijzer N, . . . Hoogenraad CC (2011b). NMDA receptor activation suppresses microtubule growth and spine entry. J Neurosci 31:8194-8209. https://doi.org/10.1523/jneurosci.6215-10.2011

Kappert K, Peters KG, Böhmer FD, Ostman A (2005). Tyrosine phosphatases in vessel wall signaling. Cardiovasc Res 65:587-598. https://doi.org/10.1016/j.cardiores.2004.08.016

Karaman S, Leppänen VM, Alitalo K (2018). Vascular endothelial growth factor signaling in development and disease. Development 145. https://doi.org/10.1242/dev.151019

Karasawa T, Lombroso PJ (2014). Disruption of striatal-enriched protein tyrosine phosphatase (STEP) function in neuropsychiatric disorders. Neurosci Res 89:1-9. https://doi.org/10.1016/j.neures.2014.08.018

Karkkainen MJ, Haiko P, Sainio K, Partanen J, Taipale J, Petrova TV, . . . Alitalo K (2004). Vascular endothelial growth factor C is required for sprouting of the first lymphatic vessels from embryonic veins. Nat Immunol 5:74-80. https://doi.org/c

Karpanen T, Wirzenius M, Mäkinen T, Veikkola T, Haisma HJ, Achen MG, . . . Alitalo K (2006). Lymphangiogenic growth factor responsiveness is modulated by postnatal lymphatic vessel maturation. Am J Pathol 169:708-718. https://doi.org/10.2353/ajpath.2006.051200

Kawashima T, Kitamura K, Suzuki K, Nonaka M, Kamijo S, Takemoto-Kimura S, . . . Bito H (2013). Functional labeling of neurons and their projections using the synthetic activity-dependent promoter E-SARE. Nat Methods 10:889-895. https://doi.org/10.1038/nmeth.2559

Kessels MM, Schwintzer L, Schlobinski D, Qualmann B (2011). Controlling actin cytoskeletal organization and dynamics during neuronal morphogenesis. Eur J Cell Biol 90:926-933. https://doi.org/10.1016/j.ejcb.2010.08.011

Khaibullina AA, Rosenstein JM, Krum JM (2004). Vascular endothelial growth factor promotes neurite maturation in primary CNS neuronal cultures. Dev Brain Res 148:59-68. https://doi.org/10.1016/j.devbrainres.2003.09.022

Kim BW, Choi M, Kim YS, Park H, Lee HR, Yun CO, . . . Son H (2008). Vascular endothelial growth factor (VEGF) signaling regulates hippocampal neurons by elevation of intracellular calcium and activation of calcium/calmodulin protein kinase II and mammalian target of rapamycin. Cell Signal 20:714-725. https://doi.org/10.1016/j.cellsig.2007.12.009

Kleele T, Marinković P, Williams PR, Stern S, Weigand EE, Engerer P, . . . Misgeld T (2014). An assay to image neuronal microtubule dynamics in mice. Nat Commun 5:4827. https://doi.org/10.1038/ncomms5827

Klein S, Dieterich LC, Mathelier A, Chong C, Sliwa-Primorac A, Hong YK, . . . Detmar M (2016). DeepCAGE transcriptomics identify HOXD10 as a transcription factor regulating lymphatic endothelial responses to VEGF-C. J Cell Sci 129:2573-2585. https://doi.org/10.1242/jcs.186767

Klugmann M, Wymond Symes C, Leichtlein CB, Klaussner BK, Dunning J, Fong D, . . . During MJ (2005). AAV-mediated hippocampal expression of short and long Homer 1 proteins differentially affect cognition and seizure activity in adult rats. Mol Cell Neurosci 28:347-360. https://doi.org/10.1016/j.mcn.2004.10.002

Koch M, Dettori D, Van Nuffelen A, Souffreau J, Marconcini L, Wallays G, . . . Dewerchin M (2009). VEGF-D deficiency in mice does not affect embryonic or postnatal lymphangiogenesis but reduces lymphatic metastasis. J Pathol 219:356-364. https://doi.org/10.1002/path.2605

Koch S, Tugues S, Li X, Gualandi L, Claesson-Welsh L (2011). Signal transduction by vascular endothelial growth factor receptors. Biochem J 437:169-183. https://doi.org/10.1042/bj20110301

Koleske AJ (2013). Molecular mechanisms of dendrite stability. Nat Rev Neurosci 14:536-550. https://doi.org/10.1038/nrn3486

Kolomeets NS, Orlovskaya DD, Uranova NA (2007). Decreased numerical density of CA3 hippocampal mossy fiber synapses in schizophrenia. Synapse 61:615-621

Konietzny A, Bär J, Mikhaylova M (2017). Dendritic Actin Cytoskeleton: Structure, Functions, and Regulations. Front Cell Neurosci 11:147. https://doi.org/10.3389/fncel.2017.00147

Korobova F, Svitkina T (2010). Molecular architecture of synaptic actin cytoskeleton in hippocampal neurons reveals a mechanism of dendritic spine morphogenesis. Mol Biol Cell 21:165-176. https://doi.org/10.1091/mbc.e09-07-0596

Koscielny A, Malik AR, Liszewska E, Zmorzynska J, Tempes A, Tarkowski B, Jaworski J (2018). Adaptor Complex 2 Controls Dendrite Morphology via mTOR-Dependent Expression of GluA2. Mol Neurobiol 55:1590-1606. https://doi.org/10.1007/s12035-017-0436-3

Koskinen M, Hotulainen P (2014). Measuring F-actin properties in dendritic spines. Front Neuroanat 8:74. https://doi.org/10.3389/fnana.2014.00074

Krieg M, Fläschner G, Alsteens D, Gaub BM, Roos WH, Wuite GJL, . . . Müller DJ (2019). Atomic force microscopy-based mechanobiology. Nat Rev Phys 1:41-57. https://doi.org/10.1038/s42254-018-0001-7

Kulkarni VA, Firestein BL (2012). The dendritic tree and brain disorders. Mol Cell Neurosci 50:10-20. https://doi.org/10.1016/j.mcn.2012.03.005

Künnapuu J, Bokharaie H, Jeltsch M (2021). Proteolytic Cleavages in the VEGF Family: Generating Diversity among Angiogenic VEGFs, Essential for the Activation of Lymphangiogenic VEGFs. Biology (Basel) 10. https://doi.org/10.3390/biology10020167

Lamalice L, Houle F, Jourdan G, Huot J (2004). Phosphorylation of tyrosine 1214 on VEGFR2 is required for VEGF-induced activation of Cdc42 upstream of SAPK2/p38. Oncogene 23:434-445. https://doi.org/10.1038/sj.onc.1207034

Lamarche N, Tapon N, Stowers L, Burbelo PD, Aspenström P, Bridges T, . . . Hall A (1996). Rac and Cdc42 induce actin polymerization and G1 cell cycle progression independently of p65PAK and the JNK/SAPK MAP kinase cascade. Cell 87:519-529. https://doi.org/10.1016/s0092-8674(00)81371-9

Lampugnani MG, Orsenigo F, Gagliani MC, Tacchetti C, Dejana E (2006). Vascular endothelial cadherin controls VEGFR-2 internalization and signaling from intracellular compartments. J Cell Biol 174:593-604. https://doi.org/10.1083/jcb.200602080

Lan Y, Papoian GA (2008). The stochastic dynamics of filopodial growth. Biophys J 94:3839-3852. https://doi.org/10.1529/biophysj.107.123778

Lange C, Storkebaum E, de Almodóvar CR, Dewerchin M, Carmeliet P (2016). Vascular endothelial growth factor: a neurovascular target in neurological diseases. Nature Reviews Neurology 12:439-454. https://doi.org/10.1038/nrneurol.2016.88

Larimore JL, Chapleau CA, Kudo S, Theibert A, Percy AK, Pozzo-Miller L (2009). Bdnf overexpression in hippocampal neurons prevents dendritic atrophy caused by Rett-associated MECP2 mutations. Neurobiol Dis 34:199-211

Lasserre R, Charrin S, Cuche C, Danckaert A, Thoulouze MI, de Chaumont F, . . . Alcover A (2010). Ezrin tunes T-cell activation by controlling Dlg1 and microtubule positioning at the immunological synapse. EMBO J 29:2301-2314. https://doi.org/10.1038/emboj.2010.127

Lau D, Bengtson CP, Buchthal B, Bading H (2015). BDNF Reduces Toxic Extrasynaptic NMDA Receptor Signaling via Synaptic NMDA Receptors and Nuclear-Calcium-Induced Transcription of inhba/Activin A. Cell Rep 12:1353-1366. https://doi.org/10.1016/j.celrep.2015.07.038

Laurent CE, Delfino FJ, Cheng HY, Smithgall TE (2004a). The human c-Fes tyrosine kinase binds tubulin and microtubules through separate domains and promotes microtubule assembly. Mol Cell Biol 24:9351-9358. https://doi.org/10.1128/mcb.24.21.9351-9358.2004

Laurent CE, Smithgall TE (2004b). The c-Fes tyrosine kinase cooperates with the breakpoint cluster region protein (Bcr) to induce neurite extension in a Rac- and Cdc42-dependent manner. Exp Cell Res 299:188-198. https://doi.org/10.1016/j.yexcr.2004.05.010

Lavoie-Cardinal F, Bilodeau A, Lemieux M, Gardner MA, Wiesner T, Laramée G, . . . De Koninck P (2020). Neuronal activity remodels the F-actin based submembrane lattice in dendrites but not axons of hippocampal neurons. Sci Rep 10:11960. https://doi.org/10.1038/s41598-020-68180-2

Le Bras B, Barallobre MJ, Homman-Ludiye J, Ny A, Wyns S, Tammela T, . . . Thomas JL (2006). VEGF-C is a trophic factor for neural progenitors in the vertebrate embryonic brain. Nat Neurosci 9:340-348. https://doi.org/10.1038/nn1646

Leggere JC, Saito Y, Darnell RB, Tessier-Lavigne M, Junge HJ, Chen Z (2016). NOVA regulates Dcc alternative splicing during neuronal migration and axon guidance in the spinal cord. Elife 5. https://doi.org/10.7554/eLife.14264

Lei Y, Cao YX, Xu CB, Zhang Y (2008). The Raf-1 inhibitor GW5074 and dexamethasone suppress sidestream smoke-induced airway hyperresponsiveness in mice. Respir Res 9:71. https://doi.org/10.1186/1465-9921-9-71

Leicht DT, Balan V, Kaplun A, Singh-Gupta V, Kaplun L, Dobson M, Tzivion G (2007). Raf kinases: Function, regulation and role in human cancer. Biochim Biophys Acta 1773:1196-1212. https://doi.org/10.1016/j.bbamcr.2007.05.001

Lein ES, Hawrylycz MJ, Ao N, Ayres M, Bensinger A, Bernard A, . . . Jones AR (2007). Genome-wide atlas of gene expression in the adult mouse brain. Nature 445:168-176. https://doi.org/10.1038/nature05453

Lemmon MA, Schlessinger J (2010). Cell signaling by receptor tyrosine kinases. Cell 141:1117-1134. https://doi.org/10.1016/j.cell.2010.06.011

Leondaritis G, Eickholt BJ (2015). Short Lives with Long-Lasting Effects: Filopodia Protrusions in Neuronal Branching Morphogenesis. PLoS Biol 13:e1002241. https://doi.org/10.1371/journal.pbio.1002241

Leppänen V-M, Jeltsch M, Anisimov A, Tvorogov D, Aho K, Kalkkinen N, . . . Alitalo K (2011). Structural determinants of vascular endothelial growth factor-D receptor binding and specificity. Blood 117:1507-1515. https://doi.org/10.1182/blood-2010-08-301549

Leppänen VM, Tvorogov D, Kisko K, Prota AE, Jeltsch M, Anisimov A, . . . Alitalo K (2013). Structural and mechanistic insights into VEGF receptor 3 ligand binding and activation. Proc Natl Acad Sci U S A 110:12960-12965. https://doi.org/10.1073/pnas.1301415110

Leterrier C (2018). The Axon Initial Segment: An Updated Viewpoint. The Journal of Neuroscience 38:2135-2145. https://doi.org/10.1523/jneurosci.1922-17.2018

Licht T, Eavri R, Goshen I, Shlomai Y, Mizrahi A, Keshet E (2010). VEGF is required for dendritogenesis of newly born olfactory bulb interneurons. Development 137:261-271. https://doi.org/10.1242/dev.039636

Licht T, Goshen I, Avital A, Kreisel T, Zubedat S, Eavri R, . . . Keshet E (2011). Reversible modulations of neuronal plasticity by VEGF. Proc Natl Acad Sci U S A 108:5081-5086. https://doi.org/10.1073/pnas.1007640108

Lim L, Bui H, Farrelly O, Yang J, Li L, Enis D, . . . Kahn ML (2019). Hemostasis stimulates lymphangiogenesis through release and activation of VEGFC. Blood 134:1764-1775. https://doi.org/10.1182/blood.2019001736

Lin Y-C, Koleske AJ (2010). Mechanisms of Synapse and Dendrite Maintenance and Their Disruption in Psychiatric and Neurodegenerative Disorders. Annu Rev Neurosci 33:349-378. https://doi.org/10.1146/annurev-neuro-060909-153204

Litke C, Bading H, Mauceri D (2018). Histone deacetylase 4 shapes neuronal morphology via a mechanism involving regulation of expression of vascular endothelial growth factor D. J Biol Chem 293:8196-8207. https://doi.org/10.1074/jbc.RA117.001613

Litke C, Hagenston AM, Kenkel A-K, Paldy E, Lu J, Kuner R, Mauceri D (2022). Organic anion transporter 1 is an HDAC4-regulated mediator of nociceptive hypersensitivity in mice. Nat Commun 13:875. https://doi.org/10.1038/s41467-022-28357-x

Lohela M, Bry M, Tammela T, Alitalo K (2009). VEGFs and receptors involved in angiogenesis versus lymphangiogenesis. Curr Opin Cell Biol 21:154-165. https://doi.org/10.1016/j.ceb.2008.12.012

London M, Häusser M (2005). Dendritic computation. Annu Rev Neurosci 28:503-532. https://doi.org/10.1146/annurev.neuro.28.061604.135703

López-Muñoz F, Boya J, Alamo C (2006). Neuron theory, the cornerstone of neuroscience, on the centenary of the Nobel Prize award to Santiago Ramón y Cajal. Brain Res Bull 70:391-405. https://doi.org/10.1016/j.brainresbull.2006.07.010

Lowery LA, Van Vactor D (2009). The trip of the tip: understanding the growth cone machinery. Nat Rev Mol Cell Biol 10:332-343. https://doi.org/10.1038/nrm2679

Lu R, Liu X, Long H, Ma L (2012). Effects of prenatal cocaine and heroin exposure on neuronal dendrite morphogenesis and spatial recognition memory in mice. Neurosci Lett 522:128-133. https://doi.org/10.1016/j.neulet.2012.06.023

Luck R, Urban S, Karakatsani A, Harde E, Sambandan S, Nicholson L, . . . Ruiz de Almodóvar C (2019). VEGF/VEGFR2 signaling regulates hippocampal axon branching during development. Elife 8. https://doi.org/10.7554/eLife.49818

Ma Y-Y, Li K-Y, Wang J-J, Huang Y-L, Huang Y, Sun F-Y (2009). Vascular endothelial growth factor acutely reduces calcium influx via inhibition of the Ca2+ channels in rat hippocampal neurons. J Neurosci Res 87:393-402. https://doi.org/10.1002/jnr.21859

Magariños M, Aburto MR, Sánchez-Calderón H, Muñoz-Agudo C, Rapp UR, Varela-Nieto I (2011). RAF Kinase Activity Regulates Neuroepithelial Cell Proliferation and Neuronal Progenitor Cell Differentiation during Early Inner Ear Development. PLoS One 5:e14435. https://doi.org/10.1371/journal.pone.0014435

Mahaman YAR, Huang F, Embaye KS, Wang X, Zhu F (2021). The Implication of STEP in Synaptic Plasticity and Cognitive Impairments in Alzheimer's Disease and Other Neurological Disorders. Front Cell Dev Biol 9:680118. https://doi.org/10.3389/fcell.2021.680118

Mak H, Naba A, Varma S, Schick C, Day A, SenGupta SK, . . . Elliott BE (2012). Ezrin phosphorylation on tyrosine 477 regulates invasion and metastasis of breast cancer cells. BMC Cancer 12:82. https://doi.org/10.1186/1471-2407-12-82

Mäkinen T, Jussila L, Veikkola T, Karpanen T, Kettunen MI, Pulkkanen KJ, . . . Alitalo K (2001a). Inhibition of lymphangiogenesis with resulting lymphedema in transgenic mice expressing soluble VEGF receptor-3. Nat Med 7:199-205. https://doi.org/10.1038/84651

Mäkinen T, Veikkola T, Mustjoki S, Karpanen T, Catimel B, Nice EC, . . . Alitalo K (2001b). Isolated lymphatic endothelial cells transduce growth, survival and migratory signals via the VEGF-C/D receptor VEGFR-3. EMBO J 20:4762-4773. https://doi.org/10.1093/emboj/20.17.4762

Mallavarapu A, Mitchison T (1999). Regulated actin cytoskeleton assembly at filopodium tips controls their extension and retraction. J Cell Biol 146:1097-1106. https://doi.org/10.1083/jcb.146.5.1097

Marin-Padilla M (1972). Structural abnormalities of the cerebral cortex in human chromosomal aberrations: a Golgi study. Brain Res 44:625-629

Masurkar AV (2018). Towards a circuit-level understanding of hippocampal CA1 dysfunction in Alzheimer's disease across anatomical axes. J Alzheimers Dis Parkinsonism 8

Matsumoto T, Bohman S, Dixelius J, Berge T, Dimberg A, Magnusson P, . . . Claesson-Welsh L (2005). VEGF receptor-2 Y951 signaling and a role for the adapter molecule TSAd in tumor angiogenesis. EMBO J 24:2342-2353. https://doi.org/10.1038/sj.emboj.7600709

Matsumoto Y, Inden M, Tamura A, Hatano R, Tsukita S, Asano S (2014). Ezrin mediates neuritogenesis via down-regulation of RhoA activity in cultured cortical neurons. PLoS One 9:e105435. https://doi.org/10.1371/journal.pone.0105435

Mauceri D, Buchthal B, Hemstedt TJ, Weiss U, Klein CD, Bading H (2020). Nasally delivered VEGFD mimetics mitigate stroke-induced dendrite loss and brain damage. Proc Natl Acad Sci U S A 117:8616-8623. https://doi.org/10.1073/pnas.2001563117

Mauceri D, Freitag HE, Oliveira AM, Bengtson CP, Bading H (2011). Nuclear calcium-VEGFD signaling controls maintenance of dendrite arborization necessary for memory formation. Neuron 71:117-130. https://doi.org/10.1016/j.neuron.2011.04.022

Mauceri D, Hagenston AM, Schramm K, Weiss U, Bading H (2015). Nuclear Calcium Buffering Capacity Shapes Neuronal Architecture. J Biol Chem 290:23039-23049. https://doi.org/10.1074/jbc.M115.654962

Maurer J, Yanez A, Bengtson CP, Bading H, Draguhn A, Mauceri D, Both M (2020). VEGF-D Downregulation in CA1 Pyramidal Neurons Exerts Asymmetric Changes of Dendritic Morphology without Correlated Electrophysiological Alterations. Neuroscience 448:28-42. https://doi.org/10.1016/j.neuroscience.2020.09.012

McAllister AK (2000). Cellular and Molecular Mechanisms of Dendrite Growth. Cereb Cortex 10:963-973. https://doi.org/10.1093/cercor/10.10.963

McAllister AK, Lo DC, Katz LC (1995). Neurotrophins regulate dendritic growth in developing visual cortex. Neuron 15:791-803. https://doi.org/10.1016/0896-6273(95)90171-x

McClure C, Cole KL, Wulff P, Klugmann M, Murray AJ (2011). Production and Titering of Recombinant Adeno-associated Viral Vectors. JoVE:e3348. https://doi.org/10.3791/3348

McColl BK, Baldwin ME, Roufail S, Freeman C, Moritz RL, Simpson RJ, . . . Achen MG (2003). Plasmin activates the lymphangiogenic growth factors VEGF-C and VEGF-D. J Exp Med 198:863-868. https://doi.org/10.1084/jem.20030361

McColl BK, Paavonen K, Karnezis T, Harris NC, Davydova N, Rothacker J, . . . Achen MG (2007). Proprotein convertases promote processing of VEGF-D, a critical step for binding the angiogenic receptor VEGFR-2. The FASEB Journal 21:1088-1098. https://doi.org/10.1096/fj.06-7060com

McDonald NQ, Hendrickson WA (1993). A structural superfamily of growth factors containing a cystine knot motif. Cell 73:421-424. https://doi.org/10.1016/0092-8674(93)90127-c

McMullen M, Keller R, Sussman M, Pumiglia K (2004). Vascular endothelial growth factor-mediated activation of p38 is dependent upon Src and RAFTK/Pyk2. Oncogene 23:1275-1282. https://doi.org/10.1038/sj.onc.1207243

Medeiros NA, Burnette DT, Forscher P (2006). Myosin II functions in actin-bundle turnover in neuronal growth cones. Nat Cell Biol 8:216-226. https://doi.org/10.1038/ncb1367

Meissirel C, Ruiz de Almodovar C, Knevels E, Coulon C, Chounlamountri N, Segura I, . . . Carmeliet P (2011). VEGF modulates NMDA receptors activity in cerebellar granule cells through Src-family kinases before

synapse formation. Proc Natl Acad Sci U S A 108:13782-13787. https://doi.org/10.1073/pnas.1100341108

Merino P, Diaz A, Manrique LG, Cheng L, Yepes M (2018). Urokinase-type plasminogen activator (uPA) promotes ezrin-mediated reorganization of the synaptic cytoskeleton in the ischemic brain. J Biol Chem 293:9234-9247. https://doi.org/10.1074/jbc.RA118.002534

Metz AE, Yau H-J, Centeno MV, Apkarian AV, Martina M (2009). Morphological and functional reorganization of rat medial prefrontal cortex in neuropathic pain. Proc Natl Acad Sci U S A 106:2423-2428. https://doi.org/10.1073/pnas.0809897106

Meyer RD, Sacks DB, Rahimi N (2008). IQGAP1-dependent signaling pathway regulates endothelial cell proliferation and angiogenesis. PLoS One 3:e3848. https://doi.org/10.1371/journal.pone.0003848

Mikhaylova M, Rentsch J, Ewers H (2020). Actomyosin Contractility in the Generation and Plasticity of Axons and Dendritic Spines. Cells 9. https://doi.org/10.3390/cells9092006

Minegishi T, Kastian RF, Inagaki N (2023). Mechanical regulation of synapse formation and plasticity. Semin Cell Dev Biol 140:82-89. https://doi.org/10.1016/j.semcdb.2022.05.017

Mitchison T, Kirschner M (1984). Dynamic instability of microtubule growth. Nature 312:237-242

Mitchison T, Kirschner M (1988). Cytoskeletal dynamics and nerve growth. Neuron 1:761-772. https://doi.org/10.1016/0896-6273(88)90124-9

Moccia F, Negri S, Shekha M, Faris P, Guerra G (2019). Endothelial Ca(2+) Signaling, Angiogenesis and Vasculogenesis: just What It Takes to Make a Blood Vessel. Int J Mol Sci 20. https://doi.org/10.3390/ijms20163962

Monaghan RM, Page DJ, Ostergaard P, Keavney BD (2020). The physiological and pathological functions of VEGFR3 in cardiac and lymphatic development and related diseases. Cardiovasc Res 117:1877-1890. https://doi.org/10.1093/cvr/cvaa291

Moolman DL, Vitolo OV, Vonsattel JP, Shelanski ML (2004). Dendrite and dendritic spine alterations in Alzheimer models. J Neurocytol 33:377-387. https://doi.org/10.1023/b:Neur.0000044197.83514.64

Muller YA, Li B, Christinger HW, Wells JA, Cunningham BC, de Vos AM (1997). Vascular endothelial growth factor: crystal structure and functional mapping of the kinase domain receptor binding site. Proc Natl Acad Sci U S A 94:7192-7197. https://doi.org/10.1073/pnas.94.14.7192

Murchie R, Guo CH, Persaud A, Muise A, Rotin D (2014). Protein tyrosine phosphatase σ targets apical junction complex proteins in the intestine and regulates epithelial permeability. Proc Natl Acad Sci U S A 111:693-698. https://doi.org/10.1073/pnas.1315017111

Naba A, Reverdy C, Louvard D, Arpin M (2008). Spatial recruitment and activation of the Fes kinase by ezrin promotes HGF-induced cell scattering. EMBO J 27:38-50. https://doi.org/10.1038/sj.emboj.7601943

Nian Q, Li Y, Li J, Zhao L, Rodrigues Lima F, Zeng J, . . . Ye Z (2024). U2AF1 in various neoplastic diseases and relevant targeted therapies for malignant cancers with complex mutations (Review). Oncol Rep 51. https://doi.org/10.3892/or.2023.8664

Nichol RI, Hagen KM, Lumbard DC, Dent EW, Gómez TM (2016). Guidance of Axons by Local Coupling of Retrograde Flow to Point Contact Adhesions. J Neurosci 36:2267-2282. https://doi.org/10.1523/jneurosci.2645-15.2016

Nilsson I, Bahram F, Li X, Gualandi L, Koch S, Jarvius M, . . . Claesson-Welsh L (2010). VEGF receptor 2/-3 heterodimers detected in situ by proximity ligation on angiogenic sprouts. EMBO J 29:1377-1388. https://doi.org/10.1038/emboj.2010.30

Nirschl JJ, Ghiretti AE, Holzbaur ELF (2017). The impact of cytoskeletal organization on the local regulation of neuronal transport. Nat Rev Neurosci 18:585-597. https://doi.org/10.1038/nrn.2017.100

Njoo C, Agarwal N, Lutz B, Kuner R (2015). The Cannabinoid Receptor CB1 Interacts with the WAVE1 Complex and Plays a Role in Actin Dynamics and Structural Plasticity in Neurons. PLoS Biol 13:e1002286. https://doi.org/10.1371/journal.pbio.1002286

Nurmi H, Saharinen P, Zarkada G, Zheng W, Robciuc MR, Alitalo K (2015). VEGF-C is required for intestinal lymphatic vessel maintenance and lipid absorption. EMBO Mol Med 7:1418-1425. https://doi.org/10.15252/emmm.201505731

Oliva A, Fernández-Ruiz A, Buzsáki G, Berényi A (2016). Role of Hippocampal CA2 Region in Triggering Sharp-Wave Ripples. Neuron 91:1342-1355. https://doi.org/10.1016/j.neuron.2016.08.008

Oliveira AM, Litke C, Paldy E, Hagenston AM, Lu J, Kuner R, . . . Mauceri D (2019). Epigenetic control of hypersensitivity in chronic inflammatory pain by the de novo DNA methyltransferase Dnmt3a2. Mol Pain 15:1744806919827469. https://doi.org/10.1177/1744806919827469

Olofsson B, Jeltsch M, Eriksson U, Alitalo K (1999). Current biology of VEGF-B and VEGF-C. Curr Opin Biotechnol 10:528-535. https://doi.org/10.1016/s0958-1669(99)00024-5

Olsson A-K, Dimberg A, Kreuger J, Claesson-Welsh L (2006). VEGF receptor signalling ? in control of vascular function. Nature Reviews Molecular Cell Biology 7:359-371. https://doi.org/10.1038/nrm1911

Omotade OF, Pollitt SL, Zheng JQ (2017). Actin-based growth cone motility and guidance. Mol Cell Neurosci 84:4-10. https://doi.org/10.1016/j.mcn.2017.03.001

Orlandini M, Marconcini L, Ferruzzi R, Oliviero S (1996a). Identification of a c-fos-induced gene that is related to the platelet-derived growth factor/vascular endothelial growth factor family. Proc Natl Acad Sci U S A 93:11675-11680. https://doi.org/10.1073/pnas.93.21.11675

Orlandini M, Marconcini L, Ferruzzi R, Oliviero S (1996b). Identification of a c-fos-induced gene that is related to the platelet-derived growth factor/vascular endothelial growth factor family. Proc Natl Acad Sci U S A 93:11675-11680. https://doi.org/10.1073/pnas.93.21.11675

Pajusola K, Aprelikova O, Armstrong E, Morris S, Alitalo K (1993). Two human FLT4 receptor tyrosine kinase isoforms with distinct carboxy terminal tails are produced by alternative processing of primary transcripts. Oncogene 8:2931-2937

Pajusola K, Aprelikova O, Pelicci G, Weich H, Claesson-Welsh L, Alitalo K (1994). Signalling properties of FLT4, a proteolytically processed receptor tyrosine kinase related to two VEGF receptors. Oncogene 9:3545-3555

Pannese E (2011). Morphological changes in nerve cells during normal aging. Brain Struct Funct 216:85-89. https://doi.org/10.1007/s00429-011-0308-y

Papadia S, Stevenson P, Hardingham NR, Bading H, Hardingham GE (2005). Nuclear Ca2+ and the cAMP response element-binding protein family mediate a late phase of activity-dependent neuroprotection. J Neurosci 25:4279-4287. https://doi.org/10.1523/jneurosci.5019-04.2005

Paredes I, Himmels P, Ruiz de Almodóvar C (2018). Neurovascular Communication during CNS Development. Dev Cell 45:10-32. https://doi.org/10.1016/j.devcel.2018.01.023

Paridaen JT, Huttner WB (2014). Neurogenesis during development of the vertebrate central nervous system. EMBO reports 15:351-364. https://doi.org/10.1002/embr.201438447

Park J-H, Kim S-H, Choi M-C, Lee J, Oh D-Y, Im S-A, . . . Kim T-Y (2008). Class II histone deacetylases play pivotal roles in heat shock protein 90-mediated proteasomal degradation of vascular endothelial growth factor receptors. Biochem Biophys Res Commun 368:318-322. https://doi.org/10.1016/j.bbrc.2008.01.056

Park JH, Roll-Mecak A (2018). The tubulin code in neuronal polarity. Curr Opin Neurobiol 51:95-102. https://doi.org/10.1016/j.conb.2018.03.001

Parrish JZ, Emoto K, Kim MD, Jan YN (2007). Mechanisms that Regulate Establishment, Maintenance, and Remodeling of Dendritic Fields. Annu Rev Neurosci 30:399-423. https://doi.org/10.1146/annurev.neuro.29.051605.112907

Partanen TA, Arola J, Saaristo A, Jussila L, Ora A, Miettinen M, . . . Alitalo K (2000). VEGF-C and VEGF-D expression in neuroendocrine cells and their receptor, VEGFR-3, in fenestrated blood vessels in human tissues. The FASEB Journal 14:2087-2096

Paul S, Nairn AC, Wang P, Lombroso PJ (2003). NMDA-mediated activation of the tyrosine phosphatase STEP regulates the duration of ERK signaling. Nat Neurosci 6:34-42. https://doi.org/10.1038/nn989

Paul S, Snyder GL, Yokakura H, Picciotto MR, Nairn AC, Lombroso PJ (2000). The Dopamine/D1 receptor mediates the phosphorylation and inactivation of the protein tyrosine phosphatase STEP via a PKA-dependent pathway. J Neurosci 20:5630-5638. https://doi.org/10.1523/jneurosci.20-15-05630.2000

Pchitskaya E, Kraskovskaya N, Chernyuk D, Popugaeva E, Zhang H, Vlasova O, Bezprozvanny I (2017). Stim2-Eb3 Association and Morphology of Dendritic Spines in Hippocampal Neurons. Sci Rep 7:17625. https://doi.org/10.1038/s41598-017-17762-8

Pelucchi S, Vandermeulen L, Pizzamiglio L, Aksan B, Yan J, Konietzny A, . . . Marcello E (2020). Cyclase-associated protein 2 dimerization regulates cofilin in synaptic plasticity and Alzheimer's disease. Brain Commun 2:fcaa086. https://doi.org/10.1093/braincomms/fcaa086

Pelucchi S, Vandermeulen L, Pizzamiglio L, Aksan B, Yan J, Konietzny A, . . . Marcello E (2019). CAP2 is a novel regulator of Cofilin in synaptic plasticity and Alzheimer's disease. bioRxiv:789552. https://doi.org/10.1101/789552

Perron JC, Bixby JL (1999). Distinct neurite outgrowth signaling pathways converge on ERK activation. Mol Cell Neurosci 13:362-378. https://doi.org/10.1006/mcne.1999.0753

Persico MG, Vincenti V, DiPalma T (1999) Structure, Expression and Receptor-Binding Properties of Placenta Growth Factor (PlGF). In: Claesson-Welsh L (ed) Vascular Growth Factors and Angiogenesis. Springer Berlin Heidelberg, Berlin, Heidelberg, pp 31-40

Planas-Paz L, Strilić B, Goedecke A, Breier G, Fässler R, Lammert E (2012). Mechanoinduction of lymph vessel expansion. EMBO J 31:788-804. https://doi.org/10.1038/emboj.2011.456

Polleux F, Morrow T, Ghosh A (2000). Semaphorin 3A is a chemoattractant for cortical apical dendrites. Nature 404:567-573. https://doi.org/10.1038/35007001

Ponuwei GA (2016). A glimpse of the ERM proteins. J Biomed Sci 23:35. https://doi.org/10.1186/s12929-016-0246-3

Popovici C, Isnardon D, Birnbaum D, Roubin R (2002). Caenorhabditis elegans receptors related to mammalian vascular endothelial growth factor receptors are expressed in neural cells. Neurosci Lett 329:116-120. https://doi.org/10.1016/s0304-3940(02)00595-5

Poulain FE, Sobel A (2010). The microtubule network and neuronal morphogenesis: Dynamic and coordinated orchestration through multiple players. Mol Cell Neurosci 43:15-32. https://doi.org/10.1016/j.mcn.2009.07.012

Proia P, Schiera G, Mineo M, Ingrassia AM, Santoro G, Savettieri G, Di Liegro I (2008). Astrocytes shed extracellular vesicles that contain fibroblast growth factor-2 and vascular endothelial growth factor. Int J Mol Med 21:63-67

Qu Y, Hahn I, Webb SE, Pearce SP, Prokop A (2017). Periodic actin structures in neuronal axons are required to maintain microtubules. Mol Biol Cell 28:296-308. https://doi.org/10.1091/mbc.E16-10-0727

Radley J, Sisti H, Hao J, Rocher AB, McCall T, Hof P, . . . Morrison J (2004). Chronic behavioral stress induces apical dendritic reorganization in pyramidal neurons of the medial prefrontal cortex. Neuroscience 125:1-6

Radzicki D, Chong S, Dudek SM (2023). Morphological and molecular markers of mouse area CA2 along the proximodistal and dorsoventral hippocampal axes. Hippocampus 33:133-149. https://doi.org/10.1002/hipo.23509

Ramstad C, Sundvold V, Johansen HK, Lea T (2000). cAMP-dependent protein kinase (PKA) inhibits T cell activation by phosphorylating ser-43 of raf-1 in the MAPK/ERK pathway. Cell Signal 12:557-563. https://doi.org/10.1016/s0898-6568(00)00097-8

Rapp UR, Goldsborough MD, Mark GE, Bonner TI, Groffen J, Reynolds FH, Stephenson JR (1983). Structure and biological activity of v-raf, a unique oncogene transduced by a retrovirus. Proc Natl Acad Sci U S A 80:4218-4222. https://doi.org/10.1073/pnas.80.14.4218

Raymond GV, Bauman ML, Kemper TL (1995). Hippocampus in autism: a Golgi analysis. Acta Neuropathol 91:117-119

Redmond L, Ghosh A (2005). Regulation of dendritic development by calcium signaling. Cell Calcium 37:411-416. https://doi.org/10.1016/j.ceca.2005.01.009

Redmond L, Kashani AH, Ghosh A (2002). Calcium Regulation of Dendritic Growth via CaM Kinase IV and CREB-Mediated Transcription. Neuron 34:999-1010. https://doi.org/10.1016/S0896-6273(02)00737-7

Reina S, Checchetto V (2021). Voltage-Dependent Anion Selective Channel 3: Unraveling Structural and Functional Features of the Least Known Porin Isoform. Front Physiol 12:784867. https://doi.org/10.3389/fphys.2021.784867

Reina S, Guarino F, Magrì A, De Pinto V (2016). VDAC3 As a Potential Marker of Mitochondrial Status Is Involved in Cancer and Pathology. Front Oncol 6:264. https://doi.org/10.3389/fonc.2016.00264

Ribak CE, Dashtipour K (2002). Neuroplasticity in the damaged dentate gyrus of the epileptic brain. Prog Brain Res 136:319-328. https://doi.org/10.1016/S0079-6123(02)36027-8

Riedl J, Crevenna AH, Kessenbrock K, Yu JH, Neukirchen D, Bista M, . . . Wedlich-Soldner R (2008). Lifeact: a versatile marker to visualize F-actin. Nat Methods 5:605-607. https://doi.org/10.1038/nmeth.1220

Rissanen TT, Markkanen JE, Gruchala M, Heikura T, Puranen A, Kettunen MI, . . . Ylä-Herttuala S (2003). VEGF-D is the strongest angiogenic and lymphangiogenic effector among VEGFs delivered into skeletal muscle via adenoviruses. Circ Res 92:1098-1106. https://doi.org/10.1161/01.Res.0000073584.46059.E3

Rockson SG (2010). Causes and consequences of lymphatic disease. Ann N Y Acad Sci 1207:E2-E6. https://doi.org/10.1111/j.1749-6632.2010.05804.x

Rolls MM, Thyagarajan P, Feng C (2021). Microtubule dynamics in healthy and injured neurons. Dev Neurobiol 81:321-332. https://doi.org/10.1002/dneu.22746

Roossien DH, Lamoureux P, Miller KE (2014). Cytoplasmic dynein pushes the cytoskeletal meshwork forward during axonal elongation. J Cell Sci 127:3593-3602. https://doi.org/10.1242/jcs.152611

Rosenstein JM, Krum JM, Ruhrberg C (2010). VEGF in the nervous system. Organogenesis 6:107-114. https://doi.org/10.4161/org.6.2.11687

Rosenstein JM, Mani N, Khaibullina A, Krum JM (2003). Neurotrophic Effects of Vascular Endothelial Growth Factor on Organotypic Cortical Explants and Primary Cortical Neurons. The Journal of Neuroscience 23:11036-11044. https://doi.org/10.1523/jneurosci.23-35-11036.2003

Rousseau S, Houle F, Kotanides H, Witte L, Waltenberger J, Landry J, Huot J (2000). Vascular endothelial growth factor (VEGF)-driven actin-based motility is mediated by VEGFR2 and requires concerted activation of stress-activated protein kinase 2 (SAPK2/p38) and geldanamycin-sensitive phosphorylation of focal adhesion kinase. J Biol Chem 275:10661-10672. https://doi.org/10.1074/jbc.275.14.10661

Rousseau S, Houle F, Landry J, Huot J (1997). p38 MAP kinase activation by vascular endothelial growth factor mediates actin reorganization and cell migration in human endothelial cells. Oncogene 15:2169-2177. https://doi.org/10.1038/sj.onc.1201380

Rouven Brückner B, Pietuch A, Nehls S, Rother J, Janshoff A (2015). Ezrin is a Major Regulator of Membrane Tension in Epithelial Cells. Sci Rep 5:14700. https://doi.org/10.1038/srep14700

Ruch C, Skiniotis G, Steinmetz MO, Walz T, Ballmer-Hofer K (2007). Structure of a VEGF–VEGF receptor complex determined by electron microscopy. Nat Struct Mol Biol 14:249-250. https://doi.org/10.1038/nsmb1202

Rudelli R, Brown W, Wisniewski K, Jenkins E, Laure-Kamionowska M, Connell F, Wisniewski H (1985). Adult fragile X syndrome: clinico-neuropathologic findings. Acta Neuropathol 67:289-295

Ruiz de Almodovar C, Coulon C, Salin PA, Knevels E, Chounlamountri N, Poesen K, . . . Meissirel C (2010). Matrix-binding vascular endothelial growth factor (VEGF) isoforms guide granule cell migration in the cerebellum via VEGF receptor Flk1. J Neurosci 30:15052-15066. https://doi.org/10.1523/jneurosci.0477-10.2010

Runge K, Cardoso C, de Chevigny A (2020). Dendritic Spine Plasticity: Function and Mechanisms. Front Synaptic Neurosci 12. https://doi.org/10.3389/fnsyn.2020.00036

Rust MB, Khudayberdiev S, Pelucchi S, Marcello E (2020). CAPt'n of Actin Dynamics: Recent Advances in the Molecular, Developmental and Physiological Functions of Cyclase-Associated Protein (CAP). Front Cell Dev Biol 8:586631. https://doi.org/10.3389/fcell.2020.586631

Saaristo A, Karkkainen MJ, Alitalo K (2002). Insights into the molecular pathogenesis and targeted treatment of lymphedema. Ann N Y Acad Sci 979:94-110. https://doi.org/10.1111/j.1749-6632.2002.tb04871.x

Sainath R, Gallo G (2015). Cytoskeletal and signaling mechanisms of neurite formation. Cell Tissue Res 359:267-278. https://doi.org/10.1007/s00441-014-1955-0

Saito Y, Miranda-Rottmann S, Ruggiu M, Park CY, Fak JJ, Zhong R, . . . Darnell RB (2016). NOVA2-mediated RNA regulation is required for axonal pathfinding during development. Elife 5. https://doi.org/10.7554/eLife.14371

Sakai J (2020). How synaptic pruning shapes neural wiring during development and, possibly, in disease. Proc Natl Acad Sci U S A 117:16096-16099. https://doi.org/10.1073/pnas.2010281117

Salameh A, Galvagni F, Bardelli M, Bussolino F, Oliviero S (2005). Direct recruitment of CRK and GRB2 to VEGFR-3 induces proliferation, migration, and survival of endothelial cells through the activation of ERK, AKT, and JNK pathways. Blood 106:3423-3431. https://doi.org/10.1182/blood-2005-04-1388

Salbreux G, Charras G, Paluch E (2012). Actin cortex mechanics and cellular morphogenesis. Trends Cell Biol 22:536-545. https://doi.org/10.1016/j.tcb.2012.07.001

Salib A, Jayatilleke N, Seneviratne JA, Mayoh C, De Preter K, Speleman F, . . . Marshall GM (2024). MYCN and SNRPD3 cooperate to maintain a balance of alternative splicing events that drives neuroblastoma progression. Oncogene 43:363-377. https://doi.org/10.1038/s41388-023-02897-y

Salter MW, Kalia LV (2004). Src kinases: a hub for NMDA receptor regulation. Nature Reviews Neuroscience 5:317-328. https://doi.org/10.1038/nrn1368

Sampson MJ, Decker WK, Beaudet AL, Ruitenbeek W, Armstrong D, Hicks MJ, Craigen WJ (2001). Immotile sperm and infertility in mice lacking mitochondrial voltage-dependent anion channel type 3. J Biol Chem 276:39206-39212. https://doi.org/10.1074/jbc.M104724200

Sánchez-Huertas C, Herrera E (2021). With the Permission of Microtubules: An Updated Overview on Microtubule Function During Axon Pathfinding. Front Mol Neurosci 14. https://doi.org/10.3389/fnmol.2021.759404

Sanz C, León Y, Troppmair J, Rapp UR, Varela-Nieto I (1999). Strict regulation of c-Raf kinase levels is required for early organogenesis of the vertebrate inner ear. Oncogene 18:429-437. https://doi.org/10.1038/sj.onc.1202312

Saunders A, Macosko EZ, Wysoker A, Goldman M, Krienen FM, de Rivera H, . . . McCarroll SA (2018). Molecular Diversity and Specializations among the Cells of the Adult Mouse Brain. Cell 174:1015-1030.e1016. https://doi.org/10.1016/j.cell.2018.07.028

Saygideğer-Kont Y, Minas TZ, Jones H, Hour S, Çelik H, Temel I, . . . Üren A (2016). Ezrin Enhances EGFR Signaling and Modulates Erlotinib Sensitivity in Non-Small Cell Lung Cancer Cells. Neoplasia 18:111-120. https://doi.org/10.1016/j.neo.2016.01.002

Schätzle P, Kapitein LC, Hoogenraad CC (2016). Live imaging of microtubule dynamics in organotypic hippocampal slice cultures. Methods Cell Biol 131:107-126. https://doi.org/10.1016/bs.mcb.2015.06.006

Schiera G, Proia P, Alberti C, Mineo M, Savettieri G, Di Liegro I (2007). Neurons produce FGF2 and VEGF and secrete them at least in part by shedding extracellular vesicles. J Cell Mol Med 11:1384-1394. https://doi.org/10.1111/j.1582-4934.2007.00100.x

Schlumm F, Mauceri D, Freitag HE, Bading H (2013). Nuclear calcium signaling regulates nuclear export of a subset of class IIa histone deacetylases following synaptic activity. J Biol Chem 288:8074-8084. https://doi.org/10.1074/jbc.M112.432773

Schlüter A, Aksan B, Diem R, Fairless R, Mauceri D (2020). VEGFD Protects Retinal Ganglion Cells and, consequently, Capillaries against Excitotoxic Injury. Mol Ther Methods Clin Dev 17:281-299. https://doi.org/10.1016/j.omtm.2019.12.009

Schonfeld-Dado E, Fishbein I, Segal M (2009). Degeneration of cultured cortical neurons following prolonged inactivation: molecular mechanisms. J Neurochem 110:1203-1213. https://doi.org/10.1111/j.1471-4159.2009.06204.x

Scott EK, Luo L (2001). How do dendrites take their shape? Nat Neurosci 4:359-365. https://doi.org/10.1038/86006

Secker GA, Harvey NL (2021). Regulation of VEGFR Signalling in Lymphatic Vascular Development and Disease: An Update. Int J Mol Sci 22. https://doi.org/10.3390/ijms22147760

Segev I, London M (2000). Untangling dendrites with quantitative models. Science 290:744-750. https://doi.org/10.1126/science.290.5492.744

Sheetz MP, Dai J (1996). Modulation of membrane dynamics and cell motility by membrane tension. Trends Cell Biol 6:85-89. https://doi.org/10.1016/0962-8924(96)80993-7

Shibata A, Laurent CE, Smithgall TE (2003). The c-Fes protein-tyrosine kinase accelerates NGF-induced differentiation of PC12 cells through a PI3K-dependent mechanism. Cell Signal 15:279-288. https://doi.org/10.1016/S0898-6568(02)00089-X

Shiota M, Kusakabe H, Izumi Y, Hikita Y, Nakao T, Funae Y, . . . Iwao H (2010). Heat Shock Cognate Protein 70 Is Essential for Akt Signaling in Endothelial Function. Atertio Thromb Vasc Biol 30:491-497. https://doi.org/10.1161/ATVBAHA.109.193631

Sholl DA (1953). Dendritic organization in the neurons of the visual and motor cortices of the cat. J Anat 87:387-406

Sidovar MF, Kozlowski P, Lee JW, Collins MA, He Y, Graves LM (2000). Phosphorylation of serine 43 is not required for inhibition of c-Raf kinase by the cAMP-dependent protein kinase. J Biol Chem 275:28688-28694. https://doi.org/10.1074/jbc.M909351199

Silva JAF, Qi X, Grant MB, Boulton ME (2021). Spatial and temporal VEGF receptor intracellular trafficking in microvascular and macrovascular endothelial cells. Sci Rep 11:17400. https://doi.org/10.1038/s41598-021-96964-7

Simonetti M, Hagenston AM, Vardeh D, Freitag HE, Mauceri D, Lu J, . . . Kuner R (2013). Nuclear calcium signaling in spinal neurons drives a genomic program required for persistent inflammatory pain. Neuron 77:43-57. https://doi.org/10.1016/j.neuron.2012.10.037

Simonetti M, Paldy E, Njoo C, Bali KK, Worzfeld T, Pitzer C, . . . Kuner R (2021). The impact of Semaphorin 4C/Plexin-B2 signaling on fear memory via remodeling of neuronal and synaptic morphology. Mol Psychiatry 26:1376-1398. https://doi.org/10.1038/s41380-019-0491-4

Simons M (2012). An inside view: VEGF receptor trafficking and signaling. Physiology (Bethesda) 27:213-222. https://doi.org/10.1152/physiol.00016.2012

Simons M, Gordon E, Claesson-Welsh L (2016). Mechanisms and regulation of endothelial VEGF receptor signalling. Nature Reviews Molecular Cell Biology 17:611-625. https://doi.org/10.1038/nrm.2016.87

Smith MA, Makino S, Kvetnansky R, Post RM (1995). Stress and glucocorticoids affect the expression of brain-derived neurotrophic factor and neurotrophin-3 mRNAs in the hippocampus. J Neurosci 15:1768-1777

Snyder EM, Nong Y, Almeida CG, Paul S, Moran T, Choi EY, . . . Greengard P (2005). Regulation of NMDA receptor trafficking by amyloid-beta. Nat Neurosci 8:1051-1058. https://doi.org/10.1038/nn1503

Soetanto A, Wilson RS, Talbot K, Un A, Schneider JA, Sobiesk M, . . . Arnold SE (2010). Association of anxiety and depression with microtubule-associated protein 2–and synaptopodin-immunolabeled dendrite and spine densities in hippocampal CA3 of older humans. Arch Gen Psychiatry 67:448-457

Solinet S, Mahmud K, Stewman SF, Ben El Kadhi K, Decelle B, Talje L, . . . Carreno S (2013). The actin-binding ERM protein Moesin binds to and stabilizes microtubules at the cell cortex. J Cell Biol 202:251-260. https://doi.org/10.1083/jcb.201304052

Sondell M, Lundborg G, Kanje M (1999). Vascular endothelial growth factor has neurotrophic activity and stimulates axonal outgrowth, enhancing cell survival and Schwann cell proliferation in the peripheral nervous system. J Neurosci 19:5731-5740. https://doi.org/10.1523/jneurosci.19-14-05731.1999

Sousa N, Lukoyanov N, Madeira M, Almeida O, Paula-Barbosa M (2000). Reorganization of the morphology of hippocampal neurites and synapses after stress-induced damage correlates with behavioral improvement. Neuroscience 97:253-266

Spedden E, White James D, Naumova Elena N, Kaplan David L, Staii C (2012). Elasticity Maps of Living Neurons Measured by Combined Fluorescence and Atomic Force Microscopy. Biophys J 103:868-877. https://doi.org/10.1016/j.bpj.2012.08.005

Spence EF, Kanak DJ, Carlson BR, Soderling SH (2016). The Arp2/3 Complex Is Essential for Distinct Stages of Spine Synapse Maturation, Including Synapse Unsilencing. J Neurosci 36:9696-9709. https://doi.org/10.1523/jneurosci.0876-16.2016

Spires TL, Hyman BT (2004). Neuronal structure is altered by amyloid plaques. Rev Neurosci 15:267-278. https://doi.org/10.1515/revneuro.2004.15.4.267

Spruston N (2008). Pyramidal neurons: dendritic structure and synaptic integration. Nature Reviews Neuroscience 9:206-221. https://doi.org/10.1038/nrn2286

Srivastava J, Elliott BE, Louvard D, Arpin M (2005). Src-dependent Ezrin Phosphorylation in Adhesion-mediated Signaling. Mol Biol Cell 16:1481-1490. https://doi.org/10.1091/mbc.e04-08-0721

Stacker SA, Achen MG (1999a). The Vascular Endothelial Growth Factor Family: Signalling for Vascular Development. Growth Factors 17:1-11. https://doi.org/10.3109/08977199909001058

Stacker SA, Achen MG (2018). Emerging Roles for VEGF-D in Human Disease. Biomolecules 8. https://doi.org/10.3390/biom8010001

Stacker SA, Stenvers K, Caesar C, Vitali A, Domagala T, Nice E, . . . Achen MG (1999b). Biosynthesis of vascular endothelial growth factor-D involves proteolytic processing which generates non-covalent homodimers. J Biol Chem 274:32127-32136. https://doi.org/10.1074/jbc.274.45.32127

Stepanova T, Slemmer J, Hoogenraad CC, Lansbergen G, Dortland B, De Zeeuw CI, . . . Galjart N (2003). Visualization of Microtubule Growth in Cultured Neurons via the Use of EB3-GFP (End-Binding Protein 3-Green Fluorescent Protein). J Neurosci 23:2655-2664. https://doi.org/10.1523/jneurosci.23-07-02655.2003

Stephens B, Mueller AJ, Shering AF, Hood SH, Taggart P, Arbuthnott GW, . . . Ingham CA (2005). Evidence of a breakdown of corticostriatal connections in Parkinson's disease. Neuroscience 132:741-754. https://doi.org/10.1016/j.neuroscience.2005.01.007

Su J-L, Yang P-C, Shih J-Y, Yang C-Y, Wei L-H, Hsieh C-Y, . . . Kuo M-L (2006). The VEGF-C/Flt-4 axis promotes invasion and metastasis of cancer cells. Cancer Cell 9:209-223. https://doi.org/10.1016/j.ccr.2006.02.018

Su JL, Yen CJ, Chen PS, Chuang SE, Hong CC, Kuo IH, . . . Kuo ML (2007). The role of the VEGF-C/VEGFR-3 axis in cancer progression. Br J Cancer 96:541-545. https://doi.org/10.1038/sj.bjc.6603487

Südhof TC (2008). Neuroligins and neurexins link synaptic function to cognitive disease. Nature 455:903-911

Svitkina T (2018). The Actin Cytoskeleton and Actin-Based Motility. Cold Spring Harb Perspect Biol 10. https://doi.org/10.1101/cshperspect.a018267

Sweet ES, Previtera ML, Fernández JR, Charych EI, Tseng C-Y, Kwon M, . . . Firestein BL (2011). PSD-95 Alters Microtubule Dynamics via an Association With EB3. J Neurosci 31:1038-1047. https://doi.org/10.1523/jneurosci.1205-10.2011

Takahashi S, Inatome R, Hotta A, Qin Q, Hackenmiller R, Simon MC, . . . Yanagi S (2003). Role for Fes/Fps Tyrosine Kinase in Microtubule Nucleation through Its Fes/CIP4 Homology Domain. J Biol Chem 278:49129-49133. https://doi.org/10.1074/jbc.C300289200

Takeda T, Uchihara T, Nakayama Y, Nakamura A, Sasaki S, Kakei S, . . . Yoshida M (2014). Dendritic retraction, but not atrophy, is consistent in amyotrophic lateral sclerosis-comparison between Onuf's neurons

and other sacral motor neurons. Acta Neuropathol Commun 2:11. https://doi.org/10.1186/2051-5960-2-11

Tam SJ, Watts RJ (2010). Connecting Vascular and Nervous System Development: Angiogenesis and the Blood-Brain Barrier. Annu Rev Neurosci 33:379-408. https://doi.org/10.1146/annurev-neuro-060909-152829

Tammela T, Enholm B, Alitalo K, Paavonen K (2005). The biology of vascular endothelial growth factors. Cardiovasc Res 65:550-563. https://doi.org/10.1016/j.cardiores.2004.12.002

Tammela T, Zarkada G, Nurmi H, Jakobsson L, Heinolainen K, Tvorogov D, . . . Alitalo K (2011). VEGFR-3 controls tip to stalk conversion at vessel fusion sites by reinforcing Notch signalling. Nat Cell Biol 13:1202-1213. https://doi.org/10.1038/ncb2331

Tao J, Feng C, Rolls MM (2016). The microtubule-severing protein fidgetin acts after dendrite injury to promote their degeneration. J Cell Sci 129:3274-3281. https://doi.org/10.1242/jcs.188540

Tautermann CS, Binder F, Büttner FH, Eickmeier C, Fiegen D, Gross U, . . . Zeeb M (2019). Allosteric Activation of Striatal-Enriched Protein Tyrosine Phosphatase (STEP, PTPN5) by a Fragment-like Molecule. J Med Chem 62:306-316. https://doi.org/10.1021/acs.jmedchem.8b00857

Tavosanis G (2012). Dendritic structural plasticity. Dev Neurobiol 72:73-86. https://doi.org/10.1002/dneu.20951

Terry RD, Masliah E, Salmon DP, Butters N, DeTeresa R, Hill R, . . . Katzman R (1991). Physical basis of cognitive alterations in Alzheimer's disease: synapse loss is the major correlate of cognitive impairment. Annals of Neurology: Official Journal of the American Neurological Association and the Child Neurology Society 30:572-580

Trabalza A, Colazingari S, Sgobio C, Bevilacqua A (2012). Contextual learning increases dendrite complexity and EphrinB2 levels in hippocampal mouse neurons. Behav Brain Res 227:175-183. https://doi.org/10.1016/j.bbr.2011.11.008

Trachtenberg JT, Chen BE, Knott GW, Feng G, Sanes JR, Welker E, Svoboda K (2002). Long-term in vivo imaging of experience-dependent synaptic plasticity in adult cortex. Nature 420:788-794. https://doi.org/10.1038/nature01273

Tsai FC, Kuo GH, Chang SW, Tsai PJ (2015). Ca2+ signaling in cytoskeletal reorganization, cell migration, and cancer metastasis. Biomed Res Int 2015:409245. https://doi.org/10.1155/2015/409245

Tsai J, Grutzendler J, Duff K, Gan WB (2004). Fibrillar amyloid deposition leads to local synaptic abnormalities and breakage of neuronal branches. Nat Neurosci 7:1181-1183. https://doi.org/10.1038/nn1335

Uhlén M, Fagerberg L, Hallström BM, Lindskog C, Oksvold P, Mardinoglu A, . . . Pontén F (2015). Proteomics. Tissue-based map of the human proteome. Science 347:1260419. https://doi.org/10.1126/science.1260419

UniProt (2022). UniProt: the Universal Protein Knowledgebase in 2023. Nucleic Acids Res 51:D523-D531. https://doi.org/10.1093/nar/gkac1052

Urner S, Planas-Paz L, Hilger LS, Henning C, Branopolski A, Kelly-Goss M, . . . Lammert E (2019). Identification of ILK as a critical regulator of VEGFR3 signalling and lymphatic vascular growth. The EMBO Journal 38:e99322. https://doi.org/10.15252/embj.201899322

Vahabikashi A, Park CY, Perkumas K, Zhang Z, Deurloo EK, Wu H, . . . Johnson M (2019). Probe Sensitivity to Cortical versus Intracellular Cytoskeletal Network Stiffness. Biophys J 116:518-529. https://doi.org/10.1016/j.bpj.2018.12.021

Valjent E, Pascoli V, Svenningsson P, Paul S, Enslen H, Corvol J-C, . . . Girault J-A (2005). Regulation of a protein phosphatase cascade allows convergent dopamine and glutamate signals to activate ERK in the striatum. Proc Natl Acad Sci U S A 102:491-496. https://doi.org/10.1073/pnas.0408305102

Valtola R, Salven P, Heikkilä P, Taipale J, Joensuu H, Rehn M, . . . Alitalo K (1999). VEGFR-3 and Its Ligand VEGF-C Are Associated with Angiogenesis in Breast Cancer. The American Journal of Pathology 154:1381-1390. https://doi.org/10.1016/S0002-9440(10)65392-8

Van Aelst L, Cline HT (2004). Rho GTPases and activity-dependent dendrite development. Curr Opin Neurobiol 14:297-304. https://doi.org/10.1016/j.conb.2004.05.012

Vaughn JE, Barber RP, Sims TJ (1988). Dendritic development and preferential growth into synaptogenic fields: a quantitative study of Golgi-impregnated spinal motor neurons. Synapse 2:69-78. https://doi.org/10.1002/syn.890020110

Veikkola T, Jussila L, Makinen T, Karpanen T, Jeltsch M, Petrova TV, . . . Alitalo K (2001). Signalling via vascular endothelial growth factor receptor-3 is sufficient for lymphangiogenesis in transgenic mice. EMBO J 20:1223-1231. https://doi.org/10.1093/emboj/20.6.1223

Vempati P, Popel AS, Mac Gabhann F (2014). Extracellular regulation of VEGF: isoforms, proteolysis, and vascular patterning. Cytokine Growth Factor Rev 25:1-19. https://doi.org/10.1016/j.cytogfr.2013.11.002

Venkatesh K, Mathew A, Koushika SP (2020). Role of actin in organelle trafficking in neurons. Cytoskeleton 77:97-109. https://doi.org/10.1002/cm.21580

Verma M, Lizama BN, Chu CT (2022). Excitotoxicity, calcium and mitochondria: a triad in synaptic neurodegeneration. Transl Neurodegener 11:3. https://doi.org/10.1186/s40035-021-00278-7

Vessey JP, Schoderboeck L, Gingl E, Luzi E, Riefler J, Di Leva F, . . . Macchi P (2010). Mammalian Pumilio 2 regulates dendrite morphogenesis and synaptic function. Proc Natl Acad Sci U S A 107:3222-3227. https://doi.org/10.1073/pnas.0907128107

Villalba RM, Smith Y (2018). Loss and remodeling of striatal dendritic spines in Parkinson's disease: from homeostasis to maladaptive plasticity? J Neural Transm (Vienna) 125:431-447. https://doi.org/10.1007/s00702-017-1735-6

Wakayama T, Nakata H, Kurobo M, Sai Y, Iseki S (2009). Expression, Localization, and Binding Activity of the Ezrin/Radixin/Moesin Proteins in the Mouse Testis. J Histochem Cytochem 57:351-362. https://doi.org/10.1369/jhc.2008.952440

Walker R, O'brien E, Pryer N, Soboeiro M, Voter W, Erickson H, Salmon ED (1988). Dynamic instability of individual microtubules analyzed by video light microscopy: rate constants and transition frequencies. The Journal of cell biology 107:1437-1448

Wang J, Campos B, Jamieson GA, Kaetzel MA, Dedman JR (1995). Functional Elimination of Calmodulin within the Nucleus by Targeted Expression of an Inhibitor Peptide (∗). J Biol Chem 270:30245-30248. https://doi.org/10.1074/jbc.270.51.30245

Wang X, Bove AM, Simone G, Ma B (2020). Molecular Bases of VEGFR-2-Mediated Physiological Function and Pathological Role. Front Cell Dev Biol 8:599281. https://doi.org/10.3389/fcell.2020.599281

Wang Y, Nakayama M, Pitulescu ME, Schmidt TS, Bochenek ML, Sakakibara A, . . . Adams RH (2010). Ephrin-B2 controls VEGF-induced angiogenesis and lymphangiogenesis. Nature 465:483-486. https://doi.org/10.1038/nature09002

Wang Z, Wu XL, Wang X, Tian HX, Chen ZH, Li YQ (2014). The biophysical property of A549 cells transferred by VEGF-D. Scanning 36:202-208. https://doi.org/10.1002/sca.21087

Warner-Schmidt JL, Duman RS (2006). Hippocampal neurogenesis: opposing effects of stress and antidepressant treatment. Hippocampus 16:239-249

Watanabe K, Tachibana M, Kim S, Watarai M (2009). Participation of ezrin in bacterial uptake by trophoblast giant cells. Reprod Biol Endocrinol 7:95. https://doi.org/10.1186/1477-7827-7-95

Welf ES, Miles CE, Huh J, Sapoznik E, Chi J, Driscoll MK, . . . Danuser G (2020). Actin-Membrane Release Initiates Cell Protrusions. Dev Cell 55:723-736.e728. https://doi.org/10.1016/j.devcel.2020.11.024

Wellbrock C, Karasarides M, Marais R (2004). The RAF proteins take centre stage. Nature Reviews Molecular Cell Biology 5:875-885. https://doi.org/10.1038/nrm1498

Wickham H, Averick M, Bryan J, Chang W, McGowan L, François R, . . . Yutani H (2019). Welcome to the Tidyverse. J Open Source Softw 4:1686. https://doi.org/10.21105/joss.01686

Wit CB, Hiesinger PR (2023). Neuronal filopodia: From stochastic dynamics to robustness of brain morphogenesis. Semin Cell Dev Biol 133:10-19. https://doi.org/10.1016/j.semcdb.2022.03.038

Won S, Incontro S, Li Y, Nicoll RA, Roche KW (2019). The STEP61 interactome reveals subunit-specific AMPA receptor binding and synaptic regulation. Proc Natl Acad Sci U S A 116:8028-8037. https://doi.org/10.1073/pnas.1900878116

Wong ROL, Ghosh A (2002). Activity-dependent regulation of dendritic growth and patterning. Nature Reviews Neuroscience 3:803-812. https://doi.org/10.1038/nrn941

Xu J, Chatterjee M, Baguley TD, Brouillette J, Kurup P, Ghosh D, . . . Lombroso PJ (2014). Inhibitor of the tyrosine phosphatase STEP reverses cognitive deficits in a mouse model of Alzheimer's disease. PLoS Biol 12:e1001923. https://doi.org/10.1371/journal.pbio.1001923

Xu J, Kurup P, Nairn AC, Lombroso PJ (2018). Synaptic NMDA Receptor Activation Induces Ubiquitination and Degradation of STEP61. Mol Neurobiol 55:3096-3111. https://doi.org/10.1007/s12035-017-0555-x

Xu K, Zhong G, Zhuang X (2013). Actin, spectrin, and associated proteins form a periodic cytoskeletal structure in axons. Science 339:452-456. https://doi.org/10.1126/science.1232251

Yagi H, Takabayashi T, Xie MJ, Kuroda K, Sato M (2017). Subcellular distribution of non-muscle myosin IIb is controlled by FILIP through Hsc70. PLoS One 12:e0172257. https://doi.org/10.1371/journal.pone.0172257

Yamazaki Y, Morita T (2006). Molecular and functional diversity of vascular endothelial growth factors. Mol Divers 10:515-527. https://doi.org/10.1007/s11030-006-9027-3

Yang CH, Huang CC, Hsu KS (2012). A critical role for protein tyrosine phosphatase nonreceptor type 5 in determining individual susceptibility to develop stress-related cognitive and morphological changes. J Neurosci 32:7550-7562. https://doi.org/10.1523/jneurosci.5902-11.2012

Yıldırım Y, Kocasoy Orhan E, Ugur Iseri SA, Serdaroglu-Oflazer P, Kara B, Solakoğlu S, Tolun A (2011). A frameshift mutation of ERLIN2 in recessive intellectual disability, motor dysfunction and multiple joint contractures. Hum Mol Genet 20:1886-1892. https://doi.org/10.1093/hmg/ddr070

Youn H, Jeoung M, Koo Y, Ji H, Markesbery WR, Ji I, Ji TH (2007). Kalirin is under-expressed in Alzheimer's disease hippocampus. J Alzheimers Dis 11:385-397. https://doi.org/10.3233/jad-2007-11314

Yuan A, Rao MV, Veeranna, Nixon RA (2012). Neurofilaments at a glance. J Cell Sci 125:3257-3263. https://doi.org/10.1242/jcs.104729

Yuan A, Rao MV, Veeranna, Nixon RA (2017). Neurofilaments and Neurofilament Proteins in Health and Disease. Cold Spring Harb Perspect Biol 9. https://doi.org/10.1101/cshperspect.a018309

Yuan Y-P, Zhao H, Peng L-Q, Li Z-F, Liu S, Yuan C-Y, . . . Yao L-J (2018a). The SGK3-triggered ubiquitin–proteasome degradation of podocalyxin (PC) and ezrin in podocytes was associated with the stability of the PC/ezrin complex. Cell Death Dis 9:1114. https://doi.org/10.1038/s41419-018-1161-1

Yuan Y, Xie S, Darnell JC, Darnell AJ, Saito Y, Phatnani H, . . . Darnell RB (2018b). Cell type-specific CLIP reveals that NOVA regulates cytoskeleton interactions in motoneurons. Genome Biol 19:117. https://doi.org/10.1186/s13059-018-1493-2

Yuste R, Bonhoeffer T (2001). Morphological changes in dendritic spines associated with long-term synaptic plasticity. Annu Rev Neurosci 24:1071-1089. https://doi.org/10.1146/annurev.neuro.24.1.1071

Zebisch A, Troppmair J (2006). Back to the roots: the remarkable RAF oncogene story. Cellular and Molecular Life Sciences CMLS 63:1314-1330. https://doi.org/10.1007/s00018-006-6005-y

Zeisel A, Hochgerner H, Lönnerberg P, Johnsson A, Memic F, van der Zwan J, . . . Linnarsson S (2018). Molecular Architecture of the Mouse Nervous System. Cell 174:999-1014.e1022. https://doi.org/10.1016/j.cell.2018.06.021

Zhang L, Zhou F, Han W, Shen B, Luo J, Shibuya M, He Y (2010). VEGFR-3 ligand-binding and kinase activity are required for lymphangiogenesis but not for angiogenesis. Cell Res 20:1319-1331. https://doi.org/10.1038/cr.2010.116

Zhang SJ, Steijaert MN, Lau D, Schütz G, Delucinge-Vivier C, Descombes P, Bading H (2007). Decoding NMDA receptor signaling: identification of genomic programs specifying neuronal survival and death. Neuron 53:549-562. https://doi.org/10.1016/j.neuron.2007.01.025

Zhang SJ, Zou M, Lu L, Lau D, Ditzel DA, Delucinge-Vivier C, . . . Bading H (2009). Nuclear calcium signaling controls expression of a large gene pool: identification of a gene program for acquired neuroprotection induced by synaptic activity. PLoS Genet 5:e1000604. https://doi.org/10.1371/journal.pgen.1000604

Zhang X, Cai J, Zheng Z, Polin L, Lin Z, Dandekar A, . . . Zhang K (2015). A novel ER–microtubule-binding protein, ERLIN2, stabilizes Cyclin B1 and regulates cell cycle progression. Cell Discovery 1:15024. https://doi.org/10.1038/celldisc.2015.24

Zhang Y, Abiraman K, Li H, Pierce DM, Tzingounis AV, Lykotrafitis G (2017). Modeling of the axon membrane skeleton structure and implications for its mechanical properties. PLoS Comput Biol 13:e1005407. https://doi.org/10.1371/journal.pcbi.1005407

Zhao J, Luo Z (2022). Discovery of Raf Family Is a Milestone in Deciphering the Ras-Mediated Intracellular Signaling Pathway. Int J Mol Sci 23. https://doi.org/10.3390/ijms23095158

Zhong J, Li X, McNamee C, Chen AP, Baccarini M, Snider WD (2007). Raf kinase signaling functions in sensory neuron differentiation and axon growth in vivo. Nat Neurosci 10:598-607. https://doi.org/10.1038/nn1898

Zhou R, Han B, Nowak R, Lu Y, Heller E, Xia C, . . . Zhuang X (2022). Proteomic and functional analyses of the periodic membrane skeleton in neurons. Nat Commun 13:3196. https://doi.org/10.1038/s41467-022-30720-x

Zhou R, Han B, Xia C, Zhuang X (2019). Membrane-associated periodic skeleton is a signaling platform for RTK transactivation in neurons. Science 365:929-934. https://doi.org/10.1126/science.aaw5937

Zhou Z, Hong EJ, Cohen S, Zhao W-n, Ho H-yH, Schmidt L, . . . Griffith EC (2006). Brain-specific phosphorylation of MeCP2 regulates activity-dependent Bdnf transcription, dendritic growth, and spine maturation. Neuron 52:255-269

Ziv NE, Smith SJ (1996). Evidence for a role of dendritic filopodia in synaptogenesis and spine formation. Neuron 17:91-102. https://doi.org/10.1016/s0896-6273(00)80283-4

Appendix

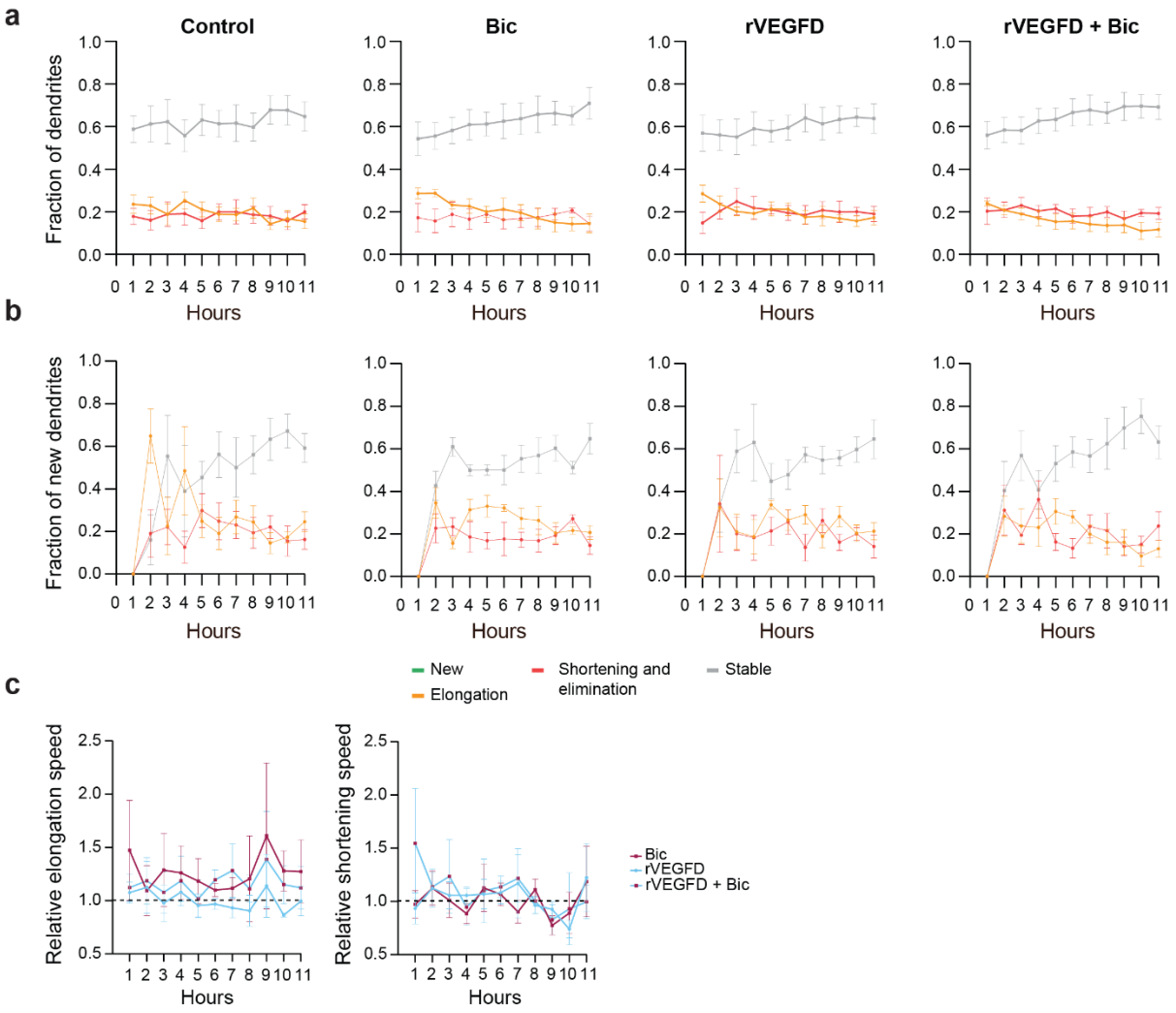

Appendix figure 1. Related to Figure 11. Activity-induced dendrite dynamics over time. *Time-lapse monitoring of dendrites of hrGFP-transfected cultured mouse hippocampal neurons with or without recombinant VEGFD (rVEGFD) and/or bicuculline (Bic) treatment.* ***a*** *Fractions of elongated (not including formation of new dendrites), shortened and/or eliminated, and stable dendrites over time in neurons treated as indicated.* ***b*** *Fractions of elongated (not including formation of new dendrites), shortened and/or eliminated, and stable new dendrites over time in neurons treated as indicated.* ***c*** *Relative elongation (includes new dendrite formations) and shortening (includes dendrite elimination) speed in neurons treated as indicated normalized on control. Two-way ANOVA followed by Dunnett's post hoc test for comparisons to basal values (c), or Tukey's post hoc test for comparisons between conditions (c). N = 4 independent culture preparations, 14-19 neurons per condition in total. Graphs display mean ± SEM.*

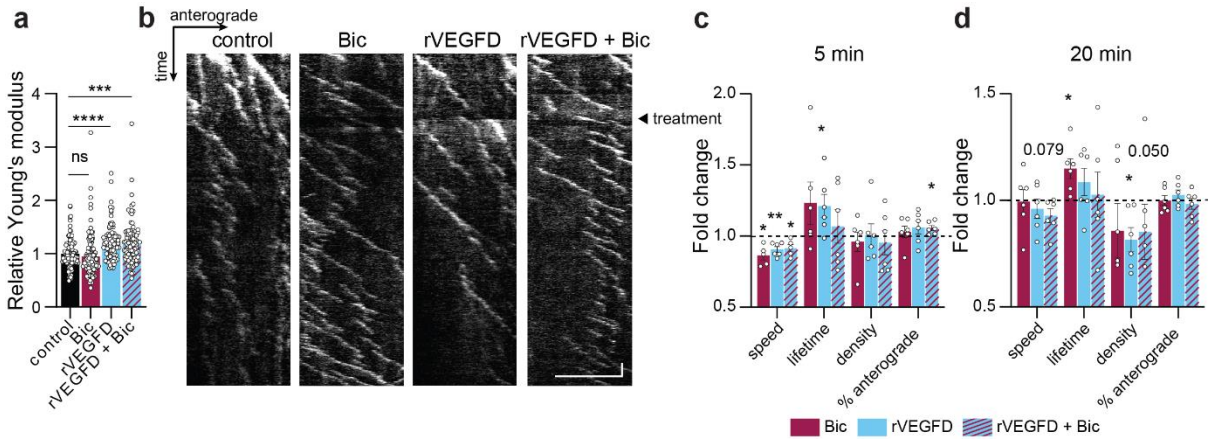

Appendix figure 2. Effect of bicuculline and recombinant VEGFD on membrane stiffness and microtubule dynamics. ***a*** *Atomic force microscopy measurements on the soma and proximal dendrites of cultured mouse hippocampal neurons treated with or without recombinant VEGFD (rVEGFD), bicuculline (Bic) or both. Young's modulus was normalized on untreated control. Kruskal-Wallis test followed by Dunn's post hoc test. N = 88-129 neurons from 3-5 independent culture preparations.* ***b-d*** *Analysis of microtubule (MT) dynamics in EB3-GFP-transfected neurons treated with or without rVEGFD, Bic treatment or both. Treatments were applied after 5 min of baseline recording and the effect monitored for 20 min.* ***b*** *Representative kymographs of dendrites from EB3-GFP-transfected neurons treated as indicated. Arrow on the right indicates treatment start. Scale bar = 5 µm, 60 s.* ***c, d*** *EB3-GFP comet speed, lifetime, density, and percentage of anterograde comet movements normalized on baseline and respective untreated control after 5 min (**c**) or 20 min (**d**) of rVEGFD, Bic or rVEGFD and Bic treatment. One sample t-test. N = 6 independent culture preparations. 10 neurons/condition in total, on average 5-8 dendrites per neuron. Graphs display mean ± SEM. Single values are represented as data points.* ****p < 0.0001; ***p<0.001; **p < 0.01; *p < 0.05; *ns p > 0.05.*

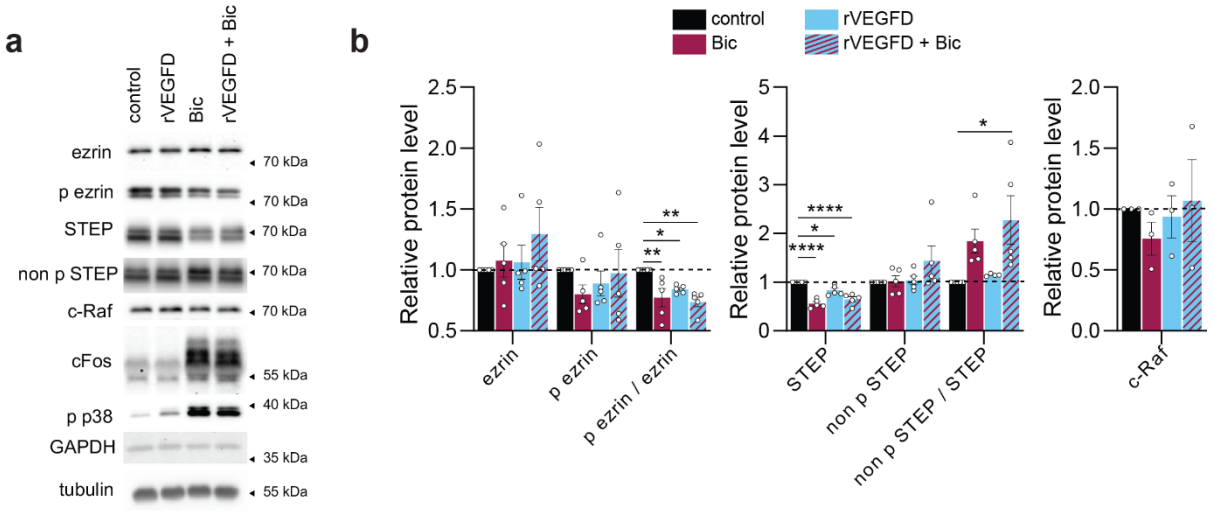

Appendix figure 3. Effect of bicuculline and recombinant VEGFD on ezrin, STEP, and c-Raf expression and phosphorylation. *Immunoblot analysis in cultured mouse hippocampal neurons treated or not with recombinant VEGFD (rVEGFD), bicuculline (Bic) or both for 2 h.* ***a*** *Representative immunoblots of indicated proteins (p ezrin refers to pY478 ezrin).* ***c*** *Quantification of ezrin, phospho Y478 ezrin and its phospho/total protein ratio; STEP, Non-phospho STEP and its phospho/total protein ratio; and c-Raf protein expression. Expression was normalized on tubulin and control. One-*

way ANOVA followed by Dunnett's post hoc test. N = 3-5 independent culture preparations. Graphs display mean ± SEM. Single values are represented as data points. ****p < 0.0001; **p < 0.01; *p < 0.05.

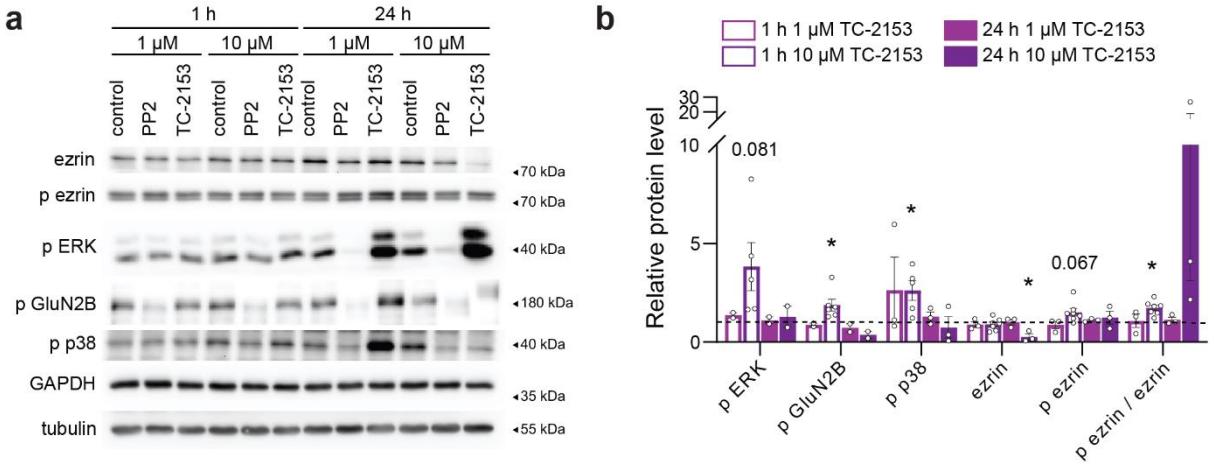

Appendix figure 4. Evaluation of STEP inhibitor TC-2153. *Immunoblot analysis in cultured mouse hippocampal neurons treated with DMSO (vector) or 1 µM/10 µM TC-2153 for 1 h or 24 h (samples from PP2-treated neurons of a parallel experiment were loaded on the same gels).* ***a*** *Representative immunoblots of ezrin, phospho Y478 ezrin, phospho ERK, phospho GluN2B, phospho p38 and tubulin.* ***b*** *Quantification of phospho ERK, phospho GluN2B, phospho p38, ezrin, phospho Y478 ezrin and the phospho Y478 ezrin/total ezrin protein ratio in TC-2153-treated neurons at indicated concentrations and timepoints. Expression was normalized on tubulin and control. One sample t-test. N = 2-5 independent culture preparations. Graphs display mean ± SEM. Single values are represented as data points. *p < 0.05.*

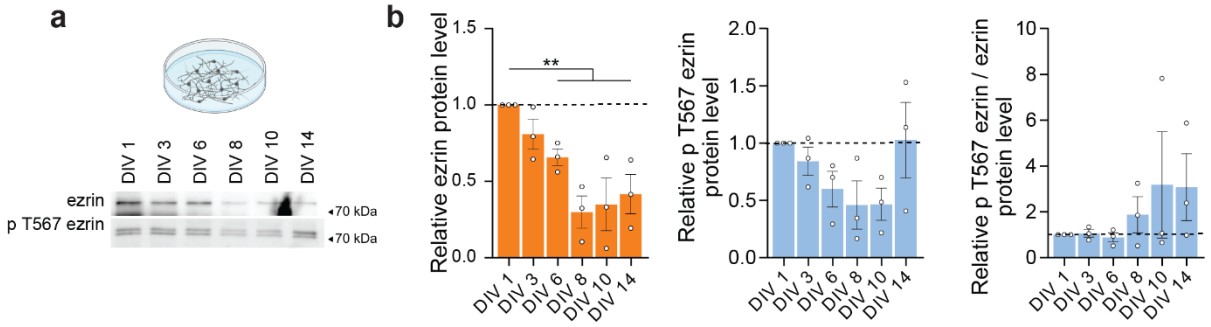

Appendix figure 5. Characterization of pT567 ezrin expression throughout development. *Immunoblot analysis of ezrin protein expression in cultured mouse hippocampal neurons at different days in vitro (DIV).* ***a*** *Representative immunoblots of ezrin and phospho T567 ezrin.* ***b*** *Quantification of ezrin, phospho T567 ezrin and its phospho/total protein ratio. Expression was only normalized to DIV 1 due to DIV-related fluctuations in GAPDH and tubulin expression (see Figure 32). One-way ANOVA followed by Dunnett's post hoc test. N = 3 independent culture preparations. Graphs display mean ± SEM. Single values are represented as data points. **p < 0.01.*

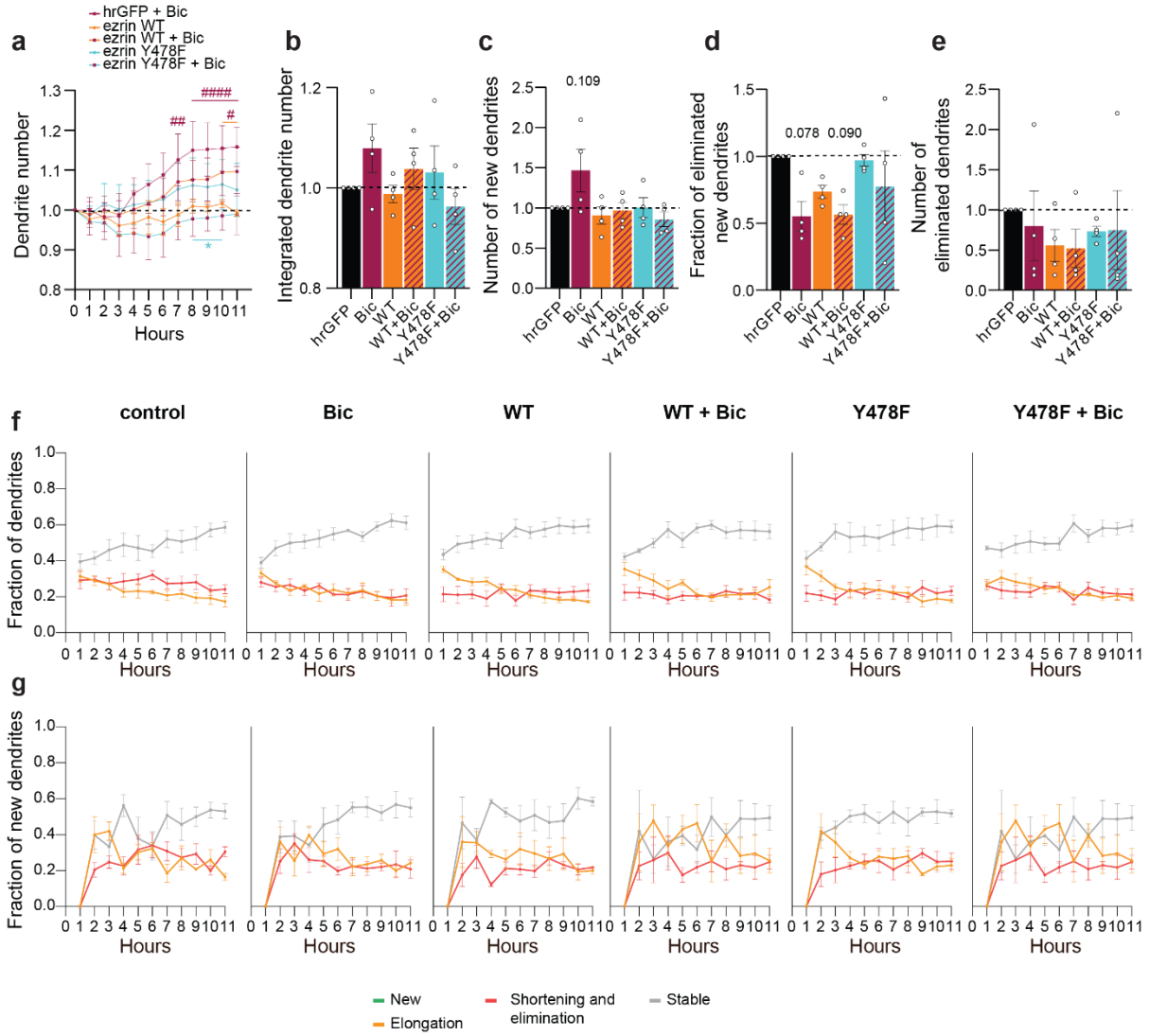

Appendix figure 6. Related to Figure 30. Activity-induced dendrite dynamics in ezrin-overexpressing neurons over time. *Time-lapse monitoring of dendrites of hrGFP (vector) and/or WT or Y478F ezrin-transfected cultured mouse hippocampal neurons with or without bicuculline (Bic) treatment.* ***a*** *Total dendrite number over time normalized on the first timepoint and untreated control.* ***b*** *Integration of data shown in (**a**).* ***c*** *Total number of new dendrites normalized on untreated control.* ***d*** *Fraction of new dendrites that were then eliminated normalized on untreated control.* ***e*** *Total number of eliminated dendrites normalized on untreated control.* ***f*** *Fractions of elongated (not including formation of new dendrites), shortened and/or eliminated, and stable dendrites over time in neurons treated as indicated.* ***g*** *Fractions of elongated (not including formation of new dendrites), shortened and/or eliminated, and stable new dendrites over time in neurons treated as indicated. Two-way ANOVA followed by Dunnett's post hoc test for comparisons to basal values (a), or Tukey's post hoc test for comparisons between conditions (a; asterisk refers to comparison between Y478F+Bic and Bic); One-way ANOVA followed by Dunnett's post hoc test (b-e). N = 4 independent culture preparations, 13-16 neurons/condition in total. Graphs display mean ± SEM. Single values are represented as data points. Significance indicators include asterisks (*) for comparisons between conditions and hashtags (#) for comparisons to baseline values within each respective condition. *p < 0.05; ####p < 0.0001; ##p < 0.01; #p < 0.05.*

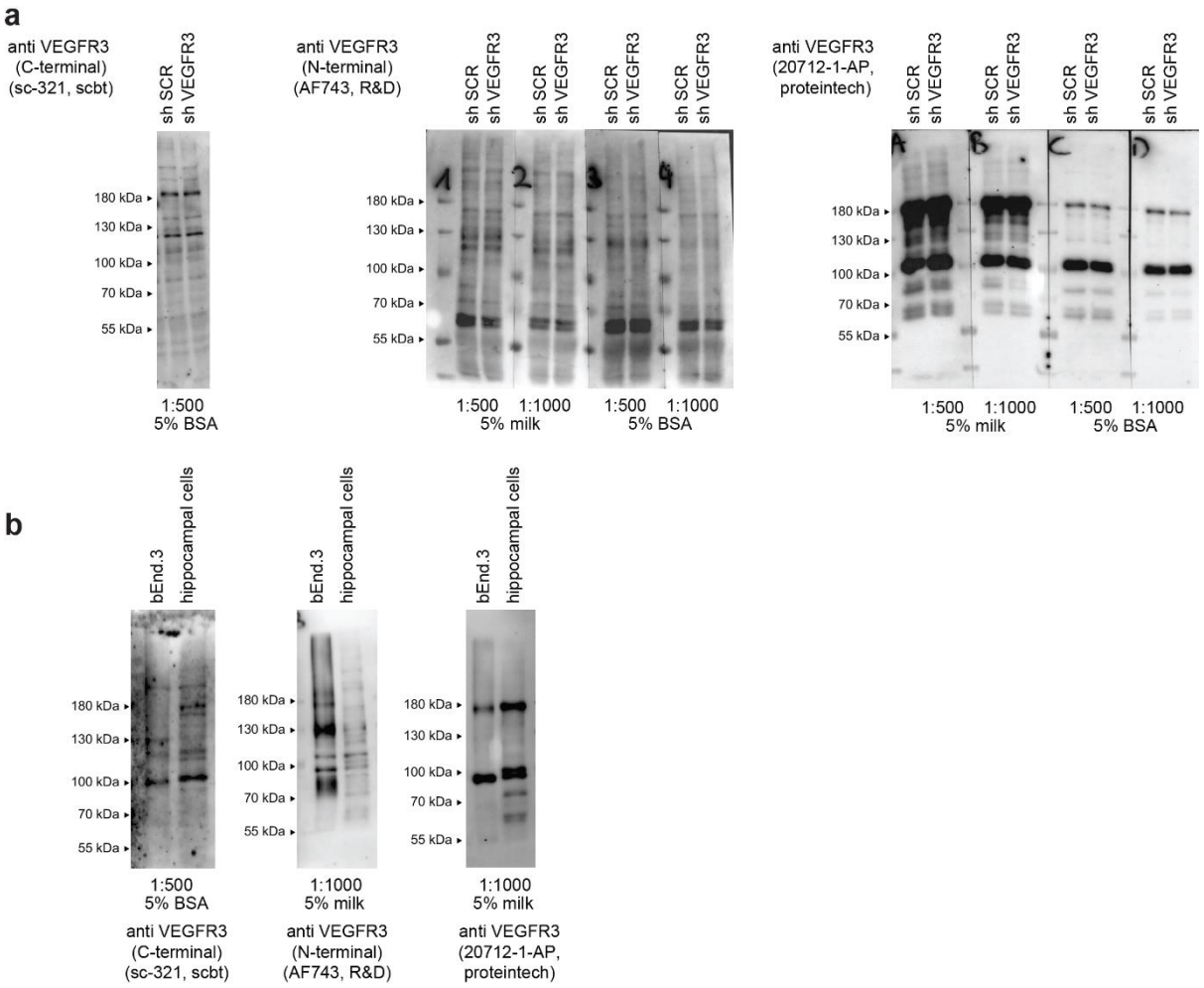

Appendix figure 7. Evaluation of VEGFR3 antibodies. ***a*** *Immunoblots using three different VEGFR3 antibodies at different concentrations and in different blocking buffers on cultured mouse hippocampal neurons rAAV-infected with shRNAs to downregulate VEGFR3. A scrambled sh sequence (SCR) served as control.* ***b*** *Immunoblots using three different VEGFR3 antibodies on bEnd.3 cells and cultured mouse hippocampal neurons.*

Sequence of VEGFR3-GFP:

MQPGAALNLRLWLCLGLLQGLANGYSMTPPTLNITEDSYVIDTGDSLSISCRGQHPLEWTWPGAQEVLTTGGKDS
EDTRVVHDCEGTEARPYCKVLLLAQTHANNTGSYHCYYKYIKAR**IEGTTAASTYVFVR**DFKHPFINKPDTLLVNRKD
SMWVPCLVSIPGLNITLRSQSSALHPDGQEVLWDDRRGMRVPTQLLRDALYLQCETTWGDQNFLSNLFVVHITG
NELYDIQLYPKKSMELLVGEKLVLNCTVWAEFDSGVTFDWDYPGKQAERAKWVPERRSQQTHTELSSILTIHNVSQ
NDLGPYVCEANNGIQRFRESTEVIVHEKPFISVEWLK**GPVLEATAGDELVK**LPVKLAAYPPPEFQWYKDRKAVTGR
HNPHALVLKEVTEASAGVYTLALWNSAAGLRQNISLELVVNVPPHIHEKEASSPSIYSRHSRQTLTCTAYGVPQPLSV
QWHWRPWTPCKTFAQRSLRRRQQRDGMPQCRDWKEVTTQDAVNPIESLDSWTEFVEGKNKTVSKLVIQDANV
SAMYKCVVVNKVGQDERLIYFYVTTIPDGFSIESEPSEDPLEGQSVRLSCRADNYTYEHLRWYRLNLSTLHDAQGNP
LLLDCK**NVHLFATPLEANLEEAEPGAR**HATLSLNIPRVAPEDEGDYVCEVQDRRSQDKHCHKKYLSVQALEAPRLT
QNLTDLLVNVSDSLEMRCPVAGAHVPSIVWYKDERLLEKESGIDLADSNQRLSIQRVREEDAGRYLCSVCNAKGCV
NSSASVAVEGSEDKGSMEIVILIGTGVIAVFFWVLLLLIFCNMKRPAHADIKTGYLSIIMDPGEVPLEEQCEYLSYDAS
QWEFPRERLHLGRVLGHGAFGKVVEASAFGINKGSSCDTVAVKMLKEGATASEHRALMSELKILIHIGNHLNVVNL
LGACTKPNGPLMVIVEFCKYGNLSNFLRVKRDTFNPYAEKSPEQRRRFRAMVEGAKADRRRPGSSDRALFTRFLM
GKGSARRAPLVQEAEDLWLSPLTMEDLVCYSFQVAR**GMEFLASR**KCIHRDLAAR**NILLSESDIVKICDFGLAR**DIYK
DPDYVRKGSARLPLKWMAPESIFDKVYTTQSDVWSFGVLLWEIFSLGASPYPGVQINEEFCQRLKDGTRMRAPEL

ATPAIRHIMQSCWSGDPKARPAFSDLVEILGDLLQGGGWQEEEEERMALHSSQSSEEDGFMQASTTALHITEADA DDSPPSMHCHSLAAR**YYNCVSFPGR**LARGTKTPGSSR**MKTFEELPMTPTTYKASMDNQTDSGMVLASEEFEELE SR**HRPEGSFSCK**GPGQHMDIPR**GHPDPQGRRRRPTQGAQGGKVFYNNEYGEVSQPCTEGDCCPSAGSTFFADS SYAAALEISIG - GFP starts from here - MVSK**GEELFTGVVPILVELDGDVNGHKFSVSGEGEGDATYGKLTLKFICTTGK**LPVPWPTLVTTLTYGVQCFSR**YP DHMKQHDFF**K**SAMPEGYVQERTIFFKDDGNYKTRAEVKFEGDTLVNRIELKGIDFKEDGNILGHKLEYNYNSHN VYIMADKQK**NGIKVNFK**IRHNIEDGSVQLADHYQQNTPIGDGPVLLPDNHYLSTQSALSK**DPNEKR**DHMVLLEF VTAAGITLGMDELYK**

Detected peptide sequences are marked bold.

Appendix figure 8. Mass spectrometry peptide coverage of VEGFR3-GFP.

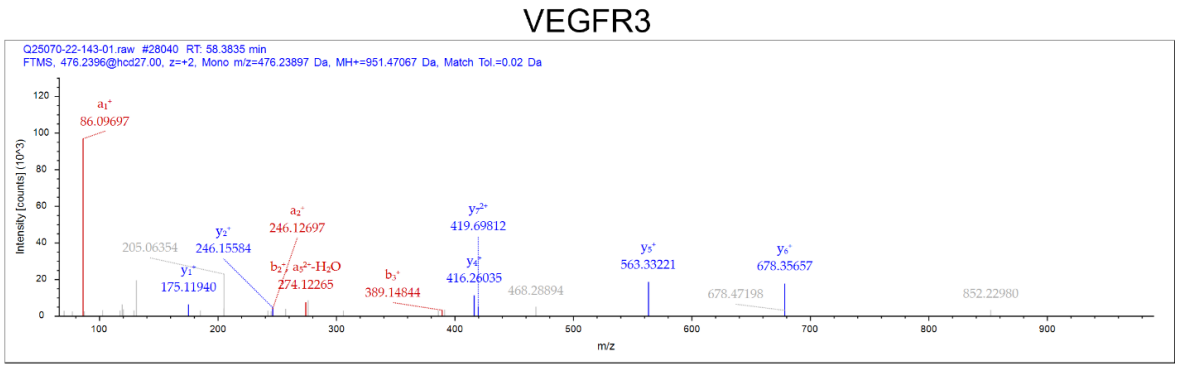

Sequence : ICDFGLAR, C2-Carbamidomethyl (57.02146 Da)
Charge: +2, Monoisotopic m/z: 476.23897 Da (-0.5 mmu/-1.04 ppm), MH+: 951.47067 Da, RT: 58.3835 min, Identified with: Sequest HT (v1.17); XCorr:1.46, Percolator q-Value:4.2e-4, Percolator PEP:2.3e-3,

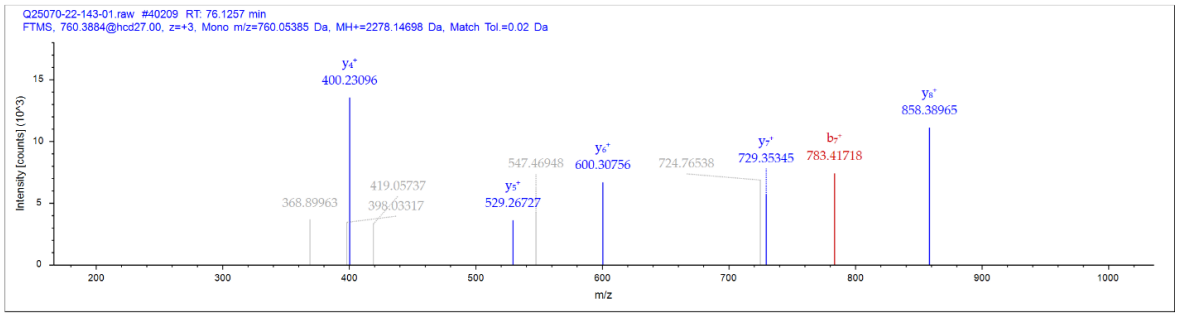

Sequence: NVHLFATPLEANLEEAEPGAR
Charge: +3, Monoisotopic m/z: 760.05385 Da (+0.25 mmu/+0.33 ppm), MH+: 2278.14698 Da, RT: 76.1257 min, Identified with: Sequest HT (v1.17); XCorr:0.62, Percolator q-Value:8.2e-5, Percolator PEP:7.7e-5,

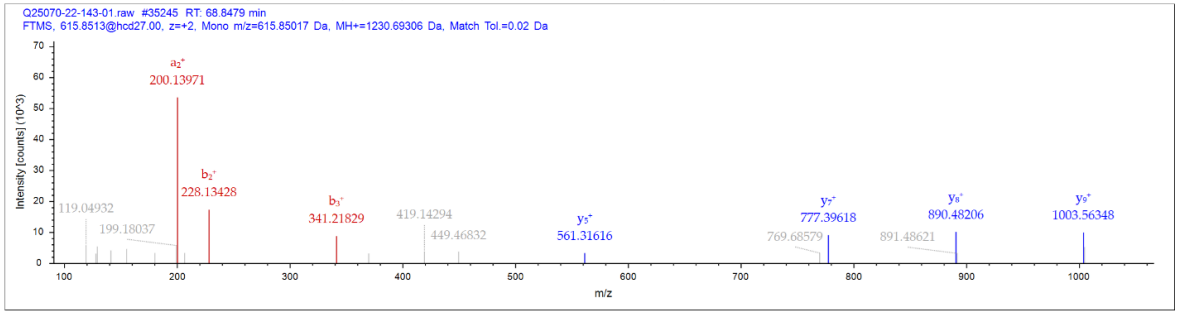

Sequence: NILLSESDIVK
Charge: +2, Monoisotopic m/z: 615.85017 Da (-0.47 mmu/-0.76 ppm), MH+: 1230.69306 Da, RT: 68.8479 min, Identified with: Sequest HT (v1.17); XCorr:1.61, Percolator q-Value:1.3e-3, Percolator PEP:6.0e-3,

Appendix figure 9. Mass spectrometry fragment spectra of the most abundantly detected VEGFR3 peptides in VEGFR3-GFP expressing neurons.

Nova2

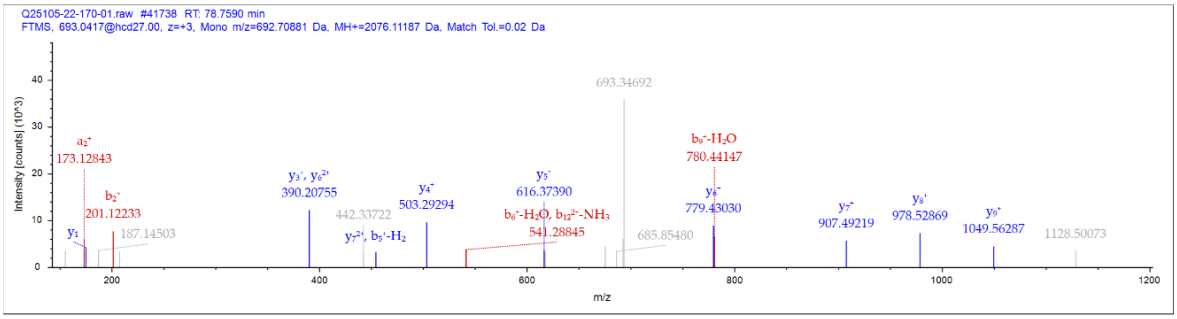

Sequence: VTITGSPAATQAAQYLISQR
Charge: +3, Monoisotopic m/z: 692.70881 Da (+1.16 mmu/+1.68 ppm), MH+: 2076.11187 Da, RT: 78.7590 min, Identified with: Sequest HT (v1.17); XCorr:1.86, Percolator q-Value:8.2e-5, Percolator PEP:2.7e-6,

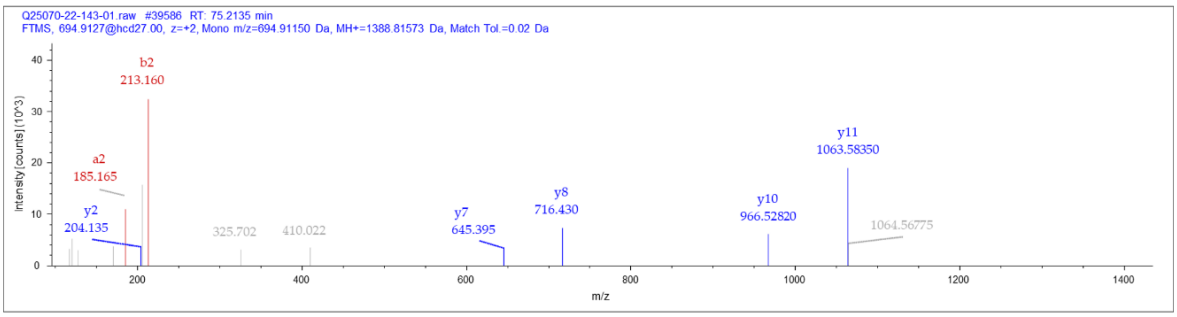

Sequence: VLIPSYAAGSIIGK
Charge: +2, Monoisotopic m/z: 694.91150 Da (+0.47 mmu/+0.68 ppm), MH+: 1388.81573 Da, RT: 75.2135 min, Identified with: Sequest HT (v1.17); XCorr:0.96, Percolator q-Value:8.2e-5, Percolator PEP:1.5e-4,
Fragment match tolerance used for search: 0.02 Da

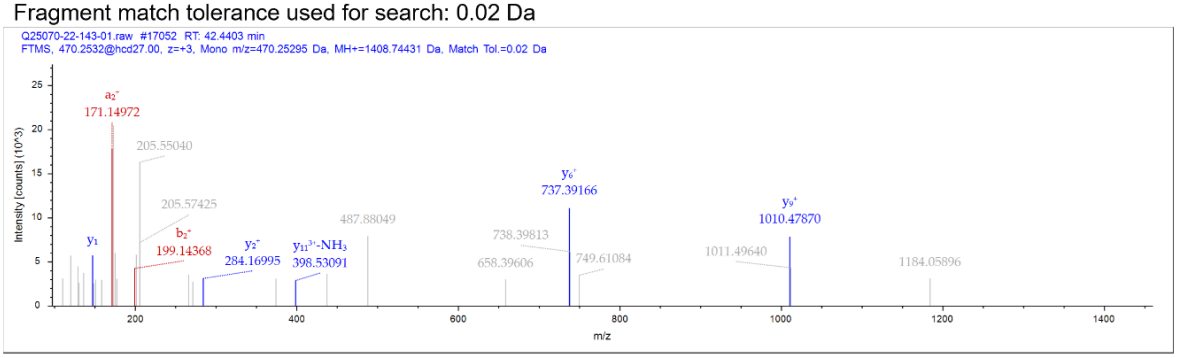

Sequence: VVTVSGEPEQVHK
Charge: +3, Monoisotopic m/z: 470.25295 Da (+0.41 mmu/+0.88 ppm), MH+: 1408.74431 Da, RT: 42.4403 min, Identified with: Sequest HT (v1.17); XCorr:0.62, Percolator q-Value:2.3e-3, Percolator PEP:1.5e-2,

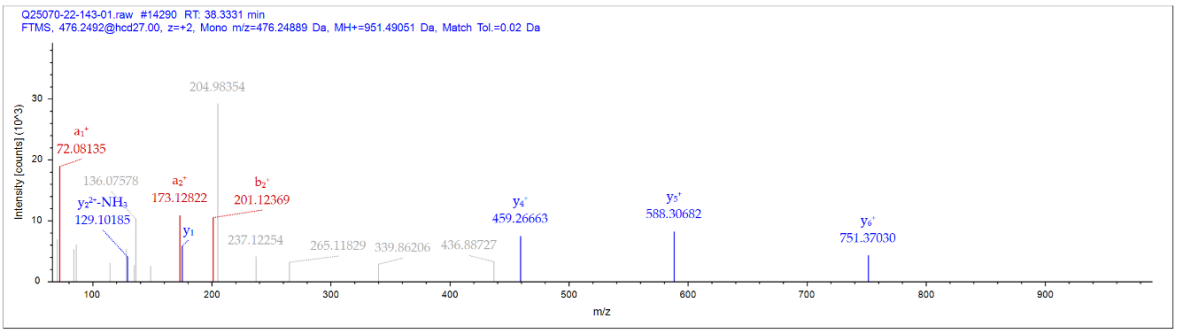

Sequence: VTYEQGVR
Charge: +2, Monoisotopic m/z: 476.24889 Da (+0.54 mmu/+1.14 ppm), MH+: 951.49051 Da, RT: 38.3331 min, Identified with: Sequest HT (v1.17); XCorr:0.58, Percolator q-Value:2.5e-3, Percolator PEP:1.6e-2,

Appendix figure 10. Mass spectrometry fragment spectra of the most abundantly detected nova2 peptides in VEGFR3-GFP expressing neurons.

Table 21. Less stringent list of proteins enriched in VEGFR3-GFP-expressing neurons detected by mass spectrometry.

		fold enrichment in VEGFR3-GFP/GFP control			
Accession number	**Protein name**	**in culture 1**	**in culture 2**	**in culture 3**	**Detected peptides number**
D3YVV7	nova2	only detected in VEGFR3-GFP	only detected in VEGFR3-GFP	2.529	8
Q9D883	u2af1	3.849	only detected in VEGFR3-GFP	1.600	6
P62320	snrpd3	2.536	2.079	2.256	3
Q91Z49	fyttd1	only detected in VEGFR3-GFP	only detected in VEGFR3-GFP	1.703	6
P99027	rplp2	only detected in VEGFR3-GFP	only detected in VEGFR3-GFP	1.518	4
Q8BFZ9	erlin2	only detected in VEGFR3-GFP	only detected in VEGFR3-GFP	2.016	3
Q60931	vdac3	only detected in VEGFR3-GFP	1.775	2.204	4
P84091	ap2m1	4.289	2.256	1.769	15
Q3UJB0	sf3b2	only detected in VEGFR3-GFP	only detected in VEGFR3-GFP	1.258	6
Q9D0T1	snu13	2.775	only detected in VEGFR3-GFP	1.314	4
Q9WV02	rbmx	2.463	only detected in VEGFR3-GFP	1.423	19
P17182	eno1	1.298	only detected in VEGFR3-GFP	6.718	6
Q61937	npm1	6.065	10.636	1.314	7
P14733	lmnb1	1.377	2.183	only detected in	32

				VEGFR3-GFP	
Q91W39	ncoa5	2.014	2.050	1.387	11
P15864	h1-2	2.483	1.967	1.222	11
Q6ZWN5	rps9	4.665	1.578	1.251	5
P63017	hspa8	5.856	1.450	1.238	31
P61089	ube2n	4.581	1.315	1.464	4
P62267	rps23	2.225	1.275	1.570	6

Criteria: ≥3 peptides, ≥1.2-fold enrichment in all and ≥1.5-fold enrichment or only detected in VEGFR3-GFP in at least two independent culture preparations.

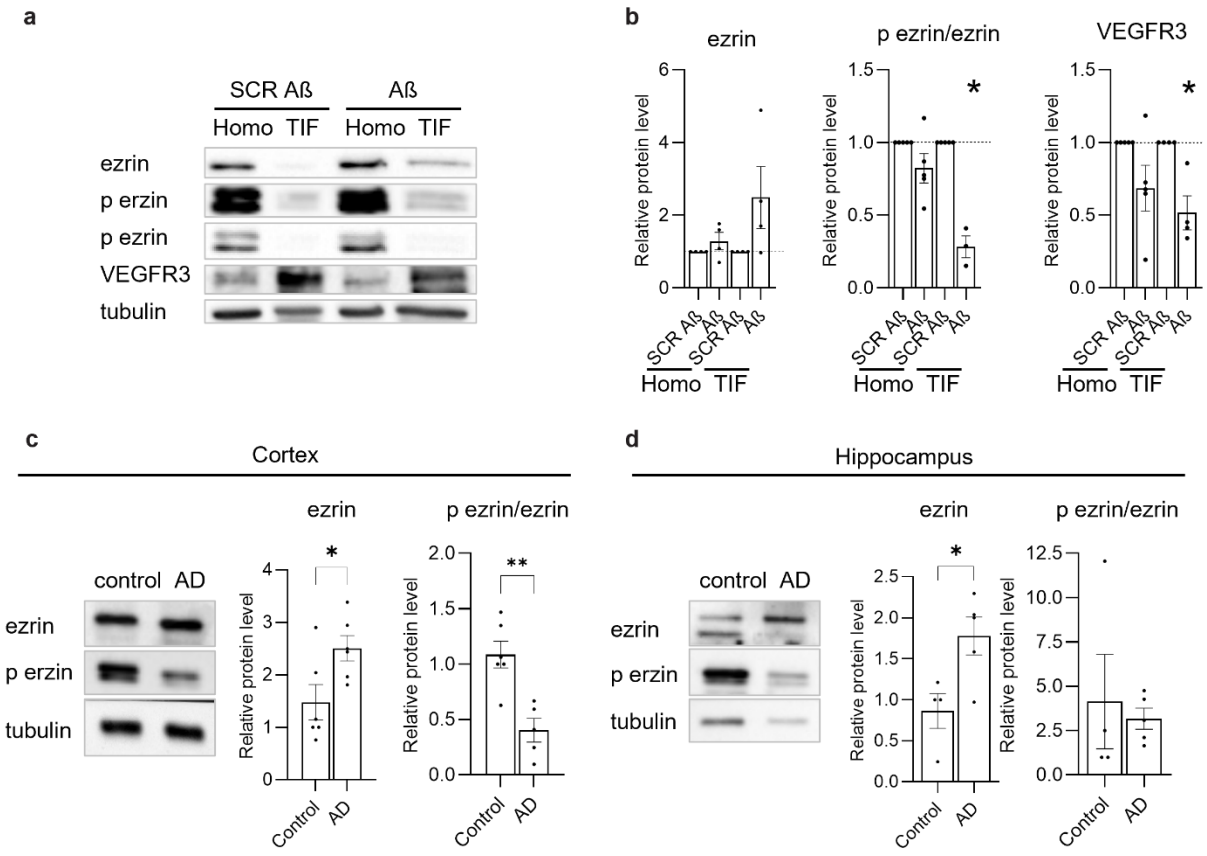

Appendix figure 11. Characterization of ezrin, phospho ezrin and VEGFR3 expression in Alzheimer's Disease. ***a, b*** *Immunoblot analysis of ezrin, phospho Y478 ezrin, and VEGFR3 protein expression in homogenates (homo) and triton insoluble fractions (TIF) enriched in postsynaptic proteins from lysates derived from rat cultured hippocampal neurons treated for 30 min with Aß or scrambled (SCR) Aß as control.* ***a*** *Representative immunoblots of ezrin, phospho Y478 ezrin (two different exposure times are displayed), VEGFR3, and tubulin.* ***b*** *Quantification of ezrin, phospho Y478/total ezrin ratio, and VEGFR3 protein expression. Expression was normalized on tubulin and SCR within a fraction.*

Two-tailed unpaired Student's t-test. N = 3-5 independent culture preparations. ***c, d*** *Immunoblot analysis of ezrin protein expression and phosphorylation in cortical or hippocampal lysates derived from Alzheimer's Disease (AD) patients (Braak 4-5) or age-matched controls (age: 80-91 years; male and female).* ***c*** *Quantification of ezrin and phospho Y478/total ezrin ratio. Expression was normalized on tubulin and control. Two-tailed unpaired Student's t-test. N = 4-6 individuals. Graphs display mean ± SEM. Single values are represented as data points. **p < 0.01; *p < 0.05. Samples were kindly provided by Dr. Elena Marcello.*

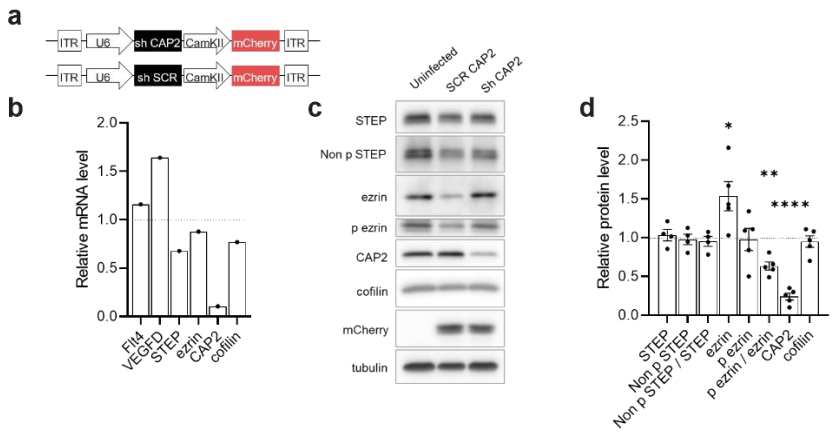

Appendix figure 12. Effect of shRNA-mediated downregulation of CAP2 on VEGFD signaling pathways. *rAAV infection of shRNAs for downregulation of CAP2 expression in cultured mouse hippocampal neurons. A scrambled sh CAP2 sequence (SCR CAP2) served as control.* ***a*** *Schema of rAAV constructs.* ***b*** *QRT-PCR analysis of mRNA expression of indicated genes (Flt4 = VEGFR3) in neurons infected with sh CAP2. Expression was normalized on gusb and SCR CAP2. N = 1 independent culture preparation.* ***c, d*** *Immunoblot analysis in neurons infected as indicated.* ***c*** *Representative immunoblots.* ***d*** *Quantification of protein expression and phosphorylation of indicated proteins in neurons infected with sh CAP2 (p ezrin refers to pY478 ezrin). Expression was normalized on tubulin and SCR CAP2. One sample t-test. N = 4-5 independent culture preparations. Graphs display mean ± SEM. Single values are represented as data points. ****p < 0.0001; **p < 0.01; *p < 0.05.*

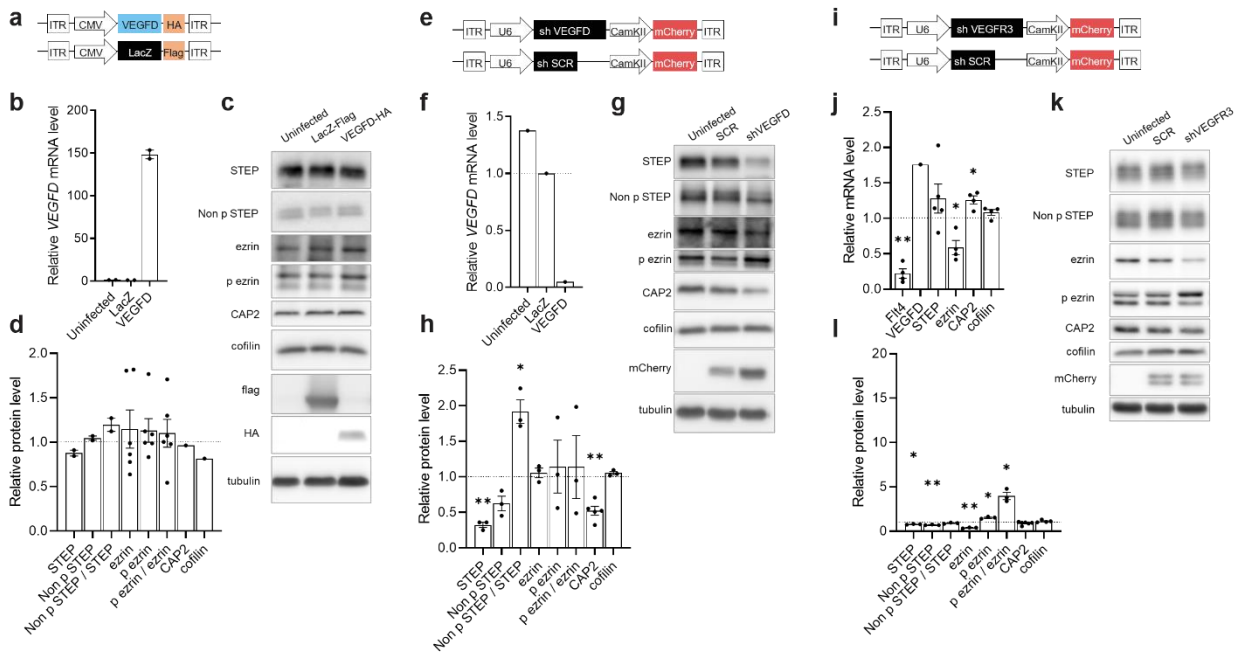

Appendix figure 13. Effect of modulation of VEGFD and VEGFR3 expression on VEGFD and CAP2 signaling pathways. ***a-d*** *rAAV infection to drive overexpression of VEGFD-HA or LacZ-Flag in cultured mouse hippocampal neurons.* ***a*** *Schema of rAAV constructs.* ***b*** *QRT-PCR analysis of VEGFD mRNA expression in neurons infected as indicated. Expression was normalized on gusb and LacZ. N = 2 independent culture preparations.* ***c, d*** *Immunoblot analysis in neurons infected as indicated.* ***c*** *Representative immunoblots.* ***d*** *Quantification of protein expression and phosphorylation of indicated proteins in neurons infected with VEGFD-HA (p ezrin refers to pY478 ezrin). Expression was normalized on tubulin and LacZ. One sample t-test. N = 1-6 independent culture preparations.* ***e-h*** *rAAV infection of shRNAs for downregulation of VEGFD expression in cultured mouse hippocampal neurons. A scrambled sh sequence (SCR) served as control.* ***e*** *Schema of rAAV constructs.* ***f*** *QRT-PCR analysis of VEGFD mRNA expression in neurons infected as indicated. Expression was normalized on gusb and SCR. N = 1 independent culture preparation.* ***g, h*** *Immunoblot analysis in neurons infected as indicated.* ***g*** *Representative immunoblots.* ***h*** *Quantification of protein expression and phosphorylation of indicated proteins in neurons infected with sh VEGFD (p ezrin refers to pY478 ezrin). Expression was normalized on tubulin and SCR. One sample t-test. N = 3-5 independent culture preparations.* ***i-l*** *rAAV infection of shRNAs for downregulation of VEGFR3 expression in cultured mouse hippocampal neurons. A scrambled sh sequence (SCR) served as control.* ***i*** *Schema of rAAV constructs.* ***j*** *QRT-PCR analysis of mRNA expression of indicated genes (Flt4 = VEGFR3) in neurons infected as indicated. Expression was normalized on gusb and SCR. One sample t-test. N = 1-5 independent culture preparations.* ***k, l*** *Immunoblot analysis in neurons infected as indicated.* ***k*** *Representative immunoblots.* ***l*** *Quantification of protein expression and phosphorylation of indicated proteins in neurons infected with sh VEGFR3 (p ezrin refers to pY478 ezrin). Expression was normalized on tubulin and SCR. One sample t-test. N = 3-6 independent culture preparations. Graphs display mean ± SEM. Single values are represented as data points. **p < 0.01; *p < 0.05.*

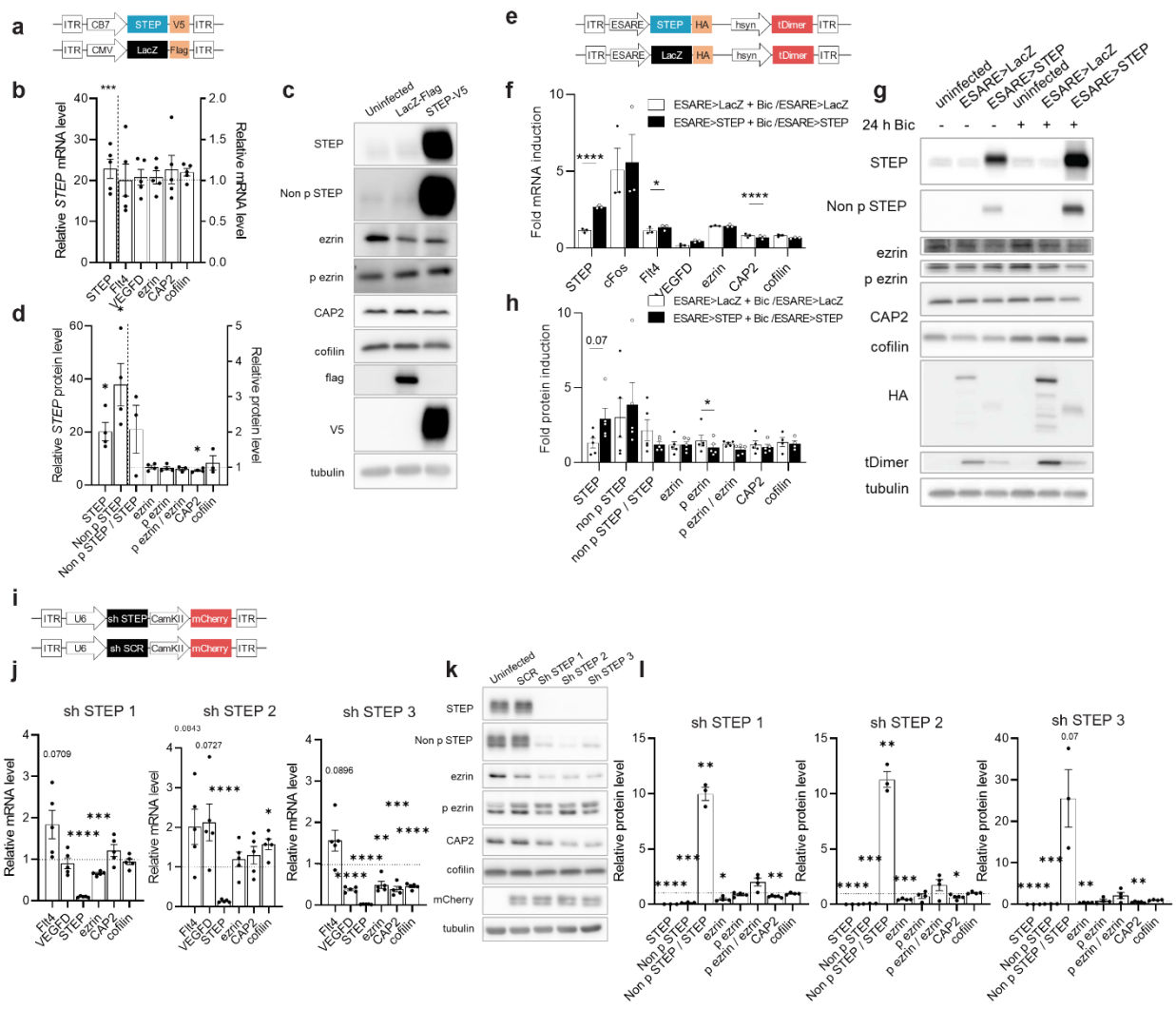

Appendix figure 14. Effect of modulation of STEP expression on VEGFD and CAP2 signaling pathways. ***a-d*** *rAAV infection to drive overexpression of STEP-V5 or LacZ-Flag in cultured mouse hippocampal neurons.* ***a*** *Schema of rAAV constructs.* ***b*** *QRT-PCR analysis of mRNA expression of indicated genes (Flt4 = VEGFR3) in neurons with STEP-V5. Expression was normalized on gusb and LacZ. One sample t-test. N = 5 independent culture preparations.* ***c, d*** *Immunoblot analysis in neurons infected as indicated.* ***c*** *Representative immunoblots.* ***d*** *Quantification of protein expression and phosphorylation of indicated proteins in neurons infected with STEP-V5 (p ezrin refers to pY478 ezrin). Expression was normalized on tubulin and LacZ. One sample t-test. N = 3-4 independent culture preparations.* ***e-h*** *rAAV infection to drive overexpression under the control of the activity-dependent ESARE promoter of STEP-HA or LacZ-HA. Neurons were treated for 24 h with bicuculline (Bic) or not to activate the promoter.* ***e*** *Schema of rAAV constructs.* ***f*** *QRT-PCR analysis of mRNA expression of indicated genes (Flt4 = VEGFR3) in neurons infected and treated as indicated. Expression was normalized on gusb and respective untreated control. Two-tailed unpaired Student's t-test. N = 3 independent culture preparations.* ***g, h*** *Immunoblot analysis in neurons infected and treated as indicated.* ***g*** *Representative immunoblots.* ***h*** *Quantification of protein expression and phosphorylation of indicated proteins (p ezrin refers to pY478 ezrin). Expression was normalized on tubulin and respective untreated control. Two-tailed unpaired Student's t-test. N = 4-5 independent culture preparations.* ***i-l*** *rAAV infection of shRNAs for downregulation of STEP expression in cultured mouse hippocampal neurons. A scrambled sh sequence (SCR) served as control. Three different shRNA sequences were used (sh STEP 1-3).* ***i*** *Schema of rAAV constructs.* ***j*** *QRT-PCR analysis of mRNA expression of indicated genes (Flt4 = VEGFR3) in neurons infected as indicated. Expression was*

normalized on gusb and SCR. One sample t-test. N = 5 independent culture preparations. ***k, l*** *Immunoblot analysis in neurons infected as indicated.* ***k*** *Representative immunoblots.* ***l*** *Quantification of protein expression and phosphorylation of indicated proteins in neurons infected as indicated (p ezrin refers to pY478 ezrin). Expression was normalized on tubulin and SCR. One sample t-test. N = 3-4 independent culture preparations. Graphs display mean ± SEM. Single values are represented as data points. ****p < 0.0001; ***p < 0.001; **p < 0.01; *p < 0.05.*

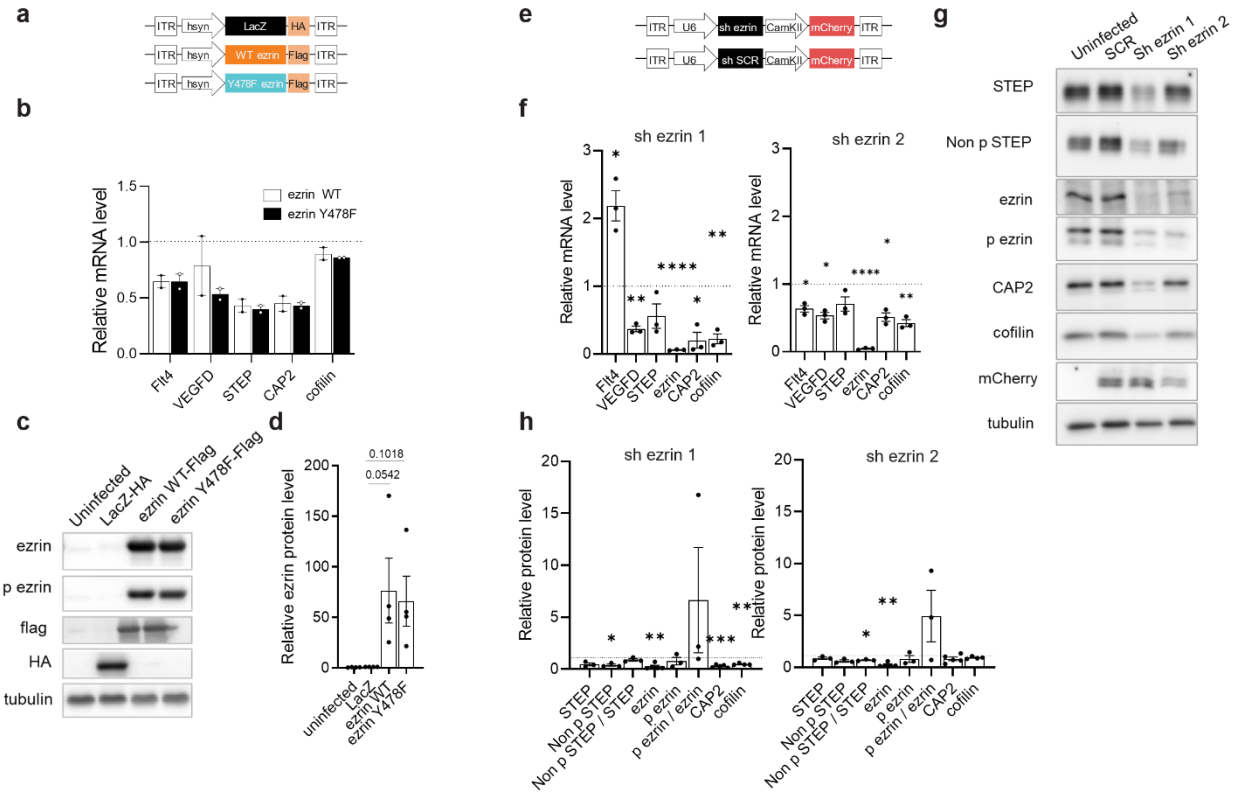

Appendix figure 15. Effect of modulation of ezrin expression and phosphorylation on VEGFD and CAP2 signaling pathways. ***a-d*** *rAAV infection to drive overexpression of wildtype (WT) ezrin-Flag, phospho-mutant Y478F ezrin-Flag or LacZ-HA in cultured mouse hippocampal neurons.* ***a*** *Schema of rAAV constructs.* ***b*** *QRT-PCR analysis of mRNA expression of indicated genes (Flt4 = VEGFR3) in neurons infected as indicated. Expression was normalized on gusb and LacZ. N = 2 independent culture preparations.* ***c, d*** *Immunoblot analysis in neurons infected as indicated.* ***c*** *Representative immunoblots.* ***d*** *Quantification of protein expression and phosphorylation of indicated proteins (p ezrin refers to pY478 ezrin). One-way ANOVA followed by Dunnett's post hoc test.* ***e-h*** *rAAV infection of shRNAs for downregulation of ezrin expression in cultured mouse hippocampal neurons. A scrambled sh sequence (SCR) served as control. Two different shRNA sequences were used (sh ezrin 1, 2).* ***e*** *Schema of rAAV constructs.* ***f*** *QRT-PCR analysis of mRNA expression of indicated genes (Flt4 = VEGFR3) in neurons infected as indicated. Expression was normalized on gusb and SCR. N = 3 independent culture preparations.* ***g, h*** *Immunoblot analysis in neurons infected as indicated.* ***g*** *Representative immunoblots.* ***h*** *Quantification of protein expression and phosphorylation of indicated proteins (p ezrin refers to pY478 ezrin). Expression was normalized on tubulin and SCR. One sample t-test. N = 3-5 independent culture preparations. Graphs display mean ± SEM. Single values are represented as data points. ****p < 0.0001; ***p < 0.001; **p < 0.01; *p < 0.05.*